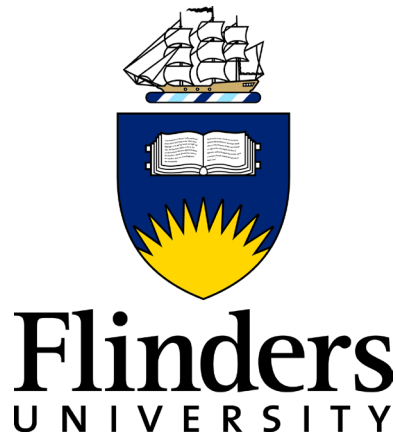


Fabrication and Application of Carbon Nanotube/Silicon Nanostructures



Thesis submitted to the School of Chemical and Physical Sciences,

Faculty of Science and Engineering, Flinders University

in fulfilment of the requirements for the degree of

Doctor of Philosophy

October 2011

Cameron J. Shearer

Supervisors: Joe Shapter, Amanda Ellis and Nico Voelcker

The best things in life are beyond money, their price is agony and sweat and devotion...

- Robert A. Heinlein in *Starship Troopers*

The Scientific man does not aim at an immediate result. He does not expect that his advanced ideas will be readily taken up. His work is like that of the planter – for the future. His duty is to lay the foundation for those who are to come, and point the way. He lives and labours and hopes.

- Nikola Tesla

Any sufficiently advanced technology is indistinguishable from magic.

- Arthur C. Clarke

Table of contents

Table of contents.....	i
Summary	vii
Declaration.....	ix
Acknowledgements.....	xi
List of figures.....	xiii
List of tables	xxv
Glossary of abbreviations	xxvii
List of publications.....	xxix
Chapter 1	
Introduction.....	1
1.1 Overview	2
1.2 Carbon nanotubes.....	5
1.2.1 History and structure.....	5
1.2.2 Properties and applications	9
1.2.3 Synthesis	12
1.3 Silicon	15
1.3.1 Bulk silicon.....	15
1.3.2 Porous silicon.....	16
1.4 Chemical attachment of carbon nanotubes to surfaces.....	20
1.4.1 Carbon nanotube chemistry	20
1.4.2 Carbon nanotube surface attachment.....	20
1.4.3 Experimental results	22
1.5 Carbon nanotubes for water filtration	25
1.5.1 Background.....	25
1.5.2 Theoretical studies	26
1.5.3 Experimental studies.....	29

1.6	Field emission from carbon nanotubes.....	35
1.6.1	Background and theory	35
1.6.2	Field emission from carbon nanotubes.....	39
1.7	Carbon nanotubes as biointerfacial substrates.....	45
1.7.1	Background	45
1.7.2	Carbon nanotube biointerfaces	45
1.8	Motivation	51
1.9	References	52

Chapter 2

Experimental details	65	
2.1 Carbon nanotubes.....	66	
2.1.1	Single-walled carbon nanotubes..... 66	
2.1.2	Carbon nanotube filtration..... 66	
2.1.3	Carbon nanotube suspension in dimethyl sulfoxide..... 66	
2.1.4	Double-walled carbon nanotubes	67
2.1.5	Multi-walled carbon nanotubes	67
2.2 Silicon.....	68	
2.2.1	Silicon hydroxylation	68
2.2.2	APTES monolayer formation on silicon	68
2.2.3	Porous silicon fabrication.....	69
2.2.4	APTES monolayer formation on porous silicon	69
2.3 CNT chemical attachment to silicon.....	71	
2.3.1	Direct ester attachment of CNTs to Si.....	71
2.3.2	APTES mediated attachment of CNTs to Si	72
2.3.3	Ester attachment of CNTs to pSi.....	73
2.3.4	APTES mediated attachment of CNTs to pSi	74
2.3.5	Patterned attachment of SWCNTs	74
2.4 CNT growth by chemical vapour deposition.....	76	
2.5 Surface characterisation techniques.....	78	
2.5.1	Atomic force microscopy (AFM).....	78

2.5.2	Scanning electron microscopy (SEM)	79
2.5.3	Confocal Raman spectroscopy and spectral imaging	80
2.5.4	X-ray photoelectron spectroscopy (XPS)	85
2.5.5	Fourier transform infrared (FTIR) spectroscopy and microscopy....	86
2.5.6	Contact angle	86
2.6	References	88

Chapter 3

Device fabrication	89
3.1 Introduction	90
3.2 SWCNT attachment to silicon	92
3.2.1 Chemical functionalisation of SWCNTs	92
3.2.2 Direct ester attachment of SWCNTs to silicon.....	93
3.2.3 Attachment of SWCNTs to APTES functionalised Si	99
3.3 SWCNT attachment to pSi	102
3.3.1 Porous silicon.....	102
3.3.2 Direct ester attachment of SWCNTs to pSi.....	104
3.3.3 Attachment of SWCNTs to APTES functionalised pSi	105
3.4 DWCNT attachment to silicon	111
3.4.1 Chemical functionalisation of DWCNTs.....	111
3.4.2 Attachment of DWCNTs to silicon	112
3.5 MWCNT attachment to silicon.....	115
3.5.1 Chemical functionalisation of MWCNTs.....	115
3.5.2 Attachment of MWCNT to silicon	116
3.6 CNT growth via chemical vapour deposition.....	118
3.7 Conclusions.....	125
3.8 References	126

Chapter 4

Controlled carbon nanotube placement.....	131
4.1 Introduction	132

4.2	Experimental methods	135
4.2.1	Fabrication of pSi with pore size gradient.....	135
4.2.2	Fabrication of an APTES gradient	135
4.3	Patterned attachment of SWCNTs	137
4.4	SWCNT surface coverage gradients.....	143
4.4.1	pSi topographical gradient.....	143
4.4.2	APTES chemical gradient	148
4.5	Conclusions.....	154
4.6	References	155

Chapter 5

Mass transport through CNT and pSi membranes	159	
5.1	Introduction	160
5.2	Experimental details.....	164
5.2.1	Fabrication and functionalisation of pSi membranes	164
5.2.2	Dye transport properties through pSi membranes.....	165
5.2.3	Water transport.....	166
5.2.4	Fabrication of SWCNT membrane.....	167
5.3	Mass transport through pSi.....	169
5.3.1	Fabrication and characterisation of pSi membranes.....	169
5.3.2	Dye transport and selectivity properties of functionalised pSi membranes	175
5.3.3	Pressure driven water transport through pSi membranes.....	181
5.4	Mass transport through SWCNT membrane	183
5.4.1	Fabrication of SWCNT membrane.....	183
5.4.2	Water transport through SWCNT membrane.....	193
5.5	Conclusions.....	200
5.6	References	201

Chapter 6

Field emission from CNT electrodes	203
---	------------

6.1	Introduction	204
6.2	Experimental details	206
6.3	Field emission from SWCNTs	208
6.3.1	Effect of SWCNT attachment time.....	208
6.3.2	Field emission from polymer encapsulated SWCNTs.....	213
6.4	Field emission from DWCNTs and MWCNTs	215
6.5	Field emission stability from CNTs.....	219
6.5.1	SWCNT field emission stability.....	219
6.5.2	DWCNT field emission stability.....	227
6.5.3	MWCNT field emission stability.....	229
6.6	Conclusions.....	232
6.7	References	233

Chapter 7

	CNTs as biointerfacial substrates.....	235
7.1	Introduction	236
7.2	Experimental details	238
7.2.1	SWCNT biointerface fabrication.....	238
7.2.2	Cell culture and staining.....	238
7.2.3	Fluorescence microscopy.....	239
7.2.4	Gene transfection by permeabilisation	240
7.2.5	Gene transfection by electroporation.....	240
7.3	Cell immobilisation	242
7.3.1	Cell morphology and proliferation	242
7.3.2	AFM and SEM imaging.....	249
7.4	Gene transfection.....	252
7.4.1	Gene transfection by permeabilisation	252
7.4.2	Gene transfection by electroporation.....	261
7.5	Conclusions.....	266
7.6	References	267

Chapter 8

Conclusions	271
8.1 Conclusions.....	272
8.2 Future directions	274
8.3 References	280

Summary

The amazing electrical and mechanical properties of carbon nanotubes (CNTs) make them ideal for use in a variety of applications, many of which require the CNTs to be surface bound. Here the applicability of nanostructures based upon CNTs chemically attached to silicon to the fields of water filtration, field emission and as biomaterial interfaces is investigated.

Initial experiments studied the chemical attachment and alignment of different CNT types to silicon. Single-walled carbon nanotubes (SWCNTs) were found to form vertically aligned arrays on both flat silicon and porous silicon (pSi). Double-walled carbon nanotubes (DWCNTs) were found to exhibit both vertical and random alignment while multi-walled carbon nanotubes (MWCNTs) exhibited an exclusive horizontal orientation. The variation in alignment is attributed to the level of crystallinity and functionalisation of each CNT type as determined by Raman spectroscopy.

The control of the placement of SWCNTs on silicon was further investigated by fabricating both surface coverage gradients and patterns of SWCNTs. Gradients were fabricated following two protocols, both of which produced surfaces which consist of all possible SWCNT coverage's. SWCNT patterns were produced by forming an initial chemical pattern on the silicon surface for subsequent selective SWCNT chemical attachment.

CNT membranes for water filtration were fabricated by chemically attaching SWCNTs to permeable pSi membranes. Gaps between the SWCNTs were filled by spin coating polystyrene onto the surface. The SWCNT tips were revealed by etching the polystyrene matrix via water plasma treatment. The fabricated membranes were found to have a water permeability of $0.022 \text{ mm}^3 \text{ cm}^{-2} \text{ s}^{-1} \text{ atm}^{-1}$. Comparisons to commercial nanofiltration membranes and other published CNT membranes are made and improvements to membrane fabrication are discussed.

Field emission experiments were completed for all CNT types chemically attached to silicon. All samples exhibited field emission of electrons with characteristics varying with CNT diameter and vertical alignment. The emission

stability of each CNT type was investigated with the SWCNTs exhibiting the most stable emission. Comparison of emission characteristics and stability to other CNT field emission substrates are made.

The behaviour of a mammalian neuronal cell line on SWCNTs chemically attached to porous silicon was investigated. Fluorescence microscopy revealed that the cells had a strong affinity for the SWCNT substrate and that the SWCNTs may compromise the cell membrane allowing small fluorescent molecules to enter the nuclear envelope. Experiments to determine if plasmid DNA could be inserted into the cell via the SWCNTs was completed with results indicating the SWCNTs did not promote DNA transfection for the neuronal cell line.

Declaration

I certify that this Thesis does not incorporate without acknowledgment any material previously submitted for a degree or diploma in any university; and that to the best of my knowledge and belief it does not contain any material previously published or written by another person except where due reference is made in the text.

Cameron J. Shearer

Acknowledgements

This Thesis would not have been possible without the assistance of many people who I should acknowledge. Chapter 1 contains parts of a review article published in *Advanced Materials*; this work was co-authored with Kristina Constantopoulos, Amanda Ellis, Nico Voelcker and Joe Shapter. The pattern work presented in Chapter 4 was inspired by an original idea of Ben Flavel, Martin Sweetman then came up with a protocol to form silane patterns which I then used for nanotube attachment. The porous silicon membrane dye transport in Chapter 5 was completed by Leonora Velleman, she also analysed and interpreted the data. The pressure driven water transport, also in Chapter 5, was completed at the University of Bath in the laboratory of Davide Mattia with the help of Fernando Acosta. An ARNAM student travel grant assisted in the travel and accommodation costs for that trip. The field emission experiments shown in Chapter 6 were all completed at the University of Newcastle. I would like to thank Paul Dastoor for allowing me to visit on three occasions. The field emission experiments were assisted originally by Kane O'Donnell and Lars Thomsen, and by Adam Fahy and Matthew Barr on the final visit. The field emission work would never have been completed without the influence of Jamie Quinton, and I thank him for making the most enjoyable and successful aspect of my PhD possible. Fran Harding completed most of the cell culture, cell staining and fluorescence microscopy in Chapter 7, the remainder was completed by Qi Peng. The data presented in Chapter 7 was largely championed by Nico Voelcker who urged collaboration between Fran and myself which became a nice side-project to focus upon when other experiments weren't going as hoped.

I have had the privilege to work in the Smart Surface Structures group at Flinders. Despite only having a single fumehood and rarely containing a post-doc we seem to meet or beat the output of any other group. I think this is largely in part to the hard working culture imparted by Matt Nussio and Ben Flavel. Mark, Lachlan, Chris, Kate, Sam, Anders, Adam, Dan, Ash and others I have forgotten have all been fun to work with. I also spent some time in the Voelcker lab, particularly early in my PhD, where I was helped immensely by the pilots in the cockpit: Steve, Martin and Andy J.

Final professional thank you goes to my supervisors. Amanda and Nico were always willing to chat with me about my research and give advice when requested. Joe has been the perfect supervisor for me; his adaptability has suited my varying style perfectly. When I wanted meetings, Joe would make himself available. When I didn't want meetings, Joe was content to have five minute chats. Thanks for making the entire PhD as stress free and enjoyable as possible.

I am lucky to have two families that have helped me throughout these years of study. Both my parents and Lauren's parents have been happy for me to be poor for another few years in the hope that I will eventually get a real job. I am extremely lucky to have Lauren in my life, she has been very supportive and happy to be the bread winner for the past few years. Hopefully I can repay your kindness in the future.

List of Figures

- Figure 1.1:** Comparison of (a) top-down and (b) bottom-up approaches toward miniaturisation. In (a), miniature bulls were fabricated following a two-photon polymerisation technique, scale bars, 2 μm . In (b), individual xenon atoms are moved using a scanning tunnelling microscope to form 0.5 nm high letters.....3
- Figure 1.2:** ‘Ball and stick’ representation of (a) single-walled CNT (SWCNT), (b) double-walled CNT (DWCNT) and (c) multi-walled CNT (MWCNT). Images made using Nanotube Modeller (www.jcrystal.com).6
- Figure 1.3:** (a) Schematic of unrolled SWCNT showing chiral vector C and how different values of the integers n and m affect the electronic property of the SWCNT. (b, c, d) The direction of the chiral vector affects the appearance of the nanotube showing (b) (4,4) armchair shape, (c) (6,0) zig-zag shape and (d) (5, 3) example of a chiral shape.....8
- Figure 1.4:** (a, b, c, d) Band structures in reciprocal space, as calculated by the tight binding method, of (a, b) graphene, (c) metallic (4, 4) SWCNT, (d) semi-conducting (5, 3) SWCNT showing the wave-vectors as yellow lines and the K-points (Fermi-level points) as red dots. The blue dot represents energy maxima and the pink points represent saddle (M) points. (e, f) represent electronic band structures of (e) (4, 4) metallic nanotube where wave vectors cross a K-point and (f) (5, 3) semiconducting nanotube where no wave vectors cross a K-point.....9
- Figure 1.5:** Summary of CNT synthesis methods (a) arc discharge, (c) laser ablation, and (e) chemical vapour deposition along with SEM images (b, d, f) showing the morphology of the CNTs produced. Scale bar in (d) 100 nm.13
- Figure 1.6:** Schematic of the band diagrams of (a) n-type and (b) p-type semiconductors under no bias and negative bias.16
- Figure 1.7:** (a) Schematic of the etching cell used for the anodic etching of silicon. (b) Top-down SEM of porous silicon showing the irregularly shaped pores produced.17
- Figure 1.8:** Porous silicon formation mechanism showing (a) reaction steps and (b) hole migration during pore formation.....18
- Figure 1.9:** Basic reaction scheme of the mechanism of DCC (red) assisted coupling of carboxylic acid functionalised CNTs (molecule 1, black) to amines, alcohols and thiols (molecule 3, blue).(a) The starting carboxylic acid (1) reacts with DCC to form an activated ester (2). (c) This can rearrange to form the stable unwanted by-product N-acylurea (6) or (b) it can undergo nucleophilic attack from the electron rich N, O or S to form a stable amide, ester or thioester linkage to the R_2 group (5).21

Figure 1.10: Schematics and published AFM images of SWCNTs chemically attached to (a) gold via a cystamine linkage, (b) silicon via direct ester linkage, and (c) patterned amine terminated silane on silicon.	23
Figure 1.11: Water occupancy inside a SWCNT (a) structure of hydrogen bonded chain of water molecules within the SWCNT and (b) probability distribution of water binding energies of (red) confined and (blue) bulk water, the coloured arrows indicate average binding energies.....	27
Figure 1.12: Schematic of the fabrication process of aligned MWCNT membranes by Hinds <i>et al.</i>	30
Figure 1.13: Schematic of the DWCNT membrane fabrication of Holt <i>et al.</i>	32
Figure 1.14: Field emission models showing how the shape of the potential barrier changes for (a) no field (b) an electric field, (c) a larger electric field and (d) when the Coulomb potential is included in the calculation.....	36
Figure 1.15: (a) SEM of SWCNT deposited from a paste, (b) J-V curves and (c) emission stability from varying plasma treatments.	43
Figure 1.16: (a, b, c) SEM images depicting the attachment of cells to a carpet of VA-CNTs. (a) The tips of the VA-CNTs are in intimate contact with the cell surface. (b) The bending and deformation of the tubes is occurring via biomechanical forces. (c) Neuronal cells adhere preferentially to isolated islands of pristine CNTs. (d) Confocal fluorescence image of neurons (red) and glia cells (green) on a large CNT island. Scale bar in (c, d) 10 μm	46
Figure 1.17: Schematics of electroporation. (a) Cells in suspension or (b) cells immobilised on a surfaces are exposed to an electric field in order to deliver target material.	49
Figure 1.18: Summary of results of electroporation on MWCNT showing (a) AFM image of randomly oriented MWCNTs on surface ($5 \times 5 \mu\text{m}^2$). Fluorescence microscopy images after electroporation and gene transfection of a green fluorescent plasmid showing (b) control surface without MWCNTs and (c) a MWCNT surface. Green cells in (b, c) indicate gene transfection, images $1.5 \times 1.5 \text{ mm}^2$	50
Figure 2.1: Schematic of the porous silicon etching cell.....	69
Figure 2.2: Schematic of the direct ester attachment of CNTs to silicon.	71
Figure 2.3: Schematic of the APTES mediated attachment of CNTs to silicon.....	72
Figure 2.4: Schematic of the direct ester CNT attachment to pSi.	73

Figure 2.5: Schematic of APTES mediated attachment of CNTs to pSi	74
Figure 2.6: Schematic of patterned attachment of SWCNTs to silicon.....	75
Figure 2.7: Schematic of CNT growth by chemical vapour deposition.	76
Figure 2.8: Schematic of AFM operation.....	78
Figure 2.9: Summary of possible scattering processes.....	81
Figure 2.10: (a) Cross sectional view of a SWCNT showing the radial vibration of the RBM, with (b) vibration of D-band, and (c) vibrations of G-band with G ⁺ peak arising from vibrations along the tube axis and G ⁻ peak arising from vibrations around the circumference of the tube.....	82
Figure 2.11: Schematic of principle set up of Raman microscope. Image modified from supplier.....	83
Figure 2.12: Example of how Raman spectral image is created from many individual spectra.....	84
Figure 2.13: Example of water contact angle measurement showing (a) original image and (b) after analysis using the Image J plugin DropSnaker where blue dots were manually inserted and red dots were inserted by the software to give output values.....	87
Figure 3.1: (a, b) SEM images (XL-30) of (a) pristine SWCNTs as purchased and (b) SWCNTs ‘cut’ for 8 hr, as described in Chapter 2. (c, d) Photographs of SWCNTs dispersed in DMSO after 1 day of incubation. (c) Pristine SWCNTs and (d) cut SWCNTs.....	92
Figure 3.2: AFM images of SWCNTs attached to silicon via an ester linkage with varying silicon hydroxylation methods, (a,b) 2-step base-acid method, (c) ozone treated and (d) Piranha treated. AFM images are 5 x 5 μm ² with a z scale of 50 nm.....	95
Figure 3.3: Graphs of (a) normalised SWCNT coverage and (b) average SWCNT bundle diameter vs. SWCNT attachment time, as determined by AFM. Dashed lines added to guide the eye.....	96
Figure 3.4: (a) Raman spectral image and (b) Raman spectrum of SWCNTs chemically attached to silicon via ester attachment. Raman spectrum average of 2 x 120 sec accumulation.....	98
Figure 3.5: WCA photographs of (a) Piranha treated silicon and (b) APTES modified silicon.....	99

Figure 3.6: AFM images of SWCNTs attached to silicon via APTES monolayer (a) top down and (b) 3-D. AFM images are $5 \times 5 \mu\text{m}^2$ with a z scale of 50 nm.....	100
Figure 3.7: (a) Raman spectral image and (b) Raman spectrum of SWCNTs chemically attached to silicon via an APTES monolayer. Raman spectrum average of 2 x 120 sec accumulations.....	101
Figure 3.8: AFM image of freshly etched pSi. Etching conditions: 1:1 (v/v) HF/ethanol, 66 mA, 120 sec.....	102
Figure 3.9: FTIR spectra of pSi, which has been (a) freshly etched, (b) ozone oxidised (45 min) and (c) wet chemical oxidised (Piranha solution). Spectra in (b) are offset for clarity.....	103
Figure 3.10: AFM image of SWCNTs chemically attached to pSi following the direct ester attachment method on Piranha-oxidised pSi.....	104
Figure 3.11: Schematic representation of (a) oxidised pSi, (b) oxidised pSi after reaction with a carboxylic acid containing molecule (eg., ‘cut’ SWCNT), (c) oxidised pSi after APTES immobilisation and (d) pSi after APTES immobilisation and carboxylic acid attachment.....	105
Figure 3.12: Transmission FTIR spectra of hydroxylated pSi substrates (ozone; 10 min) followed by (a) APTES functionalisation and (b) SWCNT attachment to APTES monolayer (24 hr attachment time). Inset shows zoom of amine peak area (3500 cm^{-1} to 3100 cm^{-1}) for the APTES functionalised pSi substrate. Spectra offset for clarity.....	106
Figure 3.13: AFM images of (a) pSi after 5 min of APTES treatment (0 % surface coverage, $5 \times 5 \mu\text{m}^2$, z scale 50 nm) and SWCNT attachment on APTES functionalised pSi ($5 \times 5 \mu\text{m}^2$ images, z scale 50 nm) for attachment times of (b) 5 min (18 % coverage), (c) 1 hr (48 % coverage), (d) 24 hr (52 % coverage) and (e) 3D image of (c) after 1 hr attachment.....	108
Figure 3.14: Change in percentage surface coverage with incubation time of APTES silanised pSi wafer in a SWCNT solution. Dashed line added to guide the eye.....	109
Figure 3.15: (a) Raman spectral image of SWCNTs chemically attached to pSi via the APTES attachment method and (b) Raman spectrum of SWCNTs on pSi showing the high background fluorescence of pSi. Spectrum average of 3 x 60 sec.....	110
Figure 3.16: SEM images (XL-30) of (a) pristine DWCNTs and (b) cut/functionalised DWCNTs and (c) Raman spectrum of pristine DWCNTs with zoom of RBM region (inset). Raman spectrum average of 2 x 120 sec accumulations.....	112

Figure 3.17: (a) Top down and (b) 3-D AFM as well as (c) Raman spectra of DWCNTs chemically attached to silicon with zoom showing RBM region (inset). Raman spectrum average of 2 x 60 sec accumulations.....	114
Figure 3.18: AFM images of (a) ‘cleaned’ MWCNTs and (b) Cut MWCNTs using the ‘3-acid cutting system’ drop-cast onto a silicon wafer. AFM images are 5 x 5 μm^2 with a z scale of 50 nm.....	115
Figure 3.19: (a, b) AFM images and (c) Raman spectrum of MWCNTs chemically attached to silicon via (a) direct ester attachment and (b, c) APTES mediated attachment. AFM images are 5 x 5 μm^2 with a z scale of 50 nm, Raman spectrum is the average of 2 x 120 sec acquisitions.....	117
Figure 3.20: SEM images (CamScan) of CNTs grown on silicon via CVD showing (a, b) vertical alignment, (c) zoom of side view of VA-CNTs and (d) randomly oriented CNTs.....	118
Figure 3.21: (a) Raman spectral image of CNTs grown on silicon via CVD and (b) Raman spectrum of the CVD grown CNTs. Raman spectrum is the average of 3 x 30 sec acquisitions.....	119
Figure 3.22: (a, c) AFM and (b, d) section analysis of 3 nm iron sputtered onto a silicon surface (a, b) fresh and (c, d) after heating to 750 °C under pre-CNT growth conditions.....	121
Figure 3.23: (a, c) AFM and (b, d) section analysis of (a, b) silicon surface with 10 nm of aluminium and 3 nm of iron after heating to 750 °C under pre-CNT growth conditions and (c, d) silicon surface with 10 nm of Al sputtered.....	122
Figure 3.24: Plot showing recorded temperature within tube furnace for varying input temperatures from 750 °C (red series) to 680 °C (green series) and 650 °C (blue series).....	124
Figure 4.1: Schematic illustrating the fabrication process of SWCNT patterns and gradients. (a) APTES patterning via photolithography to produce a SWCNT gradient, (b) a topographical gradient created by the asymmetric anodisation of silicon and (c) a chemical gradient created by vapour phase diffusion of APTES onto oxidised silicon.....	134
Figure 4.2: Etching cell configurations for the fabrication of ‘normal’ (left) and gradient (right) pSi.....	135
Figure 4.3: Schematic of the apparatus used for APTES gradient fabrication (top view).....	136
Figure 4.4: SEM images of photoresist patterns on silicon showing various shapes and sizes of patterns.....	137

Figure 4.5: IR mapping of APTES pattern on pSi showing (a, b) spectra of points (a) within and (b) outside of pattern (insets) with insets showing peaks of interest in more detail, (c) IR spectral map obtained by mapping peak height at 1505 cm^{-1} (indicated by * in (a, b) with (d) optical image of area and (e) overlay of spectral map over optical image.	139
Figure 4.6: Raman spectral images of SWCNT patterns on silicon. (a, b) half-half surface patterns with (a) bare silicon side and (b) Si-APTES-SWCNT side. (c) Optical microscope image of area of investigation for attachment of (c, d) SWCNTs to patterned APTES on silicon.	141
Figure 4.7: (a) Photograph of gradient pSi film indicating the three regions: (region 1) closest to electrode, (region 2) middle region and (region 3) furthest from the electrode. (b) Tapping mode AFM images showing pore size decreasing with distance from the Pt electrode. Scale bars = 500 nm.	143
Figure 4.8: Tapping mode AFM height images of SWCNTs attached to gradient pSi surfaces etched at (a) 40 mA (b) 50 mA, (c) 55 mA and (d) 60 mA showing (i) region 1, (ii) region 2 and (iii) region 3. Scale bars = 1 μm	146
Figure 4.9: Plots showing SWCNT coverage as a function of (a) the average and (b) the maximum pore size of the pSi surface.	147
Figure 4.10: (a) Digital photographs and (b) WCA values of water droplets deposited at increasing distance (from 5 – 30 mm at 5 mm intervals) from the APTES-filled reservoir.	148
Figure 4.11: Raman spectral images of G-band peak intensity at different distances from the APTES-filled reservoir on the SWCNT-decorated gradient. Scale bar = 4 μm	149
Figure 4.12: Change in average Raman G-band peak intensity with distance from APTES-filled reservoir after SWCNT covalent attachment without backfill.	150
Figure 4.13: Raman spectral images of G-band peak intensity of SWCNTs immobilised on APTES gradient after PTMS backfilling of silicon wafer at increasing distances from the APTES-filled reservoir. Scale bar 4 = μm	152
Figure 4.14: (a) Change in average Raman G-band peak intensity with distance from APTES-filled reservoir after SWCNT covalent attachment with PTMS backfill (inset) zoom of area from 15 to 20 mm. (b) Plot of average G-band peak intensity vs. WCA. The dashed line serves as a guide to the eye.	153
Figure 5.1: Comparison of CNT membrane fabrication procedures followed by (a) Hinds <i>et al.</i> and (b) Holt <i>et al.</i> Detail of fabrication given in Section 1.5.3.	161
Figure 5.2: Schematic of the assembly of a SWCNT membrane supported on a pSi substrate.	163

Figure 5.3: Schematic of the chemical modification of pSi membranes with (a) the hydrophobic fluorinated silane (PFDS), (b) the hydrophilic silane (PEGS) and (c) APTES for SWCNT attachment.	165
Figure 5.4: (a, b) Schematic of U-tube configuration used for dye diffusion experiments with the pSi membrane separating the feed and permeate cells. (a) initial configuration with solvent only in the permeate cell and (b) after experiment completed with dye in permeate cell. Structure of the two dyes investigated (c) the hydrophobic dye Rubpy and (d) the hydrophilic Rose Bengal (RB).	166
Figure 5.5: Schematic of pressure driven water transport apparatus.	167
Figure 5.6: Photographs of pSi membranes (a) attached to the silicon wafer and (b) lifted off the silicon wafer.	169
Figure 5.7: SEM images of (a) top and (b) bottom of pSi membrane, (c, d) side views of entire layer (c) and zoom of edge, and (e) pore size distribution graph from the top layer of pSi. Images (a, b, d) from the NanoLab SEM while (c) was from the CamScan.	171
Figure 5.8: XPS analysis of silanes on pSi membranes (red series) pSi-PFDS and (black series) pSi-PEGS.	173
Figure 5.9: High resolution XPS spectra of the C 1s peak from (red series) pSi-PFDS and (black series) pSi-PEGS.	174
Figure 5.10: FTIR spectra of pSi (blue series) ozone oxidised, (red series) pSi-PFDS and (black series) pSi-PEGS.	175
Figure 5.11: Transport of a hydrophobic (Rubpy, green series) and hydrophilic (RB, purple series) dye through pSi membranes. Where (a) is an unfunctionalised membrane, (b) is a hydrophobic (PFDS) functionalised membrane and (c) is a hydrophilic (PEGS) functionalised membrane.	176
Figure 5.12: Dye transport experiments of (I) Rubpy and (II) RB through (a) unfunctionalised pSi, (b) hydrophobic pSi-PFDS and (c) hydrophilic pSi-PEGS at three different initial dye concentrations.	177
Figure 5.13: Pressure driven water transport through (blue series) unfunctionalised and (red series) PFDS (hydrophobic) functionalised pSi at a constant applied pressure (inset).	182
Figure 5.14: Top down (a, c, e) and 3-D (b, d, f) AFM images of SWCNTs on pSi membrane surfaces. Figures (a, b) depict a pSi membrane surface after 1 hr of SWCNT attachment, (c, d) is the same surface after sonication in acetone to remove physisorbed SWCNTs, and (e, f) is a different pSi membrane after 2 hr of SWCNT attachment and sonication in acetone.	185

Figure 5.15: (I) AFM (II) AFM cross sectional analysis and (III) 10 x optical microscope images of polystyrene films spun onto silicon with increasing water plasma etching time: (a) 0 min, (b) 1 min, (c) 2 min, and (d) 3 min.	187
Figure 5.16: (I) Aerial AFM image (5 x 5 μm , z scale 50 nm), (II) 3-D AFM image, (III) AFM image of scratched cross and (IV) cross section analysis of polystyrene spun onto VA-SWCNTs on pSi surfaces including (a) before water plasma exposure, (b) after 1 min of water plasma exposure and (c) after 2 min of water plasma exposure.	189
Figure 5.17: (I) Optical microscope, (II) aerial (5 x 5 μm , z scale 50 nm) and (III) 3-D AFM images of different areas (a, b, c, and d) of the same sample prepared by chemically attaching SWCNTs to a permeable pSi membrane and depositing a thin film of polystyrene.	191
Figure 5.18: Schematic of effect of substrate on polymer deposition. (a) pSi film supported on Si substrate leads to even thin polymer film while for (b) the pSi membrane the vacuum can affect the polymer resulting in a inhomogeneous polymer film.	192
Figure 5.19: (a) Aerial AFM (5 x 5 μm , z scale 50 nm), (b) optical microscope image, and (c) 3-D AFM image of PS thin film deposited by the ‘spin-drop’ method onto a pSi membrane-SWCNT substrate.	193
Figure 5.20: Schematic of SWCNT membranes prepared. (a) bare pSi membrane with PS thin film deposited and pSi membrane with attached VA-SWCNTs with PS deposited before (b) and after (c) water plasma exposure.	194
Figure 5.21: Summary of pressure driven water flow through pSi-PS sample showing (a) mass of water transported and (b) applied pressure vs. time.	195
Figure 5.22: Summary of water flow through pSi-SWCNT-PS (1 min water plasma) showing (a) raw data of mass of water collected (b) applied pressure (c) zoom of area from 2.1 to 3.4 hr, and (d) scale drift removed data vs. time.	196
Figure 6.1: Schematic of prepared samples for field emission studies.	205
Figure 6.2: Field emission system at the University of Newcastle showing (a) ultra-high vacuum chamber, (b) power supply and picoammeter, (c) sample stage configuration and (d) schematic of field emission experimental apparatus.	206
Figure 6.3: Field emission sweeps for SWCNT chemically anchored to n-type silicon for varying SWCNT attachment times with (inset) Fowler-Nordheim plots.	208
Figure 6.4: Graphs of effect of SWCNT attachment time on (a) electric field enhancement factor (β) and (b) the turn-on voltage (E_{t0}).	210

Figure 6.5: J-F curve attempting to achieve maximum current output for Si-SWCNT surface. Maximum wattage output of power supply reached before maximum current from sample.....	212
Figure 6.6: FE sweeps for SWCNT surfaces with varying thickness of polystyrene.....	214
Figure 6.7: (a, b, c) Aerial and (d, e, f) 3-D AFM images of (a, d) SWCNTs, (b, e) DWCNTs and (c, f) MWCNTs chemically attached to silicon. White circles in (b) indicate laying down DWCNTs while black circles indicated VA-DWCNTs.....	215
Figure 6.8: Summary of field emission (I) J-F sweeps and (II) F-N plots for different CNT types chemically attached to silicon showing (a) low current and (b) high current sweeps.	217
Figure 6.9: A 60 hr FE stability test of a Si-SWCNT surface with a constant current of $10 \mu\text{A}$ ($\sim 10 \mu\text{A cm}^{-2}$).....	220
Figure 6.10: A 60 min FE stability test of FE from a Si-SWCNT surface at a current density of $\sim 110 \mu\text{A cm}^{-2}$	221
Figure 6.11: A 15 hr FE stability test of a Si-SWCNT surface at a constant current density output of $780 \mu\text{A cm}^{-2}$	223
Figure 6.12: FE stability of a Si-SWCNT surface coated with a thin film of PS.	225
Figure 6.13: Consecutive FE stability experiments from Si-SWCNT-polystyrene electrodes showing the change in time for the roll-off behaviour to occur.	226
Figure 6.14: FE stability of a DWCNT electrode at $80 \mu\text{A cm}^{-2}$ over 70 min.....	227
Figure 6.15: FE stability of a Si-DWCNT electrode at $\sim 80 \mu\text{A cm}^{-2}$ over 15 hr.....	228
Figure 6.16: FE stability of a Si-MWCNT electrode at $10 \mu\text{A cm}^{-2}$ for 45 min.....	230
Figure 7.1: Schematic detailing the preparation of (a) a SWCNT-decorated pSi substrate surface and (b) a patterned pSi-SWCNT substrate surface and the resulting attachment of neuroblastoma cells (SK-N-SH). Both preparation schemes involve the chemical attachment of SWCNTs to an amino silane (APTES) on pSi via carbodiimide (DCC) assisted coupling.	237
Figure 7.2: Schematic of the electroporation apparatus.....	241
Figure 7.3: Fluorescence microscopy images of phalloidin stained SK-N-SH neuroblastoma cells immobilised on (a, d) oxidised pSi, (b, e) APTES-functionalised pSi and (c, f) SWCNT-decorated pSi. Scale bars (a – c) = $100 \mu\text{m}$, (d – f) $50 \mu\text{m}$	243

Figure 7.4: Fluorescence microscopy images of cytoplasm stained SK-N-SH neuroblastoma cells using CMRA. (a) pSi control, (b) 1 min of SWCNT attachment (low density) and (c) 2 hr of SWCNT attachment (high density). Scale bar 50 μm	244
Figure 7.5: Fluorescence microscopy image of membrane stained SK-N-SH neuroblastoma cells using DIOC ₁₈ (3) on (a, c) oxidised pSi and (b, d) SWCNT-decorated pSi surfaces at different magnifications. Arrows added in (d) to highlight examples of dark spots observed in membrane. Scale bar 50 μm	245
Figure 7.6: Fluorescence microscopy images of SK-N-SH neuroblastoma cells stained with (a, b) propidium iodide (PI) and (c, d) fluorescein diacetate (FDA) on (a, c) oxidised pSi and (b, d) SWCNT-decorated pSi substrates. Scale bar 50 μm	246
Figure 7.7: Fluorescence microscopy images of SK-N-SH neuroblastoma cells stained with (a) propidium iodide (PI) and (b) fluorescein diacetate (FDA) on a SWCNT-decorated pSi substrates after 48 hr of cell culture. Scale bar 50 μm	247
Figure 7.8: Fluorescence microscopy images of SK-N-SH neuroblastoma cells stained with CellTracker Orange showing preferential attachment to SWCNT-decorated patterns on a pSi substrate showing (a) circle and (b) line pattern. The regions in between those decorated with nanotubes were PEG functionalised. Scale bar 100 μm	248
Figure 7.9: Summary of SEM images of SK-N-SH on pSi-SWCNT substrates showing cell culture and spreading of lamellipodia (NanoLab SEM).....	249
Figure 7.10: AFM image of edge of a SK-N-SH cell on a pSi-SWCNT substrate.	250
Figure 7.11: I pDNA fluorescence and II Hoechst staining + pDNA of SK-N-SH cells on (a) pSi, (b) pSi-APTES and (c) pSi-APTES-SWCNT substrates after the gene transfection experiment.....	253
Figure 7.12: I pDNA fluorescence and II Hoechst staining + pDNA of SK-N-SH cells on (a) pSi, (b) pSi-APTES and (c) pSi-APTES-SWCNT substrates after gene transfection experiment with Effectene added.	254
Figure 7.13: I pDNA fluorescence and II Hoechst + pDNA staining of SK-N-SH cells on (a) flat Si, (b) flat Si-APTES and (c) flat Si-APTES-SWCNT substrates after gene transfection experiment with Effectene added.....	256
Figure 7.14: Schematic of SWCNTs chemically attached to Si substrates with positively charged diethylenetriamine (DETA) electrostatically binding pDNA to the substrate prior to cell culture.	257
Figure 7.15: XPS analysis to determine if the amine containing diethylenetriamine (DETA) is bound to the surface after SWCNT attachment via (a, c) direct ester	

attachment and (b, d) APTES mediated attachment showing (a, b) survey scans and (c, d) higher resolution spectra of the N 1s peak.259

Figure 7.16: I pDNA fluorescence and II Hoechst + pDNA staining of SK-N-SH cells on (a) Si-SWCNT, (b) Si-SWCNT-DETA, (c) Si-APTES-SWCNT and (d) Si-APTES-SWCNT-DETA substrates after gene transfection experiment with Effectene added.....260

Figure 7.17: Summary of initial electroporation experiments showing fluorescence microscope images of SK-N-SH cells stained with both Hoechst and pDNA on (a) Si-SWCNT, (b) Si-SWCNT + Effectene and (c) Si + Effectene.....262

Figure 7.18: Fluorescence microscope images of electroporation of SK-N-SH cells on Si-SWCNT-DETA substrates at varying applied voltages showing (I) pDNA expressing GFP and (II) Hoechst stain.264

Figure 8.1: Publication number for articles containing both “carbon nanotube” and “field emission” obtained using SciFinder search function 8/8/11.....276

Figure 8.2: Proposed schematic of the chemical attachment of DNA to carboxy-CNTs via a cleavable linker containing a disulphide group.277

Figure 8.3: Schematic of proposed improved electroporation apparatus where both cell culture and electroporation are completed within the same cell.278

List of Tables

Table 1.1: Characteristics and applications of pressure driven membrane technologies.....	26
Table 1.2: Summary of water molecule transport, ion conductance and study of desalination potential of CNT membranes.....	28
Table 1.3: Pressure driven flow through MWCNT membranes.....	31
Table 1.4: Comparisons of the gas and water flow enhancements (over their respective theoretical models) for 3 DWCNT membranes and a commercial polycarbonate membrane.....	33
Table 1.5: Summary of field emission properties from carbon nanotubes.....	40
Table 3.1: Raman peak position and assignment for SWCNTs on silicon.....	98
Table 3.2: RBM peak positions and corresponding calculated diameter for DWCNTs.....	112
Table 4.1: AFM pore size analysis of the pore size gradients produced by different applied currents.....	144
Table 4.2: Summary of percentage SWCNT coverage on each region of the gradient pSi etched at different etching currents.....	145
Table 5.1: Advancing contact angle measurements for the unfunctionalised, PFDS functionalised and PEGS functionalised pSi membranes.....	172
Table 5.2: Flux and permeability data for Rubpy and RB transport through unfunctionalised, PFDS-functionalised and PEGS-functionalised pSi membranes.....	178
Table 5.3: Effect of water plasma exposure time on polystyrene thin film thickness.....	188
Table 5.4: Comparison of membrane permeability between experimental and theoretical carbon nanotube membranes.....	197
Table 5.5: Permeability values for commercial polyamide thin film composite nanofiltration and reverse osmosis membranes.....	199
Table 6.1: Summary of field emission characteristics of Si-SWCNT surfaces with varying polystyrene film thickness.....	214

Table 6.2: Summary of FE characteristics of SWCNTs, DWCNTs and MWCNTs chemically attached to silicon.....	218
Table 7.1: Summary of WCA and cell area measurements of neuronal cells on the three surfaces used as cell culture substrates.....	243
Table 7.2: Summary of transfection efficiencies for pDNA with Effectene on the pSi based substrates.....	254
Table 7.3: Summary of transfection efficiencies for pDNA with Effectene on the flat Si based substrates.....	256
Table 7.4: Summary of transfection efficiencies adsorbed pDNA with Effectene on SWCNT substrates.	261

Glossary of abbreviations

Abbreviation	Definition
AFM	atomic force microscopy
APTES	3-aminopropyl triethoxysilane
b	electric field enhancement factor
CMRA	CellTracker orange cytoplasm stain
CNT	carbon nanotube
CTA	chain transfer agent
CVD	chemical vapour deposition
D-band	disorder Band
DCC	dicyclohexyl carbodiimide
DETA	Diethylenetriamine
DIOC ₁₈ (3)	green fluorescent cell membrane stain
DMEM	Dulbecco's modified eagle medium
DMF	dimethyl formamide
DMSO	dimethyl Sulfoxide
DNA	deoxyribosenucleic acid
dPBS	Dulbecco's phosphate buffered saline
DWCNT	double-walled carbon nanotube
E_F	Fermi energy
E_{to}	turn-on voltage
FDA	fluorescein diacetate
FE	field emission
FET	field effect transistor
F-N	Fowler-Nordheim
FTIR	fourier transform infrared
G-band	graphene band
GFP	green fluorescent protein
GO	graphene oxide
HEK	human embryonic kidney
HF	hydrofluoric acid
ITO	indium tin oxide
LCD	liquid crystal display
MD	molecular dynamics
MWCNT	multi-walled carbon nanotube
pAl	porous alumina
pDNA	plasmid DNA
PECVD	plasma-enhanced chemical vapour deposition

Abbreviation	Definition
PEGS	polyethylene glycol silane
PEI	poly(ethylimine)
PFDS	Fluorinated silane
PI	propidium iodide
PMMA	poly(methylmethacrylate)
PS	poly(styrene)
pSi	porous silicon
PTFE	poly(tetrafluoroethylene)
PTMS	propyl trimethoxysilane
RAFT	reverse addition fragmentation chain transfer
RB	rose bengal
RBM	radial creathing mode
RNA	ribosenucleic acid
RO	reverse Osmosis
Rubpy	ruthenium based dye
SA	self assembly
SAM	self assembled Monolayer
SEM	Scanning Electron Microscopy
Si	Silicon
SK-N-SH	mammalian neuroblastoma cell line
STM	scanning tunnelling microscope
SWCNT	single-walled carbon nanotube
TEM	transmission electron microscopy
VA	vertically aligned
WCA	water contact angle
XPS	X-ray photoelectron spectroscopy

List of publications

- [1] C. J. Shearer, J. G. Shapter, J. S. Quinton, P. C. Dastoor, *et al.*, "Highly resilient field emission from aligned single walled carbon nanotube arrays chemically attached to n-type silicon", *Journal of Materials Chemistry*, **18**, 5753 - 60 (2008).
- [2] K. T. Constantopoulos, C. J. Shearer, J. G. Shapter, N. H. Voelcker, *et al.*, in *SPIE Smart Materials, Nano+Micro-Smart Systems, Vol. 7267*, Melbourne, 72670G (2008).
- [3] C. J. Shearer, K. T. Constantopoulos, N. H. Voelcker, J. G. Shapter, *et al.*, in *SPIE Smart Materials, Nano+Micro-Smart Systems, Vol. 7267*, Melbourne, 72670I (2008).
- [4] Z. Poh, B. S. Flavel, C. J. Shearer, J. G. Shapter, *et al.*, "Fabrication and electrochemical behavior of vertically-aligned carbon nanotube electrodes covalently attached to p-type silicon via a thioester linkage", *Materials Letters*, **63** (9-10), 757-60 (2009).
- [5] K. T. Constantopoulos, C. J. Shearer, A. V. Ellis, N. H. Voelcker, *et al.*, "Carbon Nanotubes Anchored to Silicon for Device Fabrication", *Advanced Materials*, **22** (5), 557-71 (2010).
- [6] C. J. Shearer, A. V. Ellis, J. G. Shapter, and N. H. Voelcker, "Chemically Grafted Carbon Nanotube Surface Coverage Gradients", *Langmuir*, **26** (23), 18468-75 (2010).
- [7] C. J. Shearer, J. Yu, M. Bissett, D. D. Tune, *et al.*, "Surface modifications with carbon nanotubes - what might be possible?", *Surface Coatings Australia*, **47** (4) (2010).
- [8] L. Velleman, C. J. Shearer, A. V. Ellis, D. Losic, *et al.*, "Fabrication of self-supporting porous silicon membranes and tuning transport properties by surface functionalization", *Nanoscale*, **2** (9), 1756-61 (2010).
- [9] C. J. Shearer, L. Velleman, F. Acosta, E. V. Ellis, *et al.*, "Mass transport through nanoporous materials: single walled carbon nanotubes and porous silicon", *Proceedings of the 2010 International Conference on Nanoscience and Nanotechnology (ICONN2010)*, 196-199, Sydney, (2010).

-
- [10] B. S. Flavel, M. J. Sweetman, C. J. Shearer, J. G. Shapter, *et al.*, "Micropatterned Arrays of Porous Silicon: Toward Sensory Biointerfaces", *ACS Applied Materials & Interfaces*, **3** (7), 2463-71 (2011).
- [11] M. J. Sweetman, C. J. Shearer, J. G. Shapter, and N. H. Voelcker, "Dual Silane Surface Functionalization for the Selective Attachment of Human Neuronal Cells to Porous Silicon", *Langmuir*, **27** (15), 9497-503 (2011).
- [12] K. E. Moore, B. S. Flavel, C. J. Shearer, A. V. Ellis, J. G. Shapter, "Electrochemistry of Polystyrene Intercalated Vertically Aligned Single- and Double-Walled Carbon Nanotubes on Gold Electrodes", *Electrochemistry Communications*, **13**, 1190 (2011).
- [13] M. A. Bissett, A. Barlow, C. J. Shearer, J. S. Quinton, J. G. Shapter, "Carbon Nanotube Modified Electrodes for Photovoltaic Devices", *Carbon*, *accepted* (25/8/11) (2011).
- [14] C. J. Shearer, F. Harding, M. J. Sweetman, J. G. Shapter, *et al.*, "Nanostructured biointerfaces based on carbon nanotube-decorated porous silicon films", *Soft Matter*, (under review) (2011).
- [15] C. J. Shearer, A. Fahy, M. Barr, K. E. Moore, *et al.*, "Field emission from single- double- and multi-walled carbon nanotubes chemically attached to silicon", *Journal of Applied Physics*, (under review) (2011).

Parts of the above publications have been reproduced in this Thesis as follows:

- Chapter 1 contains parts of [5]
- Chapter 3 contains parts of [2] and [3]
- Chapter 4 contains parts of [6] and [14]
- Chapter 5 contains parts of [8] and [9]
- Chapter 6 contains parts of [1] and [15]
- Chapter 7 contains parts of [14]

Science is made up of so many things that appear obvious after they are explained.

- Frank Herbert in *Dune*

We are at the very beginning of time for the human race. It is not unreasonable that we grapple with problems. But there are tens of thousands of years in the future. Our responsibility is to do what we can, learn what we can, improve the solutions, and pass them on.

- Richard P. Feynman

You want a reason? How's about "Because"?

- Joshua Homme in *Turnin' on the Screw*

Chapter 1

Introduction

Background information relative to this Thesis is given with focus upon the fabrication and application of carbon nanotube based devices. Specific attention is given toward the chemical attachment of carbon nanotubes to surfaces and the applications of water filtration, field emission and biomaterial interfaces.

1.1 Overview

Innovation has always been the driving force behind progress. In the technological age, major innovations such as the transistor^[1] and optical fibres^[2] have underpinned inventions such as the radio and the internet. More recently, research has looked toward the nanoscale where surface properties begin to dominate over those of the bulk and quantum effects become prominent. Examples of the commercialisation of nanoscale materials include: metal nanoparticles for catalysis,^[3] accelerometers in cars,^[4] integrated circuits in computers,^[5-7] self-cleaning windows,^[8, 9] and additives for bouncier tennis balls.^[10]

The advantage of utilising nanotechnology is not simply in the miniaturisation of devices but also in the enhancement of device performance and the building of new technologies from the ground up. The competing nature of the so-called “top-down” and “bottom-up” approaches is perhaps best elucidated by comparing the two images in Figure 1.1. Top-down approaches are analogous to milling or attrition where material is removed in order to make the desired structure (e.g., building a canoe from a tree). Bottom-up approaches involve the manipulation of smaller particles in order to form a functional structure (e.g., building a house from bricks). The bull in Figure 1.1 (a) was made by the specific etching of a polymeric material using a high frequency laser.^[11] The letters of IBM in Figure 1.1 (b) were spelt out by individually manipulating xenon atoms spread across a nickel (100) surface using a scanning tunnelling microscope (STM).^[12]

The atom-by-atom approach used in Figure 1.1 (b) allows, in principle, the fabrication of truly nanoscale devices such as the sub 10 nm transistor.^[13] However, such a process is quite time consuming and requires very high vacuum. The commercial scale fabrication of such devices is not possible with current technologies. Not all bottom-up approaches require atom-by-atom assembly nor do they specifically require direct manipulation. Self-assembly (SA) is a process where the formation of a structure occurs naturally under the influence of certain forces such as chemical reactions, electrostatic attraction and capillary forces.^[14] Many nanomaterials can be self-assembled including monolayers of silanes,^[15] lipid bilayers^[16] and helical organic nanotubes.^[17]

The carbon nanotube (CNT) is arguably the most famous nanomaterial. The bonding of the carbon atoms to each other in a hexagonal shape leads to some remarkable properties that can find use in a variety of applications. However, CNTs are notoriously difficult to work with and fabricating CNT based devices in a manner that is easily upscaleable for commercial uses has proven to be difficult. Recently, the directed self-assembly of vertically aligned single-walled carbon nanotubes (SWCNTs) on surfaces of varying composition has been reported.^[18-23] The self-assembly approach offers a possible route to creating surface-bound CNT substrates suitable for device application that are fabricated in a manner that is easily upscaleable.

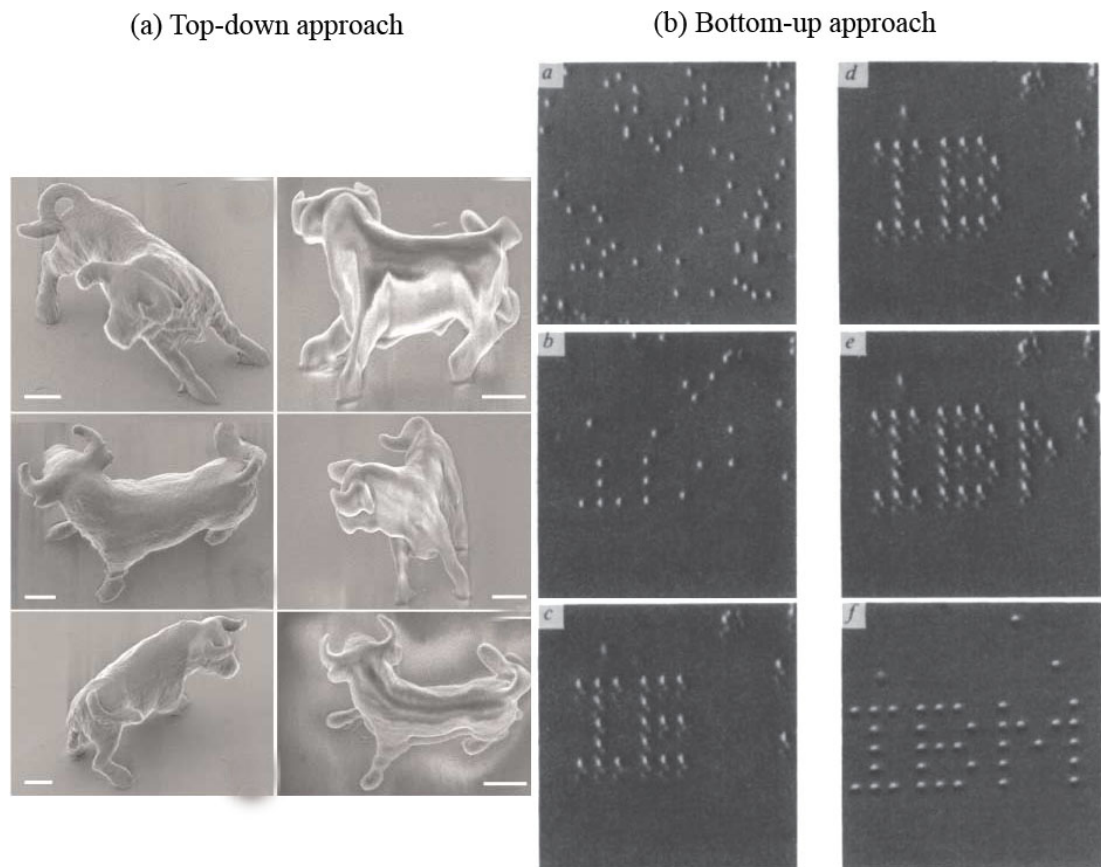


Figure 1.1: Comparison of (a) top-down and (b) bottom-up approaches toward miniaturisation. In (a), miniature bulls were fabricated following a two-photon polymerisation technique,^[11] scale bars, 2 μm . In (b), individual xenon atoms are moved using a scanning tunnelling microscope to form 0.5 nm high letters.^[12]

In this Thesis, we have investigated the applicability of CNT substrates fabricated using a directed self-assembly method for specific applications including as water filtration membranes, as field emission electron sources and as scaffolds for biomaterial immobilisation.

1.2 Carbon nanotubes

1.2.1 History and structure

Carbon nanotubes are allotropes of carbon in which the carbon atoms form a hexagonal sheet of sp^2 bonds (analogous to graphite) which is seamlessly rolled up into a cylinder that can be microns long but is only nanometres in diameter. CNTs can be separated into three distinguishable categories based upon the number of shells (or walls) they contain. SWCNTs consist of a single one atom thick wall (Figure 1.2 (a)) while double-walled CNTs (DWCNTs, Figure 1.2 (b)) and multi-walled CNTs (MWCNTs, Figure 1.2 (c)) essentially consist of two or more than two coaxial SWCNTs where one is contained within the diameter of another.

It is a common misconception that MWCNTs were first reported by Iijima in 1991.^[24] In fact the first publication that showed transmission electron microscopy (TEM) evidence of the tubular nature of some nano-sized carbon filaments appeared in the Journal of Physical Chemistry of Russia in 1952.^[25, 26] However, there is no doubt that Iijima was responsible for the nomenclature and for sparking the research interest in CNTs that followed his initial paper. SWCNTs were first reported in the June 17th issue of Nature in 1993 by two independently submitted papers, one by Iijima and Ichihashi^[27] and the other by Bethune *et al.*^[28]

The electronic properties of carbon nanotubes are highly dependent upon the chirality of the tubes or in other words how the graphene sheet is ‘rolled’ up. SWCNTs are completely described, except for their length by the chiral vector, \mathbf{C} , which is created by choosing two atoms on a planar sheet of unrolled graphene, one atom is chosen as the origin. The chiral vector is directed from the origin to the next atom and is defined by:

$$\mathbf{C} = n\mathbf{a}_1 + m\mathbf{a}_2 \quad \text{Equation 1.1}$$

as shown in Figure 1.3 (a)^[29] where, \mathbf{a}_1 and \mathbf{a}_2 are unit cell vectors of the 2D graphene lattice (which originate at the same position as \mathbf{C}) and n and m are integers. The chiral vector can be used to calculate the nanotube radius, \mathbf{R} , since^[30]

$$\mathbf{R} = \mathbf{C}/2\pi \quad \text{Equation 1.2}$$

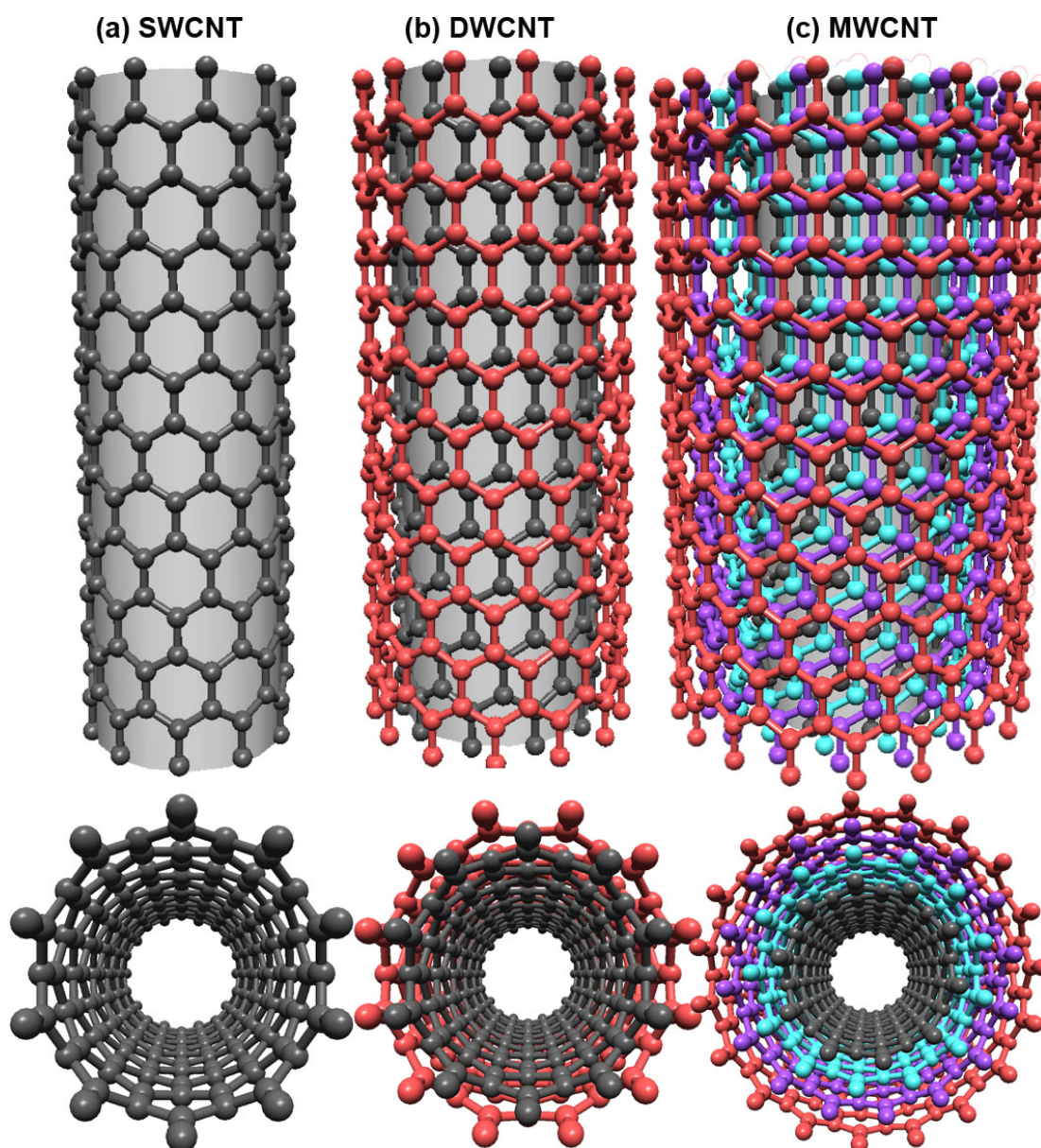


Figure 1.2: ‘Ball and stick’ representation of (a) single-walled CNT (SWCNT), (b) double-walled CNT (DWCNT) and (c) multi-walled CNT (MWCNT). Images made using Nanotube Modeller (www.jcrystal.com).

The electronic properties of the CNT can be determined: if

$$|n - m| = 3q \quad \text{Equation 1.3}$$

where q is an integer, the nanotube will be metallic otherwise the nanotubes will be semiconducting.^[31] The chiral angle, θ , which is specified as angle between \mathbf{C} and the nearest zigzag of C-C bonds ($0^\circ \geq \theta \leq 30^\circ$), can be used to describe the pattern of the CNT. The two achiral tube shapes occur when either $\theta = 30^\circ$, (n, n) the tubes are known as ‘armchair’ or if $\theta = 0^\circ$, $(n, 0)$ the tubes are ‘zigzag’. Nanotubes with a

chiral angle between 0 and 30° are called ‘chiral’ (Figure 1.3 (b - d) zigzag and armchair pattern shown in red).

Figure 1.4 (a, b) depicts the band structure of a graphene sheet, which is a semiconductor with a zero band gap, as calculated by the tight binding method.^[32] In this case, the top of the valence band has the same energy as the bottom of the conduction band, and this energy equals the Fermi energy for one special wave vector, the so-called K-point of the two-dimensional Brillouin zone (i.e., the corner point of the graphene hexagonal unit cell in reciprocal space). The rolling up of the graphene sheet to create a SWCNT imposes a periodic boundary condition, given by

$$C \cdot \mathbf{k} = 2\pi q \quad \text{Equation 1.4}$$

where C is the chiral vector which becomes the circumference of the tube and q is an integer.^[33] This condition leads to the quantisation of the wave vector \mathbf{k} , which forms a series of sub-bands (yellow lines in Figure 1.4 (c, d)). The direction of the wave vector depends upon the direction of the chiral vector. If for a given nanotube a wave vector passes through a K-point, the band structure of the nanotube will be characterised by a zero energy gap, this occurs when $|n-m| = 3q$ (metallic nanotubes from Equation 1.3, Figure 1.4 (c, e)). If for a given nanotube no wave vectors pass through a K-point, the tube will have a finite energy gap, this occurs when $|n-m| \neq 3q$ (semiconducting nanotubes, Figure 1.4 (d, f)).^[30]

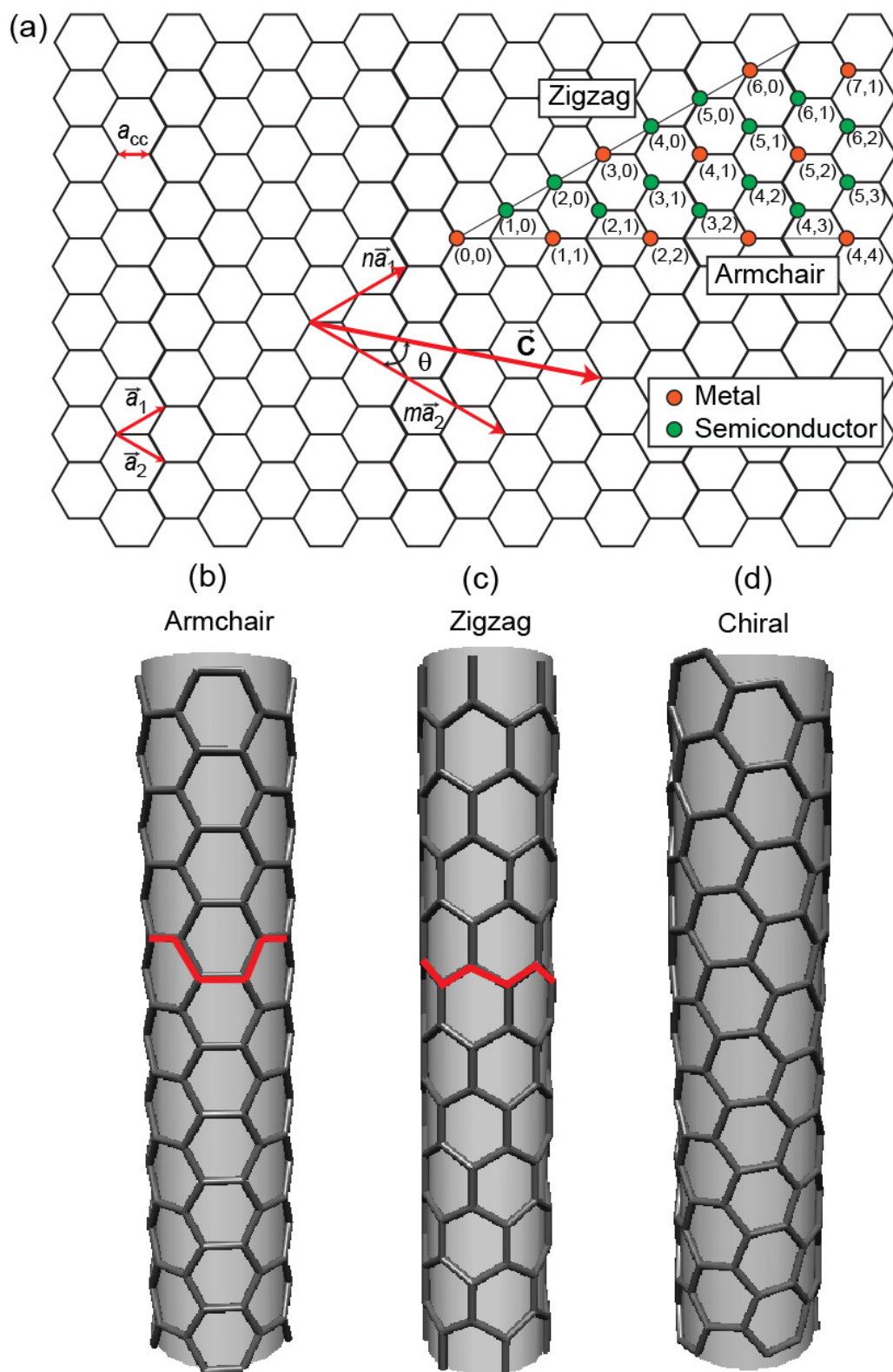


Figure 1.3: (a) Schematic of unrolled SWCNT showing chiral vector \vec{C} and how different values of the integers n and m affect the electronic property of the SWCNT. (b, c, d) The direction of the chiral vector affects the appearance of the nanotube showing (b) (4,4) armchair shape, (c) (6,0) zig-zag shape and (d) (5, 3) example of a chiral shape.

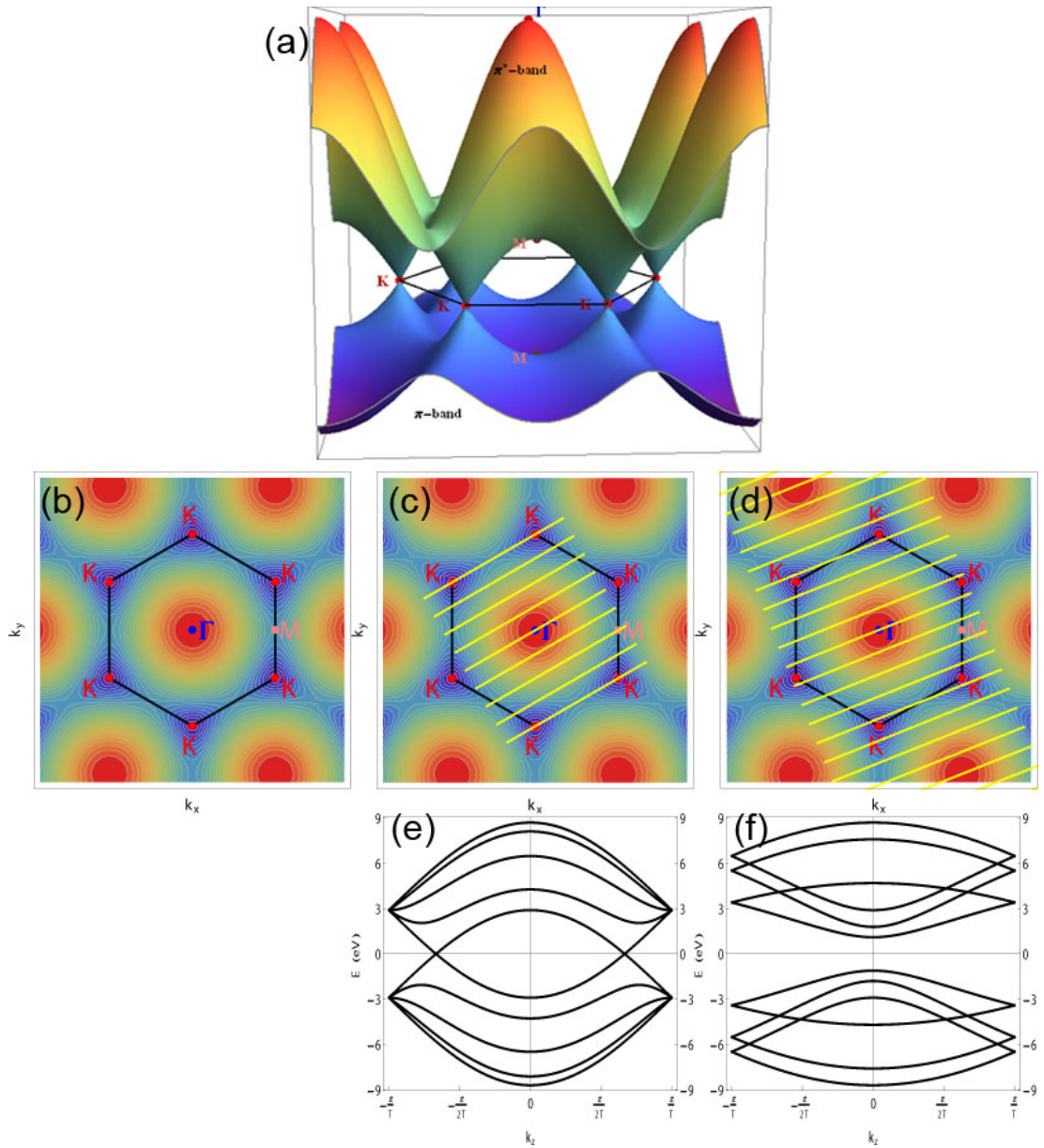


Figure 1.4: (a, b, c, d) Band structures in reciprocal space, as calculated by the tight binding method, of (a, b) graphene, (c) metallic (4, 4) SWCNT, (d) semiconducting (5, 3) SWCNT showing the wave-vectors as yellow lines and the K-points (Fermi-level points) as red dots. The blue dot represents energy maxima and the pink points represent saddle (M) points. (e, f) represent electronic band structures of (e) (4, 4) metallic nanotube where wave vectors cross a K-point and (f) (5, 3) semiconducting nanotube where no wave vectors cross a K-point.

1.2.2 Properties and applications

The properties of CNTs are a direct consequence of the nature and geometrical shape of the C – C bonds within their structure. Experimental and theoretical studies

have shown that CNTs exhibit enhanced electrical, thermal and mechanical properties.

The 1-dimensional nature and electrical properties of CNTs leads to resistance that is dependent upon the CNT contact to other electrodes. It has been shown that CNTs with a perfect contact can act as ballistic transporters of carriers such that, within the CNT, conduction can occur without resistance (no scattering).^[34] Ballistic transport can be achieved over lengths typical of modern electronic devices (<100 nm). Ballistic transport is disrupted by defects within the CNT lattice which create scattering. For a long CNT or a CNT with a high defect population, many scattering collisions can take place and the carrier mobility becomes diffusion limited. However, diffusion limited transport within CNTs can still be as high as $\sim 10^5 \text{ cm}^2 \text{ V}^{-1} \text{ s}^{-1}$ which is 1000 times larger than bulk silicon.^[34, 35] CNTs have also been shown to be capable of carrying a large current with a maximal current density of $> 10^9 \text{ A cm}^{-2}$ reported, which is ~ 100 times greater than that of copper wires.^[36]

As mentioned in Section 1.2.1 CNTs can be either semiconducting or metallic. Electrical applications of CNTs depend upon the CNT type. Metallic nanotubes with their ballistic transport of carriers (e.g., electrons and holes) could find use as high-performance interconnects within integrated circuits. In semiconducting CNTs carrier transport can be switched 'on' or 'off' and it is this effect which can be used to create field effect transistors (FET). The CNTFET, first described in 1998, offers a potentially viable method to further decrease the size of transistors on integrated circuits.^[37, 38] The incorporation of CNTs in either of these applications will require the sorting or preferential growth of CNTs with specific (metallic or semiconducting) chirality.

The stiff sp^3 bonds of diamond are recognised as one of the best thermal conductors. Therefore, a high thermal conductance should be expected for CNTs with even stronger sp^2 bonds. Indeed, it has been reported that CNTs exhibit a thermal conductivity of $\sim 6000 \text{ W m}^{-1} \text{ K}^{-1}$ which is 3 times greater than that of diamond.^[39, 40] The high value arises from a large phonon mean-free path of the order of $1 \mu\text{m}$ at low temperatures as determined experimentally and theoretically.^[41, 42] This property has recently been used to cool an integrated circuit. A CNT containing silicon chip was placed in thermal contact with the working elements on the back-side of an integrated circuit. It was found that the CNTs assisted in dissipating the

heat from the circuit, which will increase lifetime and could possibly allow further miniaturisation.^[43]

The mechanical properties of materials are perhaps best described by its Young's modulus and its tensile strength. The Young's modulus is a measure of stiffness of a material. Values of Young's modulus for CNTs have been determined to be approximately 1 TPa using a variety of experimental and theoretical methods making CNTs the stiffest material known.^[44-46] The value of Young's modulus has been found to be insensitive to diameter and chirality except at very small diameters when the C – C bonds become strained.^[40] Tensile strength is the maximum stress that a material can withstand while being stretched or pulled without breaking. CNTs have shown high tensile strength values of 150 GPa which is ~ 100 times greater than steel.^[47]

The mechanical properties of CNTs clearly make them suitable as reinforcements in high strength, light weight, high-performance composites such as those found in products such as bicycles, tennis racquets and aircraft. However, CNTs cannot simply be added as a filler because the CNTs often do not mix well and tend to aggregate with the interfacial bonding between the CNTs and the matrix material tending to be weak.^[48] Work on the functionalisation of the outer walls of CNTs in order to improve the interfacial bonding has shown promise.^[49, 50] In particular, the interfacial weakness between CNTs and polymer matrices has been used to create vibration dampening surfaces which have potential to be used in aerospace and automobile engineering.^[51]

In the scope of this Thesis not all applications of CNTs are covered. This Section is simply an attempt to demonstrate that research into CNTs could lead to a vast number of applications. CNTs have the potential to find use in a myriad of further applications such as bullet proof shirts,^[52] improved lithium batteries,^[53] scanning probe cantilevers,^[54] and even improved plant growth.^[55] This Thesis focuses upon the use of CNTs as water filtration membranes, field emission devices and as scaffolds for biomaterial immobilisation. These applications will be covered in more detail in Sections 1.5 - 7.

1.2.3 Synthesis

The preparation of high-quality CNTs with high yield has been a goal of many research endeavours. At the moment, arc discharge, laser ablation and chemical vapour deposition (CVD) are the three major methods of CNT production.

Arc discharge was the method initially used by Iijima to create MWCNTs in 1991.^[24] The process of arc discharge involves applying a direct current (dc) bias between two graphitic electrodes within an inert atmosphere (Figure 1.5 (a)). With a large bias, a plasma is produced which vaporises carbonaceous material which in turn re-forms into CNTs. The exact mechanism of CNT formation is a much argued topic.^[56] SWCNTs can be produced by incorporating catalyst nanoparticles into the carbon electrodes and using specific pressures and compositions of gases. The initial reports of SWCNT growth using arc discharge used an iron implanted graphite anode under atmosphere of 10 Torr of methane and 40 Torr of argon.^[27] The production of SWCNTs on a gram scale and MWCNTs on a kilogram scale has been achieved using arc discharge.^[57-59]

Laser ablation was first reported in 1996 by the group of Smalley where they produced SWCNTs with high yield (>70 %).^[60] A graphite rod loaded with small amounts of nickel and cobalt was vaporised by a laser beam at 1200 °C and CNTs were collected on a water-cooled collector plate (Figure 1.5 (c)).

Both laser ablation and arc discharge have the advantage of high yields of high purity CNTs of specific type (SW-, DW- or MWCNT). However, the resulting CNTs produced are very long (> 1 µm), randomly tangled together and of random chirality (Figure 1.5 (b, d)), which makes their direct use in applications difficult.

CVD growth offers a route toward specific placement and alignment of CNTs on a surface. Chemical vapour deposition involves flowing a carbon feedstock over transition metal nanoparticles at medium to high temperatures (500 – 1200 °C) where the nanoparticles catalyse and serve as nucleation sites for the initiation of CNT growth.^[59, 61] Materials grown over the catalyst are collected upon cooling the system to room temperature (Figure 1.5 (e)). Altering the carbon feedstock, catalyst and growth temperature can affect the diameter,^[62] chirality,^[63] length,^[64, 65] orientation,^[66] purity^[67] and type of CNT produced.^[68] Synthesis of MWCNTs by CVD was first reported in 1993 by Endo *et al.*^[69] who produced what they termed

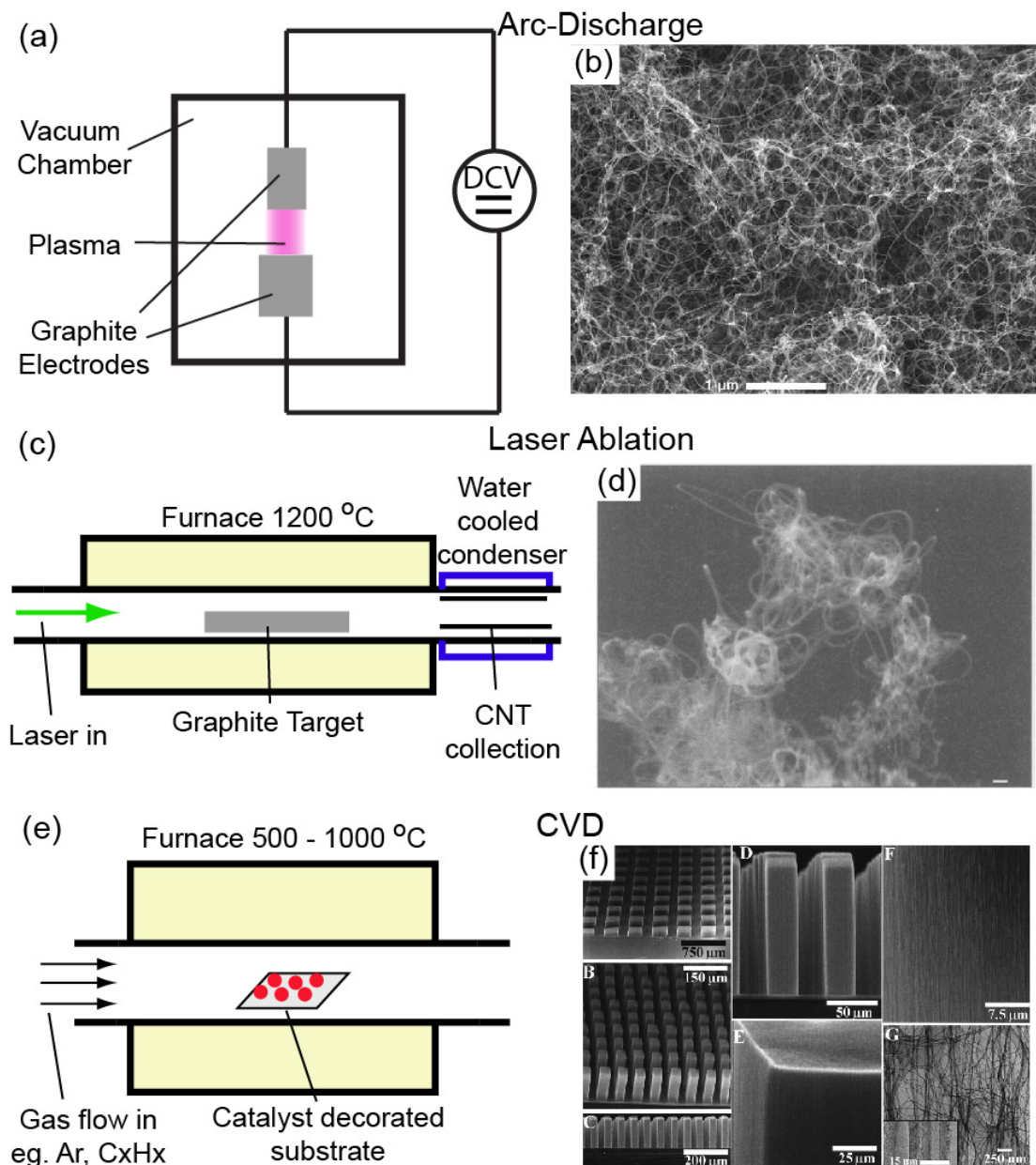


Figure 1.5: Summary of CNT synthesis methods (a) arc discharge, (c) laser ablation, and (e) chemical vapour deposition along with SEM images (b, d, f) showing the morphology of the CNTs produced.^[57, 60, 65] Scale bar in (d) 100 nm.

pyrolytic carbon nanotubes by the thermal decomposition of benzene at 1100 °C. SWCNTs were not produced via CVD until 1996 when Dai *et al.*^[70] reported that they had produced isolated SWCNTs by the disproportionation of carbon monoxide at 1200 °C, using molybdenum nanoparticles as a catalyst.

Chemical vapour deposition can control vertical alignment of CNTs by the rational design and patterning of catalyst upon the substrate (Figure 1.5 (f)).^[71] It has

been shown that vertical alignment can be achieved if a growing nanotube is supported by van der Waals interactions with neighbouring CNTs.^[65] This can be difficult because at high temperatures the metal nanoparticles tend to become mobile on the surface, disrupting the pattern.^[71] Nanoparticle mobility can be reduced by supporting the catalyst on a buffer layer such as Al₂O₃ or SiO₂.^[72] Vertical alignment has been achieved using ordinary CVD on silicon substrates,^[66] but alignment and CNT growth rate can be increased by using plasma enhanced chemical vapour deposition (PECVD).^[73]

In 2004, Hata *et al.*^[74] were looking for a method to increase the lifetime and activity of catalyst particles used in CVD growth. To achieve this, they added a weak oxidiser to selectively remove any amorphous carbon that can stick to the catalyst, stopping CNT growth, while leaving the CNTs intact. They decided to add water vapour to the reaction mixture by passing a small amount of the carrier gas through a water bubbler. CVD growth was carried out at 750 °C using ethylene as the carbon source and typical catalysts such as Fe (1 nm), Al/Fe (10 nm/1 nm) on typical substrates including silicon and quartz. Vertically aligned arrays of ultralong CNTs were formed with typical results of millimetre heights after 10 min of growth.^[74] This growth has since been dubbed ‘supergrowth’ and has been used to create arrays of vertically aligned DWCNTs^[68, 75] and MWCNTs^[76] on silicon substrates with heights greater than 1 mm.

CVD has the further advantage of being able to grow CNTs in a patterned arrangement by the pre-patterning of the catalyst nanoparticles using conventional means.^[77] However, CVD growth of CNTs produces more defects as shown by the lower value of Young’s modulus of 10 to 50 GPa found for CVD compared to the value obtained for arc discharge CNTs (up to 150 GPa).^[40]

The large scale synthesis of CNTs is a mature area of research and as such has become quite sophisticated. Arc discharge and laser ablation make the most pristine CNTs but the CNTs produced are randomly orientated, tangled and of random chirality. CVD can be used to fabricate CNT surfaces with control of placement and alignment but the CNTs produced are often of a lower quality and the CVD process is not suited to mass production.

1.3 Silicon

1.3.1 Bulk silicon

Silicon is the cornerstone of the current semiconductor microchip industry. The integration of a CNT device on a silicon substrate will be easier than on any other substrate. In addition, silicon is capable of being converted into porous silicon which could potentially act as a porous support for a CNT water filtration membrane.

Bulk (intrinsic) silicon consists of tetravalent silicon atoms packed into a face centred cubic structure with each silicon atom sharing a valence electron with each of its four neighbours.^[78] With the atoms in this arrangement, all valence electrons are used in covalent bonding, leading to a large energy band gap between the conduction and valence bands. To make silicon useful in the electronics industry, dopants are added to alter its electrical properties. These dopants are most commonly phosphorus or boron but other elements can be used. When phosphorus is used, n-type silicon is created, where the five valence phosphorus atom shares four of its electrons with its neighbours and ‘donates’ the remaining electron to the conduction band of the lattice. When boron is substituted into the lattice, p-type silicon is created; the three valence electrons of boron are shared with three of its neighbours creating a positive ‘hole’ in the valence band. An additional electron must be accepted by the semiconductor to form four covalent bonds.^[78]

When a semiconductor is doped with donor or acceptor impurities, impurity energy levels are introduced that lie within the energy band gap, effectively decreasing the size of the band gap. An n-type donor impurity (Figure 1.6 (a)) creates a donor level close to the conduction band due to the excess of electrons. This donor level increases the Fermi energy of the substrate and makes the conduction of electrons easier. When a negative bias is applied to the semiconductor, electrons in the donor level move to the conduction band, these electrons can be replaced by electrons moving from the valence band to the donor band which in turn are replaced by an electron from the bulk material. This process is more favourable than in undoped silicon because the energy required for an electron from the valence band to reach the conduction band involves two lower energy steps. A p-type acceptor impurity (Figure 1.6 (b)) creates a level of holes above the valence band that is

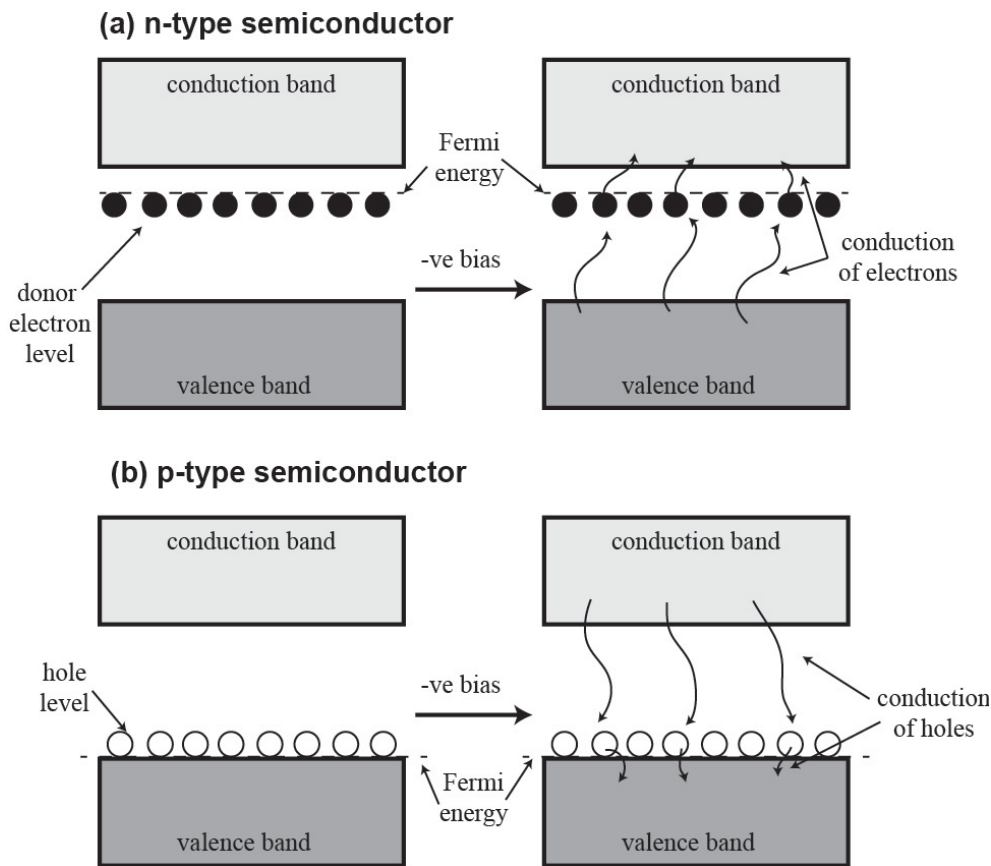


Figure 1.6: Schematic of the band diagrams of (a) n-type and (b) p-type semiconductors under no bias and negative bias.

caused by the electron deficiency of the impurity. When a negative bias is applied to the material; holes from the 'hole' band drop down to the valence band, these are replaced by holes that drop down from the conduction band.^[78] Thus an n-type semiconductor carries charge through electrons while a p-type semiconductor carries charge through holes.

1.3.2 Porous silicon

Porous silicon (pSi), as its name suggests, is bulk silicon that has been etched by some means to form pits (pores) on its surface. Porous silicon is produced through the chemical, photochemical or electrochemical etching of flat, crystalline silicon with fluoride solutions.^[79-81] Galvanostatic anodisation of flat silicon is the method most often employed to fabricate pSi because it provides greater reliability and selectivity to the surface produced. Aqueous hydrofluoric acid (HF) in ethanol is a

common etchant used. The ethanol component is used to reduce the surface tension of the etching solution and allow full wetting of the silicon substrate.^[81] The etching process is undertaken at room temperature in a specially designed etching cell made of the fluoride-resistant Teflon (Figure 1.7 (a)). The pores produced are highly 1-dimensional and are of random shape (Figure 1.7 (b)).

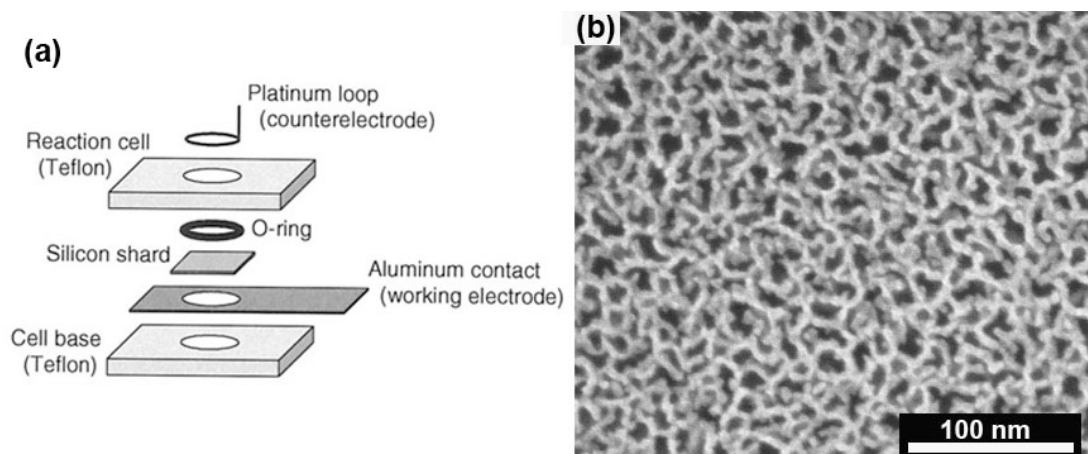


Figure 1.7: (a) Schematic of the etching cell used for the anodic etching of silicon.^[81] (b) Top-down SEM of porous silicon showing the irregularly shaped pores produced.

The generally accepted mechanism for pore formation is based on the work of Lehmann and Gösele.^[82] This mechanism relies upon the formation of pSi being limited by the charge supply to the anode (the silicon) and not by the ionic diffusion in the electrolyte. This occurs below a critical current density known as the electropolishing current density where the reaction between the surface and electrolyte is limited by the diffusion of HF, which leads to a smoothing of the surface.^[79, 83] Below the electropolishing current density, pSi formation is essentially inert against fluoride attack as long as no electronic holes (h^+) are available at the silicon surface because the electronegativity of H is similar to that of Si and therefore the induced polarisation is low. If a hole reaches the surface (step 1, Figure 1.8 (b)), polarisation of the bond occurs and nucleophilic attack on the Si-H bonds by fluoride can occur and Si-F is established (step 1, Figure 1.8 (a)). A further F^- anion can attack due to the polarising influence of the bonded F, releasing H_2 and injecting an electron into the silicon (step 2 in Figure 1.8 (a)). Due to the polarisation of the Si-F groups, the electron density of the Si-Si back bonds are lowered and these weakened bonds can now be attacked by HF or H_2O (steps 4 and 5) in a way that the silicon

surface atoms remain bonded to hydrogen (step 5).^[82] This subsequently causes the dissolution of SiF_6^{2-} ions, as well as the production of hydrogen gas.^[84] When a silicon atom is removed from an atomically flat surface by this reaction, an atomic size dip is formed (step 2, Figure 1.8 (b)). This alteration of surface geometry changes the electric field distribution in such a way that holes preferentially move to the dips, where further etching can occur, amplifying the size of the dip hence forming pores with a very large aspect ratio (step 3, Figure 1.8 (b, c)).^[82] It should be noted that although this mechanism seems to indicate a one-way only etching direction, some lateral etching does occur due to different kinetic reactivity's of the silicon crystal faces.^[81]

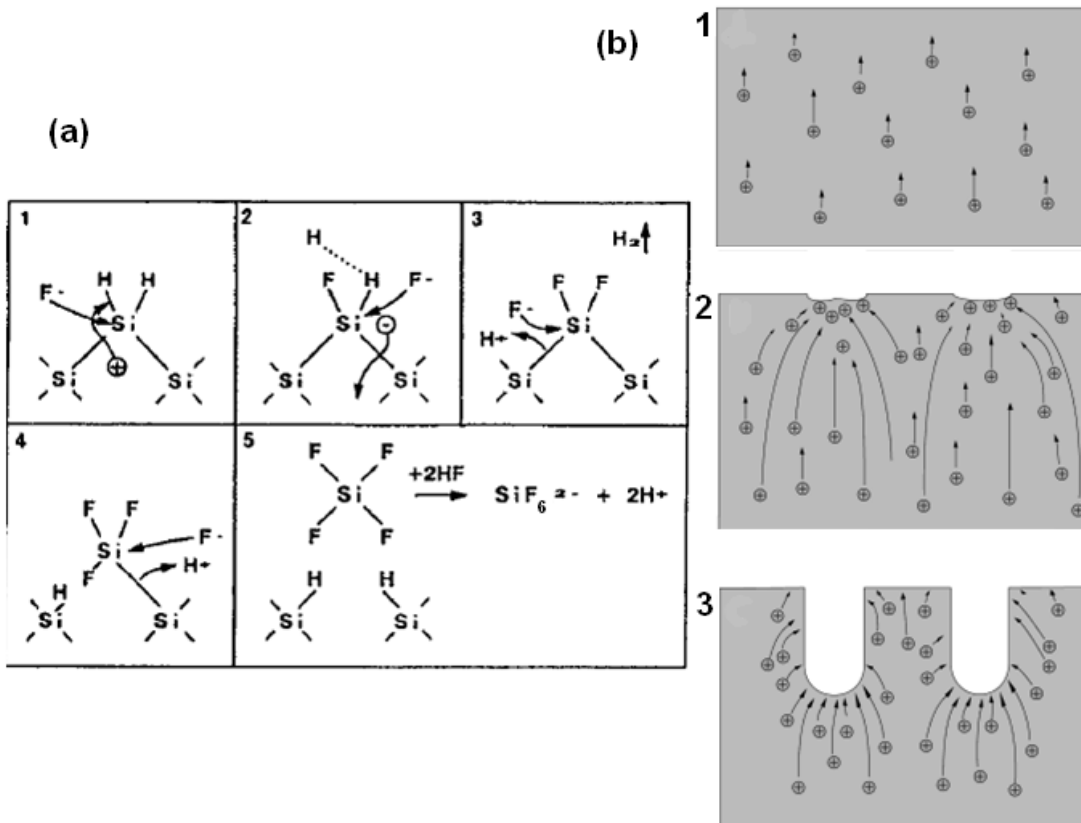


Figure 1.8: Porous silicon formation mechanism showing (a) reaction steps^[82] and (b) hole migration during pore formation.^[84]

The fabricated pores formed can be in a range of tuneable sizes from micropores (< 5 nm) to mesopores (5 – 50 nm) to macropores (>50 nm). The pore morphology is affected by the current density, dopant density, illumination and HF concentration during etching.^[79] Increasing the current density causes the holes to move higher up

the pore walls, causing lateral etching and hence increasing diameter. Increasing HF concentration increases the number of F^- anions at the solution-surface interface. This results in a quicker reaction between the F^- anion and the holes, producing pores with smaller diameters and increasing porosity.^[79] Etching time affects the depth of the etch with longer times yielding deeper pores.^[83]

HF etching of silicon yields a Si-H terminated surface. These surfaces can be modified using a number of different chemical reactions; the most common are hydrosilylation and silanisations from which a range of surface chemistries can be achieved.^[81, 85]

1.4 Chemical attachment of carbon nanotubes to surfaces

1.4.1 Carbon nanotube chemistry

As mentioned in Section 1.2.3 when produced by arc discharge, CNTs are inert, insoluble, randomly orientated micrometre long ropes of mixed chirality. To make the CNTs chemically active and to alter them to a usable size, chemical shortening/cutting can be used. Shortening can be achieved by a few different methods. A popular process is to add a mixed acid combination of 3:1 sulphuric acid:nitric acid to a few milligrams of CNTs. The mixed acid produces nitronium ions (NO_2^+) which are highly electrophilic and attack the sp^2 hybridised hexagonal lattice and can disrupt it to form sp^3 hybridised carbon. Young *et al.*^[86] propose that this is caused by the nitronium ions aligning such that an oxygen atom is adsorbed onto an aromatic carbon atom which causes the O = N bond to lengthen and strains the C - C back bonds on the tube sidewall. Since the stabilisation energy of the formation of the C - O bond is high (-2.51 eV) the otherwise unfavourable process can occur.^[86] Once a single C - O bond is formed, all carbons in the near vicinity are now more susceptible to oxidation leading to radial cutting/shortening of the CNTs. It is worth noting that NO_2^+ binds preferentially to metallic nanotubes because of the higher charge density at the Fermi level. Subsequently many metallic SWCNTs are disintegrated by this process leaving predominantly semiconducting nanotubes.^[86, 87] A positive effect is that after cutting, filtration and quenching with water to return the SWCNT to a pH of 5-7, carboxylic acid groups are left on the ends and on defect sites along the side walls.

1.4.2 Carbon nanotube surface attachment

Carboxylic acid functional groups are common crosslinking agents in biological and chemical processes. The most common are amide (peptide) bonds where a carboxylic acid (-COOH) reacts with an amine (-NH₂) and ester linkages where a carboxylic acid reacts with an alcohol (-OH). Thioester linkages are also possible where a carboxylic acid reacts with a thiol (-SH). The reaction of carboxylic acid with amines, alcohols and thiols can be enhanced by the use of coupling reagents

such as dicyclohexylcarbodiimide (DCC).^[88] Since shortened CNTs have carboxylic acid groups on their ends and on defects along their side wall, DCC mediated coupling is a simple method of chemically attaching CNTs to a substrate, and this method has been utilised recently.^[18, 22] DCC promotes the reaction by converting the carboxylic acid (molecule 1, Figure 1.9 (a)) into an activated ester (molecule 2 in Figure 1.9 (a)).^[89] The activated ester can then react in one of two ways: the activated ester can react with an amine, hydroxyl or thiol (molecule 3) where the nucleophilic nitrogen, oxygen or sulphur attack the electron deficient carbon atom on the carbonyl group of the activated ester to form the amide, ester or thioester linkage (molecule 5, Figure 1.9 (b)). This reaction is extremely favourable because it produces the stable dicyclohexyl urea (molecule 4) which drives the reaction forward. The other possible reaction is the rearrangement of the activated ester to the insoluble, stable *N*-acylurea (molecule 6, Figure 1.9 (c)).^[89] The formation of this unwanted by-product can be avoided if solvents with low dielectric constants are used. It is for this reason that the presence of water at any time during this reaction is undesirable.

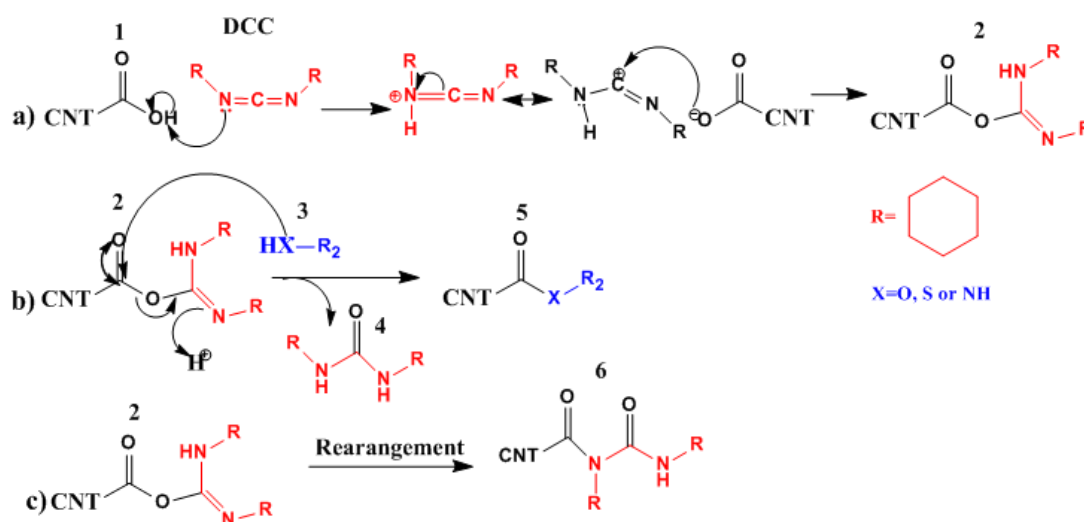


Figure 1.9: Basic reaction scheme of the mechanism of DCC (red) assisted coupling of carboxylic acid functionalised CNTs (molecule 1, black) to amines, alcohols and thiols (molecule 3, blue). (a) The starting carboxylic acid (1) reacts with DCC to form an activated ester (2). (c) This can rearrange to form the stable unwanted by-product *N*-acylurea (6) or (b) it can undergo nucleophilic attack from the electron rich N, O or S to form a stable amide, ester or thioester linkage to the R_2 group (5).

It is quite clear that the reaction mechanism explained in Figure 1.9 can be used to chemically bond the CNTs to almost anything (and vice versa) including surfaces.

This has been achieved for hydroxyl,^[22] amine^[18] and thiol^[90] terminated surfaces.^[20] The following Section will detail the key articles in CNT chemical attachment to surfaces.

1.4.3 Experimental results

The earliest use of the DCC mediated assembly of CNTs onto a surface was in 2000 when Liu *et al.*^[18] attached shortened SWCNTs to gold. In this example, the amine group from a cysteamine molecule was used to create an amide linkage to the carboxylic acid on the SWCNT, the remaining thiol group on the cysteamine was then used to attach to a gold substrate. Liu *et al.* used atomic force microscopy (AFM) in order to visualise the SWCNT-Au surfaces where they observed needle like protrusions which were described as SWCNTs perpendicularly standing on the substrate (Figure 1.10 (a)).^[18] This initial report was followed up in 2001 where they described the alignment of carboxylic acid functionalised SWCNTs on silver. In this report, the negatively charged carboxylic acid groups were electrostatically attracted to the positively charged silver surface.^[19] Since that time many further variations have been published, with CNTs assembled on gold using various amine terminated thiol monolayers with the predominant application of electrochemical sensing.^[91, 92]

Carbon nanotubes were not chemically attached to silicon until 2006 when Yu *et al.*^[93] chemically attached shortened SWCNTs to silicon by first hydrogenating a silicon (100) surface and then reacting with ethyl undecylenate to afford an ethyl undecanoate self-assembled monolayer. The ester terminus of the monolayer was reduced to an alcohol whereupon the shortened carboxylated SWCNTs were covalently attached using DCC coupling. It was found from AFM imaging that vertically aligned SWCNTs were attached to the surface. Cyclic voltammetry of the surfaces revealed the SWCNT to silicon electronic connection was not strong, indicating that the SAM hindered electron transduction.

In 2007 Yu *et al.*^[22] further refined the approach by hydroxylating silicon (100) surfaces and then chemically attaching shortened SWCNTs using DCC coupling. The SWCNT arrays formed were shown to orient vertically (Figure 1.10 (b)) and cyclic voltammetry of the surfaces demonstrated that the surface was suitable for electronic applications. In 2007, Flavel *et al.*^[94] attached SWCNTs to an amine

terminated silane layer (3-aminopropyltriethoxysilane, APTES) on silicon (Figure 1.10 (c)). This method produced well aligned SWCNT arrays using the more favourable reaction between an amine and carboxylic acid to produce a stable amide linkage.

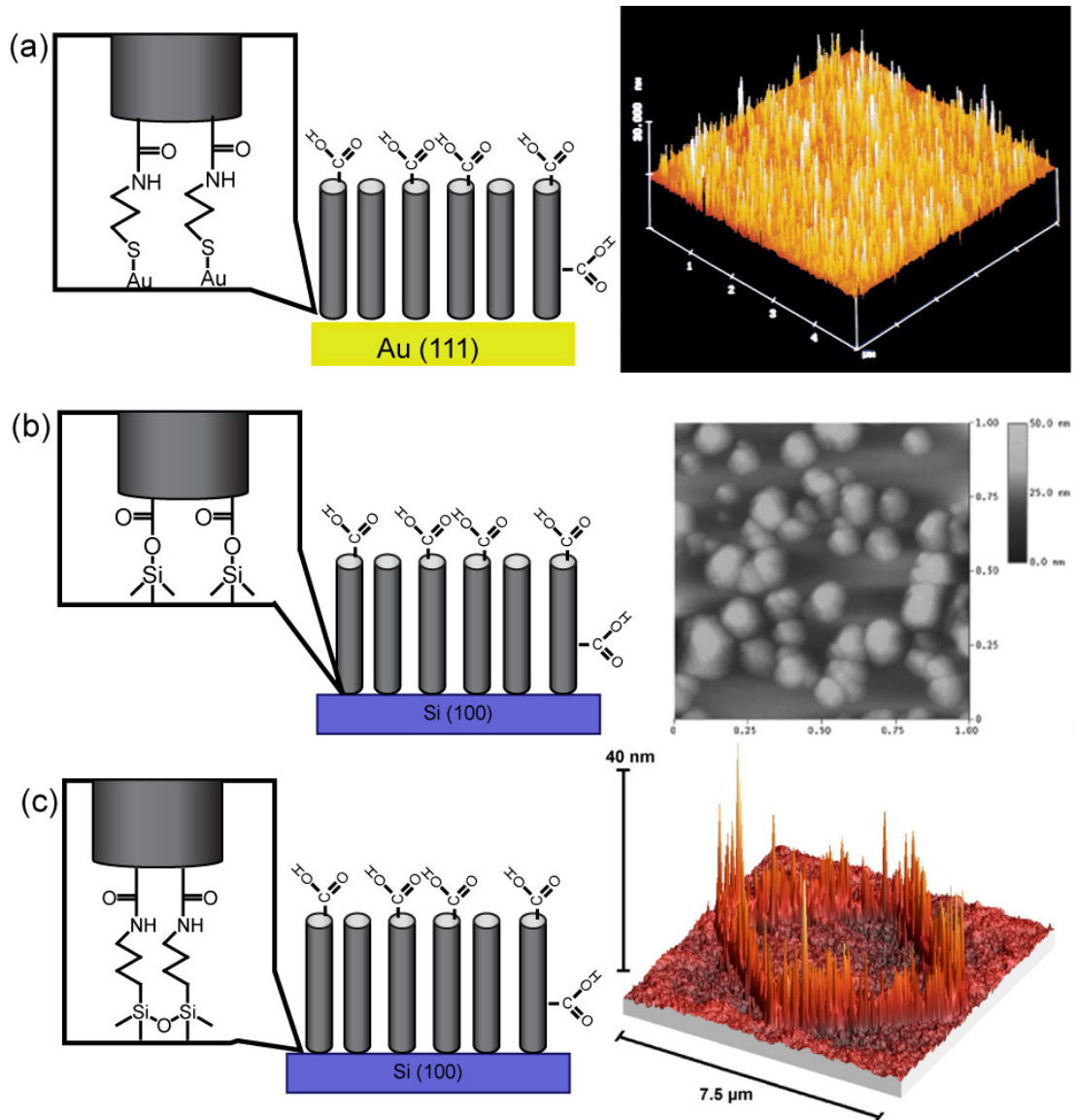


Figure 1.10: Schematics and published AFM images of SWCNTs chemically attached to (a) gold via a cystamine linkage,^[18] (b) silicon via direct ester linkage,^[22] and (c) patterned amine terminated silane on silicon.^[94]

Vertically-aligned CNT arrays produced by wet chemical assembly have been investigated as chemical sensors,^[95] biological sensors,^[92] and photovoltaic devices^[21, 23, 96] where they have shown promise as a simple method of producing functional surface bound CNT arrays. This Thesis will investigate their use in three

other specific applications, namely water filtration, field emission and as biomaterial scaffolds which will be reviewed in detail in the following Sections.

1.5 Carbon nanotubes for water filtration

1.5.1 Background

There are three basic categories of water purification: membrane technologies (including reverse osmosis membranes), thermal processes (including various types of distillation), and chemical approaches (including aggregation and flocculation). Many water purification plants use a combination of these technologies with membrane based plants being more popular in the United States and Australia and energy-hungry distillation being more popular in the oil-rich Middle East.

A membrane is a thin film of porous material that allows water molecules to pass through it, but simultaneously prevents the passage of larger, undesirable, molecules such as viruses, bacteria and salts. Membranes can be made from polymeric materials such as cellulose, acetate and nylon or from non-polymeric materials such as ceramics, metals and composites.^[97] Generally, water flow in membrane technologies is either pressure driven or electrically driven.

Several pressure driven membrane processes and a few of their applications are detailed in Table 1.1. It is obvious that there is a trade-off between selectivity and applied pressure: the more selective the membrane the more energy required.

Osmosis is the diffusion of water through a semi-permeable membrane, from a solution of low solute concentration to a high solute concentration. Reverse osmosis (RO) is the opposite of this effect where a potential barrier is overcome by applying a large pressure differential.

As detailed in Table 1.1 RO offers the potential to filter salts and other small particulates from water, however RO plants have constant problems with membrane fouling and the membranes must be replaced at regular intervals coupled to the large power requirements of RO plants. Therefore investigations are underway into new alternative technologies or improvements upon the current technologies. It has recently been discovered that membranes incorporating carbon nanotubes could potentially produce high flux, high selectivity water filters that require a lower energy input.^[98]

Table 1.1: Characteristics and applications of pressure driven membrane technologies (adapted from ref.^[99])

Membrane process	Applied pressure (psi)	Minimum particle size removed	Application (removal efficiency %)
Microfiltration	4 - 70	0.1 - 3 μm	Particle/ turbidity removal (> 99 %) Bacteria/ protozoa removal (> 99.99 %)
Nanofiltration	70 - 140	200 -4 00 Da	Turbidity removal (> 99 %) Softening (> 90 %) Sulfate removal (> 97 %) Virus removal (> 95 %)
Reverse Osmosis (Hyperfiltration)	140 - 700	50 - 200 Da	Salinity removal (> 99 %) Nitrate removal (85 – 95 %) As, Cd, Cr, Pb, Fe removal (40 to > 98 %)

1.5.2 Theoretical studies

In 2001, Gerhard Hummer was investigating whether water could fill non-polar cavities such as inside folded proteins. To achieve this Hummer *et al.*^[100] performed extensive molecular dynamics (MD) simulations on the ‘simplest’ non-polar pore: a carbon nanotube.^[98] This was achieved by designing an uncapped 1.34 nm long, 0.81 nm diameter (between carbon centres) SWCNT and simulating their dynamics while solvated in a water reservoir for 66 ns. It was found that the nanotube was quickly filled with about 5 water molecules, and remained filled for the remainder of the simulation. The water molecules in the pore formed a quasi-one-dimensional wire connected by hydrogen bonds more or less aligned with the tube axis (Figure 1.11 (a)). This means that, upon entering the nanotube, each water molecule loses 2 out of its 4 hydrogen bonds from the bulk phase. This loss of energy ($\sim 10 \text{ kcal mol}^{-1}$) is partially recovered by van der Waals interactions with the carbon atoms within the nanotube ($\sim 4 \text{ kcal mol}^{-1}$). This apparent loss of energy would indicate that water entering a CNT would be a very unlikely occurrence. However, Hummer *et al.* explain that the remainder of the energy is recovered through the thermodynamics of

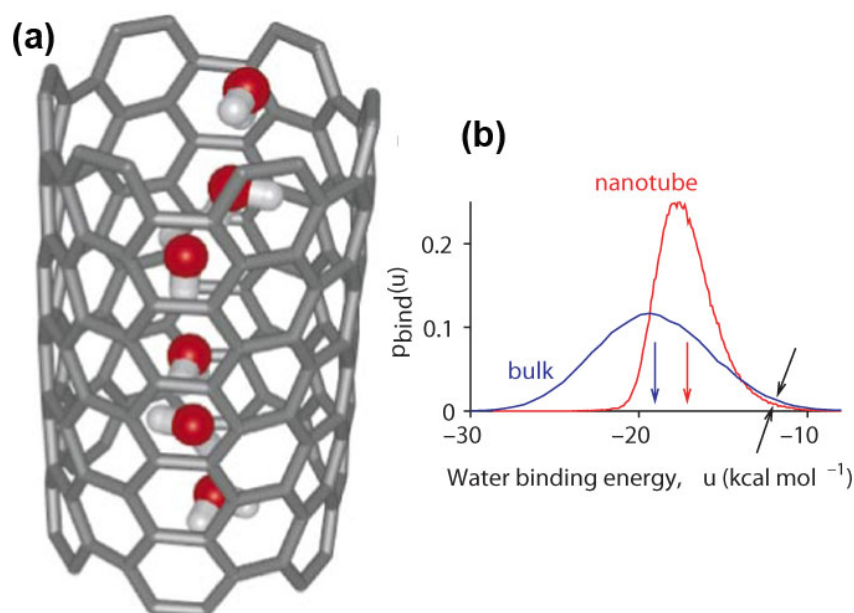


Figure 1.11: Water occupancy inside a SWCNT (a) structure of hydrogen bonded chain of water molecules within the SWCNT and (b) probability distribution of water binding energies of (red) confined and (blue) bulk water, the coloured arrows indicate average binding energies.^[98]

confinement.^[98] Upon entering the nanotube, the energy distribution becomes much narrower than in the bulk phase (Figure 1.11 (b)). This is because the water molecules have two well-formed hydrogen bonds, one accepted and one donated, causing the water molecules to effectively exist in their energetic ‘ground’ state.^[98] The confined water molecules therefore have a lower chemical potential than in the bulk state leading to filling of the CNT. The difference in chemical potential is calculated to be $\sim 0.82 \text{ kcal mol}^{-1}$ which agrees with the occupancy calculated from the simulations.^[98] Water molecules were found to not only enter the CNT, but also exit out the other side. 17 water molecules per nanosecond were calculated to pass through the tube ($51 \times 10^{-14} \text{ cm}^3 \text{ s}^{-1}$), this is of comparable flow to water through the transmembrane protein aquaporin-1.^[101] The fast flow is attributed to the frictionless, smooth, inner wall of the CNT that allows water molecules to ‘slip’ through it.

This initial paper was followed by others by Hummer *et al.*^[100, 102-104] including a report of osmotic water transport through CNT membranes.^[105] In this paper, MD simulations were used to determine if water would flow through a CNT due to osmotic force. The water was found to flow from a pure-water compartment through the CNT membrane and into a salt-solution compartment at a net water flow of 5.8

molecules per nanosecond, per CNT. This value is very similar to an analogous experiment of water travelling through aquaporin-1 at a similar osmotic gradient (3.9 per ns, per pore).^[101] An investigation on the effect of length, was also completed in this study with no variation of water flow found between a 1.34 nm and a 2.7 nm long CNT, showing that the osmotic water flow is independent of channel length (at least up to a few nanometres).^[105]

Recently, the focus of research has switched toward investigating whether CNTs can be practically used as RO membranes. Corry^[106] completed a detailed examination of a water solution containing Na⁺ and Cl⁻ ions travelling through CNTs of different diameter and length. Table 1.2 details the types of CNTs used, their respective diameters and conductance of water molecules and ions.

It was found that water filled all CNTs with the wider nanotubes unsurprisingly experiencing a higher flow rate. Single files of water molecules were formed in the (5, 5) and (6, 6) nanotubes while the wider (7, 7) nanotubes had two rows of water molecules and the wider again (8, 8) nanotubes had four rows of water molecules. It was found that the Na⁺ ions could only enter the (5, 5) CNTs if it stripped its hydration number from 6 to 2, making the process unlikely. However larger CNT diameters reduced the number of hydration shells that were required to be stripped from 3 for (6, 6) nanotubes to 1-2 for (7, 7) nanotubes to 0 for (8, 8) nanotubes. The stripping of the hydration shell creates a barrier to entry that is an order of magnitude higher than the entry barrier for water.^[106] When a hydrostatic pressure was applied

Table 1.2: Summary of water molecule transport, ion conductance and study of desalination potential of CNT membranes.^[106]

Size	Diameter (Å)	Conductance of H ₂ O (per CNT per ns)	Conductance of ions	Salt rejection	Permeability (L cm ⁻² day ⁻¹) ^a	Improvement upon commercial RO membrane ^b
(5, 5)	6.6	10.4 ± 0.4	0.0	100%	0.16	2.42
(6, 6)	8.1	23.3 ± 0.3	0.0	100%	0.27	4.21
(7, 7)	9.3	43.7 ± 0.5	0.007 ± 0.005	95%	0.42	6.39
(8, 8)	10.9	81.5 ± 1.2	0.137 ± 0.025	58%	0.65	9.76

^aFlow rate calculated for 2.5 x 10¹¹ pores per cm²

^bInfo from: (http://www.dow.com/liquidseps/prod/sw30hr_380.htm) membrane achieves salt rejection of >99.6%

to ‘push’ the water molecules through (RO simulation), salt rejections of 100 % were found for the (5, 5) and (6, 6) nanotubes while the (7, 7) nanotubes achieved 95 % and the (8, 8) nanotubes recorded 48 % salt rejection (Table 1.2). The reported flow rate improvement over the commercial RO membrane is similar to the 3 - 5 fold improvement of a similar CNT MD simulation over a poly(methylmethacrylate) membrane.^[107] These results indicate that low diameter (C-C distance of < 0.93 nm) CNTs could be used to make high efficiency, high selectivity, and high flux RO membranes.

Molecular dynamics simulations of water flow through CNTs continue to be studied with many reports concluding that CNTs have the potential to produce a membrane with high rejection at a low input pressure.^[108-111] However, without experimental results to support these MD simulations there is no advantage in continuing theoretical study.

1.5.3 Experimental studies

Hinds *et al.*^[112] prepared a CNT based membrane in 2004 that would form the blueprint for subsequent CNT membrane experiments. The fabrication process of Hinds is shown in Figure 1.12. Briefly, MWCNTs of low diameter (~ 7 nm) were grown using CVD on quartz slides. A solution of polystyrene (PS) in toluene was then spin-coated into the 5 – 10 μm thick forest of CNTs. Hydrofluoric acid was then used to remove the CNT-PS composite from the quartz substrate, producing a freestanding film of 5 – 10 μm thickness. Water plasma etching was carried out to remove the top layer of PS and reveal the CNT tips; this was achieved because the plasma etched the PS faster than the CNTs, producing a 10 – 50 nm overhang of CNTs out from the surface. This process also opens the CNT tips and functionalises them with carboxylic acid groups.^[112] Transport measurements of both nitrogen gas and a ruthenium aqueous ionic complex were carried out. Nitrogen was found to flow with a similar rate to that expected through a 7.5 nm pore according to Knudsen diffusion.^[112] The flux of the ruthenium complex was found to be similar to that of bulk aqueous-solution diffusion. Both of these results indicated that there is minimal advantageous interaction between the gas or complex with the wide diameter CNT pores.

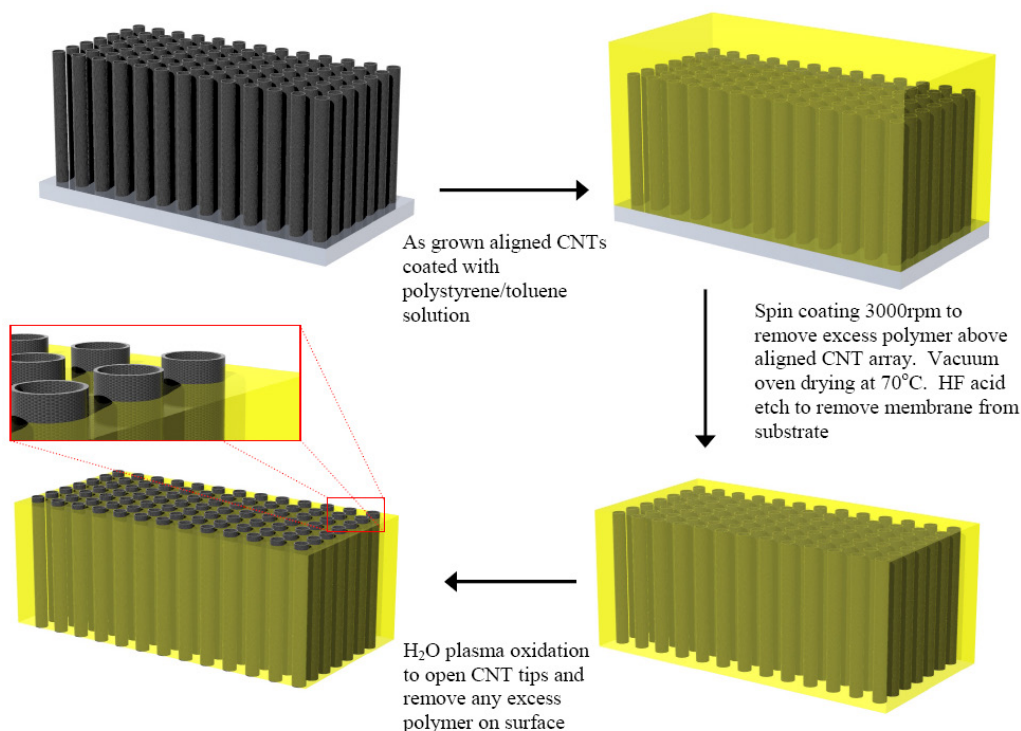


Figure 1.12: Schematic of the fabrication process of aligned MWCNT membranes by Hinds *et al.*^[112]

An explanation not mentioned by Hinds could be that most of the recorded flow came from CNTs with wider diameters (30 – 50 nm), which they observed by nitrogen adsorption but appeared to ignore within their discussion.^[112] The final experiments of their work were to chemically bind first biotin to the carboxylic acid groups on the CNTs and then to bind streptavidin to the biotin. The flux was reduced by a factor of 5.5 upon biotin attachment; this was further reduced by a factor of 15 upon streptavidin coordination. This simple experiment showed how the molecular transport through the CNT membrane can easily be gated by a variety of biological/chemical affinity pairs, leading to potential application in chemical separations and sensing.^[112]

The aforementioned paper, strangely did not mention the work of Hummer or any work involving the transport of water molecules through CNT pores. This was remedied in a brief communication published in Nature in 2005.^[113] In this article, the flow rate of various fluids through the CNT membrane described previously were calculated and compared to that expected from conventional flow (Table 1.3). The observed water flow (25 cm s^{-1}) is similar to, but less than that calculated

theoretically by Hummer of 90 cm s^{-1} but much greater than expected from conventional theory.^[98, 113]

The large increase in observed flow (compared to conventional) is attributed to the assumption made in the Hagen-Poiseuille equation that the velocity of the fluid at the pore wall is zero.^[113] The ‘frictionless’ CNT inner wall is given credit for this non-zero velocity at the wall. The non-zero flow at the pore wall explains the enhanced flow rate and the extremely large slip lengths calculated (much greater than the CNT radius). The slip length is an extrapolation of the extra pore radius required to give a zero velocity at a hypothetical pore wall.^[113] The decrease in flow and slip length observed as the fluid becomes less polar is attributed to an increased affinity for the non-polar CNT wall (Table 1.3).

Since 2005, the group of Hinds have continued their work on CNT membranes. Rather than making improvements on the membrane itself, such as by decreasing CNT diameter, they have concentrated on changing the molecules attached to the CNT ends to investigate changes in flow rate.^[114-118]

Table 1.3: Pressure driven flow through MWCNT membranes.^[113]

Liquid	Initial permeability ($\text{cm}^3 \text{ per cm}^2 \text{ min bar}$)	Observed flow velocity (cm s^{-1} at 1 bar)	Expected flow velocity (cm s^{-1} at 1 bar) [#]	Slip length (μm)
Water	0.58	25	0.00057	54
Ethanol	0.35	4.5	0.00014	28
<i>iso</i> -Propanol	0.088	1.12	0.00077	13
Hexane	0.44	5.6	0.00052	9.5
Decane	0.053	0.67	0.00017	3.4

[#]Expected flow as calculated by the Hagen-Poiseuille equation

Around the time of the work released by Hinds *et al.*,^[112, 113] Holt *et al.*^[119] reported upon the fabrication and transport properties of a lower diameter DWCNT membrane. DWCNTs with a diameter of 1.3 – 2 nm were fabricated by growing the nanotubes onto a silicon substrate via CVD. The gaps between the DWCNTs were then filled with silicon nitride. The silicon under the DWCNT arrays was etched away and the metal catalyst and excess silicon nitride was removed via Ar ion milling. The tops of the DWCNTs were then removed by reactive ion etching (Figure 1.13).^[119]

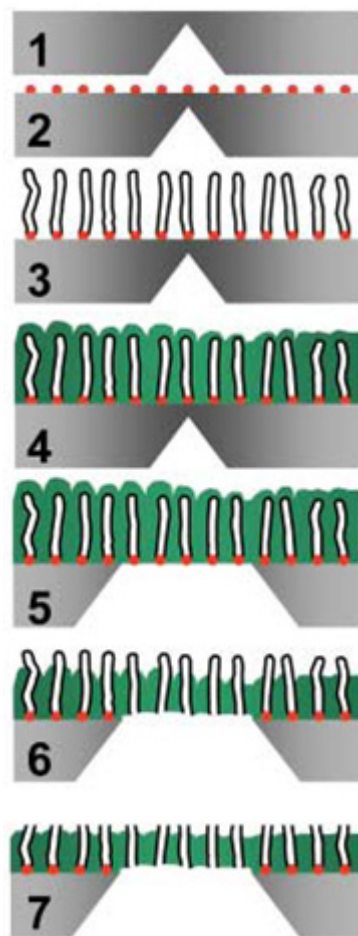


Figure 1.13: Schematic of the DWCNT membrane fabrication of Holt *et al.*^[119]

The first transport experiments carried out were size exclusion experiments where the flux of 5 nm colloidal gold, 2 nm colloidal gold and 1.3 nm $\text{Ru}^{2+}(\text{bipy})_3$ complex was measured. Of the analytes, only the ruthenium complex was found to pass through the membrane, indicating that the pore size is somewhere between 1.3 – 2 nm. Water and gas flow measurements were completed using three different DWCNT membranes and a commercial polycarbonate membrane (Nucleopore, Osmonic Inc.). Gas flow in confined dimensions, when particle-surface collisions dominate over particle-particle collisions, is commonly described by the Knudsen diffusion model.^[119] Table 1.4 displays the gas (Knudsen model) and water flow (Hagen-Poiseuille, non-slip) enhancement and their corresponding theoretical flow enhancements for the membranes investigated. The flow enhancement is very large for both the water and gas measurements with enhancements of 560 - 8400 and 16 - 120 recorded, respectively, for the DWCNT membranes whereas the commercial polycarbonate filter exhibited a lesser enhancement (3.7 and 2.1,

Table 1.4: Comparisons of the gas and water flow enhancements (over their respective theoretical models) for 3 DWCNT membranes and a commercial polycarbonate membrane.^[119]

Membrane	Pore diameter (nm)	Pore density (pores cm ⁻²)	Gas flow enhancement over Knudsen model	Water flow enhancement over Hagen-Poiseuille model	Calculated slip length (nm)
DWCNT 1	1.3-2.0	$\leq 2.5 \times 10^{11}$	40-120	1500-8400	380-1400
DWCNT 2	1.3-2.0	$\leq 2.5 \times 10^{11}$	20-80	680-3800	170-600
DWCNT 3	1.3-2.0	$\leq 2.5 \times 10^{11}$	16-60	560-3100	140-500
Polycarbonate	15	6×10^8	2.1	3.7	5.1

respectively) even though the pores of the polycarbonate are approximately 10 times larger. It should be noted that the values listed in Table 1.4 are the ‘minimum’ values. This is a consequence of the error in calculating the pore density, with the value reported indicating the lower estimate.

Recently, molecular dynamic simulations have specifically investigated the results of Holt *et al.*^[119] Joseph *et al.*^[120] created a simulation of 1.6 nm CNTs and calculated the water flow enhancement over that of the Hagen-Poiseuille model. The calculated improvement was 2052 which is well within the range of the 560-8400 observed by Holt (Table 1.4).^[119] This comparison has been investigated by Thomas *et al.*^[108] who claim that Joseph used the wrong diameter value, and if the correct value was used, the calculated enhancement would be 459. Thomas *et al.*^[108] further went on to calculate expected flow enhancements for large diameter CNTs (1.66 - 4.99 nm) and found that the flow enhancement decreased with diameter as the water molecules no longer formed ordered chains and acted more alike to bulk water. This result contradicts the findings of Hinds *et al.*,^[113] who experimentally calculated to have much higher enhancement (~ 50000), Thomas argues that Hinds *et al.* has most likely made a mistake in the calculation of the available flow area or the presence of an uncontrolled force that produced the very large flow.^[108] This conclusion seems likely as the pore area calculations were calculated from SEM analysis, which is not a suitable method for such calculations.

Very recently, the group of Hinds have discarded their CVD grown CNT membrane approach (Figure 1.12) and have adopted a ‘microtome cut’ method.^[121] The microtome cutting method involves thoroughly mixing CNTs with an epoxy resin, the epoxy is set and the hardened film is cut into 5 μm thick disks using a

conventional microtome with a quartz blade. While the CNTs are randomly mixed within the initial epoxy mixture, it is assumed that some CNTs will be aligned such that they will be open at both ends after microtome cutting. CNT membranes fabricated in this fashion have been investigated for drug delivery^[122] and electrophoretic transport.^[123]

The work of Holt and Hinds demonstrate that the fabrication of a CNT membrane that allows water to flow through it at an enhanced rate is possible. There are still many possible improvements: using SWCNTs would yield an improvement because the smaller inner diameter will allow for increased selectivity, such as ion removal for desalination^[106] and the smaller outer diameter would allow more CNTs to be placed within a membrane, increasing pore density and subsequently improving flux. A further improvement could be to use a simpler fabrication technique; CVD growth of CNTs, silicon nitride impregnation and Ar ion milling are all techniques that require specific instruments that are expensive and difficult to upscale. The use of CVD for CNT production also requires catalyst nanoparticles which could potentially block the CNT pores. The production of a SWCNT membrane via the chemical attachment of carboxy-functional SWCNTs to a porous substrate has not been previously reported.

1.6 Field emission from carbon nanotubes

1.6.1 Background and theory

Many electronic devices such as cathode ray tubes in televisions, X-ray generators and microwave amplifiers are based upon electron sources. These electron sources are generally thermionic emitters where a surface is heated to 950 – 2000 °C to eject electrons. Thermionic emission inexpensively produces high current densities but at a high energy consumption and cannot be miniaturised to micrometre-size due to insufficient heat dissipation.^[124] It is for this reason that research into so called ‘cold electron sources’ such as field emission from carbon nanotube arrays have come into the spotlight.

Field emission (FE) is the extraction of electrons from a solid by tunnelling through the surface potential barrier in the presence of an electric field.^[125] When no local electric field is applied to a surface, the potential barrier is infinitely wide and hence no tunnelling can occur (Figure 1.14 (a)).^[125] When a large local electric field is applied the potential step at the surface confining the electrons to the solid becomes (to the first approximation) triangular in shape, with the slope depending upon the electric field strength (Figure 1.14 (b, c)). A more accurate approximation is depicted in Figure 1.14 (d) where the Coulomb potential is included in the calculation of the potential barrier. As the width of the barrier gets smaller (≈ 2 nm) electrons close to the Fermi energy (E_F) have a finite probability of tunnelling through the barrier and escaping,^[124] as demonstrated in Figure 1.14 (d) where an electron with energy, E_x , tunnels through the potential barrier and escapes into vacuum where it can be attracted to a positively charged plate. This occurs when the wave function of an electron (which maps the probability its position) overlaps outside of the potential barrier, thus a smaller potential barrier (higher electric field) leads to a higher probability of field emission occurring.

increase the local electric field is to employ tip-like structures.^[128] Tip-like structures increase the current density due to the field amplification effect which is where the electric field lines concentrate around a sharp object, this leads to electric field enhancement around a tip.^[129] This enhancement is (to the first approximation) equal to the aspect ratio (height/radius)^[124] and is represented by the enhancement factor, β . Thus a tip with an aspect ratio of 100 decreases the required electric field for field emission to occur by a factor of 100.

In practice, field emission experiments are conducted by placing a sample of interest (most likely a single sharp tip or an array of tips) close (~ 1 mm) to a collecting plate in a high vacuum. A high voltage is then applied such that the sample is the cathode (negative bias) and the collector is the anode. The voltage is swept from 0 V to a desired maximum voltage and current (or current density, A cm^{-2}) with respect to applied voltage (or electric field, V/d) is plotted (known as an I-V curve). For field emission this curve shows no current while there is a zero probability of tunnelling through the potential barrier and then as the applied field becomes high enough such that the potential barrier is small enough for electrons to tunnel through it the current ‘turns-on’ and the curve takes a parabolic shape as the tunnelling probability increases and the current’s dependence on F^2 in Equation 1.5 begins to dominate.^[127]

The comparison of experimental to theoretical results of field emission is completed by using the assumption that values of μ and Φ remain constant regardless of tip position. The F-N equation can be further simplified to:

$$J = a_1 F^2 \exp\left(-\frac{a_2}{F}\right) \quad \text{Equation 1.7}$$

where a_1 and a_2 are constants including b_1 and b_2 from Equation 1.6, the Fermi energy, μ , and the work function, Φ . This simplified version of the F-N equation shows that the current density, J is essentially a function of electric field, F . In the case of the macroscopic electric field this is equal to the applied voltage, V , divided by the inter-plate distance, d , such that $F = V/d$. However as part of the argument of the phenomenon of field emission, it is the local effective electric field on the surface, not the macroscopic field that changed the shape of the potential barrier. As mentioned previously the local field is enhanced by the enhancement factor β . This is most often described following:

$$F_{(local)} = \beta F_{(applied)} = \beta \frac{V}{d} = \frac{\beta}{d} V \quad \text{Equation 1.8}$$

This is the equation most commonly used for the analysis of field emission reported in publications.^[125, 130, 131] The next step toward matching experimental and theoretical results is to change the current density, J , from Equation 1.7 into current, I . This is accomplished by multiplying both sides of Equation 1.7 by area, A . Thus Equation 1.7 becomes (substituting $F = (\beta / d) V$):

$$I = Aa_1 \left(\frac{\beta}{d} \right)^2 V^2 \exp \left(- \frac{a_2}{\beta} \frac{1}{V} \right) \quad \text{Equation 1.9}$$

where A is the effective emission area. A cannot just be termed the ‘emission area’ because that implies that the current density is uniform over the entire surface and with tip like geometries this cannot be true. As such it is commonly accepted that the calculations of area using F-N data is unreliable,^[132] however the calculation of the effective emission area can be used to compare similar field emitting devices.

To determine the values of A and β from experimental results Equation 1.9 is simplified further by rearranging and then taking the natural log of both sides to yield:

$$\ln \left(\frac{I}{V^2} \right) = - \frac{a_2}{\beta} \frac{1}{V} + \ln \left(Aa_1 \left(\frac{\beta}{d} \right)^2 \right) \quad \text{Equation 1.10}$$

hence a plot of $\ln(I / V^2)$ vs $1/V$ (known as a Fowler-Nordheim plot) should be linear for a field emission process.^[133] A good linear fit depicts good electrical contact between emitter and substrate.^[134] From the equation of the straight line and the knowledge of the values of the constants a_1 and a_2 , the field enhancement factor, β , can be calculated from the slope of the line and the effective emission area, A , can be calculated from the Y-intercept.

The advantage of having a sharp tip is the high β (which results in a low turn-on field), but since emission only occurs at the apex of the tip, the emitting area is low which causes only a small amount of current to be produced. This usually results in such field emitters being used only when high brightness is required instead of high currents such as in a scanning electron microscope.^[124] The key to creating a high brightness, high current FE system lies in using a large number of field enhanced tips

or an array of tips. To achieve a high field emission current, a high density of tips must be present on a surface. There are a few technologies present that can achieve this such as Spindt tips which are etched molybdenum tips that can be created in high density arrays.^[135] The drawbacks of these tips are the expensive production, short lifetime in vacuum and high operating voltage. An alternative to the Spindt tips is the use of carbon nanotube arrays.

1.6.2 *Field emission from carbon nanotubes*

Since the first reports of field emission with very low turn-on fields and high current densities from CNTs in 1995^[136, 137] a great deal of research has been dedicated to the fabrication of CNT field emission devices that produce a stable current at a low applied electric field.

Field emission properties are summarised by the turn-on voltage, electric field enhancement factor and emission stability. The turn-on voltage (E_{to}) is the macroscopic applied field required to produce a set current density, commonly $10 \mu\text{A cm}^{-2}$. Low E_{to} values are achieved from a surface with high β and a high density of emitting tips. High β values are achieved when the emitting tips have a high aspect ratio and are placed perpendicular to the electric field (e.g. vertically aligned). The emission stability is a measure of how consistent an emitting surface can produce a set current at a set applied field.

Field emission from CNTs typically occurs with a E_{to} of around $2 \text{ V } \mu\text{m}^{-1}$ but can vary from $\sim 1 - 10 \text{ V } \mu\text{m}^{-1}$ depending upon CNT type, orientation, coverage and geometry (Table 1.5). The E_{to} for CNTs is 50 to 100 times lower than that of molybdenum and silicon tips.^[138] Values given for β vary greatly; this is often due to the many different forms of the Fowler-Nordheim equation used.^[125, 127, 130, 139] All forms of the F-N equation use assumptions such as whether the work function of CNTs is 5 eV or 4.8 eV or whether the inclusion of the Fermi energy is relevant. The F-N equation described in Section 1.6.1 will be used herein, but some error in any comparison between the calculated values of β exists as a result in variations of the F-N equation used.

Table 1.5: Summary of field emission properties from carbon nanotubes.

Emitter	Alignment	E_{to} ($V \mu m^{-1}$)	β	Comments	Ref.
Arc SWCNT	random	2.19	4950	incorporated into In_2O_3	[140]
Arc SWCNT in paste	random	1.5 – 4.5	3600	-	[141]
SWCNT	random	3	1400	SWCNT chemically attached to glass	[130]
SWCNT in paste	quasi- vertical	2.9 – 4.3	-		[142]
CVD SWCNT	random	1.6 – 3.3	-	varied with catalyst composition	[143]
CVD DWCNT	vertical	0.8 – 1.75	1000 - 3500	varied with catalyst	[144]
CVD DWCNT	random	2.5	1349	pristine	[145]
CVD DWCNT	random	1.3	2231	Ru decorated	[145]
Arc DWCNT	random	5	997	DWCNT sprayed onto surface	[146]
Arc DWCNT	random	2.1 – 2.8	1100 - 1250	-	[147]
CVD MWCNT	random	1.25 – 2.25	1200 – 2500	‘thin’ MWCNT, diam. ~10 nm	[148]
CVD MWCNT	random	4.8	400 - 1200	patterned MWCNTs	[149]
PECVD MWCNT	vertical	3 – 12	500 - 800	dependent upon emitter spacing	[150]
PECVD MWCNT	-	3 - 4	-	dependent upon plasma oxidation	[151]
CVD MWCNT	random	3 - 9.8	450 - 1200	dependent upon CNT density	[152]
		β			
Summary	E_{to} ($V \mu m^{-1}$), range (average)		range (average)		
SWCNT	1.5 - 4.5 (2.9)		1400- 4950 (3300)		
DWCNT	0.8 – 5 (2.3)		1000 – 3500 (1632)		
MWCNT	1.25- 9.8 (4.8)		450 – 2500 (1000)		

From Table 1.5 it is apparent that SWCNTs and DWCNTs exhibit the best field emission properties, which is attributed to their low diameter. An increase in diameter decreases the aspect ratio which in turn reduces the electric field enhancement. The values shown in Table 1.5 in no way represent a comprehensive review of all CNT field emission experiments but give a rough overview from a number of different CNT types and conditions. The value for DWCNTs are perhaps skewed to the better end of FE properties because the exclusive fabrication of DWCNTs is a new technology and the DWCNT surfaces were fabricated following methods that had previously worked well for SW and MWCNTs. MWCNTs are by far the most extensively studied of the CNT types due to their ease of fabrication. However, MWCNT diameter can vary greatly and as a result a very broad range of FE characteristics are present in the literature. Vertical alignment of the CNTs is clearly an important aspect of field emission as it leads to the greatest electric field enhancement. It is a common experiment to investigate the level of vertical alignment by monitoring the field emission properties.^[144, 153] For example a recent study by Chen *et al.*^[144] investigated the field emission from vertically aligned and randomly orientated DWCNTs. The field emission properties of the randomly orientated DWCNTs were much worse with a higher E_{to} of $3.67 \text{ V } \mu\text{m}^{-1}$ and a lower β of 1085 compared to $1.67 \text{ V } \mu\text{m}^{-1}$ and 3517, respectively for the vertically aligned DWCNTs.

The field emission behaviour of opened and closed nanotubes has been widely researched with no definitive result. Experiments on MWCNTs have shown that open nanotubes emit at lower voltages,^[154] that closed nanotubes emit at lower voltages^[131] and that it varied with different attachment temperatures.^[155] A theoretical study has shown that open SWCNTs should exhibit better field emission properties because the work function is decreased at the opened end due to changes of the electronic structure.^[156]

The coverage of CNTs and the effect of coverage on field emission is of importance since high coverage is required for high current densities. However, it has been found that high coverage often leads to higher turn-on fields.^[131, 138] This is attributed to electrical screening where CNTs in close proximity to one another effectively shield each other from the applied electric field. As a result of this, it has been suggested that the ideal coverage is where the inter-CNT spacing is

approximately equal to the CNT height.^[138] This theory has been supported in practice with Bonard *et al.*^[157] describing better emission properties of CNT arrays of ‘medium’ densities over those of ‘high’ and ‘low’ densities.

Field emission properties of CNTs can be further compared to inorganic semiconducting nanostructures such as nanowires, nanorods, nano screws and nanotubes. The range of materials is vast and the emission characteristics of some structures rival that of SWCNTs depending upon the shape and composition of the nanostructure (for a detailed review^[158]). For example, zinc oxide (ZnO) nanowires produced by electrochemical deposition and vapour phase growth have recorded E_{to} values of $15.5 \text{ V } \mu\text{m}^{-1}$ and $9.5 \text{ V } \mu\text{m}^{-1}$, respectively^[159] whereas 3.3 mm long ZnO nanoribbons synthesised by molten-salt-assisted thermal evaporation have yielded emission with a E_{to} of $1.3 \text{ V } \mu\text{m}^{-1}$.^[160] Other inorganic semiconducting nanostructures based upon zinc sulfide (ZnS), silicon, tungsten oxide (WO_3), aluminium nitride (AlN), silicon carbide (SiC), and many others have been investigated.^[158] E_{to} values ranging as low as $0.8 \text{ V } \mu\text{m}^{-1}$ for Si nanowires^[161] to $17.8 \text{ V } \mu\text{m}^{-1}$ for AlN nanocones have been reported.^[162]

The field emission degradation or stability from CNT arrays is of particular importance for the commercialisation of CNT FE devices. The degradation of the emission is usually caused by several phenomena and can be reversible or permanent. Arcing, Joule heating and bombardment from ionised gas molecules (ion bombardment)^[141] can cause irreversible damage. The adsorption/desorption of molecules on the emitter surface can cause reversible damage and is often observed as deviations in the F-N plot. The degradation of SWCNTs has been shown to be a factor of 10 times faster than that of MWCNTs.^[141] The faster degradation is attributed to the single shell being more sensitive to ion bombardment and irradiation. A final cause of degradation is the breakage of the nanotube to substrate adhesion under high applied fields and high vacuum; this can be avoided if stronger adhesion such as covalent bonds are used to connect the CNTs to the substrate.^[163]

Examples of some of the most stable emission currents from MWCNTs include stable emission of 1 mA cm^{-2} for 20 hr^[164] while Saito *et al.*^[165] reported an increase of 11 % in the applied field to maintain 10 mA cm^{-2} for 8000 hr. The emission stability of CVD grown MWCNTs has recently been improved by embedding CNTs within a polymer matrix. The dielectric properties of the poly(methylmethacrylate)

(PMMA) lead to a decrease in electric field screening and an increase in emission stability. Emission stability tests were achieved by maintaining a constant voltage with an initial current of $1250 \mu\text{A cm}^{-2}$. Without polymer deposition, the emission decreased by 40 % within 15 hr whereas when PMMA was deposited within the CNTs no noticeable degradation was observed within 40 hr.^[163]

Emission stability of SWCNTs are not often reported, however there have been a few investigations. Kim and co-workers^[142] printed a SWCNT paste onto an indium tin oxide (ITO) glass plate and measured the change in current at a fixed applied field (with an initial current of $100 \mu\text{A cm}^{-2}$). After 30 hr, the current had decreased by 50 %. To improve stability, the surfaces were treated to an inert gas plasma at varying power and durations. The plasma treatment was found to markedly increase the stability but at the same time it was also found to increase the E_{to} . The time taken for the current to drop by 50 % increased from 30 hr to 5000 hr (extrapolated) while the initial voltage required to produce $100 \mu\text{A cm}^{-2}$ increased from $3.46 \text{ V } \mu\text{m}^{-1}$ to $9.1 \text{ V } \mu\text{m}^{-1}$. The emission stability reported by Kim *et al.*^[142] is easily the best for SWCNTs however; the corresponding degradation in emission properties counteracts any advantage in the use of SWCNTs. The improvement of emission stability while

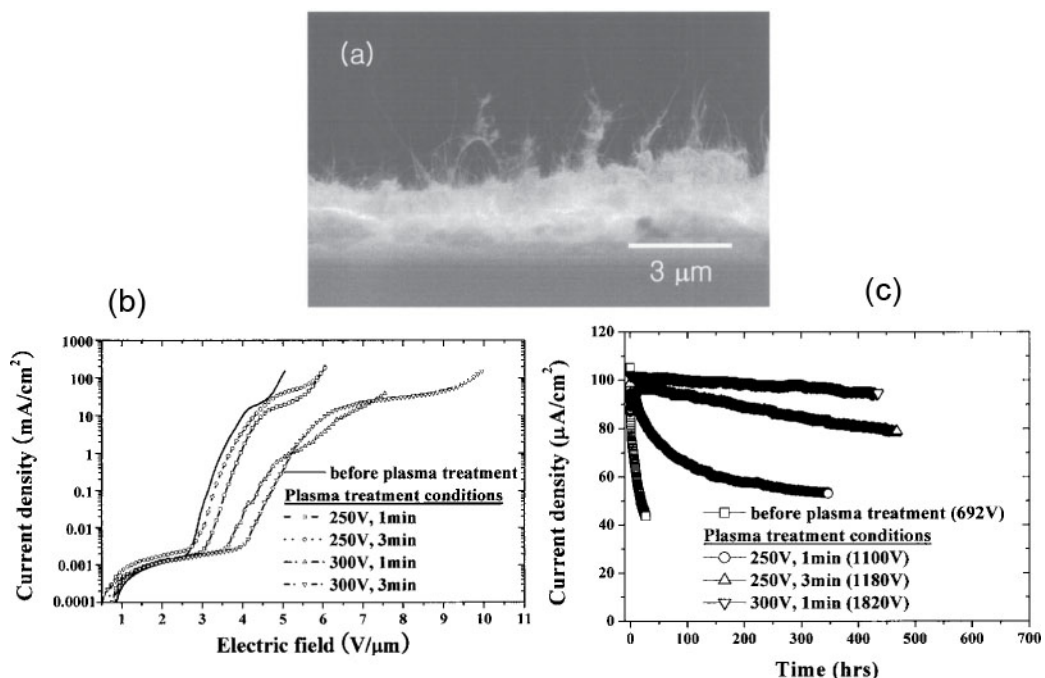


Figure 1.15: (a) SEM of SWCNT deposited from a paste, (b) J-V curves and (c) emission stability from varying plasma treatments.^[142]

not adversely affecting emission properties is a highly sought after achievement.

The big promise of vertically aligned (VA) CNT field emitting device is in applications including field emission displays,^[166] X-ray tubes,^[167] lighting filaments,^[168] and plasma and microwave sources,^[169] just to name a few. In particular, novel field emission displays are fabricated by patterning the CNTs onto the cathode using catalyst masking,^[170] lithography,^[170] or screen-printing.^[125] while the anode is coated with a phosphor array which produces coloured light when hit by an electron.^[171] The advantage of such displays over liquid crystal displays are a lower power consumption (10 mA cm⁻² required), higher brightness, a wider viewing angle, a fast response rate and a wider operating temperature range.^[171, 172] Despite the promise of CNT based FE devices no commercial products are currently available, although prototypes have been made.^[173] This is mainly due to lack of emission stability and lack of uniformity between fabricated devices.

1.7 Carbon nanotubes as biointerfacial substrates

1.7.1 Background

The intracellular structures of the cytoskeleton are composed of nanoscale protein filaments, not dissimilar in diameter and aspect ratio to CNTs. These nanoscale architectures are critical to cell and tissue function. It is therefore intriguing to consider that man-made nanoscale architectures, mimicking the natural ones, might be ideally suited to manipulate or interfere with cell behaviour. Control might be facilitated by direct interactions of individual CNTs with cellular protein components or even nucleic acids. This paradigm receives further support from the notion that one might bring to bear the exceptional electronic and mechanical properties of CNTs on cells with the aim to generate multifunctional biointerfaces. For this reason, CNTs offer fertile ground for biointerfacial studies involving mammalian cells. It is also well established that mammalian cells are able to detect and process topographical cues on a surface down to the nanoscale.^[174] CNT decorated surfaces are prime examples of controlled nanostructured topographies which cells should react to in order to achieve cell guidance and cell stimulation which may be useful for tissue regeneration.

As well as providing scaffolds for cell growth, CNT tip functionalisation could lead to delivery of a load into the cellular structure. Specific gene plasmids could be adsorbed onto the tips of the CNTs which, when loaded into the desired cell could permit precise temporal control of gene expression, which is highly relevant to stem cell technologies where phenotypic control during development is desirable. VA-CNTs are the nanoscale analogue of a bed of nails, begging the question how cells in contact with such substrate surfaces will behave.

1.7.2 Carbon nanotube biointerfaces

Whilst CNT biocompatibility remains a significant and topical issue and one of the primary targets of nanotoxicity research,^[175] there is no substantial evidence for toxicity of surface-immobilised nanotubes.^[176] Toxicity appears to rely on internalisation by cells and even then it is not always observed. Internalisation by endocytosis of functionalised SWCNTs has been exploited for molecular transport

into cells in a seminal study.^[177] Interestingly, the nanotubes did not exhibit any appreciable toxicity over 48 hr, suggesting potential applications of CNT transporters for drug delivery.^[178]

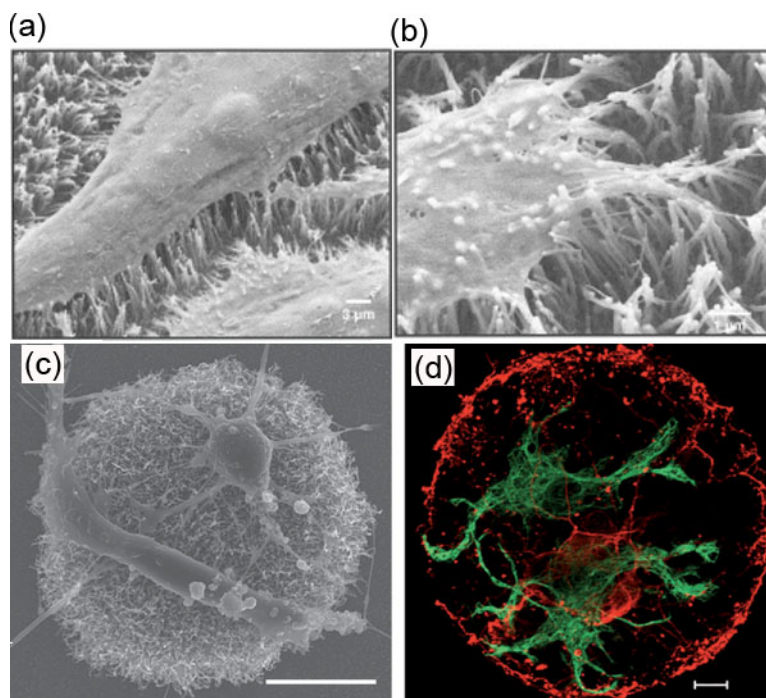


Figure 1.16: (a, b, c) SEM images depicting the attachment of cells to a carpet of VA-CNTs. (a) The tips of the VA-CNTs are in intimate contact with the cell surface. (b) The bending and deformation of the tubes is occurring via biomechanical forces.^[179] (c) Neuronal cells adhere preferentially to isolated islands of pristine CNTs. (d) Confocal fluorescence image of neurons (red) and glia cells (green) on a large CNT island. Scale bar in (c, d) 10 μm .^[180]

Several recent studies have focused on cell interactions with planar surface-bound CNTs. These studies have provided insights into cell morphology, proliferation and migration in direct response to surfaces decorated by CNTs. For example, Giannona *et al.*^[179] showed that spreading, adhesion and proliferation of osteosarcoma cells was enhanced and cell bodies were markedly elongated on VA-MWCNTs on a silicon substrate in comparison to conventional tissue culture plastic (Figure 1.16 (a)). Nanotubes attached via their tips to a cell appeared to bend towards the cell body under the forces exerted by the cell, an effect previously described for elastomeric microneedles (Figure 1.16 (b)).^[181] In addition, the authors reported that cell spreading on periodic nanotube arrays prepared by nanosphere lithography followed by CVD was aligned with the array, suggesting that mechanical signals

from the substrate are translated into migratory and shape-changing cellular signals. The achieved cell guidance and cell stimulation may be useful for tissue regeneration, in general, and bone bioengineering in particular.

Efforts are also underway to engineer electrically addressable neural networks on CNT architectures providing electrical back contacts for signal transmission.^[182] Such networks have significant potential in research efforts aimed at better understanding of brain function but also in experimental strategies for spinal cord repair. Neural clusters form as primary rat neurons migrate from low affinity sites on a silica substrate to patches of randomly oriented CNT mats defined by soft lithography. Neurites then connect these patches by tensed links following geometrical connectivity and almost exclusively bridging gaps between neighbouring clusters. This process occurs over a period of four days. The final cell density of the silica is very low, yet neurite extension does not appear to be hindered on the silica. Cell clusters show normal generation of action potentials.

Similarly, Jacob *et al.*^[180] observed neural clusters on isolated CNT electrodes and the formation of ordered networks with high fidelity after two days. Here, CNT patches were grown on lithographically defined, titanium nitride conductors on a silicon dioxide substrate. After several days in culture, the cell networks generated spontaneous electrical activity in the form of neuronal action potentials (Figure 1.16 (c, d)).

Piercing of the cell wall on the nanoscale should heal readily by diffusion of cell membrane lipids without significant perturbation of ion gradients and the cytoskeleton.^[183] This concept could be exploited for delivery of molecules into the cytoplasm.^[178] Indeed, Chen *et al.*^[184] developed a nanoscale injector by attaching a single MWCNT to a silicon AFM tip using electron beam welding.^[185] This nanoneedle penetrated the cell wall of HeLa cells without inducing harmful effects often associated with intracellular delivery technologies. Cargo attached to the CNT via a cleavable linker was delivered and released into the cytoplasm of cervical cancer (HeLa) cells.

Higher throughput delivery of cargo into CNTs has been achieved by spearing of cells with suspended CNTs driven by a magnetic field.^[186] Nickel-embedded nanotubes were prepared from vertically aligned nanotube carpets grown on silicon

by PECVD. Highly efficient gene transfer under retention of cell viability was demonstrated for hard-to-transfect cells, providing opportunities for nonviral gene therapies. Likewise, efficient gene transfer has been described using cationic-functionalised CNTs condensed with plasmid DNA.^[181]

The group of Simpson showed that vertically aligned carbon nanofibres (tip diameter 20 – 100 nm) grown on silicon facilitate DNA delivery into mammalian cells^[187, 188] by a mechanism termed ‘impalefaction’. Nanofibre arrays with a pitch of 5 µm were loaded with DNA plasmid either by adsorption or covalent attachment and cells were brought into contact with the array by means of centrifugation or, additionally, pressing the cells against a flat surface.^[187] Impalement of cells by plasmid-loaded nanofibres resulted in long-term protein expression and cell growth. Spatial registration into an array of numerically indexed 100 µm squares with around 400 nanofibres each allowed tracking of gene expression in individual cell colonies.^[188] Adsorption of DNA was enhanced by incorporation of nitrogen into the nanofibres. Nanofibre arrays with adsorbed DNA resulted in expression of green fluorescent protein (GFP), persisting over several weeks. As cells divided, progeny continued to fluoresce showing that desorbed plasmid segregated into the dividing cells. Stable expression is consistent with delivery of plasmids into the cell nucleus. This mode of delivery is not surprising given the large fractional area of the nucleus. Nevertheless, nuclear delivery is an important feat, often not achieved by other gene transfer techniques. Apart from stable gene expression, nuclear delivery shields plasmid DNA from enzymatic degradation in the cytoplasm.

Gene transfection has since been shown on glass slide coated with a mixture of graphene oxide (GO) and MWCNTs.^[189] In this report, NIH-3T3 fibroblast and HeLa cells were immobilised on the surface where it was shown that the number of focal adhesions increased for the GO/MWCNT surfaces indicating cell affinity. A plasmid DNA with a GFP was shown to be expressed in a higher efficiency for cells on the GO/MWCNT coated surfaces indicating that CNTs are a suitable scaffold for gene transfection.^[189] Interestingly, the GO only surfaces produced the highest gene transfection efficiencies which could indicate that the level of cell affinity to the hydrophobic substrate could play a key role in gene transfection, as had been observed previously.^[190]

The structure and properties of CNTs lead to another possible route toward gene transfection. Electroporation involves the use of an electric field to reversibly disrupt the cellular cytoskeleton to open small pores and to release target genes from the surface and into the newly formed pores.^[191] The opening of pores is driven by the change in transmembrane potential difference which is directly related to the cell radius and external electric field.^[192] Electric field strength is the most crucial factor for the formation of pores on the cell membrane. The electric field strength is required to be high enough to ensure that pores are formed but not too high that irreversible damage is imparted upon the cell structure. Electroporation experiments are commonly carried out by applying a large electric field across a solution containing suspended cells and gene plasmid within the electroporation solution (Figure 1.17 (a)). This process has been used to transfect cells with high efficiency and viability.^[193] However, not all cells are easily transfected and a higher, potentially damaging electric field is required. The unique shape and structure of CNTs offer the opportunity to increase the local electric field around the CNT tip while using a moderate electric field (as detailed in Section 1.6).

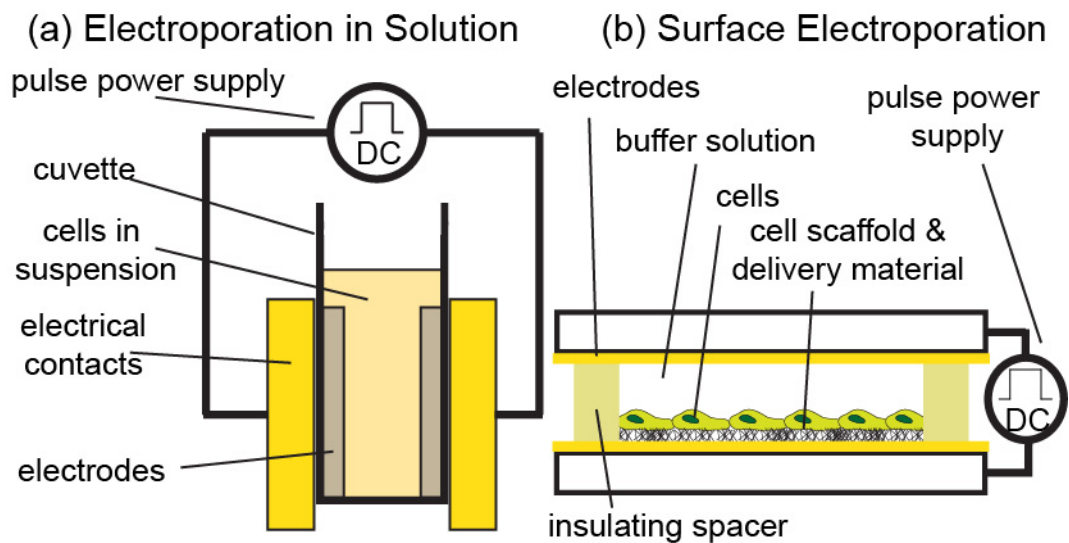


Figure 1.17: Schematics of electroporation. (a) Cells in suspension or (b) cells immobilised on a surfaces are exposed to an electric field in order to deliver target material.

The electroporation and gene transfection from cells immobilised on CNT surfaces has recently been demonstrated by Iwata *et al.*^[194] CNTs were immobilised on a gold surface by the fabrication of an amine terminated SAM followed by the

electrostatic adhesion of carboxylated MWCNTs, poly(ethylimine) (PEI) and a plasmid DNA encoded with a GFP. Electroporation of human embryonic kidney (HEK) cells was completed by applying a single 10 ms pulse of 240 V cm^{-1} (Figure 1.17 (b)). The gene transfection efficiency of the MWCNT loaded surfaces was found to be 55 % while the control surface (without MWCNT) recorded an efficiency of 30 % (Figure 1.18, transfected cells fluoresce green).^[194]

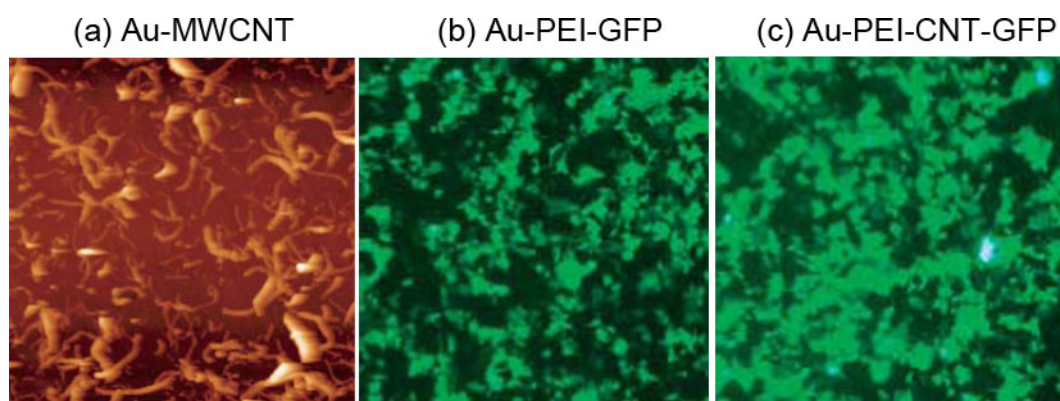


Figure 1.18: Summary of results of electroporation on MWCNT showing (a) AFM image of randomly oriented MWCNTs on surface ($5 \times 5 \mu\text{m}^2$). Fluorescence microscopy images after electroporation and gene transfection of a green fluorescent plasmid showing (b) control surface without MWCNTs and (c) a MWCNT surface. Green cells in (b, c) indicate gene transfection, images $1.5 \times 1.5 \text{ mm}^2$.^[194]

While CNT specific cytotoxicity is not an issue for surface bound CNTs, the effect of catalyst particles from CVD grown CNTs is clearly an issue where transition metal catalysts such as nickel and cobalt are often used which have been found to induce cytotoxicity.^[195] An interesting twist on the issue of CNT toxicity came as a result of a report by Allen *et al.*^[196] demonstrating the biodegradation of CNTs by common oxidative enzymes, including horseradish peroxidase. Catalytic degradation of CNTs might help to reduce CNT toxicity and spawn research into implantable CNT-based devices and drug delivery platforms in clinical applications.

1.8 Motivation

The chemical attachment of CNTs to surfaces, particularly silicon, is an up-scalable approach to producing CNTs substrates that have been shown to function effectively as chemical sensors and photovoltaic devices. This Thesis aims to investigate the applicability of chemically attached CNTs to the fields of water filtration, field emission and as biointerfacial substrates.

This Thesis consists of an experimental methods chapter (Chapter 2), a series of experimental results chapters (Chapters 3 – 7) and a concluding chapter (Chapter 8). The initial experimental results chapters (Chapter 3 and 4) focus on the preparation of Si-CNT nanostructures. Particular emphasis is placed upon the attachment of various CNT types to flat Si and SWCNTs to pSi in Chapter 3. Chapter 4 looks at the controlled placement of SWCNTs onto silicon following a number of protocols. The subsequent results chapters investigate the applicability of Si-CNT nanostructures for specific applications, namely mass transport and filtration (Chapter 5), field emission (Chapter 6) and as a scaffold for biomaterial immobilisation (Chapter 7).

1.9 References

- [1] M. Riordan, L. Hoddeson, and C. Herring, "The invention of the transistor", *Reviews of Modern Physics*, **71** (2), S336 (1999).
- [2] D. B. Keck, and P. C. Schultz, Method of Producing Optical Waveguide Fibres, US patent, 1973.
- [3] S. Bhattacharyya, and R. K. Das, "Catalytic control of automotive NOx: a review", *International Journal of Energy Research*, **23** (4), 351-69 (1999).
- [4] A. Cenk, and M. S. Andrei, "Experimental evaluation and comparative analysis of commercial variable-capacitance MEMS accelerometers", *Journal of Micromechanics and Microengineering*, **13** (5), 634 (2003).
- [5] M. Hoff, and F. Faggin, Memory system for mult-chip digital computer, US patent, 1974.
- [6] G. E. Moore, "Cramming more components onto integrated circuits", *Electronics*, **38** (8), 114 (1965).
- [7] S. Lloyd, "Ultimate physical limits to computation", *Nature*, **406** (6799), 1047-54 (2000).
- [8] C. B. Greenberg, Photocatalytically-activated self-cleaning article and method of making same, Worldwide patent, 1998.
- [9] R. Blossey, "Self-cleaning surfaces - virtual realities", *Nature Materials*, **2** (5), 301-6 (2003).
- [10] J. W. Plunkett, "Plunkett's Nanotechnology & MEMS Industry Almanac", *Plunkett Research, Ltd.*, Houston, Texas, USA, (2006).
- [11] S. Kawata, H.-B. Sun, T. Tanaka, and K. Takada, "Finer features for functional microdevices", *Nature*, **412** (6848), 697-8 (2001).
- [12] D. M. Eigler, and E. K. Schweizer, "Positioning single atoms with a scanning tunnelling microscope", *Nature*, **344** (6266), 524-6 (1990).
- [13] M. Fuechsle, Mahapatra S, F. A. Zwanenburg, M. Friesen, *et al.*, "Spectroscopy of few-electron single-crystal silicon quantum dots", *Nature Nanotechnology*, **5** (7), 502-5 (2010).
- [14] G. Cao, "Nanostructures & Nanomaterials: Synthesis, Properties & Application", *Imperial College Press*, London, (2004).
- [15] A. V. Krasnoslobodtsev, and S. N. Smirnov, "Effect of Water on Silanization of Silica by Trimethoxysilanes", *Langmuir*, **18** (8), 3181-4 (2002).
- [16] M. R. Nussio, G. Oncins, I. Ridelis, E. Szili, *et al.*, "Nanomechanical Characterization of Phospholipid Bilayer Islands on Flat and Porous Substrates: A Force Spectroscopy Study", *The Journal of Physical Chemistry B*, **113** (30), 10339-47 (2009).
- [17] T. Barclay, T. C. Kristina, and J. Matison, " Self-assembled lipid nanotubes by rational design", *Journal of Materials Reserach*, **26**, 322 - 35 (2011).
- [18] Z. Liu, Z. Shen, T. Zhu, S. Hou, *et al.*, "Organizing Single-Walled Carbon Nanotubes on Gold Using a Wet Chemical Self-Assembling Technique", *Langmuir*, **16** (8), 3569-73 (2000).
- [19] B. Wu, J. Zhang, Z. Wei, S. Cai, *et al.*, "Chemical Alignment of Oxidatively Shortened Single-Walled Carbon Nanotubes on Silver Surface", *The Journal of Physical Chemistry B*, **105** (22), 5075 (2001).
- [20] K. T. Constantopoulos, C. J. Shearer, A. V. Ellis, N. H. Voelcker, *et al.*, "Carbon Nanotubes Anchored to Silicon for Device Fabrication", *Advanced Materials*, **22** (5), 557-71 (2010).

- [21] M. A. Bissett, and J. G. Shapter, "Photocurrent Response from Vertically Aligned Single-Walled Carbon Nanotube Arrays", *The Journal of Physical Chemistry C*, **114** (14), 6778-83 (2010).
- [22] J. Yu, J. G. Shapter, J. S. Quinton, M. R. Johnston, *et al.*, "Direct attachment of well-aligned single-walled carbon nanotube architectures to silicon (100) surfaces: a simple approach for device assembly", *Physical Chemistry Chemical Physics*, **9**, 510-20 (2007).
- [23] D. D. Tune, B. S. Flavel, J. S. Quinton, A. V. Ellis, *et al.*, "Single walled carbon nanotube network electrodes for dye solar cells", *Solar Energy Materials and Solar Cells*, **94** (10), 1665-72 (2010).
- [24] S. Iijima, "Helical Microtubules of graphitic carbon", *Nature*, **354**, 56 (1991).
- [25] M. Monthieux, and V. Kuznetsov, "Who should be given the credit for the discovery of carbon nanotubes?", *Carbon*, **44** (9), 1621 (2006).
- [26] L. Radushkevich, and Lukyanovich, "O strukture ugleroda, obrazujucesja pri termiceskom razlozenii okisi ugleroda na zeleznom kontakte.", *VM Zurn Fisic Chim*, **26**, 88-95 (1952).
- [27] S. Iijima, and T. Ichihashi, "Single-shell carbon nanotubes of 1-nm diameter", *Nature*, **363**, 603 (1993).
- [28] D. Bethune, C. Kiang, M. De Vries, G. Gorman, *et al.*, "Cobalt catalysed growth of carbon nanotubes with single-atomic-layer walls", *Nature*, **363**, 605 (1993).
- [29] T. Belin, and F. Epron, "Characterization methods of carbon nanotubes: a review", *Materials Science and Engineering B*, **199**, 105-18 (2005).
- [30] V. N. Popov, "Carbon Nanotubes: properties and application", *Materials Science & Engineering R-Reports*, **43**, 61-102 (2004).
- [31] M. S. Dresselhaus, G. Dresselhaus, R. Saito, and A. Jorio, "Raman spectroscopy of carbon nanotubes", *Physics Reports-Review Section of Physics Letters*, **409** (2), 47-99 (2005).
- [32] N. W. Aschcroft, and N. D. Mermin, "Solid State Physics", *Harcourt Brace College*, Orlando, Florida, U.S.A, (1976).
- [33] E. Joselevich, "Electronic Structure and Chemical Reactivity of Carbon Nanotubes: A Chemist's View", *ChemPhysChem*, **5**, 619-24 (2004).
- [34] P. Avouris, Z. Chen, and V. Perebeinos, "Carbon-based electronics", *Nature Nanotechnology*, **2** (10), 605-15 (2007).
- [35] T. Durkop, S. A. Getty, E. Cobas, and M. S. Fuhrer, "Extraordinary Mobility in Semiconducting Carbon Nanotubes", *Nano Letters*, **4** (1), 35-9 (2004).
- [36] B. Q. Wei, R. Vajtai, and P. M. Ajayan, "Reliability and current carrying capacity of carbon nanotubes", *Applied Physics Letters*, **79**, 1172 (2001).
- [37] R. Martel, T. Schmidt, H. R. Shea, T. Hertel, *et al.*, "Single- and multi-wall carbon nanotube field-effect transistors", *Applied Physics Letters*, **73** (17), 2447-9 (1998).
- [38] S. J. Tans, A. R. M. Verschueren, and C. Dekker, "Room-temperature transistor based on a single carbon nanotube", *Nature*, **393** (6680), 49-52 (1998).
- [39] J. Hone, M. C. Llaguno, M. J. Biercuk, A. T. Johnson, *et al.*, "Thermal properties of carbon nanotubes and nanotube based materials", *Applied Physics A:Materials Science & Processing*, **74**, 339 (2002).
- [40] T. Yamamoto, K. Watanabe, and E. Hernández, Mechanical Properties, Thermal Stability and Heat Transport in Carbon Nanotubes in *Carbon Nanotubes, Vol. 111*, Springer Berlin / Heidelberg, 2008, pp. 165-94.

- [41] C. Yu, L. Shi, Z. Yao, D. Li, *et al.*, "Thermal Conductance and Thermopower of an Individual Single-Wall Carbon Nanotube", *Nano Letters*, **5** (9), 1842-6 (2005).
- [42] N. Mingo, and D. A. Broido, "Carbon Nanotube Ballistic Thermal Conductance and Its Limits", *Physical Review Letters*, **95** (9), 096105 (2005).
- [43] K. Kordas, G. Toth, P. Moilanen, M. Kumpumaki, *et al.*, "Chip cooling with integrated carbon nanotube microfin architectures", *Applied Physics Letters*, **90** (12), 123105 (2007).
- [44] E. W. Wong, P. E. Sheehan, and C. M. Lieber, "Nanobeam Mechanics: Elasticity, Strength, and Toughness of Nanorods and Nanotubes", *Science*, **277** (5334), 1971-5 (1997).
- [45] A. Krishnan, E. Dujardin, T. W. Ebbesen, P. N. Yianilos, *et al.*, "Young's modulus of single-walled nanotubes", *Physical Review B*, **58** (20), 14013 (1998).
- [46] M. M. J. Treacy, T. W. Ebbesen, and J. M. Gibson, "Exceptionally high Young's modulus observed for individual carbon nanotubes", *Nature*, **381** (6584), 678-80 (1996).
- [47] B. G. Demczyk, Y. M. Wang, J. Cumings, M. Hetman, *et al.*, "Direct mechanical measurement of the tensile strength and elastic modulus of multiwalled carbon nanotubes", *Materials Science and Engineering A*, **334** (1-2), 173-8 (2002).
- [48] M. Endo, M. Strano, and P. Ajayan, Potential Applications of Carbon Nanotubes in *Topics in Applied Physics: Carbon Nanotubes, Vol. 111*, Springer, Berlin/Heidelberg, 2008, pp. 13-61.
- [49] S. Banerjee, T. Hemraj-Benny, and S. S. Wong, "Covalent surface chemistry of single-walled carbon nanotubes", *Advanced Materials*, **17** (1), 17-29 (2005).
- [50] A. Eitan, K. Jiang, D. Dukes, R. Andrews, *et al.*, "Surface Modification of Multiwalled Carbon Nanotubes: Toward the Tailoring of the Interface in Polymer Composites", *Chemistry of Materials*, **15** (16), 3198-201 (2003).
- [51] R. F. Gibson, E. O. Ayorinde, and Y.-F. Wen, "Vibrations of carbon nanotubes and their composites: A review", *Composites Science and Technology*, **67** (1), 1-28 (2007).
- [52] M. Kausala, and L. C. Zhang, "Energy absorption capacity of carbon nanotubes under ballistic impact", *Applied Physics Letters*, **89** (12), 123127 (2006).
- [53] E. Frackowiak, and F. Béguin, "Electrochemical storage of energy in carbon nanotubes and nanostructured carbons", *Carbon*, **40** (10), 1775-87 (2002).
- [54] C. T. Gibson, S. Carnally, and C. J. Roberts, "Attachment of carbon nanotubes to atomic force microscope probes", *Ultramicroscopy*, **107** (10-11), 1118-22 (2007).
- [55] M. Khodakovskaya, E. Dervishi, M. Mahmood, Y. Xu, *et al.*, "Carbon Nanotubes Are Able To Penetrate Plant Seed Coat and Dramatically Affect Seed Germination and Plant Growth", *ACS Nano*, **3** (10), 3221-7 (2009).
- [56] E. G. Gamaly, and T. W. Ebbesen, "Mechanism of carbon nanotube formation in the arc discharge", *Physical Review B*, **52** (3), 2083 (1995).
- [57] C. Journet, W. K. Maser, P. Bernier, A. Loiseau, *et al.*, "Large-scale production of single-walled carbon nanotubes by the electric-arc technique", *Nature*, **388** (6644), 756-8 (1997).

- [58] T. W. Ebbesen, and P. M. Ajayan, "Large-scale synthesis of carbon nanotubes", *Nature*, **358** (6383), 220-2 (1992).
- [59] E. Joselevich, H. Dai, J. Liu, K. Hata, *et al.*, Carbon Nanotube Synthesis and Organization in *Carbon Nanotubes, Topics in Applied Physics, Vol. 111* (Eds.: A. Jorio, G. Dresselhaus, M. S. Dresselhaus), Springer-Verlag, Berlin Heidelberg, **2008**, pp. 101-64.
- [60] A. Thess, R. Lee, P. Nikolaev, H. Dai, *et al.*, "Crystalline Ropes of Metallic Carbon Nanotubes", *Science*, **273** (5274), 483-7 (1996).
- [61] D. Mann, Synthesis of carbon nanotubes in *Carbon Nanotubes Properties and Applications* (Ed.: M. J. O'Connell), Taylor & Francis, Boca Raton, FL, **2006**, pp. 19-49.
- [62] Y. Li, W. Kim, Y. Zhang, M. Rolandi, *et al.*, "Growth of Single-Walled Carbon Nanotubes from Discrete Catalytic Nanoparticles of Various Sizes", *The Journal of Physical Chemistry B*, **105** (46), 11424-31 (2001).
- [63] L. Qu, F. Du, and L. Dai, "Preferential Syntheses of Semiconducting Vertically Aligned Single-Walled Carbon Nanotubes for Direct Use in FETs", *Nano Letters*, **8** (9), 2682-7 (2008).
- [64] X. Ya-Qiong, F. Erica, S. Howard, E. S. Richard, *et al.*, "Effects of atomic hydrogen and active carbon species in 1 mm vertically aligned single-walled carbon nanotube growth", *Applied Physics Letters*, **89** (12), 123116 (2006).
- [65] S. Fan, M. G. Chapline, N. R. Franklin, T. W. Tomblor, *et al.*, "Self-Oriented Regular Arrays of Carbon Nanotubes and Their Field Emission Properties", *Science*, **283** (5401), 512-4 (1999).
- [66] B. Q. Wei, R. Vajtai, Y. Jung, J. Ward, *et al.*, "Microfabrication technology: Organized assembly of carbon nanotubes", *Nature*, **416** (6880), 495-6 (2002).
- [67] S. Maruyama, R. Kojima, Y. Miyauchi, S. Chiashi, *et al.*, "Low-temperature synthesis of high-purity single-walled carbon nanotubes from alcohol", *Chemical Physics Letters*, **360** (3-4), 229-34 (2002).
- [68] T. Yamada, T. Namai, K. Hata, D. N. Futaba, *et al.*, "Size-selective growth of double-walled carbon nanotube forests from engineered iron catalysts", *Nature Nanotechnology*, **1** (2), 131-6 (2006).
- [69] M. Endo, K. Takeuchi, S. Igarashi, K. Kobori, *et al.*, "The production and structure of pyrolytic carbon nanotubes (PCNTs)", *Journal of Physics and Chemistry of Solids*, **54** (12), 1841-8 (1993).
- [70] H. Dai, A. G. Rinzler, P. Nikolaev, A. Thess, *et al.*, "Single-wall nanotubes produced by metal-catalyzed disproportionation of carbon monoxide", *Chemical Physics Letters*, **260** (3-4), 471-5 (1996).
- [71] H. Dai, Nanotube Growth and Characterization in *Carbon Nanotubes, Topics in Applied Physics, Vol. 80* (Eds.: M. S. Dresselhaus, G. Dresselhaus, P. Avouris), Springer-Verlag, Berlin Heidelberg, **2001**, pp. 29-53.
- [72] R. L. Vander Wal, T. M. Ticich, and V. E. Curtis, "Substrate-support interactions in metal-catalyzed carbon nanofiber growth", *Carbon*, **39** (15), 2277-89 (2001).
- [73] Z. F. Ren, Z. P. Huang, J. W. Xu, J. H. Wang, *et al.*, "Synthesis of Large Arrays of Well-Aligned Carbon Nanotubes on Glass", *Science*, **282** (5391), 1105-7 (1998).
- [74] K. Hata, D. N. Futaba, K. Mizuno, T. Namai, *et al.*, "Water-Assisted Highly Efficient Synthesis of Impurity-Free Single-Walled Carbon Nanotubes", *Science*, **306** (5700), 1362-4 (2004).

- [75] S. Chakrabarti, K. Gong, and L. Dai, "Structural Evaluation along the Nanotube Length for Super-long Vertically Aligned Double-Walled Carbon Nanotube Arrays", *The Journal of Physical Chemistry C*, **112** (22), 8136-9 (2008).
- [76] Y. Yun, V. Shanov, Y. Tu, S. Subramaniam, *et al.*, "Growth Mechanism of Long Aligned Multiwall Carbon Nanotube Arrays by Water-Assisted Chemical Vapor Deposition", *The Journal of Physical Chemistry B*, **110** (47), 23920-5 (2006).
- [77] K. B. K. Teo, M. Chhowalla, G. A. J. Amaratunga, W. I. Milne, *et al.*, "Uniform patterned growth of carbon nanotubes without surface carbon", *Applied Physics Letters*, **79** (10), 1534-6 (2001).
- [78] S. M. Sze, and N. K. K., "Physics of Semiconductor Devices", *John Wiley & Sons, Inc*, Hoboken, New Jersey, (2007).
- [79] L. Canham, "Properties of Porous Silicon", *The Institution of Electrical Engineers*, London, United Kingdom, (1997).
- [80] N. Nobuaki, and S. Ikuo, "Luminescent porous silicon synthesized by visible light irradiation", *Applied Physics Letters*, **62** (12), 1429-31 (1993).
- [81] J. M. Schmeltzer, and J. M. Buriak, Recent Developments in the Chemistry and Chemical Applications of Porous Silicon in *The Chemistry of Nanomaterials: Synthesis, Properties and Applications* (Eds.: C. N. Rao, A. Müller, A. K. Cheetham), Wiley, Weinheim, 2005, pp. 518-50.
- [82] V. Lehmann, and U. Gosele, "Porous silicon formation: A quantum wire effect", *Applied Physics Letters*, **58** (8), 856-8 (1991).
- [83] V. Lehmann, "Electrochemistry of Silicon: Instrumentation, Science, Materials and Applications", Weinheim, Germany, (2002).
- [84] A. Ressine, S. Ekstrom, G. Marko-Varga, and T. Laurell, "Macro-/Nanoporous Silicon as a Support for High-Performance Protein Microarrays", *Analytical Chemistry*, **75** (24), 6968-74 (2003).
- [85] S. P. Low, K. A. Williams, L. T. Canham, and N. H. Voelcker, "Evaluation of mammalian cell adhesion on surface-modified porous silicon", *Biomaterials*, **27** (26), 4538-46 (2006).
- [86] H. L. Young, H. A. Kay, S. P. Jin, Y. Cheol-Min, *et al.*, "A Diameter-Selective Attack of Metallic Carbon Nanotubes by Nitronium Ions", *Journal of the American Chemical Society*, **127**, 5196-203 (2005).
- [87] H. L. Young, S. Kwanyong, A. P. Kyung, K. Changwook, *et al.*, "Chirality- and Diameter-Dependent Reactivity of NO₂ on Carbon Nanotube Walls", *Journal of the American Chemical Society*, **127**, 15724-9 (2005).
- [88] B. Neises, and W. Steglich, "Simple Method for the Esterification of Carboxylic Acids", *Angewandte Chemie International Edition in English*, **17** (7), 522-4 (1978).
- [89] E. Valeur, and M. Bradley, "Amide bond formation: beyond the myth of coupling reagents", *Chemical Society Reviews*, **38** (2), 606-31 (2009).
- [90] Z. Poh, B. S. Flavel, C. J. Shearer, J. G. Shapter, *et al.*, "Fabrication and electrochemical behavior of vertically-aligned carbon nanotube electrodes covalently attached to p-type silicon via a thioester linkage", *Materials Letters*, **63** (9-10), 757-60 (2009).
- [91] P. Diao, and Z. Liu, "Vertically Aligned Single-Walled Carbon Nanotubes by Chemical Assembly – Methodology, Properties, and Applications", *Advanced Materials*, **22** (13), 1430-49 (2010).

- [92] J. J. Gooding, R. Wibowo, J. Liu, W. Yang, *et al.*, "Protein Electrochemistry Using Aligned Carbon Nanotube Arrays", *Journal of the American Chemical Society*, **125**, 9006-7 (2003).
- [93] J. Yu, D. Losic, M. Marshall, T. B. John, *et al.*, "Preparation and characterisation of an aligned carbon nanotube array on the silicon (100) surface", *Soft Matter*, **2**, 1081-8 (2006).
- [94] B. S. Flavel, J. Yu, J. G. Shapter, and J. S. Quinton, "Patterned attachment of carbon nanotubes to silane modified silicon", *Carbon*, **45**, 2551-8 (2007).
- [95] J. Yu, J. G. Shapter, M. R. Johnston, J. S. Quinton, *et al.*, "Electron-transfer characteristics of ferrocene attached to single-walled carbon nanotubes (SWCNT) arrays directly anchored to silicon(100)", *Electrochimica Acta*, **52**, 6206-11 (2007).
- [96] J. Yu, S. Mathew, B. S. Flavel, M. R. Johnston, *et al.*, "Ruthenium Porphyrin Functionalized Single-Walled Carbon Nanotube Arrays-A Step Toward Light Harvesting Antenna and Multibit Information Storage", *Journal of the American Chemical Society*, **130** (27), 8788-96 (2008).
- [97] T. Younos, and K. E. Tulou, "Overview of desalination techniques", *Journal of Contemporary Water Research & Education*, (132), 3-10 (2005).
- [98] G. Hummer, J. C. Rasaiah, and J. P. Noworyta, "Water conduction through the hydrophobic channel of a carbon nanotube", *Nature*, **414** (6860), 188-90 (2001).
- [99] S. J. Duranceau, in *the American Membrane Technology Association's Annual Symposium*, Isle of Palms, S.C, **2001**.
- [100] G. Hummer, "Water, proton, and ion transport: from nanotubes to proteins", *Molecular Physics*, **105** (2), 201 - 7 (2007).
- [101] M. L. Zeidel, S. V. Ambudkar, B. L. Smith, and P. Agre, "Reconstitution of functional water channels in liposomes containing purified red cell CHIP28 protein", *Biochemistry*, **31** (33), 7436-40 (1992).
- [102] A. Waghe, J. C. Rasaiah, and G. Hummer, "Filling and emptying kinetics of carbon nanotubes in water", *The Journal of Chemical Physics*, **117** (23), 10789-95 (2002).
- [103] J. C. Rasaiah, S. Garde, and G. Hummer, "Water in Nonpolar Confinement: From Nanotubes to Proteins and Beyond *", *Annual Review of Physical Chemistry*, **59** (1), 713-40 (2008).
- [104] A. Berezhkovskii, and G. Hummer, "Single-File Transport of Water Molecules through a Carbon Nanotube", *Physical Review Letters*, **89** (6), 064503 (2002).
- [105] A. Kalra, S. Garde, and G. Hummer, "Osmotic water transport through carbon nanotube membranes", *Proceedings of the National Academy of Sciences*, **100** (18), 10175-80 (2003).
- [106] B. Corry, "Designing Carbon Nanotube Membranes for Efficient Water Desalination", *The Journal of Physical Chemistry B*, **112** (5), 1427-34 (2008).
- [107] M. E. Suk, A. V. Raghunathan, and N. R. Aluru, "Fast reverse osmosis using boron nitride and carbon nanotubes", *Applied Physics Letters*, **92** (13), 133120 (2008).
- [108] J. A. Thomas, and A. J. H. McGaughey, "Reassessing Fast Water Transport Through Carbon Nanotubes", *Nano Letters*, **8** (9), 2788-93 (2008).
- [109] Y. Xu, and N. R. Aluru, "Carbon nanotube screening effects on the water-ion channels", *Applied Physics Letters*, **93** (4), 043122-3 (2008).

- [110] B. Liu, X. Li, B. Li, B. Xu, *et al.*, "Carbon Nanotube Based Artificial Water Channel Protein: Membrane Perturbation and Water Transportation", *Nano Letters*, **9** (4), 1386-94 (2009).
- [111] J. Cannon, and O. Hess, "Fundamental dynamics of flow through carbon nanotube membranes", *Microfluidics and Nanofluidics*, **8** (1), 21-31 (2010).
- [112] B. J. Hinds, N. Chopra, T. Rantell, R. Andrews, *et al.*, "Aligned Multiwalled Carbon Nanotube Membranes", *Science*, **303**, 62 (2004).
- [113] M. Majumder, N. Chopra, R. Andrews, and B. J. Hinds, "Enhanced flow in carbon nanotubes", *Nature*, **438**, 44 (2005).
- [114] M. Majumder, K. Keis, X. Zhan, C. Meadows, *et al.*, "Enhanced electrostatic modulation of ionic diffusion through carbon nanotube membranes by diazonium grafting chemistry", *Journal of Membrane Science*, **316** (1-2), 89-96 (2008).
- [115] M. Majumder, X. Zhan, R. Andrews, and B. J. Hinds, "Voltage gated carbon nanotube membranes", *Langmuir*, **23** (16), 8624-31 (2007).
- [116] P. Nednoor, V. G. Gavalas, N. Chopra, B. J. Hinds, *et al.*, "Carbon nanotube based biomimetic membranes: Mimicking protein channels regulated by phosphorylation", *Journal of Materials Chemistry*, **17** (18), 1755-7 (2007).
- [117] N. Chopra, M. Majumder, and B. J. Hinds, "Bifunctional Carbon Nanotubes by Sidewall Protection", *Advanced Functional Materials*, **15** (5), 858-64 (2005).
- [118] M. Majumder, N. Chopra, and B. J. Hinds, "Effect of Tip Functionalization on Transport through Vertically Oriented Carbon Nanotube Membranes", *Journal of the American Chemical Society*, **127** (25), 9062-70 (2005).
- [119] J. Holt, H. Park, Y. Wang, M. Stadermann, *et al.*, "Fast Mass Transport Through Sub-2-Nanometer Carbon Nanotubes", *Science*, **312**, 1034 (2006).
- [120] S. Joseph, and N. R. Aluru, "Why Are Carbon Nanotubes Fast Transporters of Water?", *Nano Letters*, **8** (2), 452-8 (2008).
- [121] L. Sun, and R. M. Crooks, "Single Carbon Nanotube Membranes: A Well-Defined Model for Studying Mass Transport through Nanoporous Materials", *Journal of the American Chemical Society*, **122** (49), 12340-5 (2000).
- [122] J. Wu, K. S. Paudel, C. Strasinger, D. Hammell, *et al.*, "Programmable transdermal drug delivery of nicotine using carbon nanotube membranes", *Proceedings of the National Academy of Sciences*, **107** (26), 11698-702 (2010).
- [123] X. Sun, X. Su, J. Wu, and B. J. Hinds, "Electrophoretic Transport of Biomolecules through Carbon Nanotube Membranes", *Langmuir*, **7** (6), 3150-6 (2011).
- [124] P. Groning, P. Ruffieux, L. Schlapbach, and O. Groning, "Carbon Nanotubes for Cold Electron Sources", *Advanced Engineering Materials*, **5** (8), 541 (2003).
- [125] J. M. Bonard, M. Croci, C. Klinke, R. Kurt, *et al.*, "Carbon nanotube films as electron field emitters", *Carbon*, **40** (10), 1715-28 (2002).
- [126] R. H. Fowler, and R. Nordheim, "Electron emission in intense electric fields", *Proceedings of the Royal Society of London A*, **119**, 173-81 (1928).
- [127] K. O'Donnell, University of Newcastle (Newcastle, New South Wales), (2005).
- [128] W. Shao, M. Q. Ding, C. Chen, X. Li, *et al.*, "Micro-gated-field emission arrays with single carbon nanotubes grown on Mo tips", *Applied Surface Science*, **253**, 7559 (2007).

- [129] T. D. Wilkinson, X. Wang, K. B. K. Teo, and W. I. Milne, "Sparse Multiwall Carbon Nanotube Electrode Arrays for Liquid-Crystal Photonic Devices", *Advanced Materials*, **20** (2), 363-6 (2008).
- [130] M.-S. Jung, Y. K. Ko, D.-H. Jung, D. H. Choi, *et al.*, "Electrical and field-emission properties of chemically anchored single-walled carbon nanotube patterns", *Applied Physics Letters*, **87**, 013114 (2005).
- [131] J. M. Bonard, H. Kind, T. Stokli, and L.-O. Nilsson, "Field emission from carbon nanotubes: the first five years", *Solid-State Electronics*, **45**, 893-914 (2001).
- [132] K. L. Jensen, "Electron emission theory and its application: Fowler nordheim equation and beyond", *Journal of Vacuum Science and Tecnologies B*, **21**, 1528-44 (2003).
- [133] N. Jonge, M. Allieux, M. Doytdcheva, M. Kaiser, *et al.*, "Characterization of the field emission properties of individual thin carbon nanotubes", *Applied Physics Letters*, **85** (9), 1607 (2004).
- [134] J. M. Bonard, C. Klinke, K. A. Dean, and B. F. Coll, "Degradation and failure of carbon nanotube field emitters", *Physical Review B*, **67**, 115406 (2003).
- [135] P. R. Schwoebl, C. A. Spindt, and I. Brodie, "Electron-emission enhancement by Overcoating Molybdenum Field-emitter Arrays With Titanium, Zirconium and Hafnium", *Journal of Vacuum Science and Tecnologies B*, **13**, 1391 (1995).
- [136] L. A. Chernozatonskiib, Y. V. Gulyaevb, Z. J. Kosakovskajab, N. I. Sinitsync, *et al.*, "Electron field emission from nanofilament carbon films", *Chemical Physics Letters*, **233** (1-2), 63-8 (1995).
- [137] A. G. Rinzler, J. H. Hafner, P. Nikolaev, and L. Lou, "Unraveling nanotubes:Field emission from an atomic wire", *Science*, **269** (5230), 1550 (2005).
- [138] Y. Cheng, and O. Zhou, "Electron field emission from carbon nanotubes", *C. R. Physique*, **4**, 1021-33 (2003).
- [139] Y. N. Zhang, W. Lei, X. B. Zhang, and B. P. Wang, "Calculation of the emission performance of the carbon nanotube array", *Applied Surface Science*, **245** (1-4), 400-6 (2005).
- [140] J. Lee, W. Lee, E. Park, T. Park, *et al.*, "The electric field enhancements by single-walled carbon nanotubes in In₂S₃/In₂O₃ photoelectrochemical solar cells", *Applied Physics Letters*, **96** (17), 3 (2010).
- [141] J. M. Bonard, J.-P. Salvetat, T. Stokli, and W. A. De Heer, "Field emission from single-walled carbon nanotube films", *Applied Physics Letters*, **73** (7), 918 (1998).
- [142] W. S. Kim, J. Lee, T. W. Jeong, J. N. Heo, *et al.*, "Improved emission stability of single-walled carbon nanotube field emitters by plasma treatment", *Applied Physics Letters*, **87**, 163112 (2005).
- [143] Y. S. Chen, J. H. Huang, J. L. Hu, C. C. Yang, *et al.*, "Synthesis of single-walled carbon nanotubes produced using a three layer Al/Fe/Mo metal catalyst and their field emission properties", *Carbon*, **45** (15), 3007-14 (2007).
- [144] G. Chen, D. H. Shin, T. Iwasaki, H. Kawarada, *et al.*, "Enhanced field emission properties of vertically aligned double-walled carbon nanotube arrays", *Nanotechnology*, **19** (41), 415703 (2008).

- [145] C. Liu, K. S. Kim, J. Baek, Y. Cho, *et al.*, "Improved field emission properties of double-walled carbon nanotubes decorated with Ru nanoparticles", *Carbon*, **47** (4), 1158-64 (2009).
- [146] B. Ha, D. H. Shin, J. Park, and C. J. Lee, "Electronic Structure and Field Emission Properties of Double-Walled Carbon Nanotubes Synthesized by Hydrogen Arc Discharge", *The Journal of Physical Chemistry C*, **112** (2), 430-5 (2007).
- [147] S. I. Jung, S. H. Jo, H. S. Moon, J. M. Kim, *et al.*, "Improved Crystallinity of Double-Walled Carbon Nanotubes after a High-Temperature Thermal Annealing and Their Enhanced Field Emission Properties", *The Journal of Physical Chemistry C*, **111** (11), 4175-9 (2007).
- [148] C. Guohai, and *et al.*, "Improved field emission stability of thin multiwalled carbon nanotube emitters", *Nanotechnology*, **21** (1), 015704 (2010).
- [149] X. Xu, and G. R. Brandes, "A method for fabricating large-area, patterned, carbon nanotube field emitters", *Applied Physics Letters*, **74** (17), 2549-51 (1999).
- [150] M. Chhowalla, N. Ducati, N. L. Rupesinghe, K. B. K. Teo, *et al.*, "Field emission from short and stubby vertically aligned carbon nanotubes", *Applied Physics Letters*, **79** (13), 2079-81 (2001).
- [151] C. Y. Zhi, X. D. Bai, and E. G. Wang, "Enhanced field emission from carbon nanotubes by hydrogen plasma treatment", *Applied Physics Letters*, **81** (9), 1690-2 (2002).
- [152] J. M. Bonard, N. Weiss, H. Kind, T. Stöckli, *et al.*, "Tuning the Field Emission Properties of Patterned Carbon Nanotube Films", *Advanced Materials*, **13** (3), 184-8 (2001).
- [153] S. C. Youn, D.-H. Jung, Y. K. Ko, Y. W. Jin, *et al.*, "Vertical Alignment of Carbon Nanotubes Using the Magneto-Evaporation Method", *Journal of the American Chemical Society*, **131** (2), 742-8 (2008).
- [154] Y. Saito, K. Hamaguchi, S. Uemura, K. Uchida, *et al.*, "Field emission from multi-walled carbon nanotubes and its application to electron tubes", *Applied Physics A: Materials Science & Processing*, **67**, 95-100 (1998).
- [155] D. W. Kang, and J. S. Suh, "Fabrication temperature effect of the field emission from closed and open tip carbon nanotube arrays fabricated on anodic aluminum oxide films", *Journal of Applied Physics*, **96** (9), 5234-8 (2004).
- [156] G. Zhou, W. Duan, and B. Gu, "Electronic Structure and Field-Emission Characteristics of Open-Ended Single-Walled Carbon Nanotubes", *Physical Review Letters*, **87** (9), 095504 (2001).
- [157] J. M. Bonard, N. Weiss, H. Kind, T. Stokli, *et al.*, "Tuning the field emission from carbon nanotube films", *Advanced Materials*, **13**, 184 (2001).
- [158] X. Fang, Y. Bando, U. K. Gautam, C. Ye, *et al.*, "Inorganic semiconductor nanostructures and their field-emission applications", *Journal of Materials Chemistry*, **18** (5), 509-22 (2008).
- [159] B. Cao, X. Teng, S. H. Heo, Y. Li, *et al.*, "Different ZnO Nanostructures Fabricated by a Seed-Layer Assisted Electrochemical Route and Their Photoluminescence and Field Emission Properties", *J. Phys. Chem. C*, **111** (6), 2470-6 (2007).
- [160] W. Z. Wang, B. Q. Zeng, J. Yang, B. Poudel, *et al.*, "Aligned Ultralong ZnO Nanobelts and Their Enhanced Field Emission", *Advanced Materials*, **18** (24), 3275-8 (2006).

- [161] J. C. She, S. Z. Deng, N. S. Xu, R. H. Yao, *et al.*, "Fabrication of vertically aligned Si nanowires and their application in a gated field emission device", *Applied Physics Letters*, **88** (1), 013112 (2006).
- [162] C. Liu, Z. Hu, Q. Wu, X. Wang, *et al.*, "Synthesis and field emission properties of aluminum nitride nanocones", *Applied Surface Science*, **251** (1-4), 220-4 (2005).
- [163] A. Pandey, A. Prasad, J. P. Moscatello, and Y. K. Yap, "Stable Electron Field Emission from PMMA CNT Matrices", *ACS Nano*, **4** (11), 6760-6 (2010).
- [164] D. Xu, G. Guo, L. Gui, and Y. Tang, "Controlling growth and field emission property of aligned carbon nanotubes on porous silicon substrates", *Applied Physics Letters*, **75**, 481 (1999).
- [165] Y. Saito, and S. Uemura, "Field emission from carbon nanotubes and its application to electron sources", *Carbon*, **38** (2), 169-82 (2000).
- [166] Q. H. Wang, A. A. Setlur, J. M. Lauerhaas, J. Y. Dai, *et al.*, "A nanotube-based field-emission flat panel display", *Applied Physics Letters*, **72** (22), 2912 (1998).
- [167] G. Z. Yue, Q. Qiu, G. Bo, Y. Cheng, *et al.*, "Generation of continuous and pulsed diagnostic imaging x-ray radiation using a carbon-nanotube-based field-emission cathode", *Applied Physics Letters*, **81** (2), 355-7 (2002).
- [168] J.-H. Park, G.-H. Son, J.-S. Moon, J.-H. Han, *et al.*, "Screen printed carbon nanotube field emitter array for lighting source application", *Journal of Vacuum Science & Technology B*, **23** (2), 749-53 (2005).
- [169] K. L. Jensen, "Field emitter arrays for plasma and microwave source applications", *Physics of Plasmas*, **6**, 2241-53 (1999).
- [170] M. Chhowalla, C. Ducati, N. L. Rupesinghe, K. B. K. Teo, *et al.*, "Field emission from short and stubby vertically aligned carbon nanotubes", *Applied Physics Letters*, **79** (13), 2079-81 (2001).
- [171] R. H. Baughman, A. A. Zakhidov, and W. A. de Heer, "Carbon Nanotubes--the Route Toward Applications", *Science*, **297** (5582), 787-92 (2002).
- [172] W. Zhu, C. Bower, O. Zhou, G. Kochanski, *et al.*, "Large current density from carbon nanotube field emitters", *Applied Physics Letters*, **75** (6), 873-5 (1999).
- [173] W. B. Choi, D. S. Chung, J. H. Kang, H. Y. Kim, *et al.*, "Fully sealed, high-brightness carbon-nanotube field-emission display", *Applied Physics Letters*, **75** (20), 3129-31 (1999).
- [174] H. G. Craighead, S. W. Turner, R. C. Davis, C. James, *et al.*, "Chemical and Topographical Surface Modification for Control of Central Nervous System Cell Adhesion", *Biomedical Microdevices*, **1** (1), 49-64 (1998).
- [175] S. K. Smart, A. I. Cassady, G. Q. Lu, and D. J. Martin, "The biocompatibility of carbon nanotubes", *Carbon*, **44**, 1034-47 (2006).
- [176] K. Tuzlakoglu, N. Bolgen, A. Salgado, M. Gomes, *et al.*, "Nano- and micro-fiber combined scaffolds: A new architecture for bone tissue engineering", *Journal of Materials Science: Materials in Medicine*, **16** (12), 1099-104 (2005).
- [177] N. W. S. Kam, T. C. Jessop, P. A. Wender, and H. J. Dai, "Nanotube molecular transporters: Internalization of carbon nanotube-protein conjugates into mammalian cells", *Journal of the American Chemical Society*, **126** (22), 6850-1 (2004).
- [178] L. Lacerda, S. Raffa, M. Prato, A. Bianco, *et al.*, "Cell-penetrating CNTs for delivery of therapeutics", *Nano Today*, **2** (6), 38-43 (2007).

- [179] S. Giannona, I. Firkowska, J. Rojas-Chapana, and M. Giersig, "Vertically aligned carbon nanotubes as cytocompatible material for enhanced adhesion and proliferation of osteoblast-like cells", *Journal of Nanoscience and Nanotechnology*, **7**, 1679-83 (2007).
- [180] E. Ben-Jacob, and Y. Hanein, "Carbon nanotube micro-electrodes for neuronal interfacing", *Journal of Materials Chemistry*, **18** (43), 5181-6 (2008).
- [181] R. Singh, D. Pantarotto, D. McCarthy, O. Chaloin, *et al.*, "Binding and condensation of plasmid DNA onto functionalized carbon nanotubes: Toward the construction of nanotube-based gene delivery vectors", *Journal of the American Chemical Society*, **127** (12), 4388-96 (2005).
- [182] T. Gabay, E. Jakobs, E. Ben-Jacob, and Y. Hanein, "Engineered self-organization of neural networks using carbon nanotube clusters", *Physica A*, **350**, 611-21 (2005).
- [183] G. Vereb, J. Szollosi, J. Matko, P. Nagy, *et al.*, *Proceedings of the National Academy of Sciences of the United States of America*, **100**, 8053-8 (2003).
- [184] X. Chen, A. Kis, A. Zettl, and C. R. Bertozzi, "A cell nanoinjector based on carbon nanotubes", *Proceedings of the National Academy of Sciences of the United States of America*, **104** (20), 8218-22 (2007).
- [185] J. Martinez, T. D. Yuzvinsky, A. M. Fennimore, A. Zettl, *et al.*, "Length control and sharpening of atomic force microscope carbon nanotube tips assisted by an electron beam", *Nanotechnology*, **16**, 2493-6 (2005).
- [186] D. Cai, J. M. Mataraza, Z. H. Qin, Z. P. Huang, *et al.*, "Highly efficient molecular delivery into mammalian cells using carbon nanotube spearing", *Nature Methods*, **2** (6), 449-54 (2005).
- [187] T. E. McKnight, A. V. Melechko, G. D. Griffin, M. A. Guillorn, *et al.*, "Intracellular integration of synthetic nanostructures with viable cells for controlled biochemical manipulation", *Nanotechnology*, **14** (5), 551-6 (2003).
- [188] T. E. McKnight, A. V. Melechko, D. K. Hensley, D. G. J. Mann, *et al.*, "Tracking Gene Expression after DNA Delivery Using Spatially Indexed Nanofiber Arrays", *Nano Letters*, **4** (7), 1213-9 (2004).
- [189] S.-R. Ryoo, Y.-K. Kim, M.-H. Kim, and D.-H. Min, "Behaviors of NIH-3T3 Fibroblasts on Graphene/Carbon Nanotubes: Proliferation, Focal Adhesion, and Gene Transfection Studies", *ACS Nano*, **4** (11), 6587-98 (2010).
- [190] J.-Y. Shiu, C.-W. Kuo, W.-T. Whang, and P. Chen, "Observation of enhanced cell adhesion and transfection efficiency on superhydrophobic surfaces", *Lab on a Chip*, **10** (5), 556-8 (2010).
- [191] E. Neumann, M. Schaefer-Ridder, Y. Wang, and P. H. Hofschneider, "Gene transfer into mouse lyoma cells by electroporation in high electric fields", *EMBO*, **1** (7), 841 (1982).
- [192] T. Tryfona, and M. T. Bustard, "Enhancement of biomolecule transport by electroporation: A review of theory and practical application to transformation of *Corynebacterium glutamicum*", *Biotechnology and Bioengineering*, **93** (3), 413-23 (2006).
- [193] G. L. Prasanna, and T. Panda, "Electroporation: basic principles, practical considerations and applications in molecular biology", *Bioprocess and Biosystems Engineering*, **16** (5), 261-4 (1997).
- [194] Y. Inoue, H. Fujimoto, T. Ogino, and H. Iwata, "Site-specific gene transfer with high efficiency onto a carbon nanotube-loaded electrode", *Journal of The Royal Society Interface*, **5** (25), 909-18 (2008).

- [195] A. O. Lobo, E. F. Antunes, M. B. S. Palma, C. Pacheco-Soares, *et al.*, "Biocompatibility of multi-walled carbon nanotubes grown on titanium and silicon surfaces", *Materials Science & Engineering C-Biomimetic and Supramolecular Systems*, **28** (4), 532-8 (2008).
- [196] B. L. Allen, P. D. Kichambare, P. Gou, I. Vlasova, *et al.*, " Biodegradation of Single-Walled Carbon Nanotubes through Enzymatic Catalysis", *Nano Letters*, **8**, 3899-903 (2008).

Chapter 2

Experimental details

Common experimental methods and procedures are described in detail. In order to chemically attach carbon nanotubes (CNTs) to silicon nanostructures the CNTs must first be functionalised with carboxylic acid groups which can then react with $-OH$ or $-NH_2$ termini. Schematics on the preparation of Si-CNT nanostructures are shown with specific details of CNT functionalisation and substrate preparation. The method and fundamentals of common characterisation techniques used are also covered.

2.1 Carbon nanotubes

2.1.1 Single-walled carbon nanotubes

24 mg of SWCNTs (P2, >90 % carbonaceous purity, 1.4 nm diameter) synthesised using the DC arc discharge method with yttrium-nickel catalysts were purchased from Carbon Solutions Inc. The purchased SWCNTs were reported to be purified with low functionality. In order to introduce carboxylic acid groups onto the SWCNTs they were functionalised/cut by incubation in a 24 mL of 3:1 (v/v) H₂SO₄ (98 %, Aldrich):HNO₃ (70 %, Aldrich) in an ultrasonic bath (280 W, Elma S30 H) kept at 0 °C for 8 hr. The sonication of CNTs in so-called ‘mixed acid’ solutions is known to both functionalise and decrease the lengths of the SWCNTs.^[1] After 8 hr, the SWCNT/ mixed acid solution was diluted in 500 mL of MilliQ water (18 MΩ) and refrigerated overnight prior to filtration as covered in Section 2.1.2.

2.1.2 Carbon nanotube filtration

The diluted functionalised CNT/acid solutions were filtered through a 0.45 μm hydrophobic PTFE (polytetrafluoroethylene, Adalab Scientific, Australia) membrane following the method popularised by Smalley *et al.*^[2] During the filtration, water was constantly added to further dilute the supernatant. Water was added until the pH of the supernatant was equal to that of the MilliQ water (pH ≈ 6). The CNTs on the membrane were then dried in an oven at 100 °C overnight to remove residual water prior to suspension in dimethyl sulfoxide.

2.1.3 Carbon nanotube suspension in dimethyl sulfoxide

The dried functionalised CNTs were dispersed in dimethyl sulfoxide (DMSO, 99.9 %, ACS Spectroscopic Grade, Sigma–Aldrich) at a concentration of 0.2 mg mL⁻¹. Dispersion of the CNT film was achieved by sonication for 20 min. DCC (dicyclohexylcarbodiimide, 99 % FlukaProduction GmbH) was added to a concentration of 0.2 - 0.3 mg mL⁻¹ and ultrasonicated for a further 1 min. The CNT/DCC solution in DMSO was stored in a sealable 100 or 250 mL bottle (Schott, Germany) inside a nitrogen filled glove box until required. At all times care was taken to ensure that the CNT/DCC solution was not exposed to atmospheric water

vapour as it is known to reconfigure the CNT/DCC hybrid making it inert and insoluble in DMSO as explained in detail in Section 1.4. The solutions containing 0.2 mg mL^{-1} of both functionalised CNT and DCC were used for CNT surface attachment to both alcohol and amine functionalised silicon, as described in Section 2.2.

2.1.4 Double-walled carbon nanotubes

DWCNTs (>90 % carbonaceous purity, >60 % DWCNT purity, >5 nm outer diameter, ShenZhen Nanotech Port Co., China) were functionalised/cut by a 2 step process. This was required since the 1-step process used for SWCNTs did not produce a stable suspension of DWCNTs. 24 mg of DWCNT powder was added to 10 mL of 70 % HNO_3 and 40 mL of water (making a 3 M concentration of HNO_3) and refluxed overnight. This process is known to remove carbonaceous material, reduce catalyst nanoparticles and partially oxidise defect sites on the CNT sidewall.^[3] The DWCNTs were then filtered through a $0.45 \mu\text{m}$ PTFE membrane in order to remove the HNO_3 solution. The ‘cleaned DWCNTs’ were then added to 24 mL of 3:1 (v/v) H_2SO_4 : HNO_3 and ultrasonicated at 0°C for 2 hr. After ultrasonication the DWCNT/acid solution was diluted in 500 mL of MilliQ water and refrigerated overnight prior to filtration, as covered in Section 2.1.2.

2.1.5 Multi-walled carbon nanotubes

MWCNTs (L-MWNT-2040, >95 % carbonaceous purity, 20 - 40 nm outer diameter, Shenzhen Nanotech Port Co. Ltd, China) were functionalised following a 3-step process. Similar to the DWCNTs, a multi-step process was required in order to produce a stable suspension of functionalised MWCNTs. 40 mg of MWCNTs were first refluxed in 3 M HNO_3 for 3 hr. The MWCNT solution was then filtered through a $0.45 \mu\text{m}$ PTFE filter followed by sonication in 7:3 H_2SO_4 : HNO_3 mixed acid for 3 hr at room temperature. Finally, the MWCNTs were filtered again and sonicated in a solution of 2 M HCl (36 %, Ajax Finechem, Australia) for 20 min. The final step known as an ‘acid wash’ was used to protonate the carboxylic acid functionalities. The final step is more important for acid chloride functionalisation of the MWCNTs, which was the initial purpose. After the acid wash the MWCNTs were diluted in 500 mL of MilliQ water prior to filtration, as covered in Section 2.1.2.

2.2 Silicon

2.2.1 Silicon hydroxylation

The silicon wafers used varied, specifically the dopant type and concentration, depending upon desired application. Silicon type for each application will be detailed within the experimental Section of each corresponding chapter. When not specifically stated, p-type (boron doped, 3 – 6 Ω cm, Virginia Semiconductor Inc., USA) silicon wafers were used. Silicon wafers were cut to size depending upon application, normally 1 x 1 cm² and initially cleaned ultrasonically in acetone (99 %, Sigma) for 2 min. In order to hydroxylate the Si wafers a 2-step base-acid method was used. First, the Si wafers were washed with water (MilliQ), dried under a stream of nitrogen and immersed in a solution of 1:1:5 NH₄OH (30 %, Sigma-Aldrich):H₂O₂ (30 %, Sigma-Aldrich):MilliQ water for 20 min at 80 °C. This was followed by washing with MilliQ water, drying under nitrogen and immersing in a 1:1:5 solution of HCl: H₂O₂:MilliQ water for 20 min at 80°C. Each hydroxylated wafer was then washed with MilliQ water and dried with nitrogen. The acid-base method of hydroxylation was used for the direct ester attachment of CNTs to silicon.

2.2.2 APTES monolayer formation on silicon

Silicon wafers were cut to a preferred size and ultrasonically cleaned in acetone for 2 min. The wafers were washed with MilliQ water, dried under nitrogen and immersed into what is known as Piranha solution for 20 min at 80 °C. Piranha is a mixture of 3:1 H₂SO₄:H₂O₂ and is a simple 1-step method to oxidise a silicon wafer. The Si was then washed in water, dried under nitrogen and immersed into a solution of 0.5 % (v/v) 3-aminopropyltriethoxysilane (APTES, 99 %, Sigma-Aldrich) in dry toluene for 5 min. The wafer was then washed sequentially in chloroform (Ajax-Finechem), acetone, MilliQ water and dried under nitrogen. The APTES modification produces an amine terminated surface which can be used for APTES mediated CNT attachment.

2.2.3 Porous silicon fabrication

The pSi etching cell is shown in Figure 2.1. Etching conditions (HF concentration, etching time, applied current and silicon type) varied depending upon application and are given in detail within each corresponding chapter. If not otherwise mentioned, the following etching conditions were used. Si (100 orientation, boron doped, 3 - 6 Ω cm resistivity, Virginia Semiconductor) was etched in a 1:1 (v/v) solution of 49 % aqueous hydrofluoric acid (HF, Merck):ethanol (100 % undenatured, Chem-Supply) for 90 sec at an applied current of 66 mA over a surface area of 1.767 cm². After etching, the HF was removed and the wafer was rinsed sequentially with methanol, acetone and dichloromethane before being dried under a stream of nitrogen.

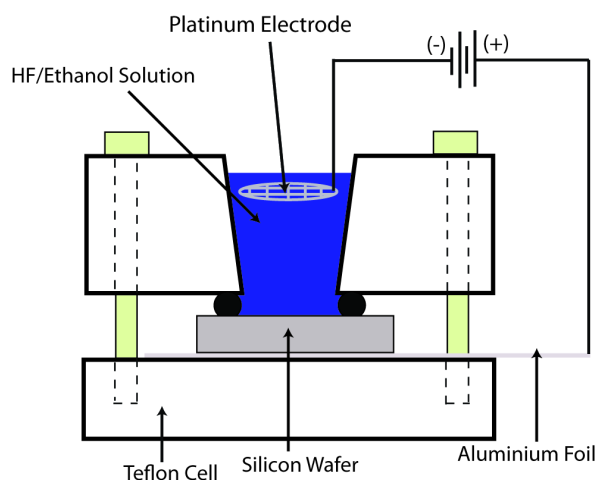


Figure 2.1: Schematic of the porous silicon etching cell.

2.2.4 APTES monolayer formation on porous silicon

After etching the pSi surfaces were Si-H terminated. In order to attach CNTs, the pSi was first oxidised and then reacted with APTES. Oxidation was done in two ways. The first was thermal oxidation by heating to 400 °C for 1 hr in air using a tube furnace while the alternative oxidation method was ozonolysis. Ozone hydroxylation was carried out by exposing freshly etched pSi to ozone using a Fischer ozone generator with the current set at 1.2 A and an O₃ flow rate of 3.2 g hr⁻¹ for 10 - 60 min.

The oxidised pSi wafers were then immersed into a solution of 0.5 % (v/v) APTES (99 %, Sigma-Aldrich) in dry toluene for 5 min. The wafer was then washed sequentially in chloroform, acetone, MilliQ water and dried under nitrogen.

2.3 CNT chemical attachment to silicon

2.3.1 Direct ester attachment of CNTs to Si

Direct ester attachment of CNTs to Si was undertaken with SWCNTs, DWCNTs, and MWCNTs. A schematic of the direct ester attachment of CNTs to Si is shown in Figure 2.2. To achieve the ester attachment of CNTs, a 100 mL round bottom flask was charged with a hydroxylated Si wafer (as described in Section 2.2.1) and approximately 5 mL of functionalised/cut CNTs (as described in Section 2.1) within a nitrogen-filled glove box such that the Si substrate was completely immersed. The flask was then stoppered, removed from the glove box and Parafilm was wrapped around the seal. Fibre glass tape was then wrapped around the Parafilm to ensure the seal remained closed for the duration of the CNT attachment. The flask was placed into an 80 °C oven and left for the desired amount of time (typically 2 – 72 hr). The time that the flask remained in the oven is referred to as the CNT ‘attachment time’.

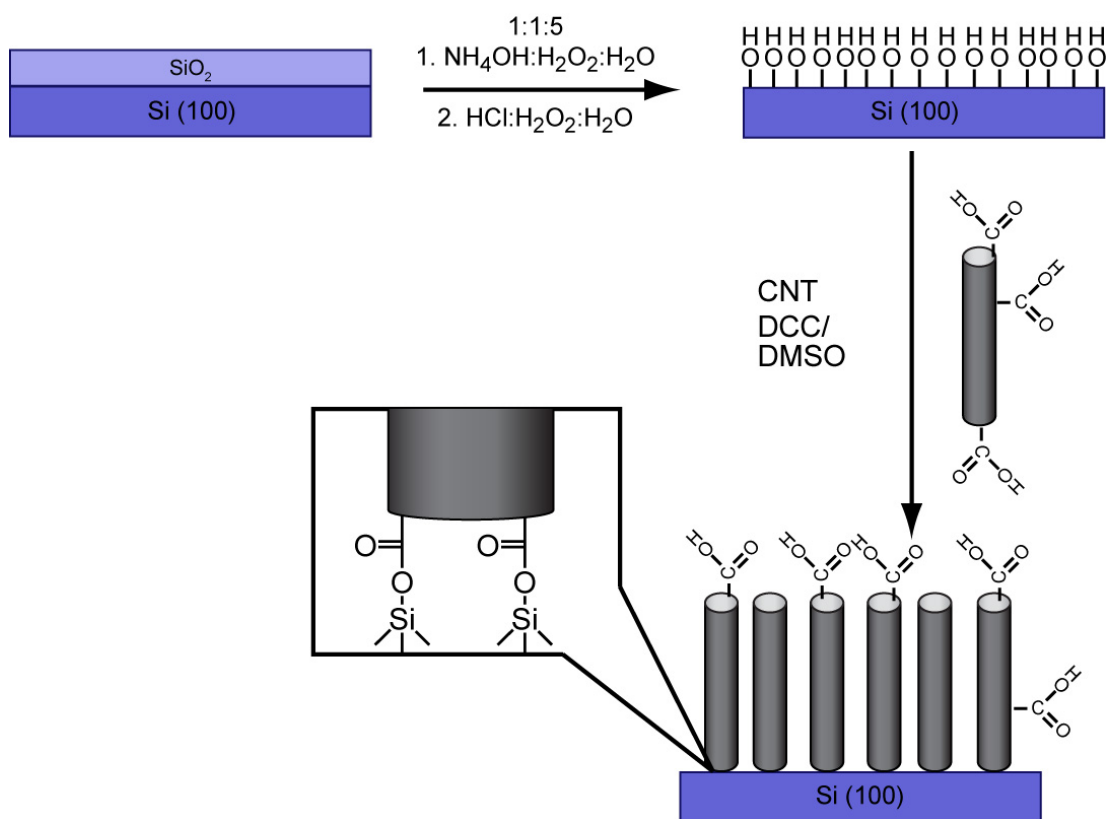


Figure 2.2: Schematic of the direct ester attachment of CNTs to silicon.

such that the sonicating solution had a temperature of 50 – 65 °C. After being immersed in the solution the silicon wafer was left at room temperature for the desired attachment time before being removed and washed thoroughly with acetone.

2.3.3 Ester attachment of CNTs to pSi

The direct ester attachment of CNT to pSi is shown in Figure 2.4. This was achieved following the same method as for flat silicon with the pSi surface prepared following that described in Section 2.2. This attachment was only attempted using SWCNTs.

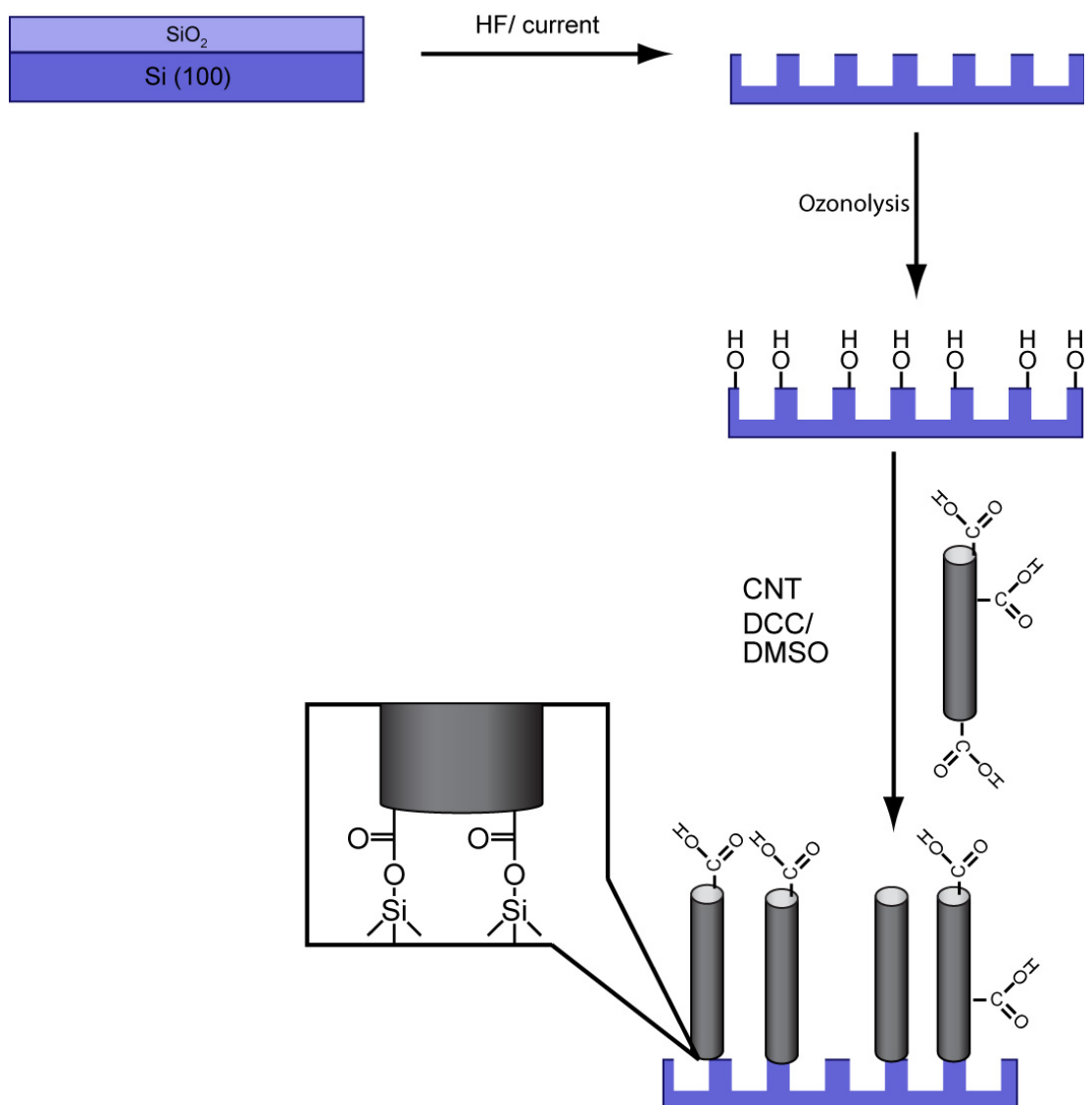


Figure 2.4: Schematic of the direct ester CNT attachment to pSi.

2.3.4 APTES mediated attachment of CNTs to pSi

Figure 2.5 shows the APTES mediated attachment of CNTs to pSi. This was achieved for SWCNTs only following the same method as for flat Si with the pSi surface prepared following that described in Section 2.2.

2.3.5 Patterned attachment of SWCNTs

The patterning procedure is schematically depicted in Figure 2.6. Si surfaces were first oxidised (20 min piranha for Si, 2 hr ozone for pSi) followed by the deposition of positive tone photoresist AZ1518 (Microchemicals, Germany) by spin coating at

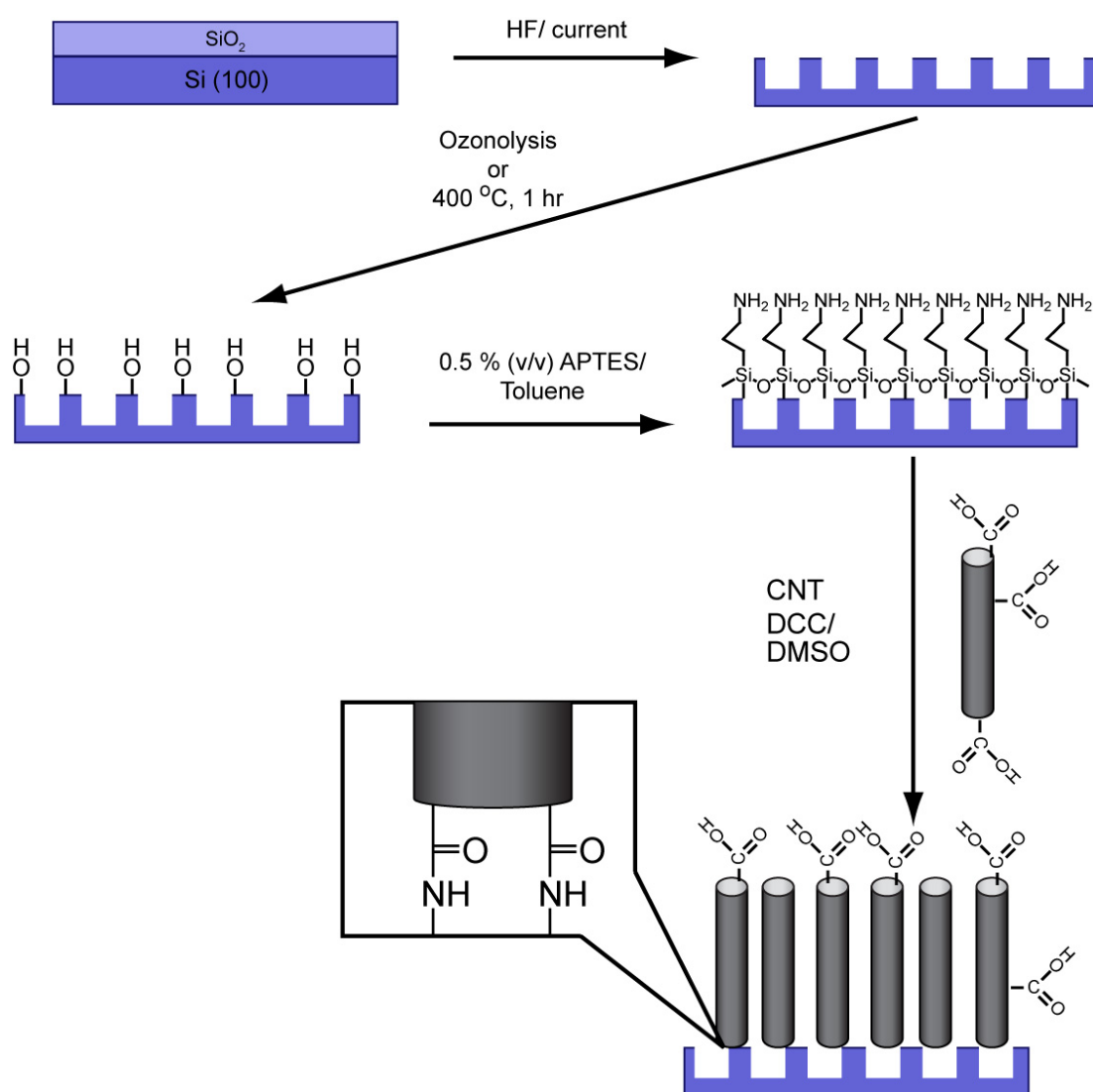


Figure 2.5: Schematic of APTES mediated attachment of CNTs to pSi.

3000 rpm for 30 sec. The substrates were then soft baked at 100 °C for 1 min prior to being patterned by exposure to a UV light source (S1000, 100 W, EXFO Life Science and Industrial Division, Canada) for 5 sec (flat Si) or 10 sec (pSi) through a chrome on glass mask. Following UV exposure, the photoresist was immediately developed in AZMIF326 developer (Microchemicals) for approximately 10 sec (Si) or 30 sec (pSi) and then washed with deionised water and dried under a stream of compressed air. The patterned photoresist was then hard baked at 115 °C for 2 min. APTES and was then deposited onto the exposed regions of the surface for 15 min, following the method described in Section 2.2.2. After APTES immobilisation, the surface was washed with chloroform, acetone, soaked in acetone for 1 min, rinsed with MilliQ water and dried under a stream of nitrogen. The acetone rinse and soak were used to remove the photoresist from the surface. At this point, SWCNT attachment proceeded as described in Section 2.3.2 or a second silane could be deposited onto the remaining bare Si outside the patterned region. The second ‘back-fill’ silane was deposited at a concentration of 0.5 % (v/v) in anhydrous toluene for 10 min. Both propyl trimethoxysilane (PTMS, 99 %, Sigma) and *N*-(triethoxysilylpropyl)-*O*-polyethylene oxide urethane (PEGS, Flurochem, UK) were used as back-fill silanes. After backfill silane deposition, SWCNT attachment could proceed as described in Section 2.3.2.

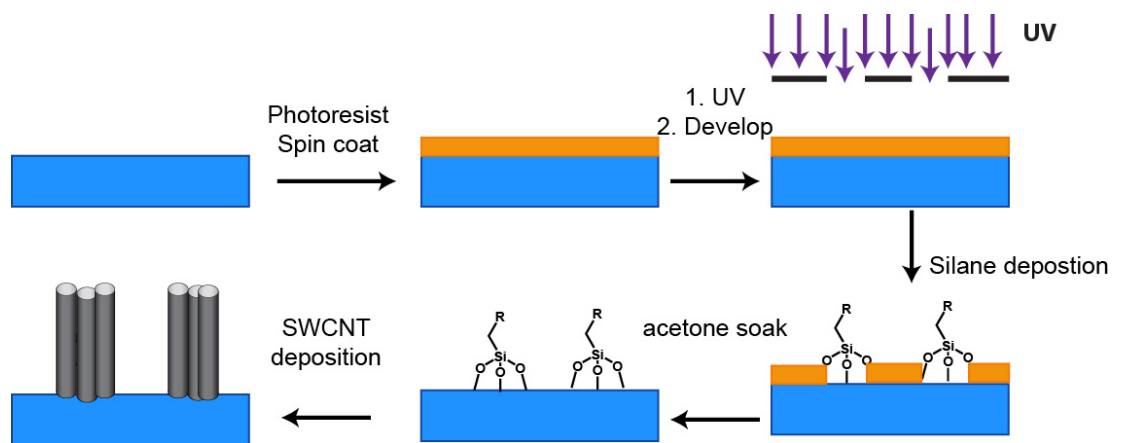


Figure 2.6: Schematic of patterned attachment of SWCNTs to silicon.

2.4 CNT growth by chemical vapour deposition

Figure 2.7 shows the general method of growth of CNTs by chemical vapour deposition (CVD). A Si wafer was cleaned by sonication in ethanol for 5 min, washed with MilliQ water and dried under a stream of nitrogen. A thin layer of iron (99.998 %, Koch-Light Laboratories) was sputtered onto the surface to a desired thickness (most commonly 5 nm) as determined by the in-built quartz crystal microbalance within the sputter coating system (K757X, Quorum Technologies, UK). The iron covered Si wafers were then placed in the middle of a quartz tube in a tube furnace (Thermolyne 21100, Thermo Scientific, US) and heated to 750 °C under a flow of 1.5 sccm Ar and 0.5 sccm H₂. The heating of the iron film under a reducing atmosphere is known to split the film into nanoparticles of iron. The wafers were left under these conditions for a further 10 min once 750 °C was reached. After that time ethylene was added as the carbon feedstock and a catalytic amount of water was

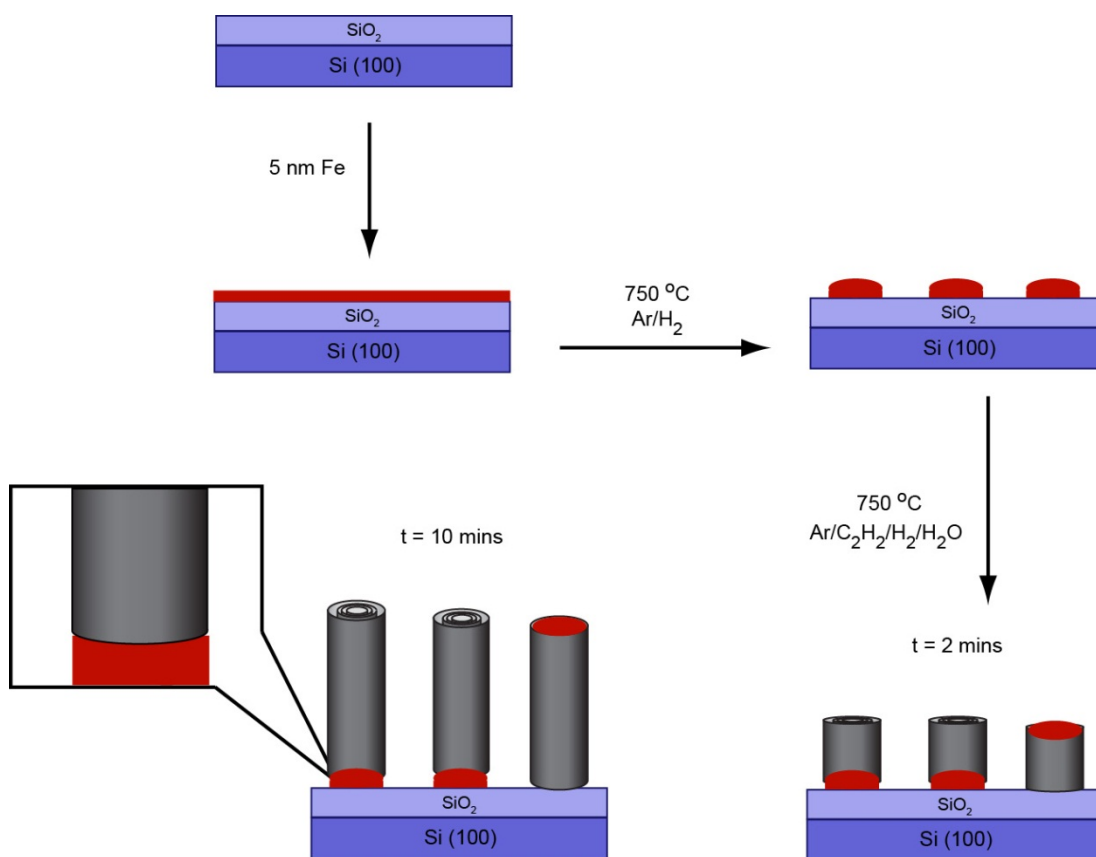


Figure 2.7: Schematic of CNT growth by chemical vapour deposition.

added by passing Ar gas through a water bubbler. The most common growth conditions were 1.5 sccm Ar, 0.5 sccm H₂, 0.2 sccm C₂H₂, 2.8 sccm Ar/H₂O. The CNT growth was typically carried out for 10 min after which all gases were closed off except the Ar, which remained at 1.5 sccm while the furnace cooled.

CNT growth conditions were varied by changing the iron film thickness, iron film pre-treatment, CNT growth gas composition, CNT growth gas ratios, CNT growth temperature, and CNT growth time. Above are the conditions found to be most successful for the growth of a thick layer of CNTs.

2.5 Surface characterisation techniques

2.5.1 Atomic force microscopy (AFM)

Atomic force microscopy (AFM) was used to probe the topographical structure of the nanostructures produced. Specifically, AFM was used to investigate coverage and alignment of CNTs on Si, pore size of pSi and depth of thin polymer films.

AFM is a scanning probe technique where a sharp tip is placed onto a spring-like cantilever. The tip is brought close to, and raster scanned across, a surface of interest where interactions between the tip and the surface are measured by a reflected laser (Figure 2.8). In tapping mode AFM the cantilever oscillates along the surface with fixed amplitude. Changes to the height of the surface result in subsequent changes in the interaction between the surface and the AFM tip which cause changes in oscillation amplitude. Feedback circuits within the AFM then move the relative z -position of the cantilever such that the oscillation amplitude remains constant, the distance moved is measured and a topographical map of the surface can be

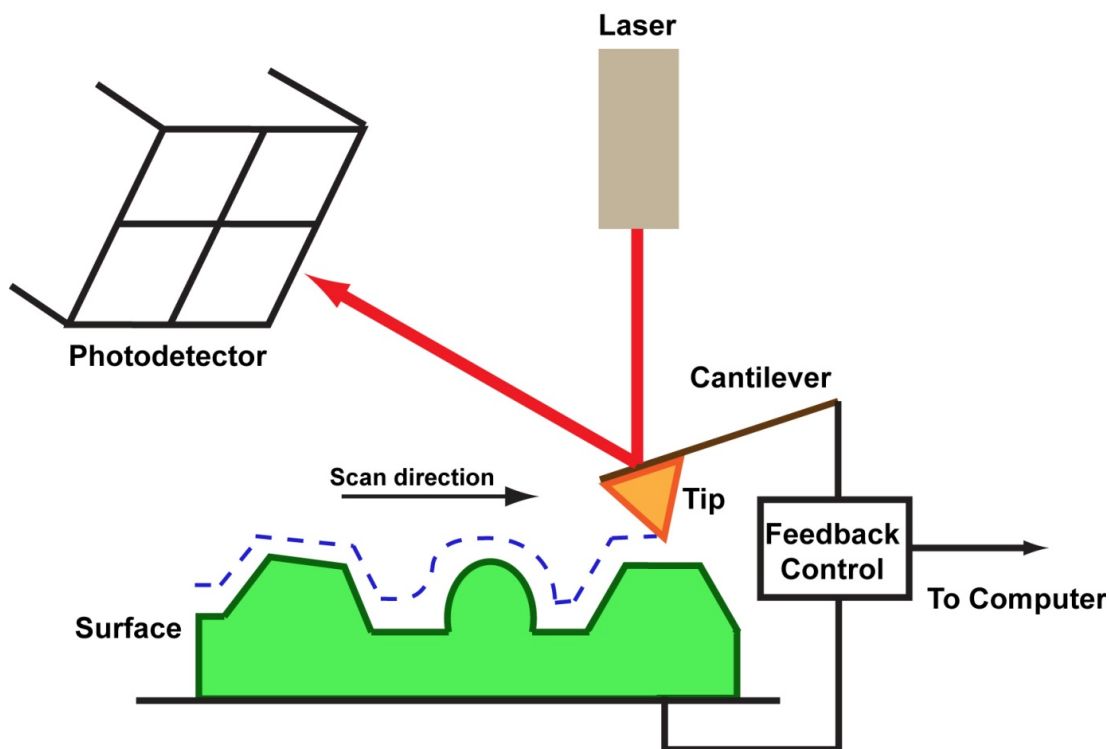


Figure 2.8: Schematic of AFM operation.

obtained.^[4]

AFM tapping mode images were taken in ambient conditions with a Multimode head and a Nanoscope IV controller (Digital Instruments, Veeco, Santa Barbara). Silicon cantilevers (15 series, MikroMasch) with a fundamental resonance frequency of between 265 – 400 kHz and nominal spring constant of 40 N m^{-1} were used. Images were obtained using a scan rate of 1 Hz with the parameters of set point, amplitude and feedback control optimised manually for each sample. The images presented have been flattened using Nanoscope IV software. The CNT coverage was calculated using the bearing analysis tool on the Nanoscope IV software with the threshold set manually to define the percentage of surface covered with CNTs.

2.5.2 Scanning electron microscopy (SEM)

In a typical scanning electron microscope (SEM) a source of electrons is focused into a beam with a small spot size ($< 5 \text{ nm}$) and raster scanned across a surface. As the electrons interact with the surface a number of processes can occur including the emission of electrons.^[5] SEM images are obtained by collecting the emitted electrons on a cathode ray tube. Changes in contrast of the resulting image are a consequence of differences in the topography and electronic properties across the sample under investigation.^[4] A coating of a thin conductive film, commonly platinum, can render the obtained image exclusively dependent upon topographical data.

SEM was used to probe the surface structure of fabricated nanostructures. SEM was particularly useful when probing surfaces where z dimensions were not required to be measured such as for pSi pore size/ depth or CNT length. SEM was also used to image surfaces that were too rough for AFM such as CNTs in powdered form.

Three different SEMs were used for sample analysis. The instrument used for each image will be mentioned in the image caption.

The ‘XL-30’ images were obtained with a Philips XL30 (Adelaide Microscopy) field emission scanning electron microscope with an accelerating voltage of 10 kV.

The ‘Nanolab’ images were obtained using a Helios NanoLab DualBeam (FEI, Adelaide Microscopy) SEM microscope with an accelerating voltage of 15 kV.

The ‘CamScan’ images were taken using a CamScan MX2500 (CamScan Electron Optics Limited, UK) using a secondary electron detector. The electron source was a tungsten filament and the accelerating voltage used was 10 kV.

2.5.3 *Confocal Raman spectroscopy and spectral imaging*

Raman spectroscopy was used to determine CNT type, CNT concentration across large sample areas and also to determine the level of CNT functionalisation after different cutting processes.

In 1928, the phenomenon of inelastic light scattering was noticed and documented by Sir Chandrasekhara Venkata Raman. Raman observed that radiation that had scattered from a sample contained photons identical to the incident photons (elastically scattered), but also contained photons that had been shifted to a different energy level (inelastically scattered).^[6]

When light is incident upon a gas or surface; energy, $h\nu$, can be transferred from the photons to the gas/surface species. This gives the species energy equivalent to that of the incident photons and in doing so excites the species to a higher energy state. Once this higher energy state is achieved, the species can then relax to their original energy state and in doing so release a photon of light; it can do this in three ways: Rayleigh (elastic), Stokes (inelastic) and anti-Stokes (inelastic).

Rayleigh scattering occurs when the photon is absorbed with energy $h\nu$ and emitted with the same energy (Figure 2.9 (a)). Stokes scattering occurs when once the species is excited, it returns to an rotational or vibrational excited state and releases a photon with energy of $h\nu - h\nu_m$, where $h\nu_m$ is equal to the excess energy of the vibrational excited state (Figure 2.9 (b)). Anti-Stokes scattering occurs when a photon is absorbed by the species already in an excited rotational/ vibrational state, which is excited to a virtual state and relaxes releasing a photon which has an energy of $h\nu + h\nu_m$ (Figure 2.9 (c)).^[7] The three possibilities correspond to the selection rule for the rotational transitions for the angular momentum quantum number, $\Delta J \pm 1$, since Rayleigh, Stokes and anti-Stokes scattering are 2 photon processes, the 3 possibilities are $\Delta J = 0, +2, -2$.^[8]

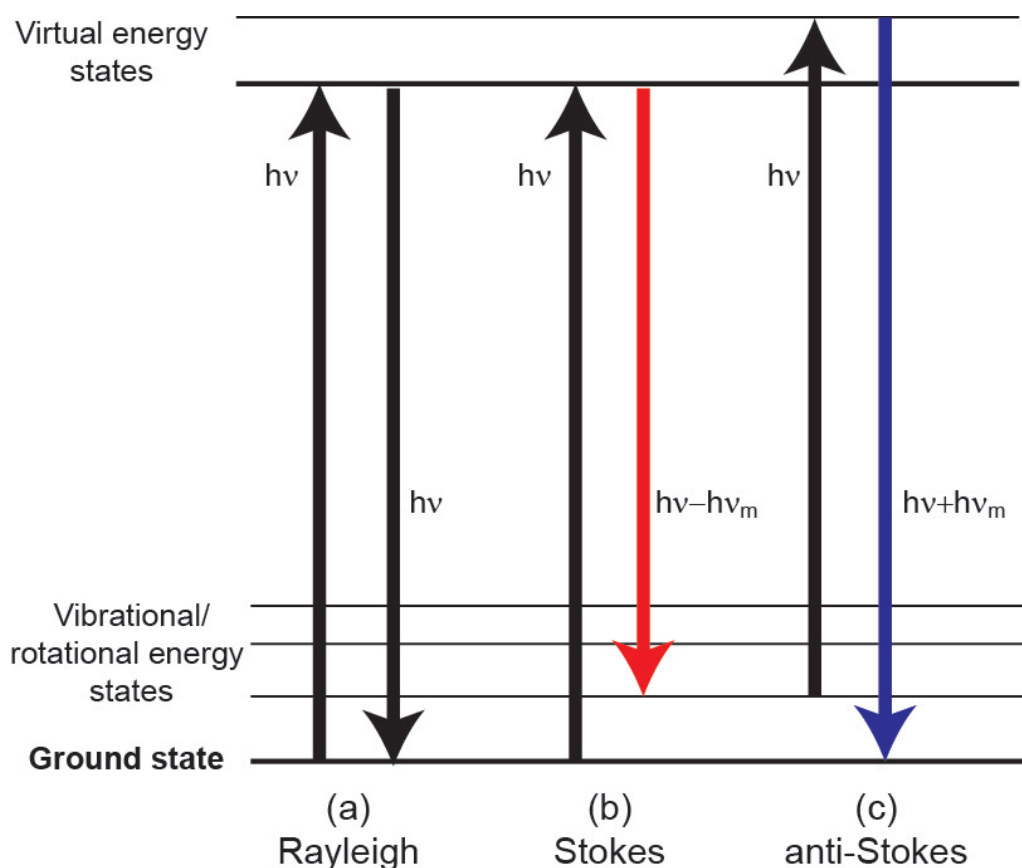


Figure 2.9: Summary of possible scattering processes.

Rayleigh scattering is by far the most common of the scattering processes with only one in every 10^7 photons inelastically scattered. Raman spectroscopy is completed by measuring the intensity of the scattered light as a function of frequency downshift of the scattered light (compared to the incident light), giving a measure of the low frequency transitions within the material.

In CNTs the low frequency transitions that are observed as Raman shifts are phonon transitions. Phonons arise in materials such as CNTs, which have rigid, one-dimensional covalent connections between atoms. The displacement of one or more atoms from their equilibrium positions will give rise to a set of low frequency vibrational waves that propagate through the lattice. These surface waves can both absorb and release energy to excited molecules, causing inelastic (Raman) scattering.^[7] The Raman peaks of SWCNTs correspond to different phonon modes in the hexagonal carbon lattice. The major peaks are the radial breathing mode (RBM), the disorder band (D-band) and the tangential or graphitic band (G-band).

The RBM occurs around $100 - 300 \text{ cm}^{-1}$ and corresponds to the symmetric in-phase motion of all carbon atoms in a radial direction, as if it were breathing (Figure 2.10 (a)). The RBM peak position is inversely related to the CNT diameter where wider diameter CNTs show RBM peaks at lower wavenumbers. This relationship results in RBM peaks unique to SWCNTs and low diameter DWCNTs.^[9]

The D-band occurs at around $1300 - 1350 \text{ cm}^{-1}$, depending upon incident laser energy^[10] and corresponds to vibrations caused by collective in-plane vibrational movement of atoms towards and away from the centre of the covalently (sp^3) bound hexagons of carbon atoms (Figure 2.10 (b)).^[9] The curvature of a pristine carbon nanotube restricts these vibrations resulting in minimal D-band absorptions. This allows the intensity of the D-band feature to determine the quantity of disordered or amorphous sp^3 hybridised carbon material present in a sample.

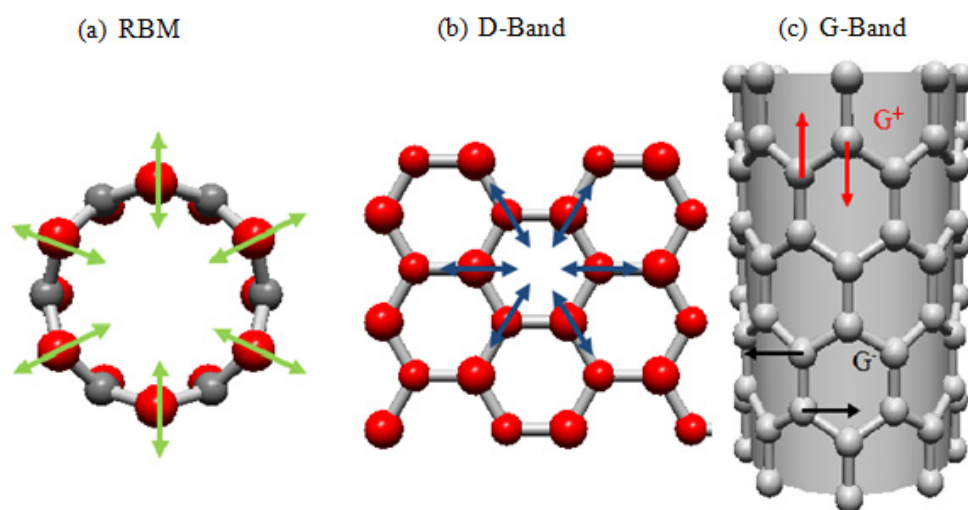


Figure 2.10: (a) Cross sectional view of a SWCNT showing the radial vibration of the RBM, with (b) vibration of D-band, and (c) vibrations of G-band with G^+ peak arising from vibrations along the tube axis and G^- peak arising from vibrations around the circumference of the tube.

The G-band is derived from the Raman-allowed E_{2g} tangential stretching of the carbon-carbon bonds.^[7] This stretching can be in two directions, and as such two peaks are observed in the G-band: The G^+ peak occurs at around 1590 cm^{-1} and is caused by vibrations along the nanotube axis and the G^- peak occurs at around 1570 cm^{-1} and is a result of vibrations along the circumferential direction of the SWCNT (Figure 2.10 (c)). Wider diameter CNTs such as DWCNT and MWCNT do

not show the splitting of the G-band. The size of the G-band is approximately dependent upon the amount of nanotube present.^[11] Therefore, if all conditions are kept equal (scan area, integration time, laser energy etc.) the peak area of the G-band can give a rough, relative quantification of CNT surface coverage. Since the G-band can show the amount of carbon nanotube present and the D-band shows the approximate amount of disordered or amorphous sp^3 hybridised carbon material present, the peak area ratio of amorphous/disordered carbon to ordered CNT, D/G can relatively quantify the purity of a CNT array.

A confocal microscope utilises a point light source which is focused onto a sample (Figure 2.11). The reflected light is collected with the same objective and focused through a pinhole in front of the detector. The pinhole blocks out all light that is not within the focal plane. Given a small enough pinhole, diffraction limited

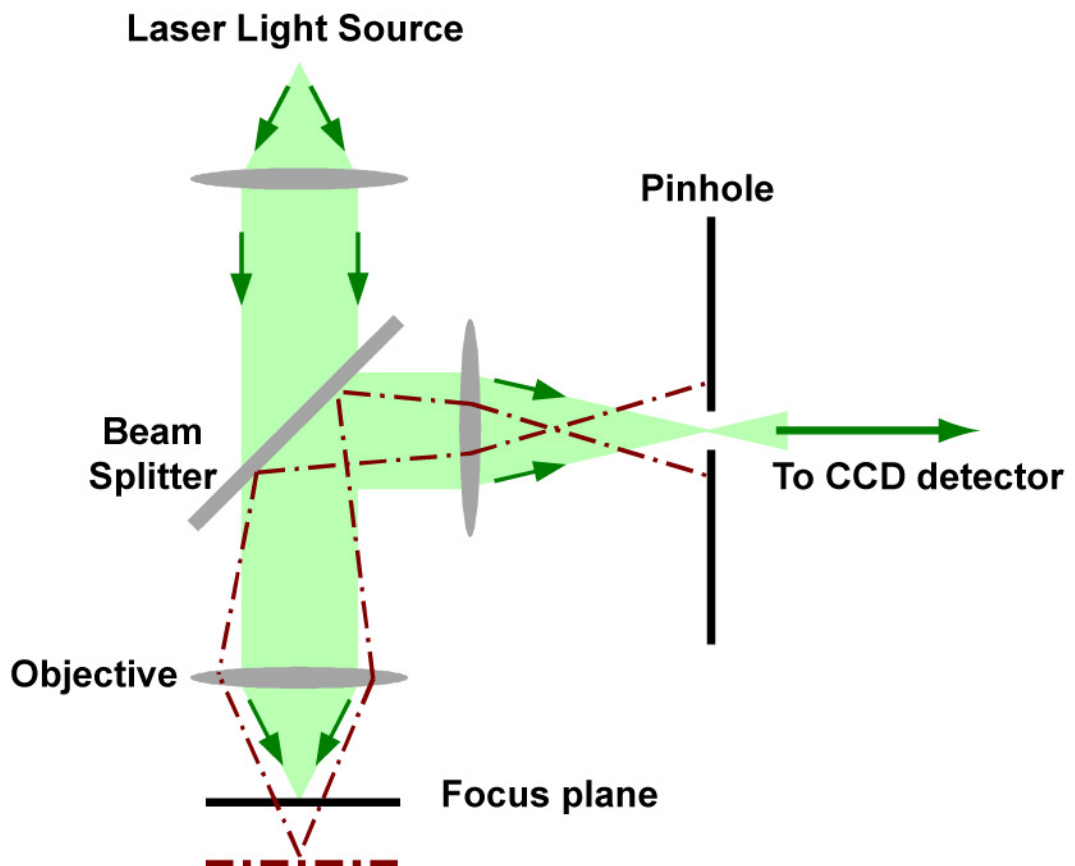


Figure 2.11: Schematic of principle set up of Raman microscope. Image modified from supplier.

resolution can be achieved (Figure 2.11). A confocal Raman microscope utilises the resolution of a confocal microscope with a laser light source. This allows for high resolution imaging of a particular surface and if coupled with a controlled scanning stage can lead to Raman spectral imaging.

A Raman spectral image is obtained by raster scanning the surface with the confocal Raman microscope and collecting a spectrum at set intervals. For example a $20 \times 20 \mu\text{m}^2$ area can be scanned taking 100 lines of 100 individual spectra in the process. From the collected spectra an image can be produced by mapping the intensity of an individual peak. Figure 2.12 shows an example of a CNT surface where the G-band ($\sim 1600 \text{ cm}^{-1}$) is mapped and brighter areas correspond to regions of high G-band intensity and dark areas correspond to low G-band intensity, as designated by the colour scale bar on the right of Figure 2.12.

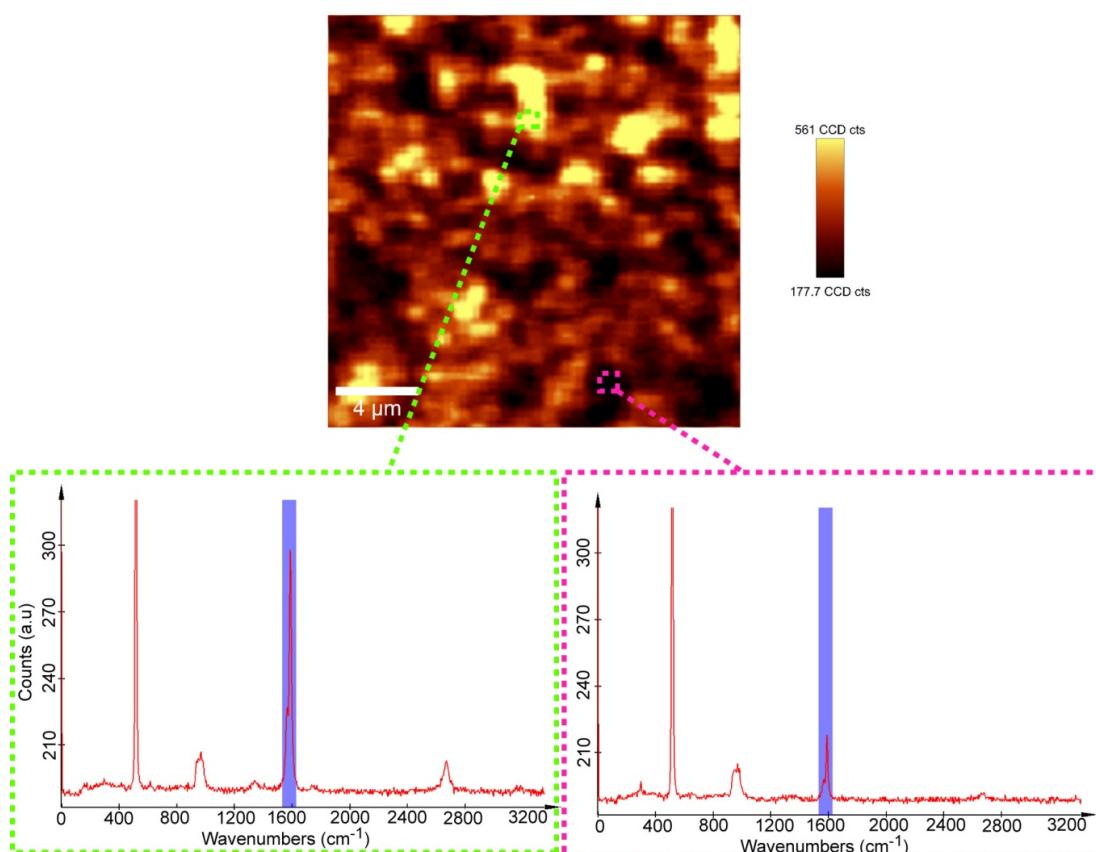


Figure 2.12: Example of how Raman spectral image is created from many individual spectra.

Confocal Raman spectra were recorded on a Witec Alpha 300RS confocal Raman microscope fitted with a 532 nm laser (60 mW) using both a 100x (0.9 numerical aperture (NA), working distance (WD) 0.23 mm) and a 40x (0.6 NA, WD 3.7 to 2.7 mm) objective. The individual spectra were taken as an average of at least 3 scans with integration time and number of scans averaged given in caption for each spectrum. Raman confocal spectral images were obtained by taking 100 lines of 100 spectra with an average integration time of 0.1 sec. The confocal Raman images represent the relative height of the G-band (1530 - 1630 cm^{-1}) for each individual spectrum. The experiments were carried out using Witec Control 1.42 software and the analysis was completed using Witec project 1.90 software.

2.5.4 X-ray photoelectron spectroscopy (XPS)

X-ray photoelectron spectroscopy (XPS) is a surface sensitive technique used to determine the elemental composition of a material. High energy monochromatic x-rays are incident upon a surface where they excite and eject an electron. From the energy of the ejected electron its original binding energy can be determined. An intensity vs. binding energy plot is obtained from which the elemental composition and some information on the electronic state of the surface atoms can be obtained.

XPS was used to confirm the presence of thin layers of molecules chemically attached to a surface.

XPS spectra were obtained using 1252.6 eV X-rays from an Mg K_{α} source (Specs, Germany) with a 20 eV pass energy. Ejected electrons were collected and analysed using a Leybold-Heraeus LHS-10 controlled by an in-house written LabView program. Data was collected at room temperature within a vacuum chamber of base pressure $\sim 1 \times 10^{-9}$ Torr with a working pressure of $< 5 \times 10^{-8}$ Torr. Survey spectra were taken in constant retarding ratio mode. High resolution spectra were taken as an average of at least 4 spectra in fixed analyser transmission mode.

2.5.5 *Fourier transform infrared (FTIR) spectroscopy and microscopy*

FTIR spectra were recorded on a Nicolet Avatar 370MCT spectrometer (Thermo Electron Corporation). The spectrometer was fitted with a transmission accessory, all spectra were recorded over a range of 650 - 4000 cm^{-1} at a resolution of 2 cm^{-1} as an average of 64 scans and analysed using OMNIC version 7.3 software. All FTIR spectra were collected with a background of clean flat/non-functionalised Si wafer of the same type as the samples.

IR microscopy was performed on a Nicolet iN10 infrared microscope (Thermo Electron Corporation, USA). IR microscopy data was collected using transmission mode. IR spectra were captured using an aperture size of 30 μm^2 and were recorded over a range of 1200 - 4000 cm^{-1} , at a resolution of 8 cm^{-1} and taken as an average of 16 scans. Analysis of IR microscopy data was performed using OMNIC picta software (Thermo Electron Corporation, USA).

2.5.6 *Contact angle*

The static water contact angle (WCA) on the surfaces was determined with a custom-built contact angle goniometer. Samples were affixed to a glass slide and a droplet of MilliQ water (1 μL) was applied to the surface. Images of the drops were recorded using a CCD camera fitted with a macrolens. WCA measurements were determined from drop images using a plugin analysis software for Image J (DropSnake, NIH, USA). The DropSnake plugin required a manual trace (blue dots in Figure 2.13 (b)) which it then compared to contrast in the image in order to calculate the WCA values (red dots and values). The reflective nature of the Si surface made the analysis difficult as little contrast existed at the base of the drop. As a result many values were excluded where the software could not recognise the drop/surface/air interface. The mean value of the WCAs was calculated from at least 3 individual measurements taken at different locations on the examined substrates.

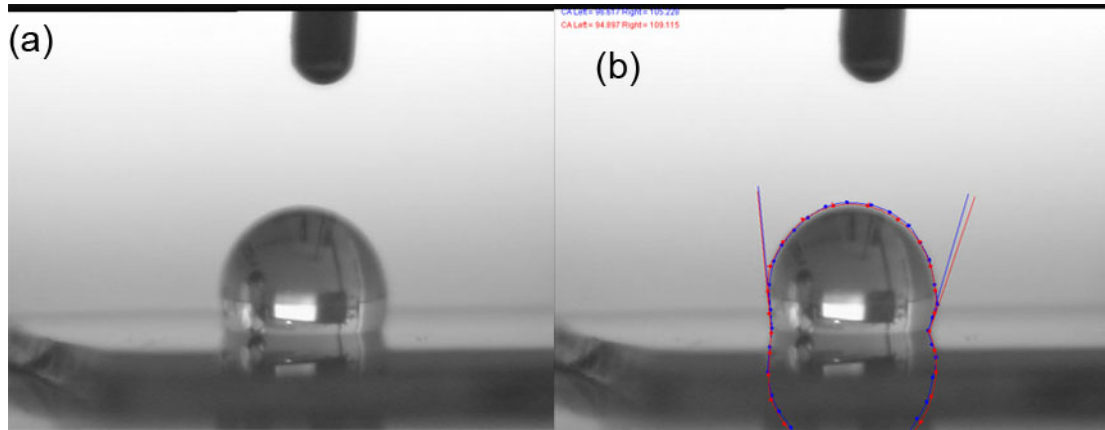


Figure 2.13: Example of water contact angle measurement showing (a) original image and (b) after analysis using the Image J plugin DropSnaker where blue dots were manually inserted and red dots were inserted by the software to give output values.

2.6 References

- [1] M. Marshall, S. Popa-Nita, and J. G. Shapter, "Measurement of functionalised carbon nanotube carboxylic acid groups using a simple chemical process", *Carbon*, **44**, 1137-41 (2006).
- [2] J. Liu, A. G. Rinzler, H. Dai, J. H. Hafner, *et al.*, "Fullerene Pipes", *Science*, **280** (5367), 1253-6 (1998).
- [3] J. Zhang, H. Zou, Q. Qing, Y. Yang, *et al.*, "Effect of Chemical Oxidation on the Structure of Single-Walled Carbon Nanotubes", *The Journal of Physical Chemistry B*, **107** (16), 3712-8 (2003).
- [4] S. N. Magonov, and N. A. Yerina, Visualization of Nanostructures with Atomic Force Microscopy in *Handbook of Microscopy for Nanotechnology* (Eds.: N. Yao, Z. L. Wang), Springer Science, New York, **2005**, pp. 113 - 56.
- [5] G. Cao, "Nanostructures & Nanomaterials: Synthesis, Properties & Application", *Imperial College Press*, London, (2004).
- [6] C. V. Raman, "The Raman Effect: Investigations on Molecular Structure by Light Scattering", *Transactions of the Faraday Society*, **25**, 781-92 (1929).
- [7] M. S. Dresselhaus, G. Dresselhaus, R. Saito, and A. Jorio, "Raman spectroscopy of carbon nanotubes", *Physics Reports-Review Section of Physics Letters*, **409** (2), 47-99 (2005).
- [8] N. B. Colthup, L. H. Daly, and S. E. Wiberly, "Introduction to Infrared and Raman Spectroscopy", *Academic Press*, New York and London, (1964).
- [9] N. R. Raravikar, P. Keblinski, A. M. Rao, M. S. Dresselhaus, *et al.*, "Temperature dependance of radial breathing mode Raman frequency of single-walled carbon nanotubes", *Phys. Rev. B*, **66**, 235424 (2002).
- [10] J. Wei, B. Jiang, X. Zhang, H. Zhu, *et al.*, "Raman study on double-walled carbon nanotubes", *Chemical Physics Letters*, **376** (5-6), 753-7 (2003).
- [11] M. Picher, E. Anglaret, R. Arenal, and V. Jourdain, "Self-Deactivation of Single-Walled Carbon Nanotube Growth Studied by in Situ Raman Measurements", *Nano Letters*, **9** (2), 542-7 (2009).

Chapter 3

Device fabrication

Fabrication and characterisation of carbon nanotube/silicon nanostructures is described in detail. Chemical attachment of single-walled carbon nanotubes (SWCNTs) to both silicon and porous silicon (pSi) is investigated, and in particular SWCNT attachment is described in detail as they are considered to have the largest application potential. The chemical attachment of both double-walled (DWCNTs) and multi-walled carbon nanotubes (MWCNTs) to silicon is also investigated. Particular interest is placed upon the CNT coverage and alignment, as determined by atomic force microscopy (AFM), as these are major factors in device application. The growth of CNTs via chemical vapour deposition (CVD) is also investigated as a comparison to chemically attached CNTs.

3.1 Introduction

As discussed in Section 1.2 the physical, mechanical and electronic properties of CNTs have led to a great deal of research into their potential use in devices such as scanning probe tips,^[1, 2] energy storage devices,^[3-5] chemical and biochemical sensors,^[6, 7] field emission sources,^[8-10] biomaterial interface scaffolds^[11-13] and water filtration membranes.^[14-16] All of these applications require the controlled placement of CNTs onto a substrate. If the placement of CNTs could be achieved on a silicon substrate it will allow an easier integration into existing technologies.^[17]

Surface bound CNTs can be directly fabricated by CVD where a metallic catalyst is deposited upon a substrate and is then used to catalyse CNT growth. This has been successfully achieved to produce SWCNTs,^[18] DWCNTs^[19, 20] and MWCNTs.^[21, 22] However, the CNTs produced are often covered in sp^3 carbonaceous material which inhibits some of the advantageous properties. Additionally, the CNTs are weakly bound to the substrate by metal-substrate interactions and CVD growth is a high temperature, high energy operation, making large scale fabrication impractical.

A recent alternative is the chemical attachment of CNTs to surfaces using carboxylic acid functionalised CNTs. Treatment of pristine CNTs, fabricated using the arc discharge method, by strong acid and sonication both shortens and imparts functionality upon the CNTs.^[23] The carboxylic acid groups can then be used to attach to surface bound chemical groups such as alcohols and amines.^[24] This has been achieved for SWCNTs on silver,^[25] gold,^[26] glass^[27] and more recently silicon.^[28, 29]

This Thesis investigates the potential application of CNT/Si nanostructures for water filtration, field emission and as scaffolds for biomaterial immobilisation. As discussed in Chapter 1 the chemical attachment of single-, double-, and multi-walled CNTs to silicon has the potential to allow the fabrication of devices in an up-scalable fashion while also improving performance.

In this Chapter, the chemical attachment of SWCNTs, DWCNTs and MWCNTs to silicon will be investigated. SWCNT attachment will be completed on both silicon and porous silicon (pSi) following the direct ester method developed by Yu *et al.*^[28] and also following CNT attachment to an amino silane layer first introduced by

Flavel *et al.*^[30] SWCNT attachment to pSi has not been previously reported and will be investigated in detail and compared to SWCNT attachment to flat silicon. DWCNTs and MWCNTs have not previously been chemically attached to substrates so a new method to carboxylate and attach these CNTs to silicon is introduced and compared to SWCNTs in terms of CNT alignment and coverage. The growth of CNTs via CVD will also be investigated as a comparison to the chemically attached CNTs. The practicality of each CNT-Si surface for a range of possible device applications is discussed.

3.2 SWCNT attachment to silicon

3.2.1 Chemical functionalisation of SWCNTs

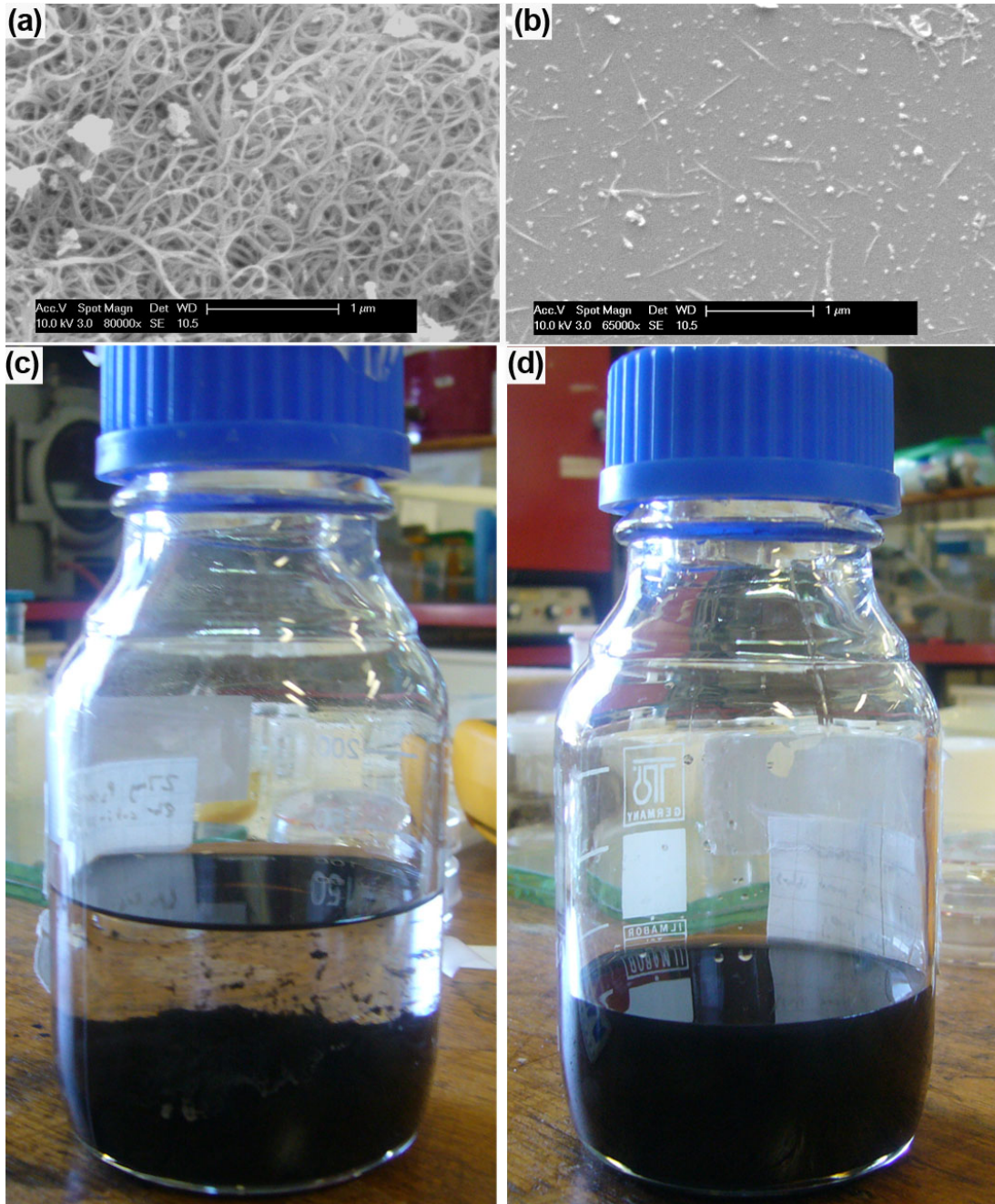


Figure 3.1: (a, b) SEM images (XL-30) of (a) pristine SWCNTs as purchased and (b) SWCNTs 'cut' for 8 hr, as described in Chapter 2. (c, d) Photographs of SWCNTs dispersed in DMSO after 1 day of incubation. (c) Pristine SWCNTs and (d) cut SWCNTs.

When purchased, SWCNTs come in the form of an inert, insoluble black powder. SEM imaging shows a tangled mess of SWCNTs with varying lengths ($>1 \mu\text{m}$) and purities (Figure 3.1 (a)). Dispersing the as prepared SWCNTs in DMSO yields an unstable suspension that precipitates out of solution within 1 min (Figure 3.1 (c)). To increase the chemical reactivity, solubility and to shorten the CNTs to a more usable length ‘cutting’ was carried out by sonicating the SWCNTs in a mixed acid solution.^[29] An SEM image after ‘cutting’ is shown in Figure 3.1 (b) where the lengths of the SWCNTs have been shortened and have been found previously to have a log normal distribution with a mean of 360 nm, as found by AFM.^[31] Another positive side effect of the ‘cutting’ process is that the SWCNTs become decorated in carboxylic acid functional groups and become stably suspended in polar aprotic solvents such as DMSO or dimethyl formamide (DMF) (Figure 3.1 (d)).

Carboxylic acid groups are commonly used in many organic reactions. In particular, they react with alcohol groups to form ester bonds and with amine groups to form amide bonds.

3.2.2 *Direct ester attachment of SWCNTs to silicon*

To form an ester linkage between the carboxylic acid groups on the SWCNTs and a silicon surface, there must be surface bound hydroxyl groups. Hydroxyl groups can be generated following a number of methods, but the simplest involves the direct oxidation of silicon in acidic solution or ozone atmosphere.^[32] The most common of these procedures is the 2-step (base-acid) cleaning procedure which is known to produce a high percentage of surface hydroxyl groups.^[32] An AFM image of a silicon wafer hydroxylated by the 2-step method and then immersed in a SWCNT solution for 2 hr is shown in Figure 3.2 (a, b). Direct ester SWCNT attachment was achieved using carbodiimide coupling as described in Section 2.3.1. Once SWCNT attachment was completed, the surface RMS roughness increased to more than 100 nm (flat silicon RMS roughness $\sim 3 \text{ nm}$) and circular protrusions could be observed on the surface. These protrusions have been previously observed^[7, 28-30] and are attributed to vertically aligned SWCNT bundles. Vertical alignment of the SWCNTs is the result of two main effects; the hydrophilic hydroxyl groups on the surface ‘repelling’ the hydrophobic walls of the SWCNTs forcing the SWCNTs away from the surface and large quantities of carboxylic acid groups on the ends of the SWCNTs promoting

end-on attachment. The vertically aligned bundles have a height range of 20 - 100 nm, as measured by AFM, with an average of approximately 40 nm and a diameter range of 20-70 nm. The height of the SWCNTs attached is much less than the average length after cutting (360 nm).^[31] This selective attachment of shorter nanotubes has been observed previously^[26, 29, 30, 33] and is attributed to the smaller SWCNTs diffusing faster to the active sites on the surface than their larger counterparts. The calculated heights from the AFM may be smaller and the calculated widths are most likely larger than the actual SWCNT heights/widths due to AFM tip convolution and other limitations of the technique. The values are given in order to directly compare with each other and are not considered actual values. The bundling of shortened SWCNTs in solution is well known and is due to tube-tube interactions such as van der Waals and hydrophobic interactions of the side walls that bring the SWCNTs together.^[34]

To investigate if other surface hydroxylation methods yield higher CNT concentrations, ozone and Piranha treated surfaces were investigated. Figure 3.2 (c) shows an AFM image of SWCNTs on silicon that has been exposed to an ozone atmosphere for 20 min. An AFM image of SWCNTs on silicon that has been treated with Piranha solution is shown in Figure 3.2 (d). No SWCNTs were observed to lie down for any of the three hydroxylation techniques investigated. This supports the theory that the hydrophilic surface plays an important part in the vertical alignment of the SWCNTs. There is a large change in SWCNT coverage across the hydroxylation methods; the 2-step process yields an average surface coverage of 22 % which is much higher than for both ozone (2 %) and Piranha treatment (10 %). The change in coverage is likely due to the number of surface hydroxyl groups formed in each method, although each produces a hydrophilic surface, the number of observed SWCNTs clearly indicate that there is a difference surface functionalisation.

Considering the high surface density and high level of vertical alignment, the 2-step method for producing hydroxylated silicon will be used in all future experiments involving the direct ester attachment of CNTs to silicon. Surfaces fabricated in this fashion have previously been shown to have excellent electronic properties and have been used as biochemical and chemical sensors,^[6, 35] solar cells^[36, 37] and have also been discussed as potential logic memory devices.^[38, 39]

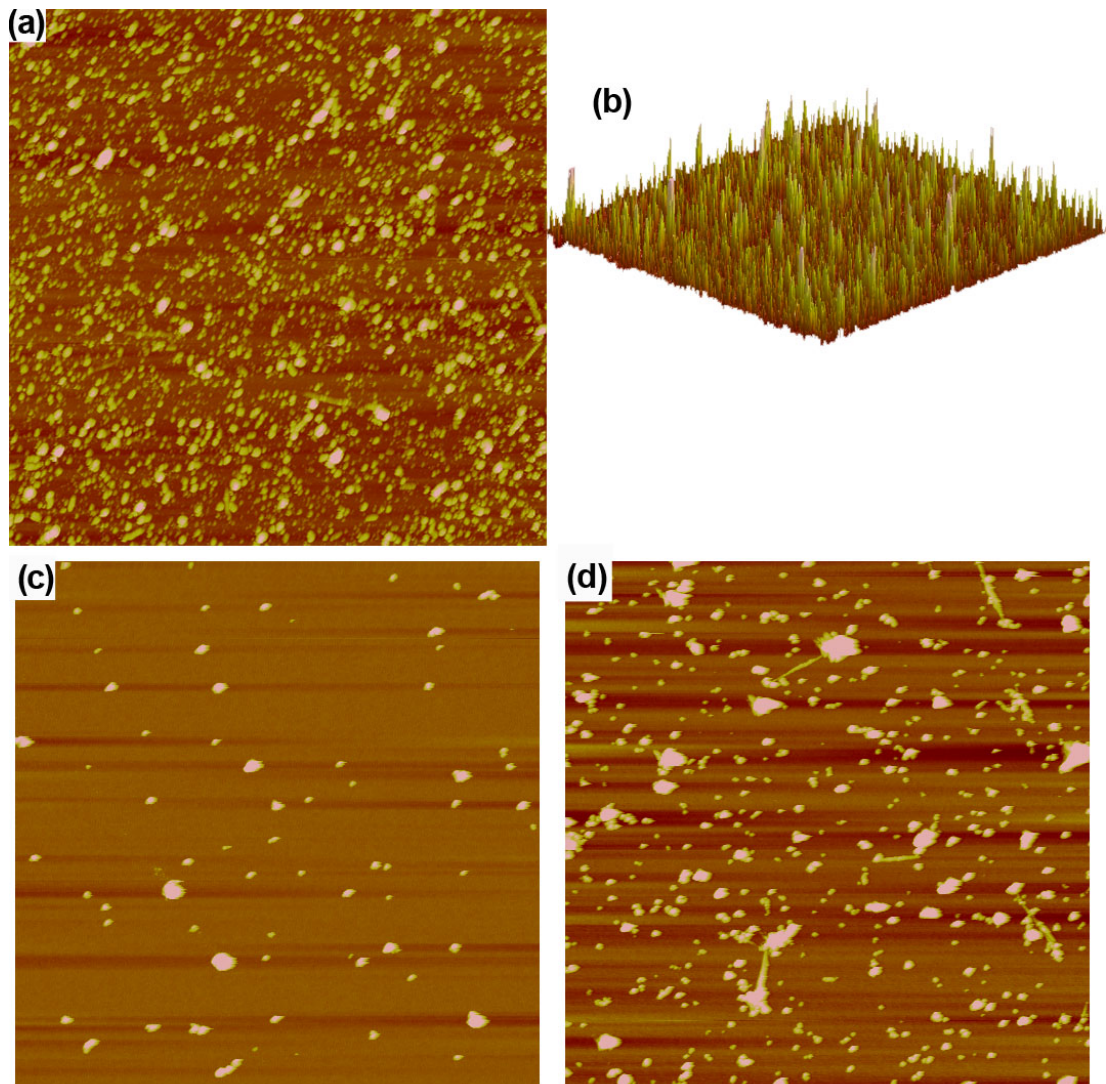


Figure 3.2: AFM images of SWCNTs attached to silicon via an ester linkage with varying silicon hydroxylation methods, (a,b) 2-step base-acid method, (c) ozone treated and (d) Piranha treated. AFM images are $5 \times 5 \mu\text{m}^2$ with a z scale of 50 nm.

Further study into the effect of the incubation time of the silicon wafer in the SWCNT solution on both SWCNT coverage and bundle size yielded the results shown in Figure 3.3. The SWCNT coverage increases at a quasi-steady rate for the first 12 hr of incubation time after which the SWCNT coverage ceases to increase and remains constant within the margin of error. This finding is consistent with Langmuir kinetics where monolayer coverage is obtained in two steps, a fast initial coverage increase followed by a slow final step.^[40] The variation of coverage observed by AFM imaging becomes quite large for incubations longer than 12 hr. Some surfaces were observed to have a higher coverage than the 12 hr incubation

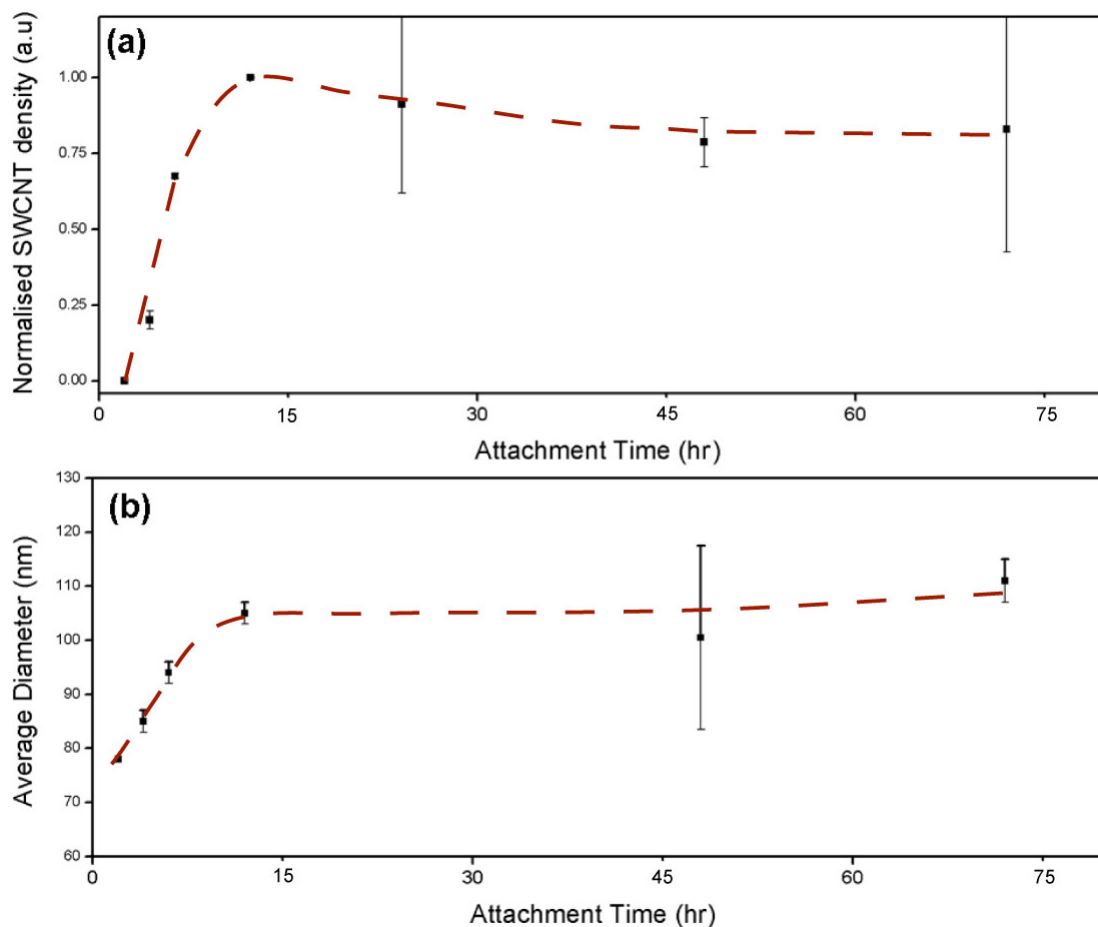


Figure 3.3: Graphs of (a) normalised SWCNT coverage and (b) average SWCNT bundle diameter vs. SWCNT attachment time, as determined by AFM. Dashed lines added to guide the eye.

while other samples were observed to have quite low SWCNT coverage. The variation is clearly apparent from the size of the error bars for the 24, 48 and 72 hr incubation values (Figure 3.3 (a)). The variation is attributed to the slow infiltration of water vapour into the reaction vessel with incubation time. As water vapour enters the reaction vessel, it can have two effects; it can cleave already formed ester bonds and it can assist in the re-arrangement of the DCC activated esters into the inactive *N*-acyclurea composites, discussed in Chapter 1.4, which leaves the SWCNTs unreactive toward the surface.

The rearrangement is visually observed by the transformation of the SWCNT/DMSO solution from an even black liquid to a clear liquid with a black precipitate. The occurrence and rate of water intake is not controlled (experiments completed within an in-house built nitrogen filled glove box) and the effect can be

large or not apparent as is indicated by the wide error range in the values for SWCNT coverage obtained. The change in SWCNT bundle diameter is shown in Figure 3.3 (b) where a similar trend to Figure 3.3 (a) is observed. The bundle size increases rapidly at first but slows after 12 hr of incubation as the amount of available surface area decreases. Due to these findings, SWCNT incubations of less than 12 hr will be used for the remainder of experiments in order to achieve consistent CNT coverage across samples.

As a further proof that the artefacts observed in Figure 3.2 (a) are SWCNTs, Raman spectroscopy and spectral imaging were completed on the Si-ester-SWCNT surfaces. Figure 3.4 (a) was obtained by collecting a spectrum at each (x, y) coordinate and converting the value for the maximum height of the G-band ($\sim 1580 \text{ cm}^{-1}$) into a colour, as shown in the colour scale in Figure 3.4. The range of the scale is from 100 to 700 counts, which indicates that even in the darker regions on the image SWCNTs are present. The scale was chosen to best illustrate the changes in coverage across the surface. Figure 3.4 (b) shows a Raman spectrum of the Si-ester-SWCNT surface; the peaks observed in the spectrum are detailed in Table 3.2. The region from $200 - 1200 \text{ cm}^{-1}$ is dominated with peaks from the silicon surface and no SWCNT Raman peaks are discernable. The Raman data confirms the presence of SWCNTs on the surface showing the RBM band which is only present in SWCNTs (and small diameter DWCNTs). The position of the RBM (ω_{RBM}) gives information on the diameter of the SWCNTs using the expression:

$$\omega_{RBM} = A/d_t + B \quad \text{Equation 3.1}$$

where d_t is the diameter of the SWCNTs investigated and A , B are parameters dependent upon the CNT environment.^[41] For bundled SWCNTs on a Si surface at a high density, A and B have previously been calculated to be $223.5 \text{ cm}^{-1} \text{ nm}$ and 25.5 cm^{-1} , respectively^[42] Using these values the average diameter of SWCNTs on the silicon surface was calculated to be 1.5 nm ; which is in agreement with the diameter quoted by the supplier (1.4 nm). A common calculation in Raman spectroscopy of CNTs is the D/G-band intensity ratio. The D-band is commonly described as an indicator of disorder or contamination within the CNT and as such its relative height when compared to the graphite like G-band is used as a measure of

CNT purity. The chemically attached SWCNT on silicon gave a D/G value of ~ 0.08 which is a low value compared to other Raman spectroscopy studies of SWCNTs.^[41]

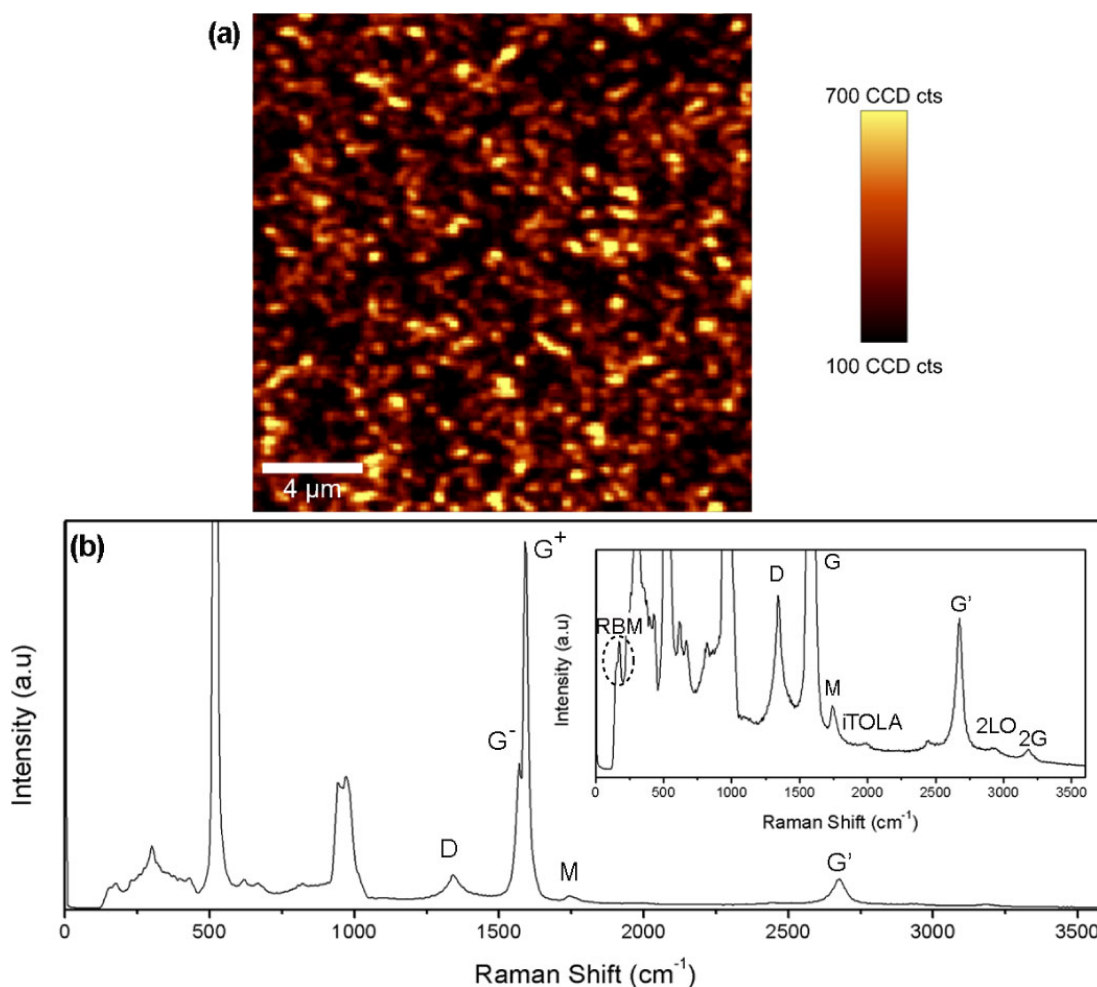


Figure 3.4: (a) Raman spectral image and (b) Raman spectrum of SWCNTs chemically attached to silicon via ester attachment. Raman spectrum average of 2 x 120 sec accumulation.

Table 3.1: Raman peak position and assignment for SWCNTs on silicon.

Peak Position (cm ⁻¹)	Acronym	Assignment
166	RBM	radial breathing mode
1337	D-band	disorder band
1570	G ⁻ -band	graphitic band (circumferential)
1586	G ⁺ -band	graphitic band (axial)
1725	M-band	IR active mode
1950	iTOLA	combination band
2664	G'-band	overtone of D
2900	2LO	overtone of intervalley scattering
3180	2G	overtone of G-band

With a decent coverage and good vertical alignment in the absence of a chemical spacer between the SWCNT and the silicon, Si-ester-SWCNT substrates should be applicable in electronic applications such as chemical sensors, field emission electron sources or photovoltaic devices.

3.2.3 Attachment of SWCNTs to APTES functionalised Si

Although successful, the ester attachment method does have some drawbacks, the maximum surface coverage obtained was 22 % and ester bonds are known to degrade in aqueous environments. To improve both bond strength and surface coverage, the chemical attachment of ‘cut’ SWCNTs to an amine terminated silane (APTES) monolayer was investigated. The formation of an APTES layer was confirmed by contact angle measurements (Figure 3.5) where the surface water contact angle (WCA) changes from being hydrophilic after cleaning in Piranha solution (WCA $\sim 10^\circ$) to being somewhat more hydrophobic after APTES immobilisation (WCA $\sim 55^\circ$). AFM imaging was completed after SWCNT grafting onto the APTES layer with a typical image shown in Figure 3.6. From the top-down image is it clear that there are more SWCNTs on the surface (coverage of 39 %) and there are more SWCNTs lying down compared to the Si-ester-SWCNT surfaces. The increase in surface coverage is attributed to an increase in reactive surface sites and the formation of the more favourable amide bond while the loss of alignment is most likely due to the less hydrophilic APTES functionalised surface. Although lying

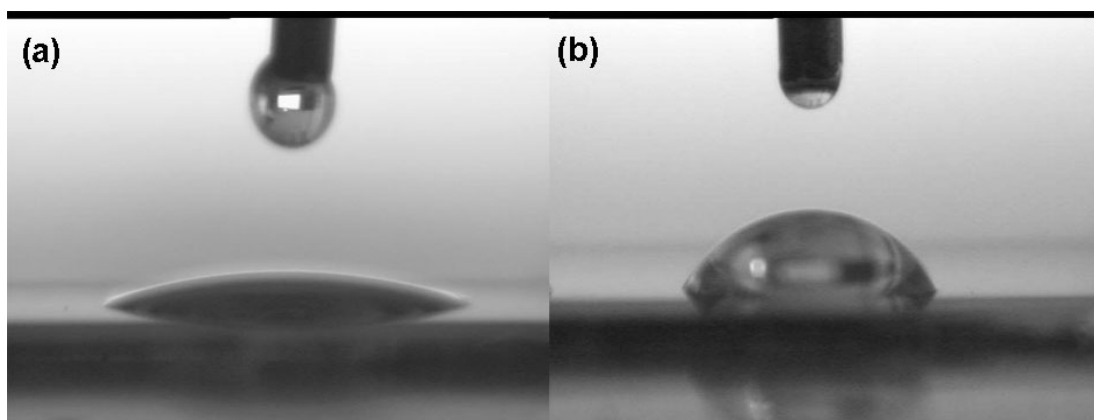


Figure 3.5: WCA photographs of (a) Piranha treated silicon and (b) APTES modified silicon.

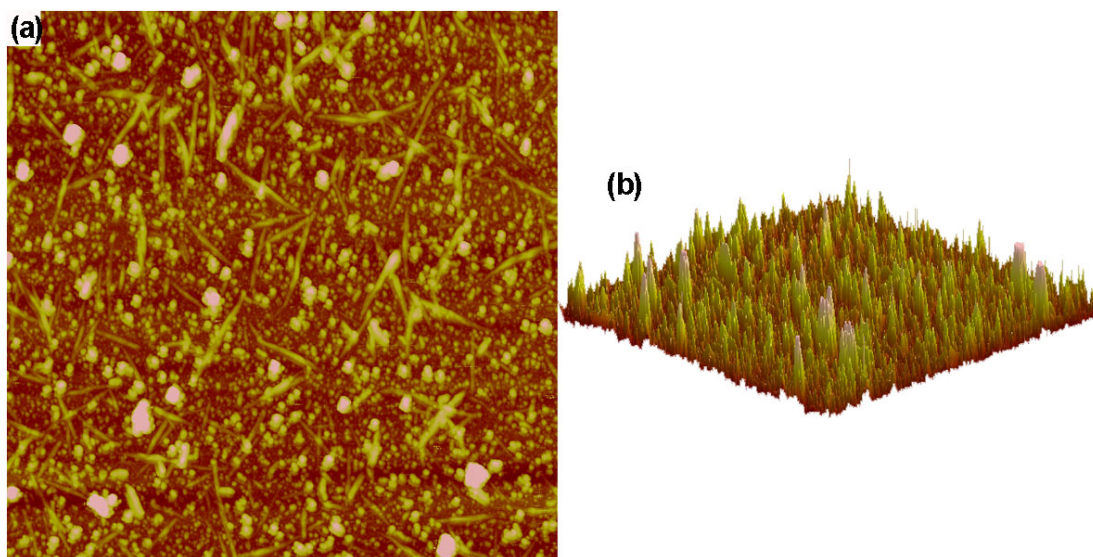


Figure 3.6: AFM images of SWCNTs attached to silicon via APTES monolayer (a) top down and (b) 3-D. AFM images are $5 \times 5 \mu\text{m}^2$ with a z scale of 50 nm.

down SWCNTs were observed, the 3-D image clearly shows that there are still a high percentage of vertically aligned SWCNTs on the surface.

Raman spectral imaging and spectroscopy was also carried out on the Si-APTES-SWCNT surfaces. The Raman spectral image (Figure 3.7 (a)) shows a higher percentage of brighter regions compared to the Si-ester-SWCNT surface, indicating a higher SWCNT coverage in accordance with the coverage increase for APTES mediated attachment observed by AFM. The comparison between the Raman data of direct ester and APTES mediated SWCNT attachment is only possible because the samples were investigated sequentially with the same laser power, integration time, image size, image resolution and were both focussed to the maximum possible G-band height. The Raman spectrum in Figure 3.7 (b) appears identical to the Si-ester-SWCNT surface which is expected because the SWCNTs on the surface are the same, they have simply been immobilised following slightly different protocols.

With a higher SWCNT coverage and a potentially stronger attachment the Si-APTES-SWCNT surfaces should be ideal for applications requiring high concentrations of SWCNT in an aqueous environment such as for biomaterial immobilisation. However, the silane spacer between the silicon and the SWCNT makes the surfaces unsuitable for electronic applications.

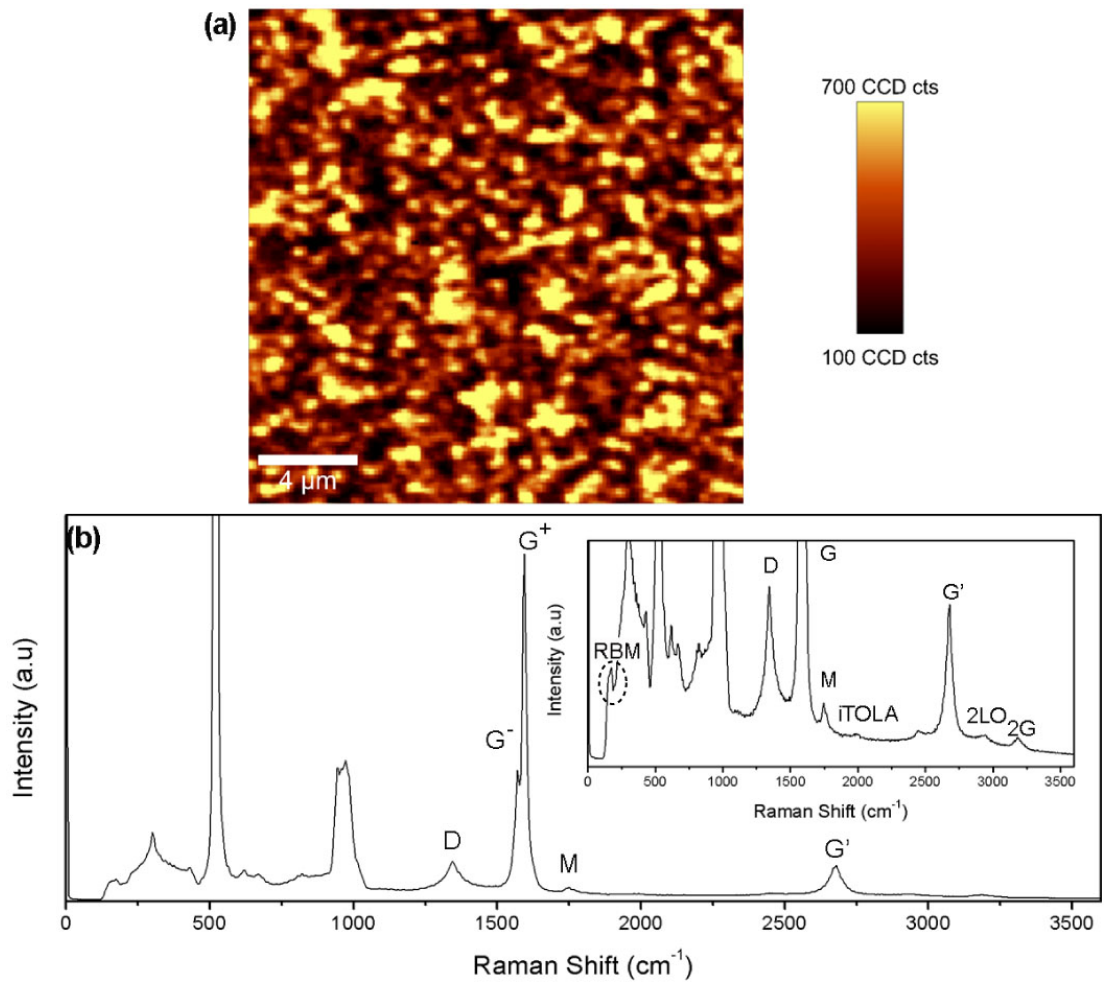


Figure 3.7: (a) Raman spectral image and (b) Raman spectrum of SWCNTs chemically attached to silicon via an APTES monolayer. Raman spectrum average of 2 x 120 sec accumulations.

3.3 SWCNT attachment to pSi

3.3.1 Porous silicon

The attachment of SWCNT to flat Si was completed following protocols previously published in literature.^[28, 30] Attachment of SWCNTs to pSi had not been demonstrated previously and so both direct ester and APTES mediated SWCNT attachment was studied in detail.

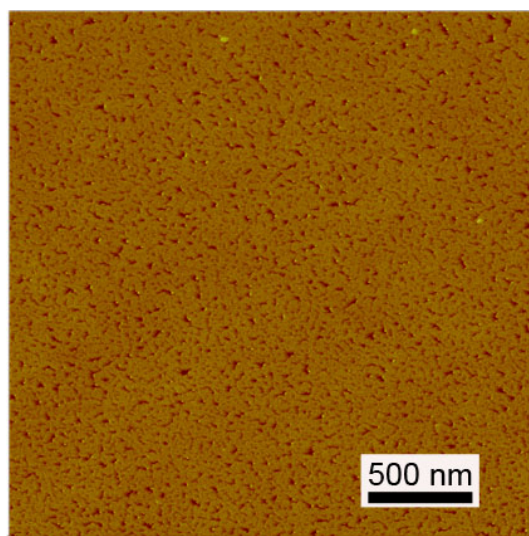


Figure 3.8: AFM image of freshly etched pSi. Etching conditions: 1:1 (v/v) HF/ethanol, 66 mA, 120 sec.

The pSi substrates created were characterised by AFM (Figure 3.8) and under the etching conditions used pores ranging from 6.5 nm to 20.0 nm (11.6 nm average) were fabricated. This pore size was considered ideal for this investigation because the pores are small enough that the SWCNT bundles will not enter the pores while they are not so small that the surface will behave in an analogous fashion to flat Si. The thickness of the porous layer was calculated to be approximately 6 μm by SEM. The calculated pore size is in agreement with previous AFM studies of pSi substrates generated under the same etching conditions.^[43]

All SWCNT attachment methods described here require silanol (Si-OH) groups on the pSi surface at some stage. The most common method of producing these groups on freshly etched pSi is through ozonolysis,^[44] however the most effective procedure of attaching SWCNTs to flat silicon used the 2-step base-acid method.^{[28,}

^{30]} Importantly, pSi degrades in basic and aqueous environments. The 2-step base-acid method could therefore not be used. Piranha oxidation was compared to ozone oxidation for CNT attachment and effectiveness of each method to produce silanol groups was investigated by FTIR. Freshly etched, hydrogen terminated, pSi (Figure 3.9 (a)) is characterised by three different Si-H stretching vibrations (Si-H at 2091 cm^{-1} , Si-H₂ at 2120 cm^{-1} , and Si-H₃ at 2140 cm^{-1}) and a Si-H₂ scissor vibration at 906 cm^{-1} .^[45] The freshly etched pSi also shows a weak oxidation (Si-O) peak at 1070 cm^{-1} which occurs spontaneously when pSi is exposed to ambient conditions.^[46] Upon oxidation by both ozone (45 min, Figure 3.9 (b)) and Piranha solution (Figure 3.9 (c)), the 4 Si-H_x peaks disappear and are replaced by a strong broad peak at 1100 cm^{-1} attributed to Si-O valence vibrations, a small weak oxidation peak also appears at 1600 cm^{-1} attributed to Si-OH bending,^[47] as well as a broad -OH stretching band around 3400 cm^{-1} due to hydrogen bonded -OH groups and perhaps some chemisorbed H₂O.^[48] The small peak at 3715 cm^{-1} is attributed to isolated silanol stretches on the pSi surface.^[49] The presence of silanol peaks for both oxidation processes indicates that they are both potentially suitable for SWCNT attachment.

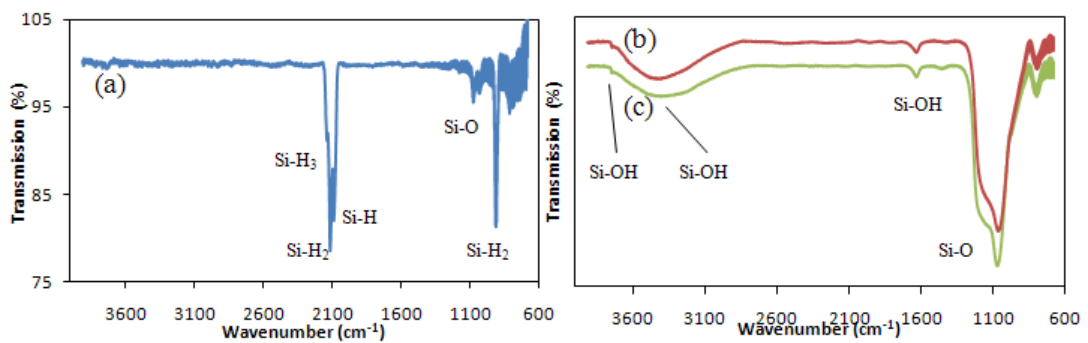


Figure 3.9: FTIR spectra of pSi, which has been (a) freshly etched, (b) ozone oxidised (45 min) and (c) wet chemical oxidised (Piranha solution). Spectra in (b) are offset for clarity.

FTIR was carried out for pSi substrates exposed to 10 - 60 min of ozone showing a slight increase in the -OH and Si-OH peak intensities observed. Ozone is considered the better of the two oxidation methods since it does not damage the pSi substrate while the chemical oxidation gradually dissolved the pSi film.

3.3.2 Direct ester attachment of SWCNTs to pSi

AFM imaging after SWCNT attachment on ozone oxidised pSi (not shown here) showed little or no SWCNT attachment. Longer ozonolysis times were attempted with little improvement. Piranha treatment was used to hydroxylate the pSi substrate followed by 4 hr of SWCNT attachment. The SWCNT coverage after 4 hr is shown in Figure 3.10 where vertically aligned bundles of SWCNTs are clearly observed with measured heights between 20 to 50 nm.

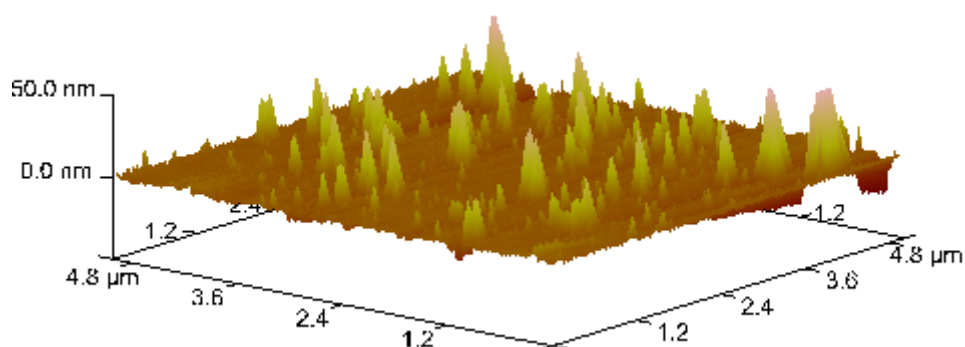


Figure 3.10: AFM image of SWCNTs chemically attached to pSi following the direct ester attachment method on Piranha-oxidised pSi.

The calculated SWCNT coverage of SWCNTs on pSi in Figure 3.10 is 7% compared to 22% for the same attachment on flat Si. This reduction in coverage is thought to be due to the formation of geminal silyl esters on the pSi substrate. Silyl esters are susceptible to degradation because the bond can be cleaved by attack at either the carbonyl or the silicon atom.^[50] Degradation of silyl esters has been found to increase depending upon the environment of the silicon. Hydroxylated flat silicon (100) consists of one Si atom with one hydroxyl group. pSi on the other hand can have 1, 2 or 3 hydrogen atoms on the surface Si atoms after etching which means it could have 1 - 3 hydroxyl groups on each surface Si atom after hydroxylation.^[51] If a Si atom forms an ester linkage with two or more SWCNTs (known as a geminal ester) the degradation is found to be much faster because of the loss of steric and electronic stability (Figure 3.11 (a, b)).^[52, 53] Raman spectral imaging was not attempted on the pSi-ester-SWCNT surfaces due to the low coverage of SWCNTs obtained. Besides the low CNT coverage the Piranha treatment noticeably degraded

the pSi surface. The ester attachment of CNTs to pSi is therefore not a viable fabrication method.

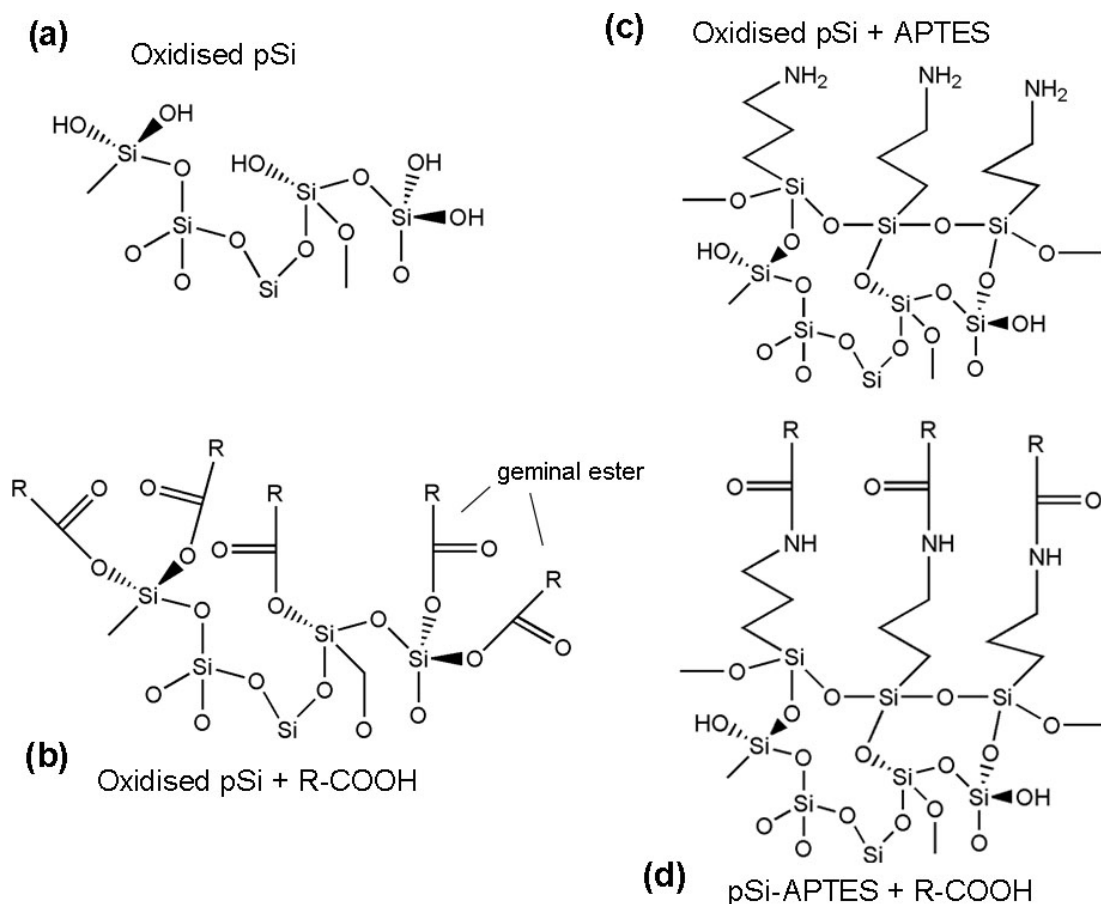


Figure 3.11: Schematic representation of (a) oxidised pSi, (b) oxidised pSi after reaction with a carboxylic acid containing molecule (eg., ‘cut’ SWCNT), (c) oxidised pSi after APTES immobilisation and (d) pSi after APTES immobilisation and carboxylic acid attachment.

3.3.3 Attachment of SWCNTs to APTES functionalised pSi

To increase the coverage of SWCNTs on the pSi surface, a layer of APTES was deposited to produce an amine-terminated monolayer. FTIR analysis of the APTES functionalised pSi (Figure 3.12 (a)) shows that while the silanol and -OH stretches have disappeared in the region of $3300\text{--}3700\text{ cm}^{-1}$, two small primary amine peaks at 3361 cm^{-1} and 3295 cm^{-1} appear, as well as two broad peaks at 1640 cm^{-1} and 1560 cm^{-1} attributed to N-H_2 scissoring and N-H bending.^[54] The peaks at around 2900 cm^{-1} are attributed to C-H stretching (2932 cm^{-1} , 2877 cm^{-1}) and a HC-NH_2 stretch at 2972 cm^{-1} .^[55] The Si-O stretch at 1100 cm^{-1} is still present from Si-O bonds

in the backbone structure of the pSi. Upon SWCNT attachment (Figure 3.12 (b)), the primary amine peaks disappear, the C-H stretching peaks remain and two new peaks appear at 1638 cm^{-1} and 1528 cm^{-1} which are attributed to the N-H bending and C-N stretching of secondary amides.^[54] The FTIR spectra support the formation of an amine-terminated monolayer and the creation of an amide linkage between the APTES and functionalised SWCNTs.

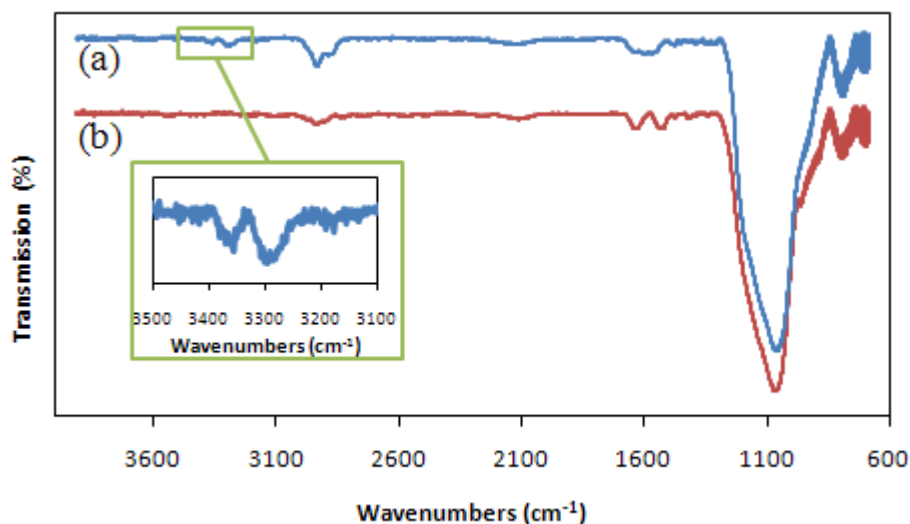


Figure 3.12: Transmission FTIR spectra of hydroxylated pSi substrates (ozone; 10 min) followed by (a) APTES functionalisation and (b) SWCNT attachment to APTES monolayer (24 hr attachment time). Inset shows zoom of amine peak area (3500 cm^{-1} to 3100 cm^{-1}) for the APTES functionalised pSi substrate. Spectra offset for clarity.

After APTES functionalisation (5 min, Figure 3.13 (a)), the pSi surface is featureless like the freshly etched surface indicating that minimal silane polymerisation has taken place (Figure 3.8). Figure 3.13 (b - d) shows the AFM images of the SWCNT attachment to pSi via an amide linkage. All images show similar features to those observed in Figure 3.10 but yield a higher coverage. The observed higher coverage is due to the favourable and stable amide linkage as well as the fact that the silane layer does not include any geminal groups (Figure 3.11 (c, d)), further increasing the stability of the attachment. Various SWCNT attachment times were investigated and imaged by means of AFM. The lowest coverage was observed after 5 min (18 %, Figure 3.13 (b)). Coverage increased rapidly up to 48 % after 1 hr of nanotube suspension exposure (Figure 3.13 (c)) then continued to rise to 52 % up

after 24 hr of exposure (Figure 3.13 (d)). This change in surface coverage with attachment time is shown graphically in Figure 3.14. This trend has previously been observed for the direct ester attachment of SWCNTs on flat silicon (Figure 3.3 (a)).^[28] Previous work on SWCNT attachment to APTES functionalised flat silicon has shown that the maximum SWCNT coverage occurs after 4 hr of attachment.^[30] The 3D image (Figure 3.13 (e)) clearly demonstrates the vertical alignment of CNTs on these surfaces.

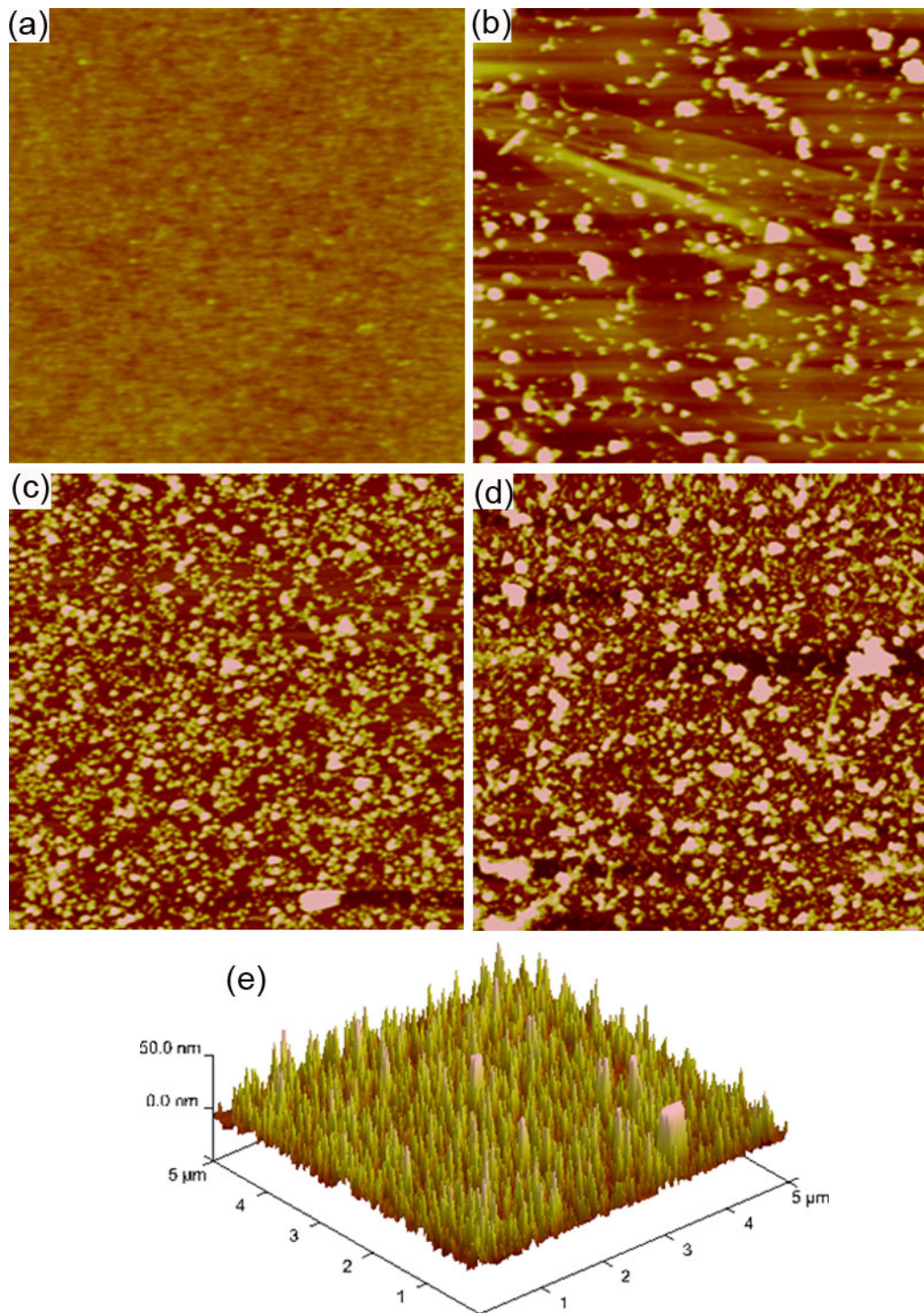


Figure 3.13: AFM images of (a) pSi after 5 min of APTES treatment (0 % surface coverage, $5 \times 5 \mu\text{m}^2$, z scale 50 nm) and SWCNT attachment on APTES functionalised pSi ($5 \times 5 \mu\text{m}^2$ images, z scale 50 nm) for attachment times of (b) 5 min (18 % coverage), (c) 1 hr (48 % coverage), (d) 24 hr (52 % coverage) and (e) 3D image of (c) after 1 hr attachment.

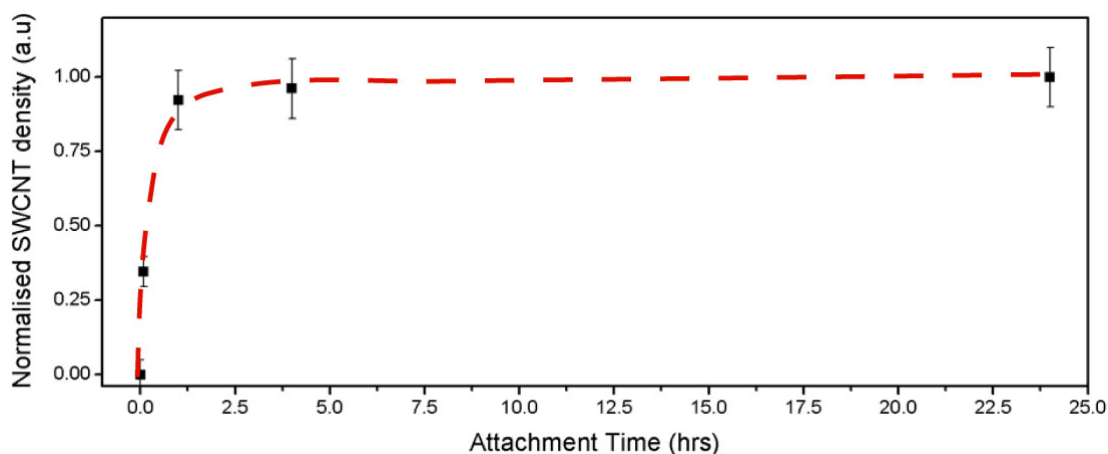


Figure 3.14: Change in percentage surface coverage with incubation time of APTES silanised pSi wafer in a SWCNT solution. Dashed line added to guide the eye.

Figure 3.15 (a) shows a Raman spectral image showing SWCNTs over the entire image area. The Raman spectrum (Figure 3.15 (b)) features the major SWCNT peaks (RBM, G-band) but does not show any of the minor peaks as observed for the silicon-ester-SWCNT surfaces, shown previously in Figure 3.4 (b). This is due to the background fluorescence of the pSi substrate which increases the background noise level in the signal and makes it impossible to observe the less intense SWCNT Raman peaks (eg., iTOLA, 2LO, 2G). The relative size of the background fluorescence appears to depend upon the pore dimensions (diameter and depth) such that some etching conditions lead to surfaces that are suitable for Raman (such as the etching conditions used in this case) while other etching conditions result in complete loss of the SWCNT signal.

Due to the large increase in SWCNT density, while maintaining a high level of vertical alignment, the APTES mediated attachment was considered the best method to produce VA-SWCNT on pSi.

The intrinsic biocompatibility of pSi makes these surfaces suitable for biomaterial scaffolds. Additionally, the pSi pores can be loaded with a therapeutic material which can be released in a controlled fashion. The SWCNT bundles appear to transcend the pores which could lead to application in water filtration if the pSi substrate were open at both ends. The attachment of SWCNT to pSi membranes will be covered in more detail in Chapter 5. The effect of pore size on SWCNT attachment is investigated as part of Chapter 4.

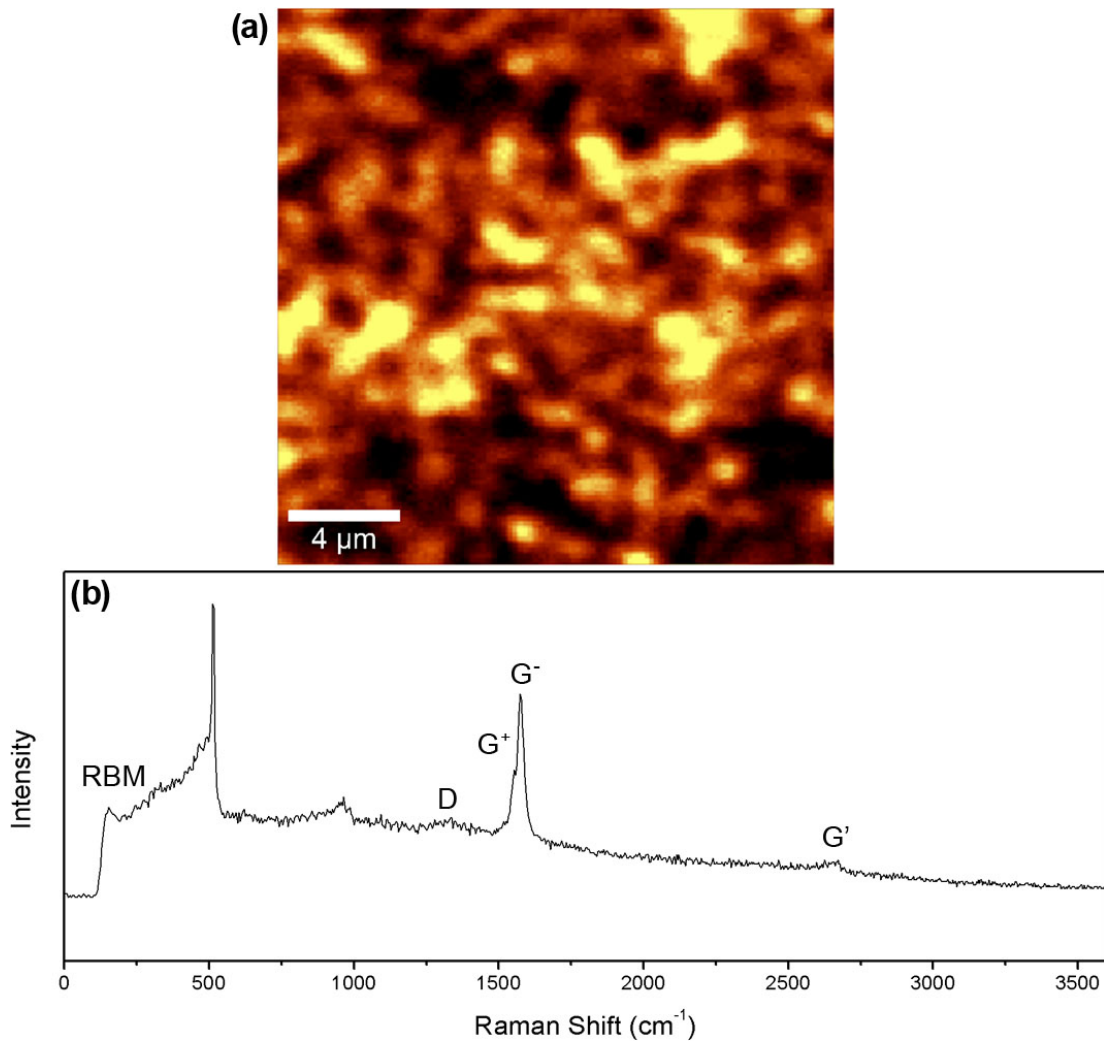


Figure 3.15: (a) Raman spectral image of SWCNTs chemically attached to pSi via the APTES attachment method and (b) Raman spectrum of SWCNTs on pSi showing the high background fluorescence of pSi. Spectrum average of 3 x 60 sec.

3.4 DWCNT attachment to silicon

3.4.1 Chemical functionalisation of DWCNTs

In order to chemically attach DWCNTs to Si a suitable cutting/functionalisation protocol had to be established. Early attempts involved changing the time of sonication in mixed acid but the DWCNT solutions were not stable in DMSO and dropped out of suspension within 24 hr. Eventually, a 2-step method was attempted where the DWCNTs were initially refluxed in 3 M nitric acid overnight followed by a shorter 3 hr sonication in mixed acid (identical to the SWCNT cutting procedure). The DWCNT solution obtained after following this protocol remained suspended within DMSO for more than 3 months, which was similar to that of the SWCNT suspensions. Figure 3.16 (a) shows a SEM image of the pristine DWCNT powder. Similar to the SWCNT powder (Figure 3.1 (a)), the DWCNTs exist as long tangled randomly oriented tubes of $>2 \mu\text{m}$ length. After cutting, the DWCNTs (Figure 3.16 (b)) are straighter, shorter and more dispersed with a calculated average length of $1.1 \mu\text{m} \pm 0.4 \mu\text{m}$. This average length is higher than the 380 nm calculated for the SWCNTs and is probably a result of the shorter cutting time in mixed acid. It should also be noted that the SEM could not image any smaller DWCNTs than those observed so the value given may be higher than the actual number.

The Raman spectrum of pristine DWCNT powder in Figure 3.16 (c) elucidates one major difference to that of the SWCNTs. The RBM band ($100 - 350 \text{ cm}^{-1}$, inset) consists of 5 discernable peaks, compared to 1 for the SWCNTs. Each peak is due to a distinct diameter of CNTs within the DWCNT, as shown in Table 3.2. The multiple peaks observed indicate that DWCNTs of different inner and outer wall diameter are present in the sample, as well as the possibility of some SWCNTs.^[56] Not all the possible diameters are shown because not all the CNT diameters are excited by the 532 nm laser used.^[57] Additionally, any RBM peaks below 150 cm^{-1} are cut off by the grating in the spectrometer. Hence, no CNTs with a diameter greater than 1.8 nm were observed.

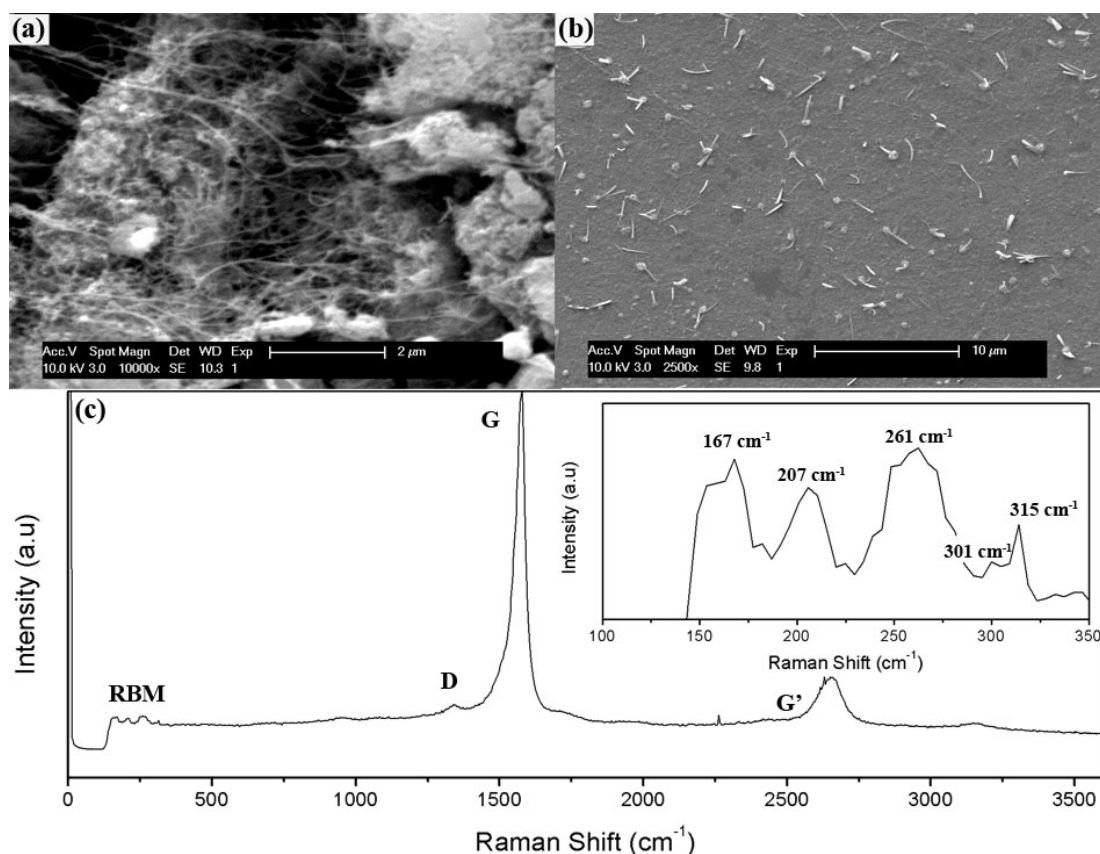


Figure 3.16: SEM images (XL-30) of (a) pristine DWCNTs and (b) cut/functionalised DWCNTs and (c) Raman spectrum of pristine DWCNTs with zoom of RBM region (inset). Raman spectrum average of 2 x 120 sec accumulations.

Table 3.2: RBM peak positions and corresponding calculated diameter for DWCNTs.

Peak Position (cm^{-1})	Diameter (nm)
167	1.58
207	1.23
261	0.950
301	0.811
315	0.772

3.4.2 Attachment of DWCNTs to silicon

Figure 3.17 (a) shows an AFM image of DWCNTs chemically attached following the direct ester attachment method to silicon. Both circular and rod-like features are observed on the surface which corresponds to both vertically aligned and bundles of

DWCNTs lying down (horizontally aligned). The presence of both lying down and vertically aligned DWCNTs is considered to be due to the DWCNT functionalisation process. During functionalisation, carboxylic acid groups will initially attack defect sites on the side-walls of the CNT. The production process used for DWCNTs (CVD) is known to create more defect sites along the sidewalls than that used for SWCNT production (arc discharge). The defect sites on the side walls of the DWCNT that are present after fabrication will be oxidised during the functionalisation process leading to a DWCNT that is decorated with carboxylic groups both at its ends and along its sidewalls.^[23, 58] When these DWCNTs are attached to the Si surface; attachment can occur at either their ends or their side walls leading to both vertical and horizontal attachment. The diameter of the bundles of DWCNTs was calculated to be 68 ± 20 nm.

A Raman spectrum of DWCNTs on Si is shown in Figure 3.17 (b). The peaks observed are predominately the same as for the SWCNT surface. Two major differences in the SWCNT spectrum are observed. Firstly, the RBM now consists of two peaks at 150 cm^{-1} (1.80 nm) and 187 cm^{-1} (1.38 nm), the peaks $>200\text{ cm}^{-1}$ are now lost within the silicon background. These peaks are also in slightly different positions to that of the pristine DWCNT powder. The cutting process may be responsible for this shift, where changes to the DWCNT environment or bundling will affect the position of the RBM bands.^[59] These factors are normally taken into account by the parameters A and B in the diameter calculation. For this calculation, the values of the parameters A and B have not been changed as they are both approximations and no more accurate values were obtainable. The second difference is the increase in the D/G intensity ratio to 0.27 which is a result of the low purity of the raw material and the amount of functionalisation of the DWCNT outer walls. The increased outer wall functionalisation supports our explanation as to why the DWCNT are both vertically aligned and lying down on the surface.

The produced DWCNT surfaces could potentially be used in electronic applications to compare to SWCNTs where the outer wall functionalisation may leave the inner wall intact which could potentially improve performance. The decrease in alignment between the SWCNTs and DWCNTs make the surfaces less suitable for biomaterial immobilisation and water filtration.

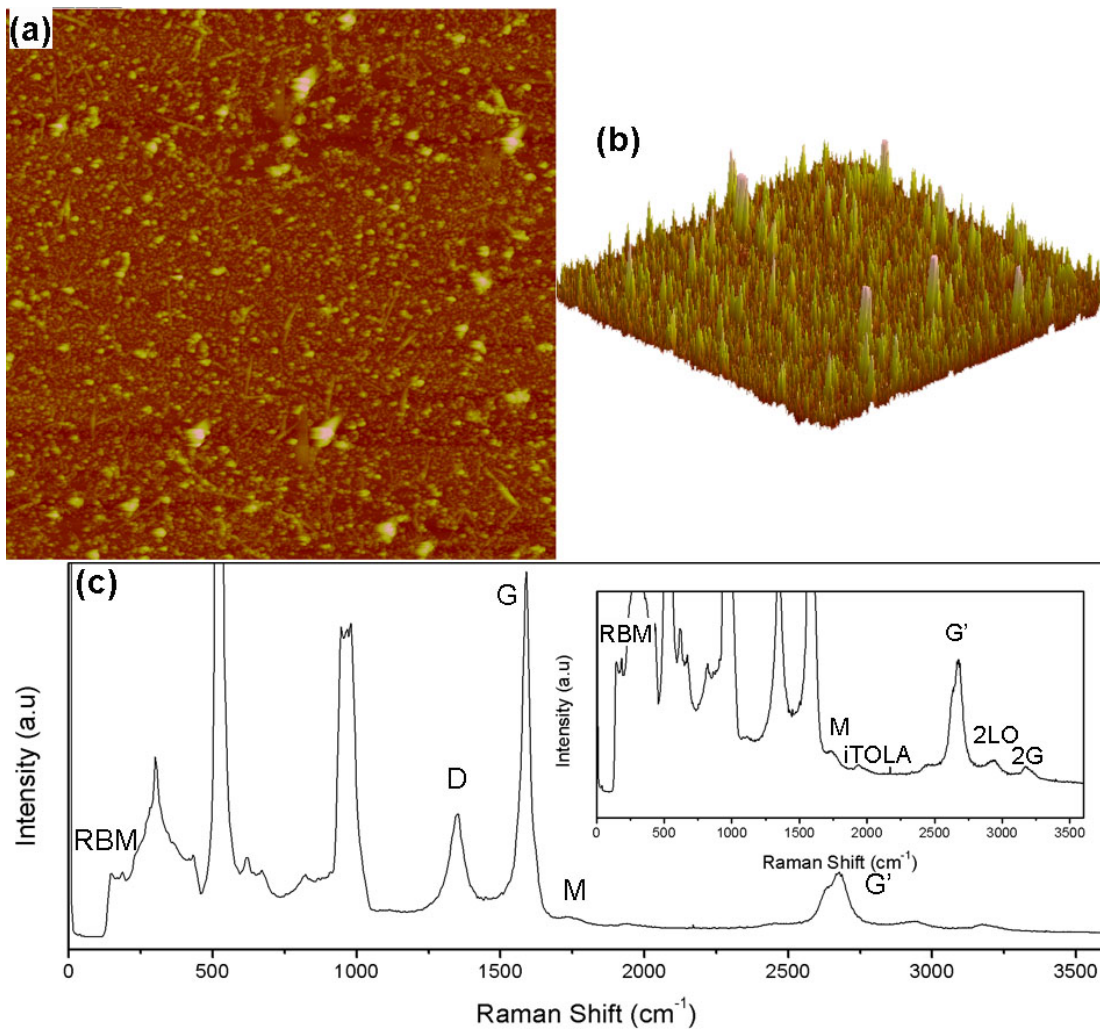


Figure 3.17: (a) Top down and (b) 3-D AFM as well as (c) Raman spectra of DWCNTs chemically attached to silicon with zoom showing RBM region (inset). Raman spectrum average of 2 x 60 sec accumulations.

3.5 MWCNT attachment to silicon

3.5.1 Chemical functionalisation of MWCNTs

In order to produce MWCNT surfaces similar to the Si-SWCNT substrates produced in Section 3.2, as purchased MWCNTs were chemically ‘cut’ to shorten and introduce carboxylic acid functionalities. In most cases in the literature only a small degree of functionalisation is imparted onto MWCNTs, leading to minimal reduction in length. To both shorten and functionalise MWCNTs, a new methodology was developed; the so-called ‘3-acid cutting system.’ The system involves an initial ‘cleaning’ via reflux in 3 M nitric acid to remove carbonaceous material and other impurities which make up a large constituent of the purchased MWCNT material. The ‘cleaning’ does not shorten the MWCNTs (as seen in Figure 3.18 (a)) with lengths ranging from 1-3 μm observed. The next two steps are a cutting via sonication in acid (the same as the process used for SWCNTs) for a shorter time (3 hr) and without maintaining a 0°C temperature. Finally, the MWCNTs were sonicated in HCl to protonate any remaining carboxylate groups. AFM imaging after completion of the cutting process (Figure 3.18 (b)) reveals MWCNTs which an average length of 380 ± 150 nm. The length scale of the

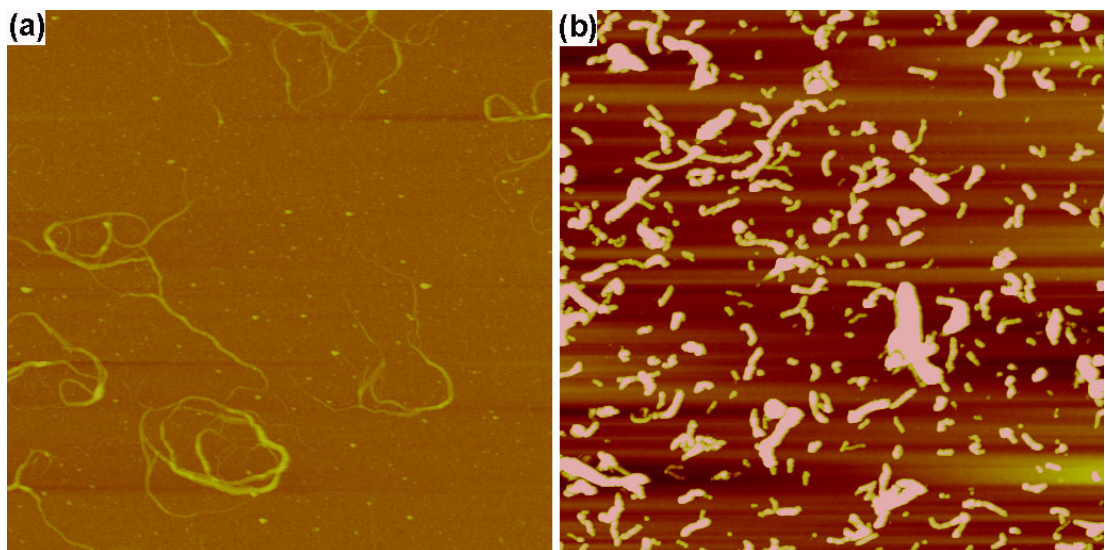


Figure 3.18: AFM images of (a) ‘cleaned’ MWCNTs and (b) Cut MWCNTs using the ‘3-acid cutting system’ drop-cast onto a silicon wafer. AFM images are $5 \times 5 \mu\text{m}^2$ with a z scale of 50 nm.

MWCNTs is very similar to the average length of the SWCNTs used earlier (360 nm) which was the desired result. Equally important was that the cut MWCNTs formed a stable suspension in DMSO, which was beneficial for chemical surface attachment.

3.5.2 Attachment of MWCNT to silicon

Both direct ester and APTES mediated MWCNT attachment to silicon were investigated following the same protocols as for SWCNTs. Figure 3.19 (a) shows an AFM image after direct ester attachment of MWCNTs to silicon. Long curved cylinders were observed on the surface which were MWCNTs lying down on the surface. No vertically aligned MWCNTs were observed. The loss of vertical alignment may be due to a number of reasons, during the cutting process defect sites are oxidised to produce carboxylic acid groups, MWCNTs are known to have a much higher number of defect sites along their outer shell (as indicated by the size of the D-band in Figure 3.19 (c)). This will lead to a higher number of carboxylic acid groups decorating the walls of the MWCNTs rendering the walls more hydrophilic and more reactive toward the surface and resulting in a higher likelihood of side-wall attachment. The AFM image of APTES mediated attachment of MWCNTs on silicon shows a similar surface topography but with a higher surface coverage (Figure 3.19 (b)). The higher coverage is most likely a result of the presence of more reactive amine groups (compared to $-OH$) that can undergo a reaction with the MWCNTs. Raman spectroscopy of the MWCNTs on silicon was carried out and a representative spectrum is displayed in Figure 3.19 (c). The obtained spectrum is considerably different to that of the SWCNTs. The difference is mainly due to the change in diameter of the CNTs where larger diameter MWCNTs do not exhibit the splitting of the G-band or the RBM band.^[41] Additionally, the D-band has become much larger with a D/G intensity ratio of 1.04 compared to 0.08 for SWCNT on Si. The D-band is due to sp^3 bonded carbon such as in defect sites in the CNT side wall. The apparent large number of defect sites, as shown by the large D-band, is a common observation in MWCNTs where the imperfect fabrication process leads to a large number of errors within the CNT lattice.

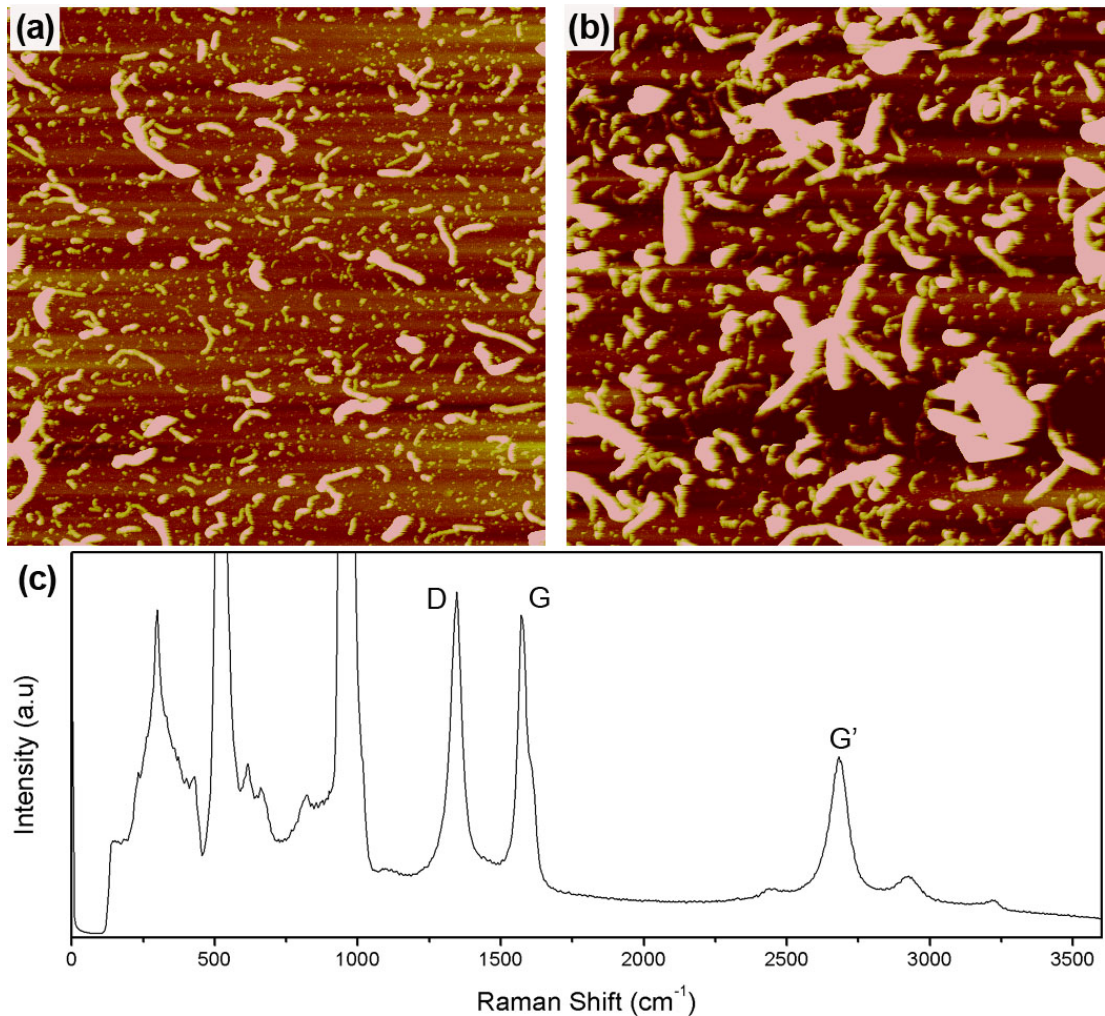


Figure 3.19: (a, b) AFM images and (c) Raman spectrum of MWCNTs chemically attached to silicon via (a) direct ester attachment and (b, c) APTES mediated attachment. AFM images are $5 \times 5 \mu\text{m}^2$ with a z scale of 50 nm, Raman spectrum is the average of 2 x 120 sec acquisitions.

MWCNTs cut following the 3-acid cutting system were suitable for chemical attachment onto silicon and potentially other surfaces. The fabricated Si-MWCNT surfaces could be beneficial in situations where vertical alignment is not critical or in situations where high surface area is advantageous such as in hydrogen storage or electrochemistry. As discussed in Section 1.6 MWCNTs are also expected to produce the most stable electron field emission.

3.6 CNT growth via chemical vapour deposition

To complement the fabrication of VA-CNT arrays via chemical attachment, the growth of VA-CNTs via CVD was attempted. It was expected that results gained on the chemically attached CNTs could be directly related and compared to that of the CVD grown CNTs. A custom, in-house built, CVD reaction tube was assembled within a tube furnace capable of reaching 1000 °C. Following a general CNT growth recipe of sputtering a thin film of iron onto a cleaned Si surface, heating to 750 °C under an Ar/H₂ atmosphere and then introducing the carbon source (acetylene) and a small amount of water vapour to the mixture CNT growth was found to occur. SEM imaging revealed that the growth of VA-CNTs was possible (Figure 3.20 (a, b)). The height of the VA-CNTs were found to vary dramatically between samples. For a

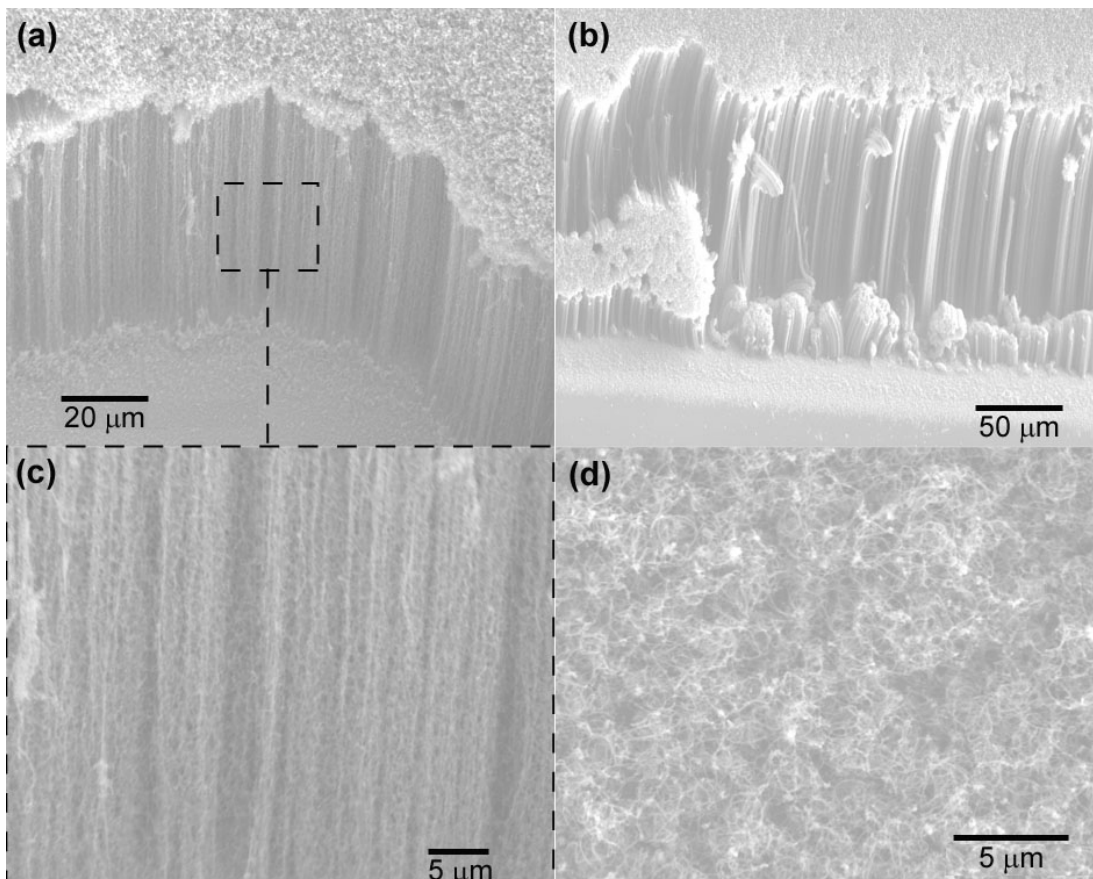


Figure 3.20: SEM images (CamScan) of CNTs grown on silicon via CVD showing (a, b) vertical alignment, (c) zoom of side view of VA-CNTs and (d) randomly oriented CNTs.

growth time of 10 min, the CNT height was observed to vary between 10 and 100 μm . Closer analysis of the VA-CNTs revealed that the individual tubes were not perfectly straight but consisted of wavy VA-CNTs. Although VA-CNTs were produced, all samples had some areas of randomly aligned CNTs and the majority of samples consisted exclusively of randomly aligned CNTs, such as those shown in Figure 3.20 (d).

Figure 3.21 shows both Raman spectral imaging and single spectra of the CVD grown CNT surfaces. The Raman spectrum shows a very large D-band, large G-band and small broad peaks in the overtone region ($2700 - 3300 \text{ cm}^{-1}$). Importantly, there is no observable RBM which indicates that the CNTs produced by CVD are

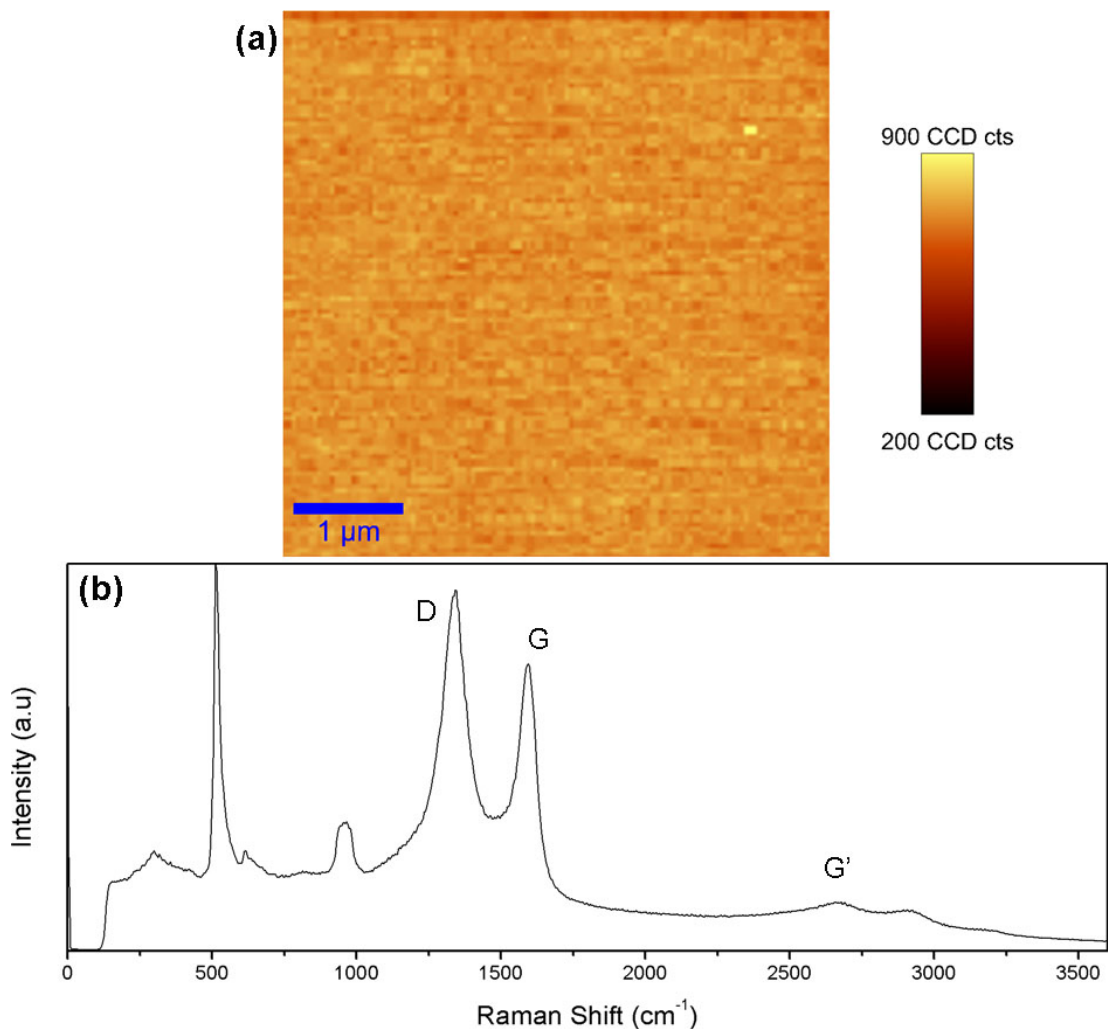


Figure 3.21: (a) Raman spectral image of CNTs grown on silicon via CVD and (b) Raman spectrum of the CVD grown CNTs. Raman spectrum is the average of 3 x 30 sec acquisitions.

MWCNTs. The large D-band indicates that there is either a lot of amorphous carbonaceous material or there is a large degree of functionalisation on the CNTs. The more likely scenario is that the large D-band is due to the production of amorphous graphitic material during CVD growth. The D/G intensity ratio for the spectrum was calculated to be 1.2 which is much larger than the 1.04 calculated for the chemically attached Si-MWCNT substrates. The Raman image obtained (Figure 3.21 (a)) shows very little variation in G-band height across the surface. This shows that the CNTs exist in a very high density across the surface.

Although the growth of CNTs was achieved, the growth of only MWCNTs and the inconsistency in vertical alignment were major issues. Two improvements were required for the surfaces to become useful for further investigation into their applications. Firstly, all the surfaces produced had to consist exclusively of VA-CNT and the CNTs grown had to be SWCNTs. The CVD growth of VA-SWCNTs is commonly reported in the literature but the reports often come from the same research groups with specialised equipment.^[60]

It is widely believed that the diameter of grown CNTs is dependent upon catalyst nanoparticle dimensions.^[61] AFM imaging of the iron catalyst layer before and after heating to 750 °C under Ar/H₂ was completed. Figure 3.22 (a) shows a 3 nm layer of iron on a silicon surface. Clumps of material are observed on the surface with heights ranging from 1 to 6 nm. Figure 3.22 (c) shows the same surface after heating to growth conditions and then removing the surface and imaging again. Much larger particles were observed with heights ranging from 10 to 40 nm which is a size increase of ~200 to 8000 %. The difference between the two AFM images clearly demonstrates that the heating of the surface induces a major change in the nanoparticle size. However, it is unknown if cooling the surface will change the nanoparticle size and shape and therefore whether the surface after cooling is a true representation of the surface prior to CNT growth. A similar investigation of the effect of CNT growth conditions (without adding carbon source) on the nanoparticles has recently been published where they found an increase in iron nanoparticle size of ~50 % after 5 min of exposure to CVD pre-treatment conditions.^[62]

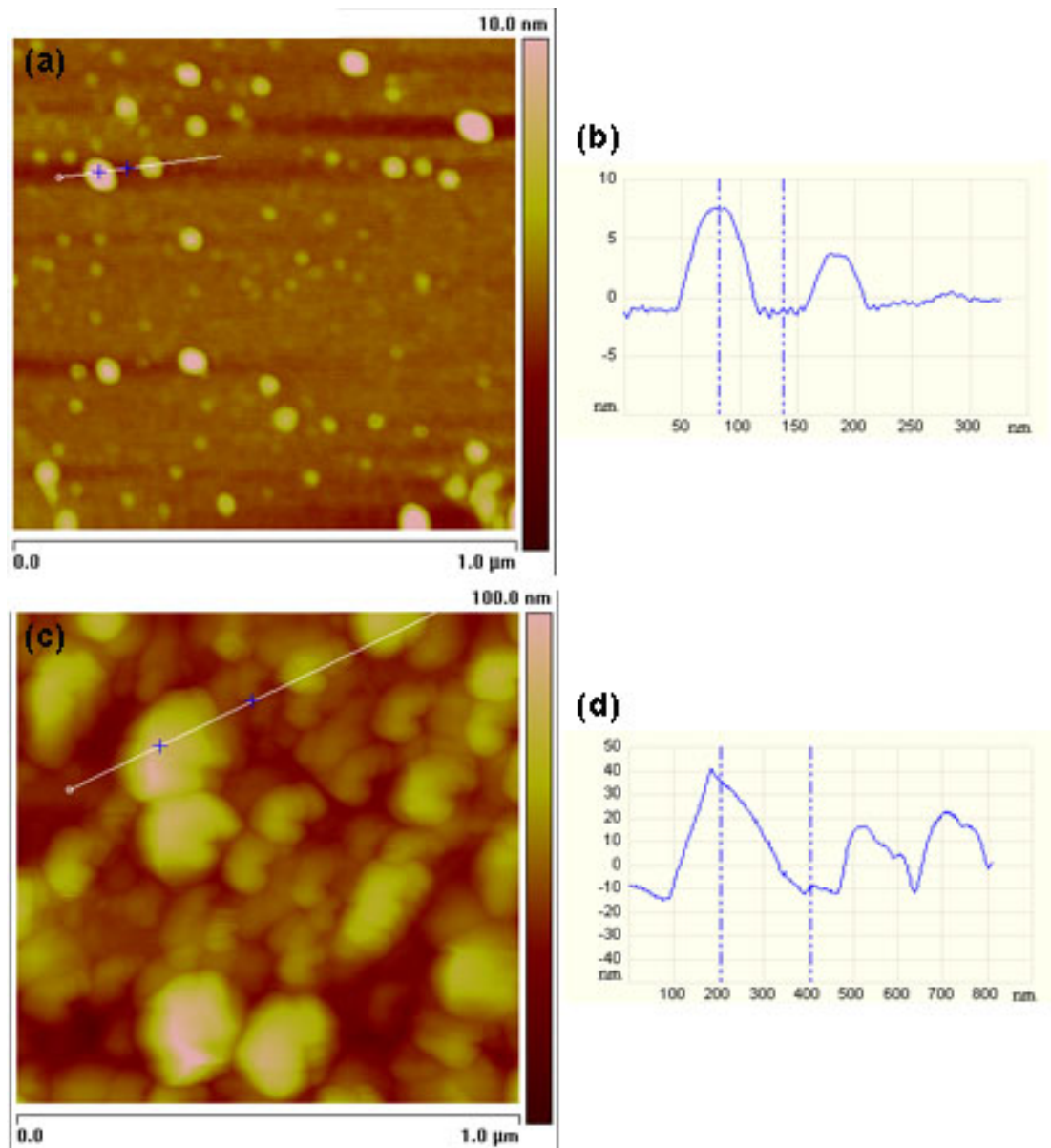


Figure 3.22: (a, c) AFM and (b, d) section analysis of 3 nm iron sputtered onto a silicon surface (a, b) fresh and (c, d) after heating to 750 °C under pre-CNT growth conditions.

The study found that adding an alumina layer between the Si and the Fe decreased the change in nanoparticle size. Therefore, 10 nm of Al was sputtered onto a cleaned silicon surface, the surface was then oxidised to convert the aluminium layer to alumina. 3 nm of Fe was deposited, and the surface was heated to 750 °C in an Ar atmosphere, cooled and imaged with the AFM the same as before. Figure 3.23 (a) shows an AFM image of the surface where particles of 5 nm to 30 nm are observed which is slightly smaller than that observed in Figure 3.22 (c) but still much larger than the original 3 nm of Fe prior to heating. To determine why the alumina layer did

not have the desired effect, AFM imaging was completed on a Si surface just after the deposition of 10 nm of Al (Figure 3.23). The surface was found to consist of 5 to 10 nm clumps of Al, not the homogeneous thin film required as a buffer layer for iron nanoparticle deposition. In order to achieve a uniform thin film of alumina a different deposition technique such as e-beam evaporation is required.

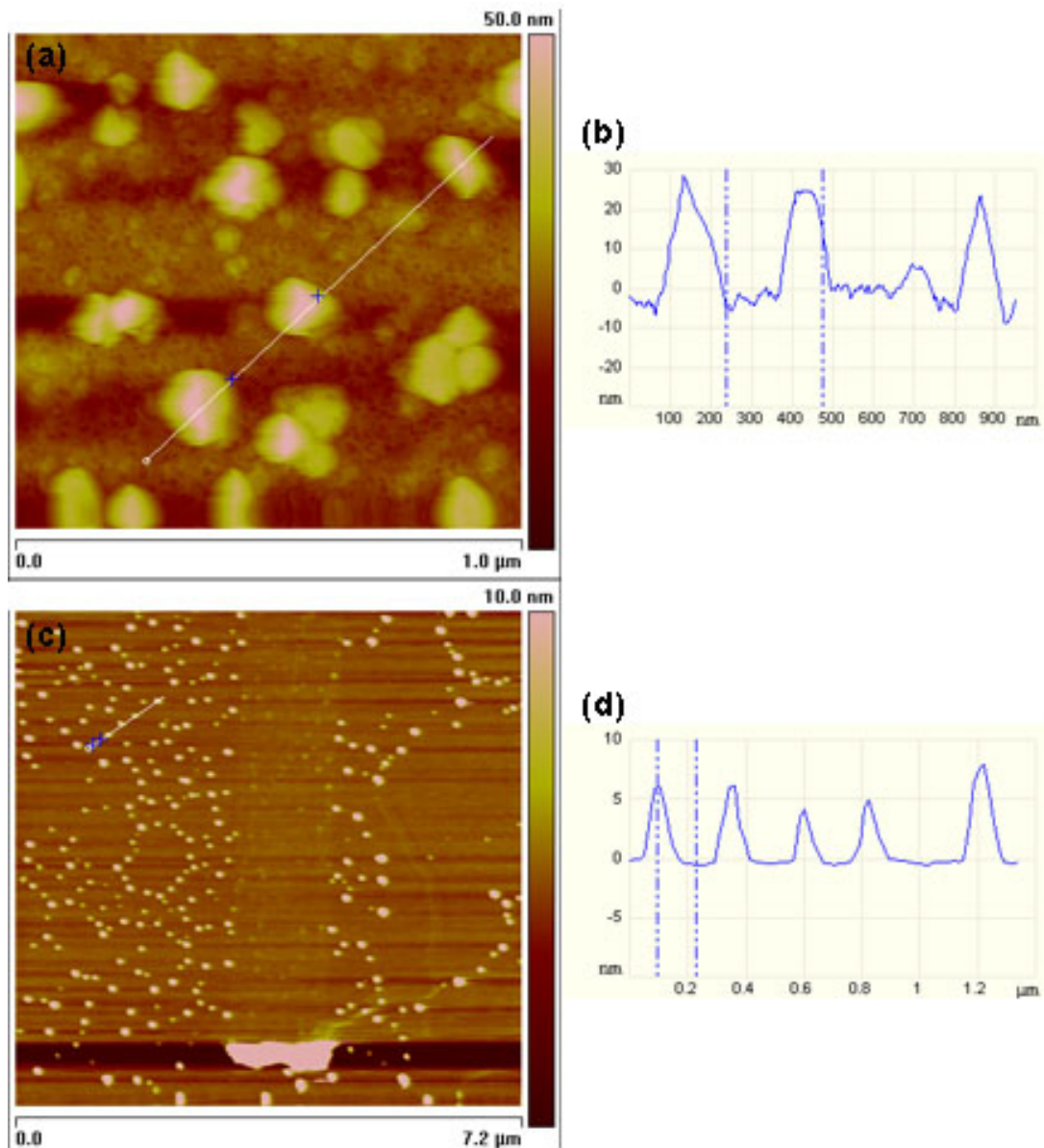


Figure 3.23: (a, c) AFM and (b, d) section analysis of (a, b) silicon surface with 10 nm of aluminium and 3 nm of iron after heating to 750 °C under pre-CNT growth conditions and (c, d) silicon surface with 10 nm of Al sputtered.

In order to understand why the vertical alignment of the CNTs was inconsistent a series of experiments was carried out to determine the cause of the inconsistency. It was hypothesised that VA-CNTs could be produced under optimised growth conditions. A number of experiments were conducted in making slight changes to the input gases and it was observed that samples closest to the gas inlet had the highest coverage of CNTs (this was found visually, the blackest samples were considered to have the highest CNT content and vertical alignment). It was concluded that this must be due to the first samples in the tube being exposed to ‘clean’ growth gas or that the temperature within the tube was not consistent. The temperature within the CVD tube was analysed using a thermocouple and it was found that the actual temperature within the tube was much higher than that set on the instrument. Figure 3.24 details the change in temperature within the CVD tube for different input temperatures. When 750 °C was set, the measured temperature varied from 767 °C 10 cm from the inlet to 830 °C in the middle of the tube. The most stable region was from 20 to 30 cm from the inlet. Since the best growth was occurring closer to the inlet, where the actual temperature was 767 °C (close to the desired temperature 750 °C), the input temperature was varied to find which input value lead to a measured temp of 750 °C within the most stable region of the tube (20 to 30 cm from inlet). An input of 680 °C was found to produce a measured temperature between 720 °C and 760 °C in the ‘stable’ region of the tube. CNT growth was carried out on multiple samples, all within the ‘stable’ region, and once again it was found that the sample closest to the gas inlet produced the highest CNT coverage. The temperature may have an effect but it was found that ‘clean’ gas was more important to CNT growth.

Subsequent growth was carried out on a single sample with an input temperature of 750 °C (because gas flow rates had been optimised for this temperature). However, with all of these constraints the consistent growth of vertically aligned CNTs still could not be achieved. The inconsistencies of CNT growth are well known in the research community. Slight changes in nanoparticle deposition, flow rate of any of the gases, heating time of the sample, CNT growth time and CNT growth temperature all lead to a change in CNT growth.^[63, 64]

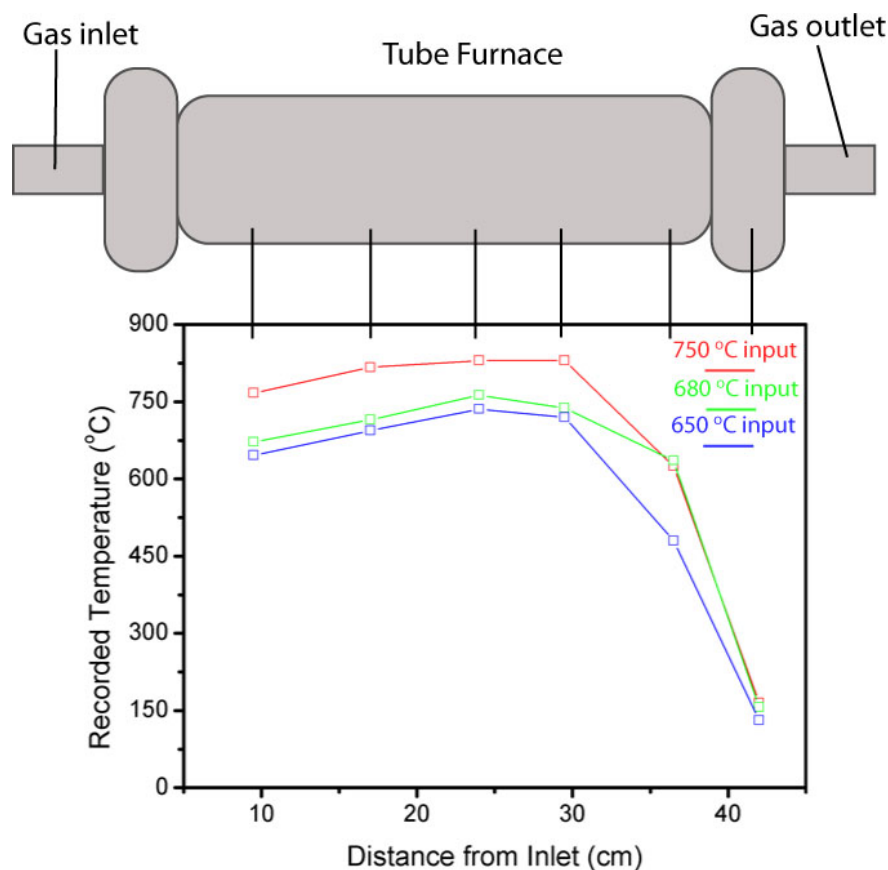


Figure 3.24: Plot showing recorded temperature within tube furnace for varying input temperatures from 750 °C (red series) to 680 °C (green series) and 650 °C (blue series).

CVD growth of CNTs is well known to be an inconsistent process. To reduce inconsistencies; precise control of sample preparation and growth conditions are required. The nanoparticle deposition and temperature could not be controlled to the accuracy required. These could be improved by the use of e-beam evaporation for nanoparticle/ buffer layer deposition and the use of better thermal shielding to maintain a constant temperature.

The scope of this Thesis is to investigate CNTs for potential applications and to improve upon already reported results. The CNT surfaces produced using the custom-built CVD reactor were not to the standard of commonly reported literature. As such no further investigations were attempted on the CVD grown CNTs.

3.7 Conclusions

CNTs were chemically functionalised to form soluble solutions in DMSO for chemical attachment to silicon. SWCNTs were chemically attached to silicon and pSi and it was found that the direct ester attachment on silicon and the APTES mediated attachment on silicon and pSi lead to a high coverage of vertically aligned SWCNTs. DWCNTs were attached to silicon following the direct ester protocol. In this case, both vertical and horizontal attachment occurred. MWCNTs were chemically attached to silicon where exclusive horizontal geometry was observed. The increase in horizontal alignment of the MWCNTs and DWCNTs was explained in terms of increased side-wall functionalisation.

CVD was used to grow both vertically aligned and randomly aligned CNTs. Control of alignment and diameter was not achieved and as such CVD growth of CNTs was abandoned.

In the following chapters, the pSi-SWCNT substrates will be further investigated for water filtration and biomaterial immobilisation. The applicability of the Si-SWCNT substrates in the applications of field emission and biomaterial immobilisation will be studied and the field emission properties of the Si-DWCNT and Si-MWCNT substrates will be explored.

3.8 References

- [1] C. T. Gibson, S. Carnally, and C. J. Roberts, "Attachment of carbon nanotubes to atomic force microscope probes", *Ultramicroscopy*, **107** (10-11), 1118-22 (2007).
- [2] J. H. Hafner, C.-L. Cheung, T. H. Oosterkamp, and C. M. Lieber, "High-Yield Assembly of Individual Single-Walled Carbon Nanotube Tips for Scanning Probe Microscopies", *The Journal of Physical Chemistry B*, **105** (4), 743-6 (2001).
- [3] E. Frackowiak, and F. Béguin, "Electrochemical storage of energy in carbon nanotubes and nanostructured carbons", *Carbon*, **40** (10), 1775-87 (2002).
- [4] G. Gundiah, A. Govindaraj, N. Rajalakshmi, K. S. Dhathathreyan, *et al.*, "Hydrogen storage in carbon nanotubes and related materials", *Journal of Materials Chemistry*, **13** (2), 209-13 (2003).
- [5] G.-P. Dai, C. Liu, M. Liu, M.-Z. Wang, *et al.*, "Electrochemical Hydrogen Storage Behavior of Ropes of Aligned Single-Walled Carbon Nanotubes", *Nano Letters*, **2** (5), 503-6 (2002).
- [6] J. J. Gooding, R. Wibowo, J. Liu, W. Yang, *et al.*, "Protein Electrochemistry Using Aligned Carbon Nanotube Arrays", *Journal of the American Chemical Society*, **125**, 9006-7 (2003).
- [7] J. Yu, J. G. Shapter, M. R. Johnston, J. S. Quinton, *et al.*, "Electron-transfer characteristics of ferrocene attached to single-walled carbon nanotubes (SWCNT) arrays directly anchored to silicon(100)", *Electrochimica Acta*, **52**, 6206-11 (2007).
- [8] C. J. Shearer, J. G. Shapter, J. S. Quinton, P. C. Dastoor, *et al.*, "Highly resilient field emission from aligned single walled carbon nanotube arrays chemically attached to n-type silicon", *Journal of Materials Chemistry*, **18**, 5753 - 60 (2008).
- [9] W. S. Kim, J. Lee, T. W. Jeong, J. N. Heo, *et al.*, "Improved emission stability of single-walled carbon nanotube field emitters by plasma treatment", *Applied Physics Letters*, **87**, 163112 (2005).
- [10] M. J. Kim, E. Haroz, Y. Wang, H. Shan, *et al.*, "Nanoscopically Flat Open-Ended Single-Walled Carbon Nanotube Substrates for Continued Growth", *Nano Letters*, **7** (1), 15-21 (2007).
- [11] E. Ben-Jacob, and Y. Hanein, "Carbon nanotube micro-electrodes for neuronal interfacing", *Journal of Materials Chemistry*, **18** (43), 5181-6 (2008).
- [12] Y. Inoue, H. Fujimoto, T. Ogino, and H. Iwata, "Site-specific gene transfer with high efficiency onto a carbon nanotube-loaded electrode", *Journal of The Royal Society Interface*, **5** (25), 909-18 (2008).
- [13] L. P. Zanello, B. Zhao, H. Hu, and R. C. Haddon, "Bone Cell Proliferation on Carbon Nanotubes", *Nano Letters*, **6** (3), 562-7 (2006).
- [14] M. Majumder, N. Chopra, R. Andrews, and B. J. Hinds, "Enhanced flow in carbon nanotubes", *Nature*, **438**, 44 (2005).
- [15] B. J. Hinds, N. Chopra, T. Rantell, R. Andrews, *et al.*, "Aligned Multiwalled Carbon Nanotube Membranes", *Science*, **303**, 62 (2004).
- [16] J. Holt, H. Park, Y. Wang, M. Stadermann, *et al.*, "Fast Mass Transport Through Sub-2-Nanometer Carbon Nanotubes", *Science*, **312**, 1034 (2006).

- [17] K. T. Constantopoulos, C. J. Shearer, A. V. Ellis, N. H. Voelcker, *et al.*, "Carbon Nanotubes Anchored to Silicon for Device Fabrication", *Advanced Materials*, **22** (5), 557-71 (2010).
- [18] L. Qu, F. Du, and L. Dai, "Preferential Syntheses of Semiconducting Vertically Aligned Single-Walled Carbon Nanotubes for Direct Use in FETs", *Nano Letters*, **8** (9), 2682-7 (2008).
- [19] S. Chakrabarti, K. Gong, and L. Dai, "Structural Evaluation along the Nanotube Length for Super-long Vertically Aligned Double-Walled Carbon Nanotube Arrays", *The Journal of Physical Chemistry C*, **112** (22), 8136-9 (2008).
- [20] T. Yamada, T. Namai, K. Hata, D. N. Futaba, *et al.*, "Size-selective growth of double-walled carbon nanotube forests from engineered iron catalysts", *Nature Nanotechnology*, **1** (2), 131-6 (2006).
- [21] M. Endo, K. Takeuchi, S. Igarashi, K. Kobori, *et al.*, "The production and structure of pyrolytic carbon nanotubes (PCNTs)", *Journal of Physics and Chemistry of Solids*, **54** (12), 1841-8 (1993).
- [22] C. Bower, W. Zhu, S. Jin, and O. Zhou, "Plasma-induced alignment of carbon nanotubes", *Applied Physics Letters*, **77** (6), 830-2 (2000).
- [23] H. L. Young, H. A. Kay, S. P. Jin, Y. Cheol-Min, *et al.*, "A Diameter-Selective Attack of Metallic Carbon Nanotubes by Nitronium Ions", *Journal of the American Chemical Society*, **127**, 5196-203 (2005).
- [24] B. Neises, and W. Steglich, "Simple Method for the Esterification of Carboxylic Acids", *Angewandte Chemie International Edition in English*, **17** (7), 522-4 (1978).
- [25] B. Wu, J. Zhang, Z. Wei, S. Cai, *et al.*, "Chemical Alignment of Oxidatively Shortened Single-Walled Carbon Nanotubes on Silver Surface", *The Journal of Physical Chemistry B*, **105** (22), 5075 (2001).
- [26] Z. Liu, Z. Shen, T. Zhu, S. Hou, *et al.*, "Organizing Single-Walled Carbon Nanotubes on Gold Using a Wet Chemical Self-Assembling Technique", *Langmuir*, **16** (8), 3569-73 (2000).
- [27] M.-S. Jung, Y. K. Ko, D.-H. Jung, D. H. Choi, *et al.*, "Electrical and field-emission properties of chemically anchored single-walled carbon nanotube patterns", *Applied Physics Letters*, **87**, 013114 (2005).
- [28] J. Yu, J. G. Shapter, J. S. Quinton, M. R. Johnston, *et al.*, "Direct attachment of well-aligned single-walled carbon nanotube architectures to silicon (100) surfaces: a simple approach for device assembly", *Physical Chemistry Chemical Physics*, **9**, 510-20 (2007).
- [29] J. Yu, D. Losic, M. Marshall, T. B. John, *et al.*, "Preparation and characterisation of an aligned carbon nanotube array on the silicon (100) surface", *Soft Matter*, **2**, 1081-8 (2006).
- [30] B. S. Flavel, J. Yu, J. G. Shapter, and J. S. Quinton, "Patterned attachment of carbon nanotubes to silane modified silicon", *Carbon*, **45**, 2551-8 (2007).
- [31] M. Marshall, S. Popa-Nita, and J. G. Shapter, "Measurement of functionalised carbon nanotube carboxylic acid groups using a simple chemical process", *Carbon*, **44**, 1137-41 (2006).
- [32] D. K. Aswal, S. Lenfant, D. Guerin, J. V. Yakhmi, *et al.*, "Self assembled monolayers on silicon for molecular electronics", *Analytica Chimica Acta*, **568** (1-2), 84-108 (2006).

- [33] J. Liu, M. J. Casavant, M. Cox, D. A. Walters, *et al.*, "Controlled deposition of individual single-walled carbon nanotubes on chemically functionalized templates", *Chemical Physics Letters*, **303**, 125-9 (1999).
- [34] B. Chen, M. Gao, J. M. Zuo, S. Qu, *et al.*, "Binding energy of parallel carbon nanotubes", *Applied Physics Letters*, **83** (17), 3570-1 (2003).
- [35] B. S. Flavel, J. Yu, J. G. Shapter, and J. S. Quinton, "Electrochemical characterisation of patterned carbon nanotube electrodes on silane modified silicon", *Electrochimica Acta*, **53** (18), 5653-9 (2008).
- [36] M. A. Bissett, and J. G. Shapter, "Photocurrent Response from Vertically Aligned Single-Walled Carbon Nanotube Arrays", *The Journal of Physical Chemistry C*, **114** (14), 6778-83 (2010).
- [37] D. D. Tune, B. S. Flavel, J. S. Quinton, A. V. Ellis, *et al.*, "Single walled carbon nanotube network electrodes for dye solar cells", *Solar Energy Materials and Solar Cells*, **94** (10), 1665-72 (2010).
- [38] J. Yu, B. S. Flavel, and J. G. Shapter, "Optical and Electrochemical Properties of Single-walled Carbon Nanotube Arrays Attached to Silicon (100) Surfaces", *Fullerenes, Nanotubes and Carbon Nanostructures*, **16** (1), 18 - 29 (2008).
- [39] J. Yu, S. Mathew, B. S. Flavel, M. R. Johnston, *et al.*, "Ruthenium Porphyrin Functionalized Single-Walled Carbon Nanotube Arrays-A Step Toward Light Harvesting Antenna and Multibit Information Storage", *Journal of the American Chemical Society*, **130** (27), 8788-96 (2008).
- [40] I. Langmuir, "The Adsorption Of Gases On Plane Surfaces of Glass, Mica and Platinum", *Journal of the American Chemical Society*, **40** (9), 1361-403 (1918).
- [41] M. S. Dresselhaus, G. Dresselhaus, R. Saito, and A. Jorio, "Raman spectroscopy of carbon nanotubes", *Physics Reports-Review Section of Physics Letters*, **409** (2), 47-99 (2005).
- [42] D. A. Heller, P. W. Barone, J. P. Swanson, R. M. Mayrhofer, *et al.*, "Using Raman Spectroscopy to Elucidate the Aggregation State of Single-Walled Carbon Nanotubes", *The Journal of Physical Chemistry B*, **108** (22), 6905-9 (2004).
- [43] M. Sweetman, S. D. Graney, and N. H. Voelcker, "Interfacing porous silicon with biomolecules", *SPIE Smart Materials, Nano+Micro-Smart Systems*, **6799** (BioMEMS and Nanotechnology III), 679907 (2007).
- [44] S. P. Low, K. A. Williams, L. T. Canham, and N. H. Voelcker, "Evaluation of mammalian cell adhesion on surface-modified porous silicon", *Biomaterials*, **27** (26), 4538-46 (2006).
- [45] L. C. P. M. deSmet, H. Zuilhof, E. J. R. Sudholter, L. H. Lie, *et al.*, "Mechanism of the Hydrosilylation Reaction of Alkenes at Porous Silicon: Experimental and Computational Deuterium Labeling Studies", *The Journal of Physical Chemistry B*, **109** (24), 12020-31 (2005).
- [46] J. T. C. Wojtyk, K. A. Morin, R. Boukherroub, and D. D. M. Wayner, "Modification of Porous Silicon Surfaces with Activated Ester Monolayers", *Langmuir*, **18** (16), 6081-7 (2002).
- [47] D. Xu, L. Sun, H. Li, L. Zhang, *et al.*, "Hydrolysis and silanization of the hydrosilicon surface of freshly prepared porous silicon by an amine catalytic reaction", *New Journal of Chemistry*, **27** (2), 300-6 (2003).
- [48] L. Canham, "Properties of Porous Silicon", *The Institution of Electrical Engineers*, London, United Kingdom, (1997).

- [49] P. Hoffmann, and J. A. Lobo, "Identification of diverse silanols on protonated ZSM-5 zeolites by means of FTIR spectroscopy", *Microporous and Mesoporous Materials*, **106** (1-3), 122-8 (2007).
- [50] M. Cazacu, G. Munteanu, C. Racles, A. Vlad, *et al.*, "New ferrocene-containing structures: Poly(silyl ester)s", *Journal of Organometallic Chemistry*, **691** (17), 3700-7 (2006).
- [51] T. Uchino, N. Kurumoto, and N. Sagawa, "Structure and formation mechanism of blue-light-emitting centers in silicon and silica-based nanostructured materials", *Physical Review B (Condensed Matter and Materials Physics)*, **73** (23), 233203-4 (2006).
- [52] M. Wang, J. M. Weinberg, and K. L. Wooley, "Synthesis, Characterization and Degradation of Poly(silyl ester)s", *Macromolecules*, **31** (22), 7606-12 (1998).
- [53] M. Wang, J. M. Weinberg, and K. L. Wooley, "Geminal poly(silyl ester)s: Highly labile degradable polymers", *Journal of Polymer Science Part A: Polymer Chemistry*, **37** (18), 3606-13 (1999).
- [54] B. H. Stuart, "Infrared Spectroscopy: Fundamentals and Applications", *Wiley-VCH*, Chichester, England, (2004).
- [55] V. K. S. Hsiao, J. R. Waldeisen, Y. Zheng, P. F. Lloyd, *et al.*, "Aminopropyltriethoxysilane (APTES)-functionalized nanoporous polymeric gratings: fabrication and application in biosensing", *Journal of Materials Chemistry*, **17** (46), 4896-901 (2007).
- [56] Y. Saito, T. Nakahira, and S. Uemura, "Growth Conditions of Double-Walled Carbon Nanotubes in Arc Discharge", *The Journal of Physical Chemistry B*, **107** (4), 931-4 (2003).
- [57] L. Alvarez, A. Righi, T. Guillard, S. Rols, *et al.*, "Resonant Raman study of the structure and electronic properties of single-wall carbon nanotubes", *Chemical Physics Letters*, **316** (3-4), 186-90 (2000).
- [58] H. L. Young, S. Kwanyong, A. P. Kyung, K. Changwook, *et al.*, "Chirality- and Diameter-Dependent Reactivity of NO₂ on Carbon Nanotube Walls", *Journal of the American Chemical Society*, **127**, 15724-9 (2005).
- [59] A. V. Ellis, and A. Bubendorfer, "Raman scattering analysis of changes induced by chemical treatment of double-walled carbon nanotubes", *Chemical Physics Letters*, **412** (4-6), 449-53 (2005).
- [60] K. Hasegawa, and S. Noda, "Millimeter-Tall Single-Walled Carbon Nanotubes Rapidly Grown with and without Water", *ACS Nano*, **5** (3), 975-84 (2011).
- [61] Y. Li, W. Kim, Y. Zhang, M. Rolandi, *et al.*, "Growth of Single-Walled Carbon Nanotubes from Discrete Catalytic Nanoparticles of Various Sizes", *The Journal of Physical Chemistry B*, **105** (46), 11424-31 (2001).
- [62] P. B. Amama, C. L. Pint, S. M. Kim, L. McJilton, *et al.*, "Influence of Alumina Type on the Evolution and Activity of Alumina-Supported Fe Catalysts in Single-Walled Carbon Nanotube Carpet Growth", *ACS Nano*, **4** (2), 895-904 (2010).
- [63] M. J. Bronikowski, H. M. Manohara, and B. D. Hunt, "Growth of carbon nanotube bundle arrays on silicon surfaces", *Journal of Vacuum Science & Technology A*, **24**, 1318 (2006).
- [64] P. T. A. Reilly, and W. B. Whitten, "The role of free radical condensates in the production of carbon nanotubes during the hydrocarbon CVD process", *Carbon*, **44** (9), 1653-60 (2006).

Chapter 4

Controlled carbon nanotube placement

To further investigate the chemical attachment of SWCNTs to silicon, two types of surfaces were prepared to control the placement of nanotubes on the substrate: SWCNT patterns and SWCNT gradients. Surface patterning of SWCNTs is a prerequisite for a number of applications. The patterning of SWCNTs on silicon has been achieved via the pre-patterning of an amino silane layer prior to SWCNT chemical attachment. Since there is likely to be an optimal SWCNT surface coverage for each individual application, the most efficient method to determine the optimal coverage is to produce a gradient of SWCNTs to investigate all possible coverage's on a single substrate. SWCNT gradients were fabricated by using a topographical pSi pore size gradient and chemical APTES gradient on silicon.

4.1 Introduction

The use of CNTs in a range of applications requires the control of their placement, orientation and coverage.^[1] In particular, CNT surface coverage has been found to have a profound effect in applications including photovoltaics,^[2] cell adhesion,^[3] and thin-film transistors.^[4] In order to optimise the CNT surface coverage, it is important to develop methods for placing CNTs into well-defined environments. Creating such surface environments has been pursued intensely by means of techniques such as lithographically designed catalyst placement for CVD growth,^[5-7] soft lithography manipulation of CVD grown CNTs,^[8] inkjet printing of CNT solutions,^[9] and CNT adsorption or chemical attachment onto lithographically designed surface patterns^[10-12] in order to accomplish the goal of controlled CNT coverage.

The production of chemically attached SWCNT patterns has been achieved by a number of various substrate pre-patterning techniques including AFM nanolithography^[10, 13] e-beam lithography^[14] and sputtering of metals through a TEM grid.^[12] These methods have successfully controlled the placement of SWCNTs, however, the nanolithography method is time consuming and the sputtering of metal leads to an inhomogenous substrate which restricts further use.

All of the methods of organising CNTs into specific architectures are potentially useful in practical applications. However, they always result in sharp boundaries between regions covered with CNTs and those which are bare. In order to optimise CNT coverage it is useful to employ a platform where the coverage of CNTs varies gradually across the entire length of the surface.

Such lateral gradients of coverage have been described for a multitude of species including biomolecules,^[15] nanoparticles,^[16, 17] macromolecules,^[18, 19] and SAMs.^[20-22] These gradients are typically fabricated by first generating a gradient of a desired surface chemistry or by gradually changing the topography of a surface.^[23] These surfaces are then reacted with the desired species to produce gradients of coverage of that species.

The production of topographical gradients on pSi has recently been reported.^[15, 24, 25] Pore size gradients can be achieved by orienting the counter electrode perpendicular to the Si surface during pSi formation.^[24] In this orientation, the

potential at the solid silicon/solution interface decreases as a function of distance from the counter electrode due to the resistance of the solution. The decrease in applied potential across the surface leads to a decrease in etching current resulting in a decrease in pore size across the surface. The resulting surface consists of large diameter pores in the area near the counter electrode and pores gradually decreasing in diameter when moving away from the counter electrode.^[15, 24] Pore size gradients have previously been utilised to study the influence of surface topography upon the behaviour of neuroblastoma cells when adsorbed on the surface.^[15] Pores ranging from 5 nm to 3 μm were prepared on a single Si piece and it was found that the pore size had a profound effect on cell morphology, density, length and area.^[15]

Surface chemistry gradients can be achieved by a number of strategies^[23] including masked palladium deposition,^[26] controlled immersion and withdrawal of a surface into a solution,^[27] the liquid diffusion techniques,^[28, 29] RF plasma,^[30, 31] and the vapour phase diffusion method.^[22] Of these, possibly the most popular method is vapour phase diffusion, which was first developed by Chaudhury and Whitesides in 1992^[22] and involves placing an oxidised Si wafer near a reservoir containing a volatile low molecular weight organosilane. The silane molecules vaporise and form a concentration gradient in the vapour phase and eventually land on the substrate and chemisorb by reacting with the surface hydroxyl groups. By restricting the deposition time, the concentration of the deposited silane was observed to decrease as a function of the distance from the silane source.^[15]

CNT attachment to an aminosilane gradient, which had been produced using the vapour phase diffusion method, has been attempted previously by Usrey *et al.*^[27] In this seminal study, SWCNTs modified with benzoic acid and phenol functionalities were reacted with a surface gradient of aminosilane (APTES). It was found that although an APTES gradient was generated along the surface, there was low coverage of SWCNTs across the gradient, and no modulation in coverage was observed.^[27]

In this Chapter, the fabrication of SWCNT patterns and gradients will be investigated. Patterns are produced by first pre-patterning the surface with an APTES pattern defined by photolithography (Figure 4.1 (a)). Gradients of immobilised SWCNT coverage are then generated utilising both topographical and chemical surface gradients. Pore size gradients from pSi are used as a topographical gradient,

where the pSi surface is oxidised and treated with APTES to create an aminosilane layer. Carboxylated SWCNTs are then deposited upon the surface, and the change in the area of the top surface with change in pore size gives rise to a gradient in SWCNT coverage (Figure 4.1 (b)). The chemical gradient was created by vapour phase diffusion of APTES onto oxidised flat silicon. The surface gradient of aminosilane was then utilised to deposit SWCNTs (Figure 4.1 (c)).

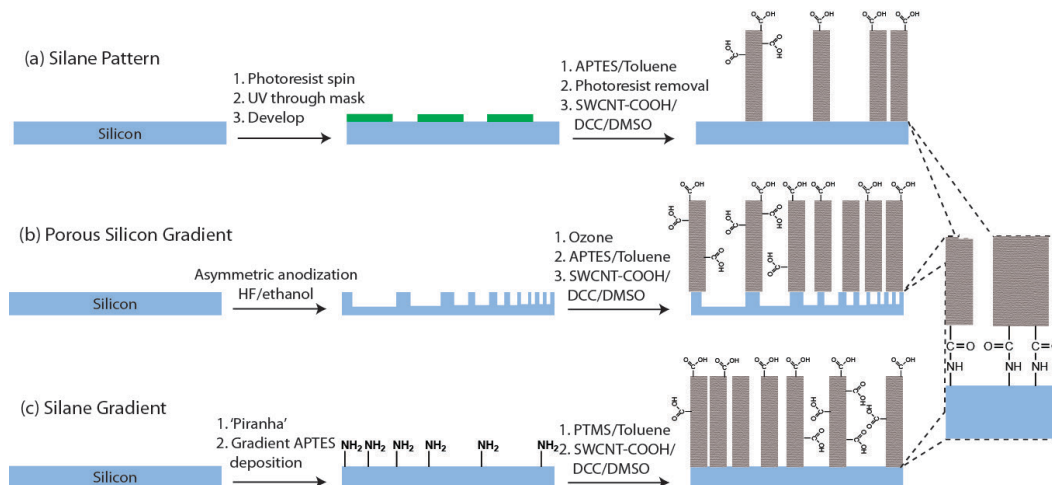


Figure 4.1: Schematic illustrating the fabrication process of SWCNT patterns and gradients. (a) APTES patterning via photolithography to produce a SWCNT gradient, (b) a topographical gradient created by the asymmetric anodisation of silicon and (c) a chemical gradient created by vapour phase diffusion of APTES onto oxidised silicon.

4.2 Experimental methods

4.2.1 Fabrication of pSi with pore size gradient

The preparation of pSi with a pore size gradient has been described previously.^[15] Briefly, silicon (100 orientation, boron doped, 0.00055 – 0.001 Ω cm resistivity, Virginia Semiconductor) was etched in a 1:1 (v/v) solution of 49 % aqueous HF (Merck)/ethanol (Chem-Supply) for 90 sec by placing a Pt electrode perpendicular to the silicon surface at one end of a custom-built Teflon etching cell (Figure 4.2). Currents of 40, 50, 55, and 60 mA over a surface area of 1.767 cm² were applied. After etching, pSi oxidation, APTES deposition and SWCNT attachment were carried out following the same methods as for ‘normal’ pSi, as described earlier (Section 2.2.3).

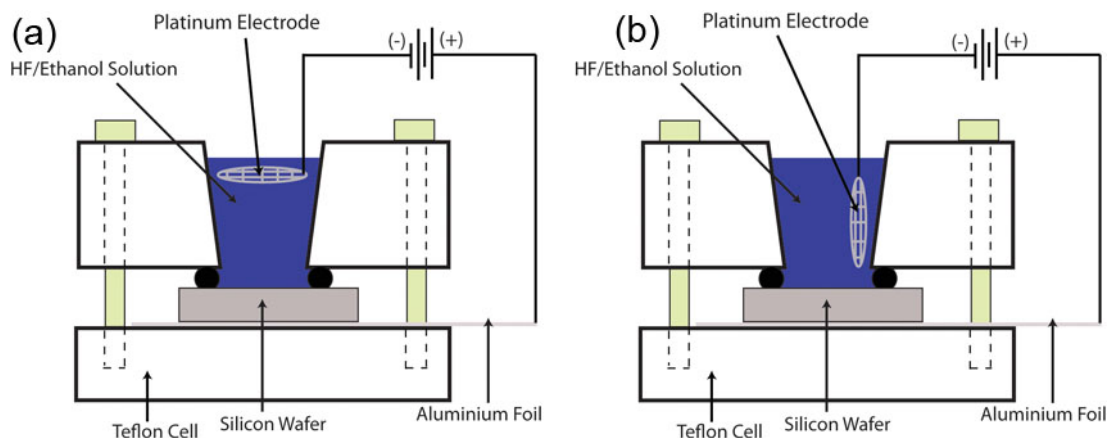


Figure 4.2: Etching cell configurations for the fabrication of ‘normal’ (left) and gradient (right) pSi.

4.2.2 Fabrication of an APTES gradient

A silane gradient was created using the method first described by Chaudhury and Whitesides.^[16, 22] A Si wafer was cut into rectangular pieces (3.5 cm x 1 cm) which were then treated with Piranha solution (3:1 H₂SO₄:H₂O₂) for 20 min at 80 °C. A 1:1 (w/w) mixture of APTES and Nujol was prepared and kept in a small circular reservoir (400 μ L volume). This reservoir was placed next to the shorter edge of the rectangular piece of the silicon wafer, and the whole system was enclosed in a Petri dish at ambient conditions (Figure 4.3). After 10 min, the silicon wafer was taken out

of the container, washed with ethanol to remove any physisorbed APTES molecules, and immersed a solution 1 % (v/v) trimethoxypropylsilane (PTMS, 97 %, Aldrich) in toluene for 10 min in order to occupy the remaining surface silanol groups and prevent non-specific SWCNT attachment. SWCNT covalent attachment was then carried out following the standard method (Section 2.3).

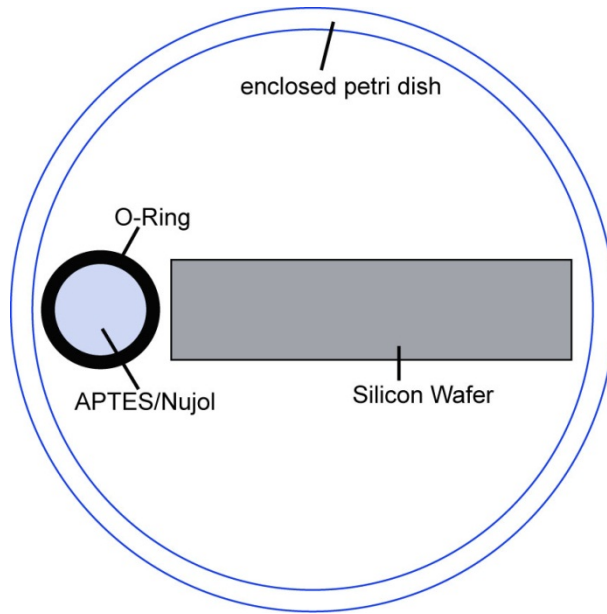


Figure 4.3: Schematic of the apparatus used for APTES gradient fabrication (top view).

4.3 Patterned attachment of SWCNTs

SWCNT patterning was achieved by means of silane substrate patterning as described in Section 2.3.5. Patterning via photolithography of a commercial photoresist was chosen as it is a method that is easily replicable in most scientific laboratories and is capable of quickly patterning entire surfaces. This was achieved by first spin-coating a photoresist, developing the resist using a chrome-on-glass mask and depositing APTES in the exposed areas. This was possible because the commercial photoresist used was found to be stable in toluene, which is the solvent used in silane deposition. The mask used for UV photolithography consisted of a variety of shapes with a range of sizes from 10 - 200 μm . After photoresist development, the surface consisted of exposed patterns of oxidised Si and areas protected by photoresist (Figure 4.4).

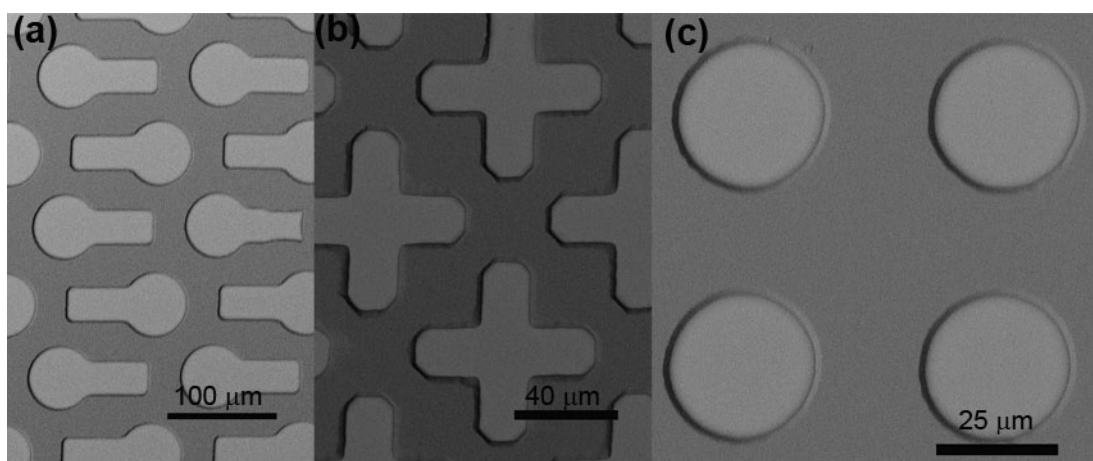


Figure 4.4: SEM images of photoresist patterns on silicon showing various shapes and sizes of patterns.

Subsequent attachment of APTES into the patterned regions was verified by IR microscopy. The patterning procedure allows for the deposition of two silanes, one in the patterned region and the other outside the patterns. The IR spectra in Figure 4.5 (a, b) and IR mapping image are of APTES-functionalised circles with oxidised silicon outside of the pattern. This particular patterning procedure was chosen to afford the highest contrast. In order to achieve IR mapping, pSi was used as the substrate since the high internal surface area of pSi leads to a higher amount of deposited silane than on flat silicon. Additionally, the photoresist developing process

in ammonium hydroxide solution slightly degrades the pSi, which allows the visual observation of the patterned regions, making the IR mapping easier (Figure 4.5 (d)). IR spectra obtained both inside (Figure 4.5 (a)) and outside (Figure 4.5 (b)) the patterns are quite similar. This is because the small aperture (80 μm) required to achieve the resolution of the IR map results in low signal. Consequently, the only difference in spectra observed is the appearance of a doublet of peaks at 1505 cm^{-1} and 1450 cm^{-1} which are related to the amine functionality in APTES.^[32] The most prominent peaks are the broad -OH stretching band at $\sim 3400\text{ cm}^{-1}$ and the strong Si-O- feature at 1100 cm^{-1} . Spectral mapping of patterns was achieved by taking a number of spectra across the surface and mapping the height of the peak at 1505 cm^{-1} . The IR spectral map shown in Figure 4.5 (c) clearly demonstrates that the APTES is confined within the circle patterned region, since the pattern observed in the IR spectral map matches the optical microscope image of the surface (Figure 4.5 (c – f)).

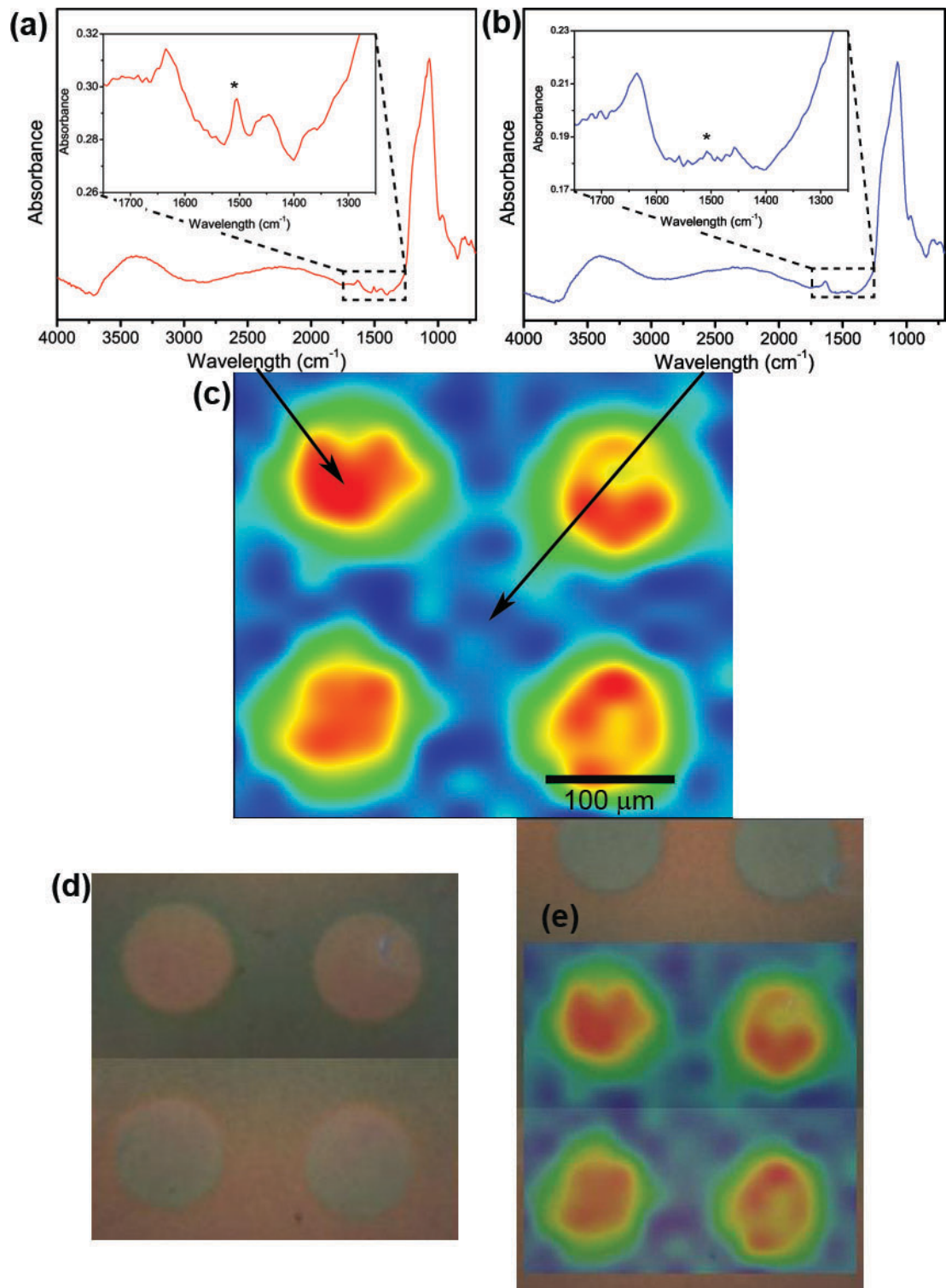


Figure 4.5: IR mapping of APTES pattern on pSi showing (a, b) spectra of points (a) within and (b) outside of pattern (insets) with insets showing peaks of interest in more detail, (c) IR spectral map obtained by mapping peak height at 1505 cm⁻¹ (indicated by * in (a, b)) with (d) optical image of area and (e) overlay of spectral map over optical image.

Raman spectral imaging was used to investigate the controlled placement of SWCNTs on silicon. Flat silicon was used for the Raman imaging as the large background fluorescence from pSi leads to a low signal to noise ratio for the Raman peaks. The intensity of the G-band in each spectrum within a scan was digitally converted into an image where the bright regions indicate areas of higher G-band intensity. The intensity of the G-band was used because it is the most prominent of the SWCNT peaks and has also been considered to best represent the amount of CNTs present in a sample.^[33] To investigate patterned SWCNT attachment, two APTES patterns were produced on silicon. A half-half pattern and the geometric pattern shown in Figure 4.4 were fabricated. The half-half pattern was produced in order to ascertain if SWCNTs could be controlled over a larger area before it was attempted to confine the SWCNTs to smaller regions. Figure 4.6 (a, b) show Raman spectral images obtained for the half-half pattern with Figure 4.6 (a) representing the APTES-free region and Figure 4.6 (b) from the APTES covered area. The APTES side of the substrate clearly shows a higher SWCNT coverage confirming controlled SWCNT placement is possible by APTES patterning. The bare silicon side of the substrate did not completely prevent SWCNT attachment. This could be improved by depositing a silane which restricts SWCNT adsorption outside the patterned region.

Figure 4.6 (d, e) shows a Raman spectral image after SWCNT attachment to an APTES pattern on a flat silicon surface. The optical image in Figure 4.6 (c) shows the area investigated. No visible pattern is discernable. In order to determine the correct area to image, the surface was rinsed in acetone and dried slowly, the difference in surface energy on the surface resulted in the acetone drying slower in the patterned regions. This allowed for short-term visualisation of the patterns during which time marks were made around the ‘small circle’ patterned area. Raman imaging of this area revealed that the circle pattern had been maintained after SWCNT deposition Figure 4.6 (d, e). The circle patterns are the smallest on the original mask and the SWCNT placement is maintained within the pattern region.

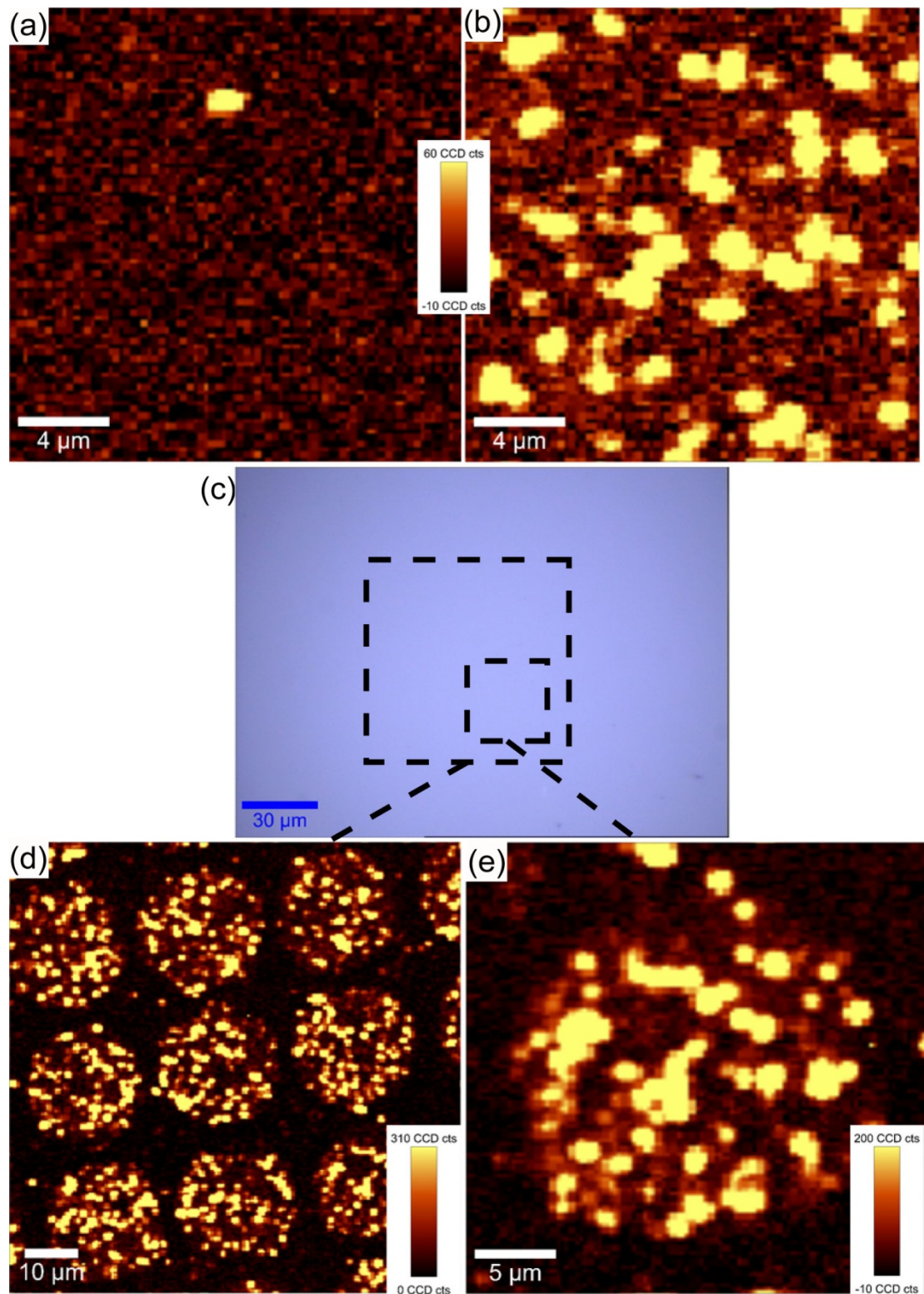


Figure 4.6: Raman spectral images of SWCNT patterns on silicon. (a, b) half-half surface patterns with (a) bare silicon side and (b) Si-APTES-SWCNT side. (c) Optical microscope image of area of investigation for attachment of (c, d) SWCNTs to patterned APTES on silicon.

With a desired pattern designed on a chrome-on-glass mask, the patterning process described here has the potential to produce patterns of any shape down to features in the region of 20 μm , limited by the quality of the original photoresist pattern. The use of more sophisticated patterning processes such as e-beam lithography could lead to smaller feature sizes. The SWCNT surface patterning could be useful in the fabrication of field emission displays, nano-electronics, and biointerfaces.

4.4 SWCNT surface coverage gradients

4.4.1 pSi topographical gradient

Several pore size gradients with different pore size ranges were fabricated in order to determine the effect of pore size on SWCNT surface coverage over a wide spectrum of pore sizes. Current density was varied to generate four different pore size regimes. Only the region closest to the electrode for the 60 mA etching current underwent electropolishing with the applied current density being too high to sustain pore formation. Once etched, the pSi films showed interference fringe patterns common to pore size/depth changes across the surface (Figure 4.7 (a)).^[15] The topography of the graded pSi films was characterised using tapping mode AFM. pSi films were divided into three different regions, as shown in Figure 4.7 (a). The region nearest to the Pt electrode is denoted region 1 and the region furthest away from the Pt electrode is denoted region 3. Figure 4.7 (b) shows representative AFM images of the gradient pSi films created where the pore size decreases from region 1, to region 2 and decreases again to region 3. Table 4.1 shows the range and average pore sizes fabricated with varying etching current. Average pore sizes ranged from 9 – 230 nm

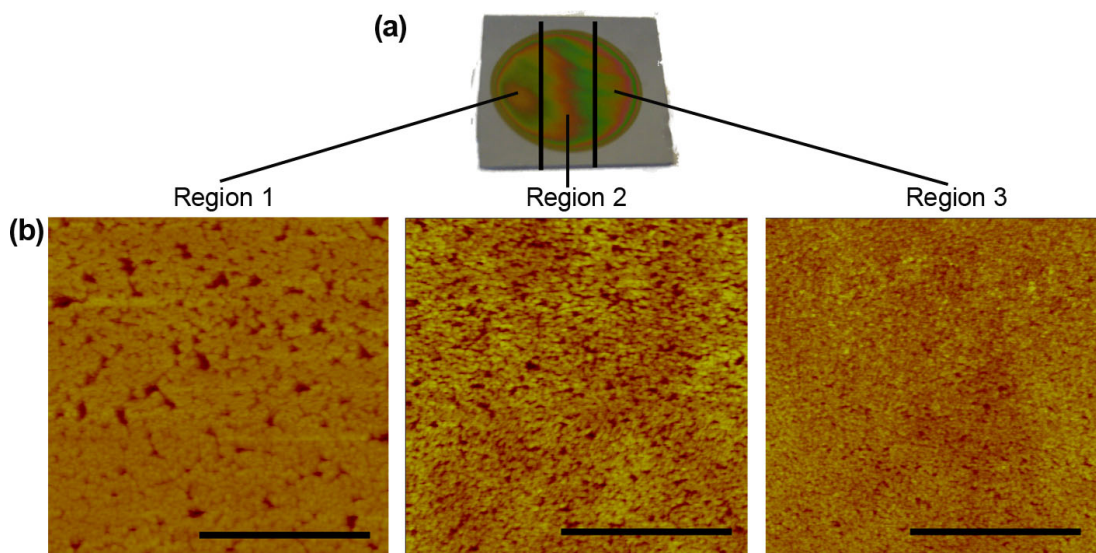


Figure 4.7: (a) Photograph of gradient pSi film indicating the three regions: (region 1) closest to electrode, (region 2) middle region and (region 3) furthest from the electrode. (b) Tapping mode AFM images showing pore size decreasing with distance from the Pt electrode. Scale bars = 500 nm.

Table 4.1: AFM pore size analysis of the pore size gradients produced by different applied currents.

Etching Current (mA)	Region 1		Region 2		Region 3	
	Pore size (nm)		Pore size (nm)		Pores size (nm)	
	Range	Avg.	Range	Avg.	Range	Avg.
40	17 - 93	39 ± 15	5 - 22	12 ± 4	4 - 17	9 ± 4
50	14 - 140	52 ± 27	5 - 48	22 ± 9	3 - 10	7 ± 2
55	36 - 304	146 ± 60	17 - 211	94 ± 38	21 - 135	60 ± 290
60	-	-	47 - 793	232 ± 133	36 - 368	130 ± 49

depending upon etching current density and region on pSi surface. A broad range of pore sizes were generated to examine the effect of pore size on CNT coverage.

After etching, the pSi substrates were further functionalised with an APTES monolayer in order to cover the surface with amine groups which are available to react with the carboxylic acid groups on the SWCNTs. After SWCNT attachment via carbodiimide coupling, AFM images were taken at the three regions of each pSi sample. For all samples vertically aligned bundles of SWCNTs chemically attached to the pSi surface were observed. As determined from the AFM software, the average diameter of the SWCNT bundles was found to be 120 nm. AFM imaging after SWCNT attachment onto the 40 mA pSi gradient (Figure 4.8 (a)) showed very little difference in percentage surface coverage between the three regions ($57 \pm 5\%$, $64 \pm 6\%$, $69 \pm 6\%$). The percentages of SWCNT coverage are summarised in Table 4.2. The 50 mA pSi gradient (Figure 4.8 (b)) showed little change in region 1 ($52 \pm 4\%$) when compared to regions 2 and 3 ($57 \pm 4\%$, $56 \pm 3\%$, Table 4.2). The 55 mA pSi gradient exhibited a significant difference in SWCNT coverage across the regions with region 1 exhibiting a SWCNT coverage of $2 \pm 1\%$ (Figure 4.8 (c) (i)) which increased to $9 \pm 4\%$ (Figure 4.8 (c) (ii)) in region 2 and increased again to $25 \pm 2\%$ in region 3 (Figure 4.8 (c) (iii)). The two regions of the 60 mA pSi gradient (Figure 4.8 (d)) also exhibited coverage variance with region 2 having a surface coverage of $3 \pm 1\%$ while region 3 had a coverage of $8 \pm 2\%$ (Table 4.2). As the pore size and hence porosity increases, the available APTES-coated area of silicon ridges for SWCNT will decrease, leading to a decrease in SWCNT coverage. Indeed, the plot of average pore size versus SWCNT coverage (Figure 4.9 (a)) shows a linear fit with a linear regression of coverage. However, the linear relationship does not

Table 4.2: Summary of percentage SWCNT coverage on each region of the gradient pSi etched at different etching currents.

Etching Current (mA)	Region 1	Region 2	Region 3
	SWCNT Coverage (%)	SWCNT Coverage (%)	SWCNT Coverage (%)
40	57 ± 5	64 ± 6	69 ± 6
50	52 ± 4	57 ± 4	56 ± 3
55	2 ± 1	9 ± 4	25 ± 2
60	-	3 ± 1	8 ± 2

hold when the maximum pore size is less than the average bundle size of the SWCNTs (120 nm, as determined by AFM, Figure 4.8). In that case, the SWCNT coverage is quasi-constant at $60 \pm 10\%$. The results suggest that the maximum average pore size below which SWCNT coverage is not affected is in the region of 50 nm.

We propose that this observation is a result of the SWCNT bundles being able to straddle the entire pore and chemically attach to both sides of the pore. As the maximum pore size increases past 120 nm, and hence the number of pores over 120 nm increases, the SWCNT coverage begins to decrease (Figure 4.9 (b)). In this case, the SWCNT bundles are only chemically attached to the surface via the ridges of the pores only, which in turn reduces the number of chemical bonds per bundle to the surface. Weakly bonded bundles are then easily removed by the sonication used in cleaning after immobilisation. As the pore size increases, this effect becomes more evident and SWCNT coverage continues to decrease to the point where strong attachment rarely occurs. Since this change in pore size occurs gradually over the length of the entire pSi substrate, the change in SWCNT coverage also changes gradually over the entire substrate, effectively generating a gradient in SWCNT coverage. Once the pSi pore size exceeds the SWCNT bundle size, it may then become possible that the SWCNT bundles deposit within the pores. The depth of the pSi pores ($>1\ \mu\text{m}$) is such that the shortened carboxylated SWCNTs will not be observed by AFM if they are immobilised within the pores.

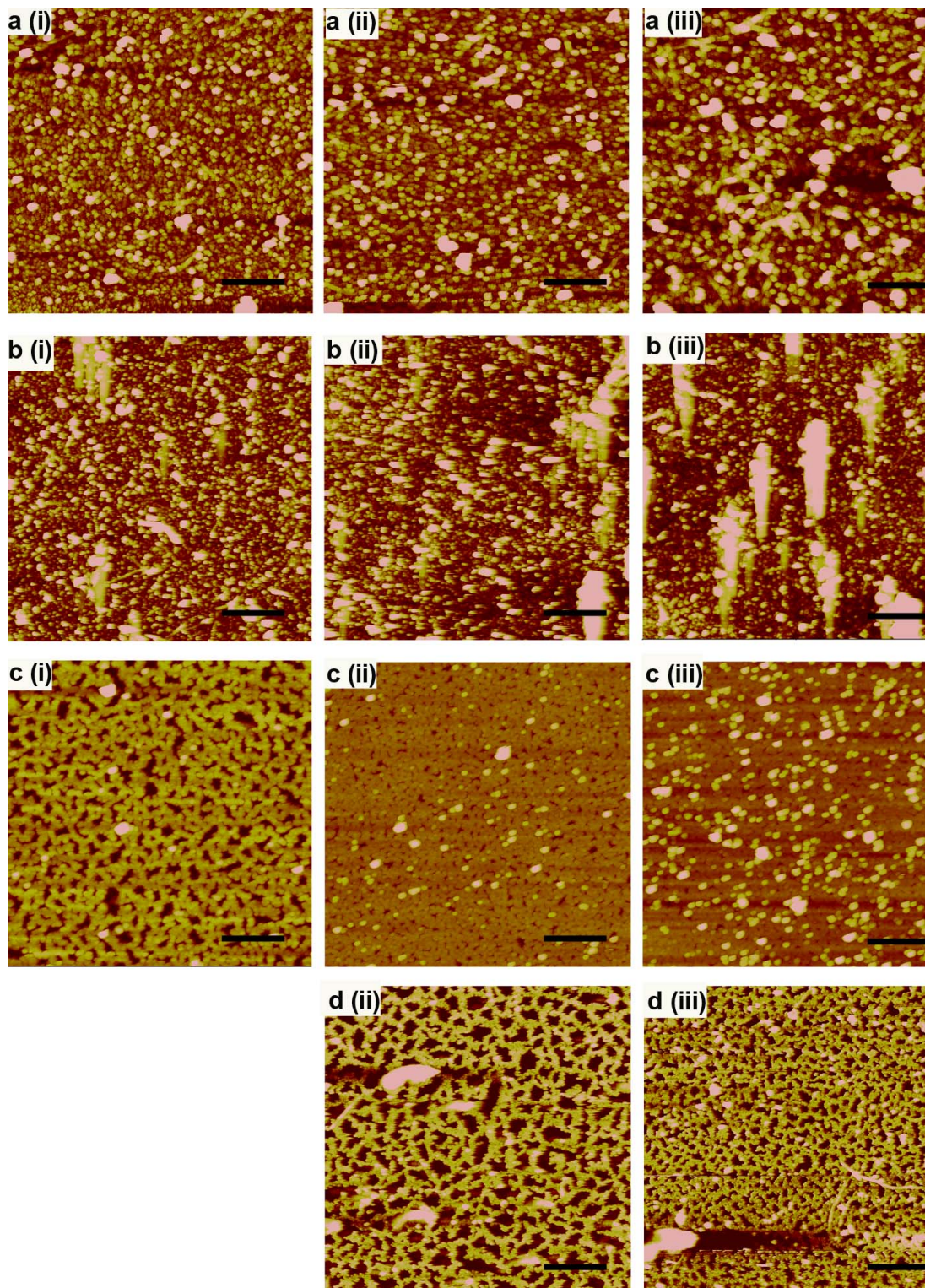


Figure 4.8: Tapping mode AFM height images of SWCNTs attached to gradient pSi surfaces etched at (a) 40 mA (b) 50 mA, (c) 55 mA and (d) 60 mA showing (i) region 1, (ii) region 2 and (iii) region 3. Scale bars = 1 μm .

Hence, using an appropriate etching current, the pSi pore size gradient leads to a SWCNT coverage gradient. This method is relatively simple, provided the equipment for pSi formation is available. However, the change in pore size may have an effect on the application of the Si-CNT device. For example a change in pore size has been found to affect cell adhesion.^[15] For the practical application of SWCNT surface coverage gradients on a pSi pore size gradient, the effects of changing pore size are required to be negligible. This is not the case in water filtration, cell adhesion or field emission and as such this method to produce a CNT gradient will not be used further in this Thesis. In order to generate a CNT gradient that does not include a change in surface topography, the formation of a CNT gradient based upon a chemical gradient was investigated.

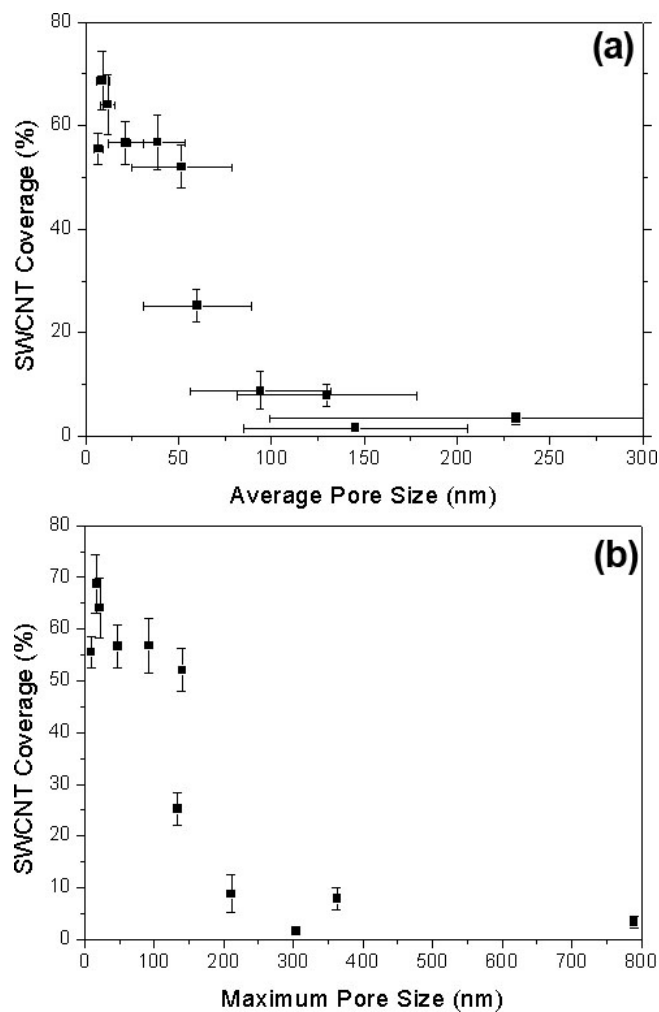


Figure 4.9: Plots showing SWCNT coverage as a function of (a) the average and (b) the maximum pore size of the pSi surface.

4.4.2 APTES chemical gradient

The fabricated APTES chemical gradients on flat silicon were analysed by sessile drop WCA measurements to confirm that a density gradient of APTES moieties had indeed been obtained using the vapour phase diffusion method. Figure 4.10 shows the variation in WCA across the surface as the distance from the APTES-filled reservoir increases. The average WCAs decrease from $32 \pm 5^\circ$ at 5 mm distance from the APTES-filled reservoir down to as low as $11 \pm 2^\circ$ at 20 mm from the APTES-filled reservoir. The higher WCA observed closer to the reservoir is consistent with

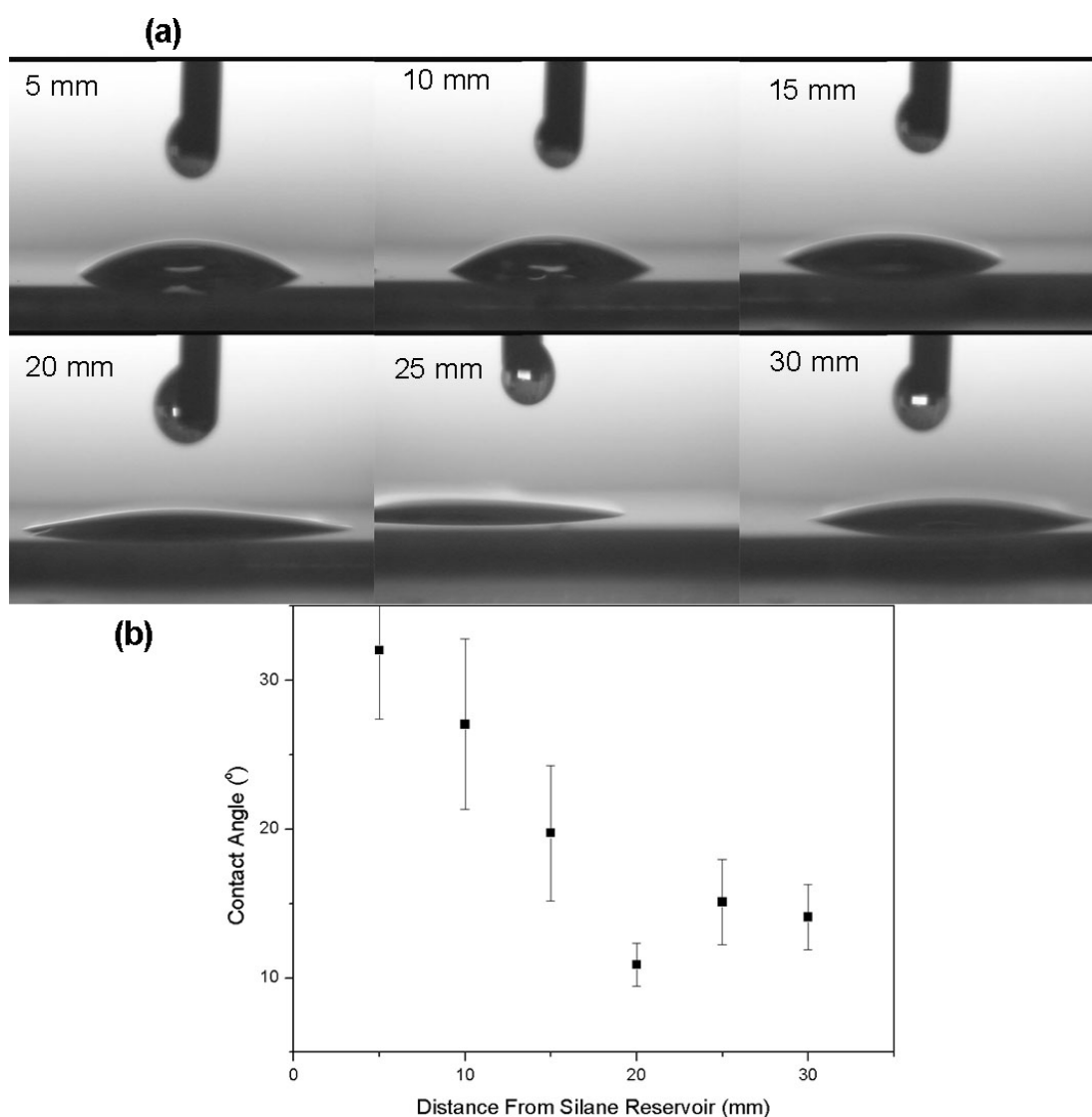


Figure 4.10: (a) Digital photographs and (b) WCA values of water droplets deposited at increasing distance (from 5 – 30 mm at 5 mm intervals) from the APTES-filled reservoir.

the somewhat hydrophobic APTES molecules being present in higher concentration. At the other end of the sample, the more hydrophilic silanol groups of the oxidised Si appear to dominate. Aminosilane gradients have been fabricated previously and have shown similar trends in contact angle variation across the surface.^[16, 27]

After covalent attachment of SWCNTs via carbodiimide coupling, the surfaces were analysed using confocal Raman spectral imaging. Figure 4.11 shows Raman spectral images across the surface of the SWCNTs directly deposited onto a vapour

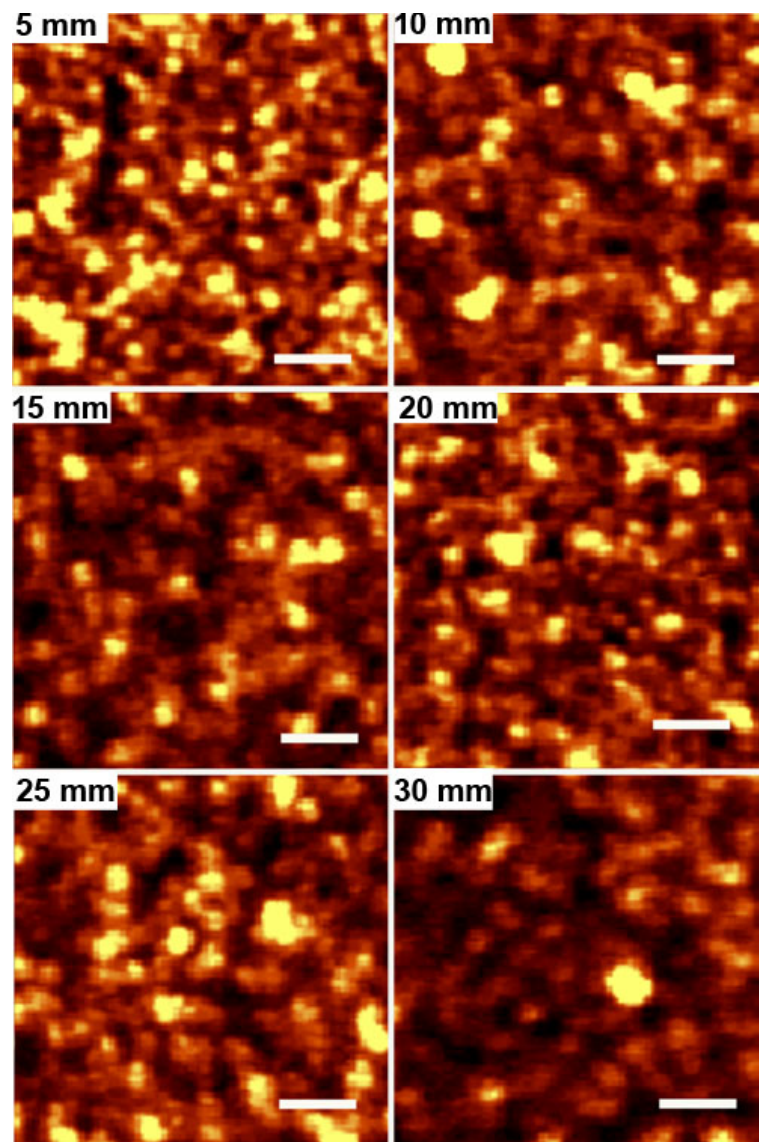


Figure 4.11: Raman spectral images of G-band peak intensity at different distances from the APTES-filled reservoir on the SWCNT-decorated gradient. Scale bar = 4 μm .

phase deposited APTES gradient. Surprisingly, there is little observable difference in the Raman images obtained across the gradient surface. Only the image at a distance of 30 mm appears to exhibit fewer bright spots than the images from the other regions across the gradient, indicating lower SWCNT coverage. Figure 4.12 plots the change in average G-band intensity ($\sim 1590 \text{ cm}^{-1}$) across the APTES gradient. Similar to the observations made for Figure 4.11, there is little change in G-band intensity and hence SWCNT coverage across the surface. We note that we have excluded the occurrence of physisorption of SWCNTs on the silicon surface as the reason for the lack of coverage contrast since rigorous washing and sonication of the surface was performed to remove any weakly bound SWCNTs. Therefore, the experimental result was unexpected: the SWCNTs should only be able to attach to the amine groups of the silane and not to the oxidised silicon surface. The expected result would be to see a decrease in SWCNT coverage as the APTES density decreases (as confirmed by the WCA experiments). Usrey *et al.*^[27] have previously created a similar APTES gradient via vapour phase deposition followed by adsorption of mildly oxidised SWCNTs. They observed no significant change in SWCNT coverage across the surface of the APTES gradient prepared by the vapour phase technique.^[27] Usrey *et al.* offer no explanation as to why the APTES gradient in their case was not effective in producing a gradient of SWCNT coverage.

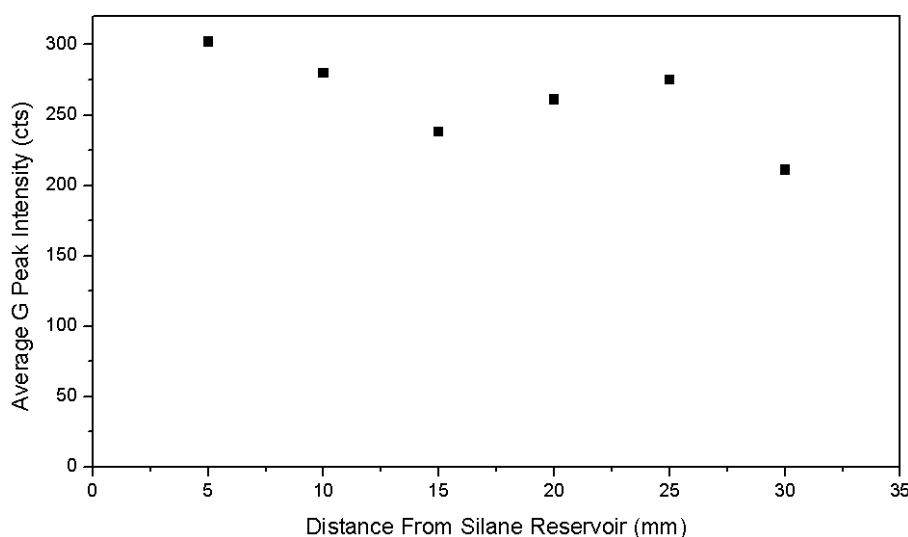


Figure 4.12: Change in average Raman G-band peak intensity with distance from APTES-filled reservoir after SWCNT covalent attachment without backfill.

A possible explanation for our results and the results by Usrey *et al.* may lie in the surface chemistry of the substrate. Prior to APTES immersion, the silicon surface chemistry consisted of silanol bonds. Although it is known that silanols condense to form Si-O-Si species after extended periods of exposure to the atmosphere it is conceivable that esterification took place between the carboxylated SWCNTs and the remaining silanol groups after exposure to APTES on the silicon surface.

In order to prevent the SWCNTs from binding to the surface via ester bonds, a PTMS layer was backfilled into the APTES gradient to block any residual silanol sites. Figure 4.13 shows the Raman spectral imaging across a thus fabricated gradient. In this case, there is a clearly observable difference between the regions closer to the APTES-filled reservoir (5 – 15 mm) when compared to the regions further away (20 – 30 mm). Figure 4.14 (a) plots the change in the average G-band peak intensity across the surface. There is a striking trend of decreasing G-band intensity and hence SWCNT coverage observed for spectra collected from spots 16 mm from the silane reservoir to 20 mm from the reservoir. The observed SWCNT coverage decrease occurs at a similar position as the WCA decrease on the Si-APTES surface observed in Figure 4.10 (prior to PTMS backfill), suggesting that the change in APTES concentration is indeed causing the change in SWCNT coverage. Figure 4.14 (b) plots the G-band peak intensity with measured WCA. A weak positive correlation is observed with higher contact angles clearly showing higher G-band peak intensity and SWCNT coverage. Note that contact angle measurements along the gradient were only taken every 5 mm, explaining the lack of data points in Figure 4.14 (b).

An APTES surface gradient is a simple method to fabricate a CNT surface coverage gradient with the potential of increasing efficiency in determining the optimal CNT coverage for a specific application. However, the formation of the APTES gradient is highly dependent upon environmental conditions (temperature, humidity etc.) and as such was found to be quite inconsistent. Consequently, the region of SWCNT coverage change (15 - 20 mm in Figure 4.14) was found to vary by ± 10 mm across the surface. As a result of this variation, each CNT gradient produced would require analysis to determine the CNT coverage at each point. Raman spectral imaging is a slow process and for the applications described in this Thesis it was found to be more time efficient to prepare individual samples of

varying SWCNT surface coverage. Therefore, given the lack of control over environmental conditions during APTES gradient formation, the use of SWCNT gradients will not be used further.

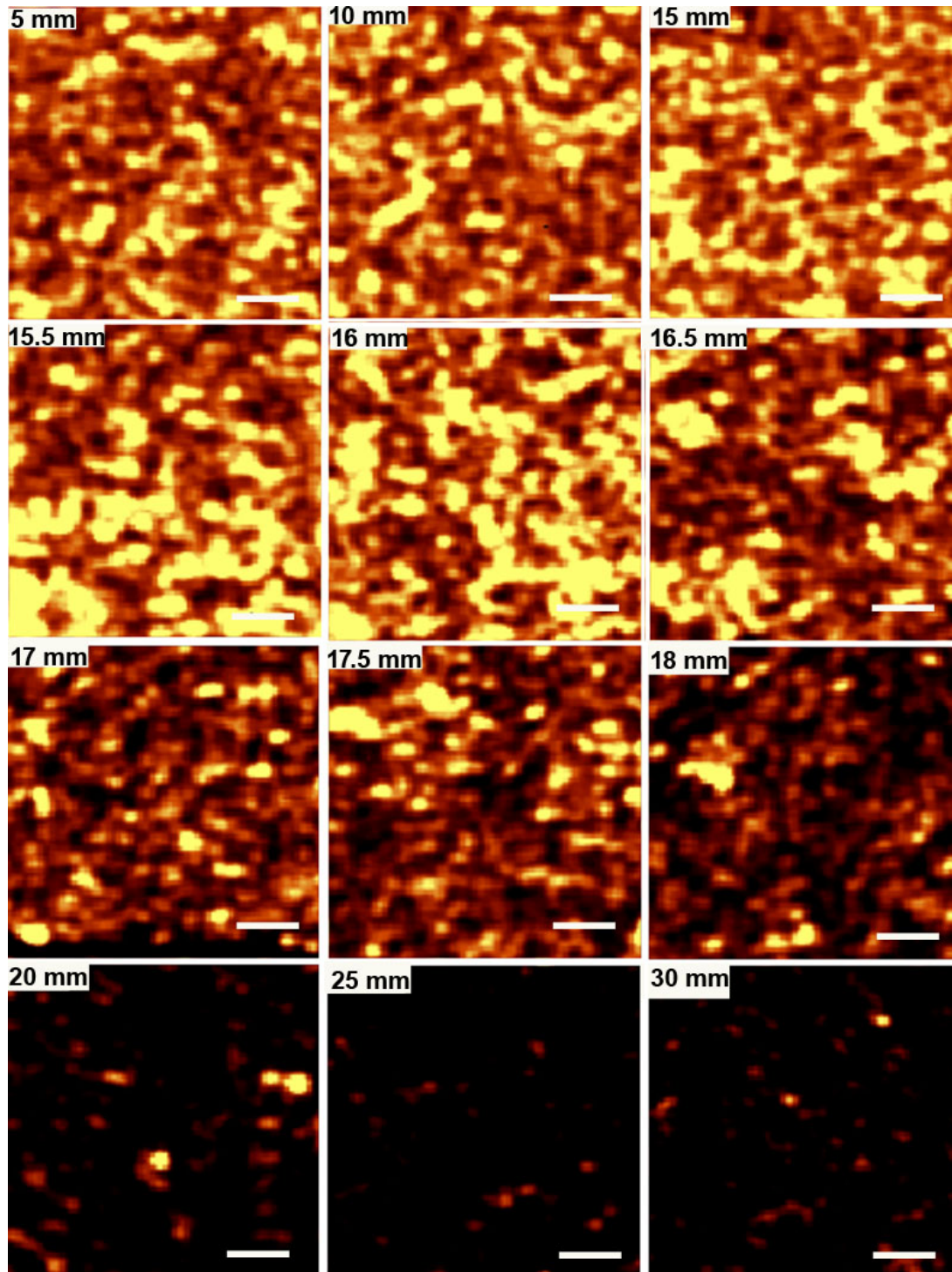


Figure 4.13: Raman spectral images of G-band peak intensity of SWCNTs immobilised on APTES gradient after PTMS backfilling of silicon wafer at increasing distances from the APTES-filled reservoir. Scale bar 4 = μm.

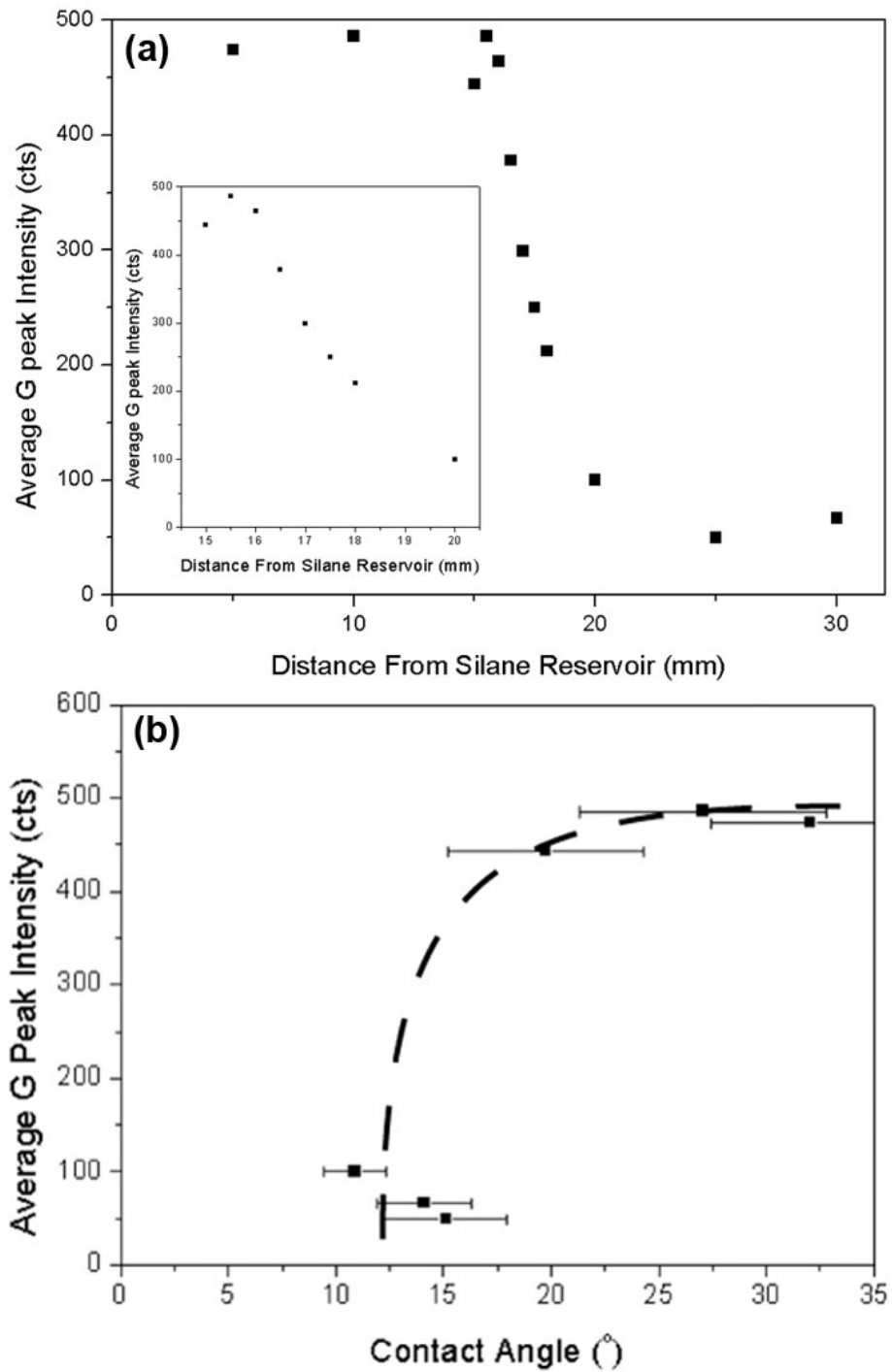


Figure 4.14: (a) Change in average Raman G-band peak intensity with distance from APTES-filled reservoir after SWCNT covalent attachment with PTMS backfill (inset) zoom of area from 15 to 20 mm. (b) Plot of average G-band peak intensity vs. WCA. The dashed line serves as a guide to the eye.

4.5 Conclusions

Patterns of SWCNTs were fabricated by first pre-patterning the surface with APTES. Conventional UV photolithography was used to create APTES patterns on both pSi and silicon. APTES patterning was confirmed by IR spectral mapping where it was found that the APTES was confined within the patterned regions. Subsequent SWCNT attachment to the APTES patterns led to SWCNT patterning as confirmed by Raman spectral imaging.

Gradients of SWCNT coverage were generated following two different methods. The first was a topographical gradient utilising a change in pSi pore size across the surface to induce a decrease in SWCNT coverage when the pore size became larger than the SWCNT bundle size. From this study, it was discovered that the maximum average pore size that does not affect CNT coverage was in the order of 50 nm. For future application the average pore size will be kept below 50 nm. The second method utilised vapour phase diffusion to fabricate APTES density gradients, which, when the remaining silanol groups were reacted with PTMS, gave rise to a conspicuous SWCNT gradient. The topographical gradient gave rise to a gradual variation of SWCNT coverage across the entire length of the substrate with changing pore size while the chemical gradient gave rise to a more acute reduction in SWCNT coverage across a small distance. Each CNT gradient formation mechanism described has its disadvantages. Application of the CNT gradient based on a pSi pores size gradient will require the effect of the changing pore size on the application to be negligible. Additionally, the CNT gradient from the APTES gradient requires a high level of control over environmental conditions in order to produce consistent results.

The controlled placement of SWCNTs is vital for a number of applications including field emission, nanoelectronics and biointerfaces. The patterning of chemically attached SWCNT in a manner that is quick and easily reproducible could potentially find use in many areas.

4.6 References

- [1] K. T. Constantopoulos, C. J. Shearer, A. V. Ellis, N. H. Voelcker, *et al.*, "Carbon Nanotubes Anchored to Silicon for Device Fabrication", *Advanced Materials*, **22** (5), 557-71 (2010).
- [2] D. D. Tune, B. S. Flavel, J. S. Quinton, A. V. Ellis, *et al.*, "Single walled carbon nanotube network electrodes for dye solar cells", *Solar Energy Materials and Solar Cells*, **94** (10), 1665-72 (2010).
- [3] E. Ben-Jacob, and Y. Hanein, "Carbon nanotube micro-electrodes for neuronal interfacing", *Journal of Materials Chemistry*, **18** (43), 5181-6 (2008).
- [4] M. C. LeMieux, M. Roberts, S. Barman, Y. W. Jin, *et al.*, "Self-Sorted, Aligned Nanotube Networks for Thin-Film Transistors", *Science*, **321** (5885), 101-4 (2008).
- [5] S. Fan, M. G. Chapline, N. R. Franklin, T. W. Tombler, *et al.*, "Self-Oriented Regular Arrays of Carbon Nanotubes and Their Field Emission Properties", *Science*, **283** (5401), 512-4 (1999).
- [6] J. Kong, H. T. Soh, A. M. Cassell, C. F. Quate, *et al.*, "Synthesis of individual single-walled carbon nanotubes on patterned silicon wafers", *Nature*, **395** (6705), 878-81 (1998).
- [7] K. B. K. Teo, M. Chhowalla, G. A. J. Amaratunga, W. I. Milne, *et al.*, "Uniform patterned growth of carbon nanotubes without surface carbon", *Applied Physics Letters*, **79** (10), 1534-6 (2001).
- [8] C. L. Pint, Y.-Q. Xu, S. Moghazy, T. Cherukuri, *et al.*, "Dry Contact Transfer Printing of Aligned Carbon Nanotube Patterns and Characterization of Their Optical Properties for Diameter Distribution and Alignment", *ACS Nano*, **4** (2), 1131-45 (2010).
- [9] K. Krisztián, M. Tero, T. Géza, J. Heli, *et al.*, "Inkjet Printing of Electrically Conductive Patterns of Carbon Nanotubes", *Small*, **2** (8-9), 1021-5 (2006).
- [10] B. S. Flavel, J. Yu, J. G. Shapter, and J. S. Quinton, "Patterned attachment of carbon nanotubes to silane modified silicon", *Carbon*, **45**, 2551-8 (2007).
- [11] R. Krupke, S. Malik, H. B. Weber, O. Hampe, *et al.*, "Patterning and Visualizing Self-Assembled Monolayers with Low-Energy Electrons", *Nano Letters*, **2** (10), 1161-4 (2002).
- [12] H. Wei, S. Kim, S. N. Kim, B. D. Huey, *et al.*, "Patterned forest-assembly of single-wall carbon nanotubes on gold using a non-thiol functionalization technique", *Journal of Materials Chemistry*, **17** (43), 4577-85 (2007).
- [13] S. Lee, J. Kim, W. S. Shin, H.-J. Lee, *et al.*, "Fabrication of nanostructures using scanning probe microscope lithography", *Materials Science and Engineering: C*, **24** (1-2), 3-9 (2004).
- [14] J. Liu, M. J. Casavant, M. Cox, D. A. Walters, *et al.*, "Controlled deposition of individual single-walled carbon nanotubes on chemically functionalized templates", *Chemical Physics Letters*, **303** (1-2), 125-9 (1999).
- [15] Y. L. Khung, G. Barritt, and N. H. Voelcker, "Using continuous porous silicon gradients to study the influence of surface topography on the behaviour of neuroblastoma cells", *Experimental Cell Research*, **314** (4), 789-800 (2008).

- [16] R. R. Bhat, D. A. Fischer, and J. Genzer, "Fabricating Planar Nanoparticle Assemblies with Number Density Gradients", *Langmuir*, **18** (15), 5640-3 (2002).
- [17] R. R. Bhat, J. Genzer, B. N. Chaney, H. W. Sugg, *et al.*, "Controlling the assembly of nanoparticles using surface grafted molecular and macromolecular gradients", *Nanotechnology*, **14** (10), 1145-52 (2003).
- [18] T. Wu, K. Efimenko, and J. Genzer, "Combinatorial Study of the Mushroom-to-Brush Crossover in Surface Anchored Polyacrylamide", *Journal of the American Chemical Society*, **124** (32), 9394-5 (2002).
- [19] T. Wu, K. Efimenko, P. Vlček, V. Subr, *et al.*, "Formation and Properties of Anchored Polymers with a Gradual Variation of Grafting Densities on Flat Substrates", *Macromolecules*, **36** (7), 2448-53 (2003).
- [20] J. Genzer, K. Efimenko, and D. A. Fischer, "Formation Mechanisms and Properties of Semifluorinated Molecular Gradients on Silica Surfaces", *Langmuir*, **22** (20), 8532-41 (2006).
- [21] R. J. Petrie, T. Bailey, C. B. Gorman, and J. Genzer, "Fast Directed Motion of "Fakir" Droplets", *Langmuir*, **20** (23), 9893-6 (2004).
- [22] M. K. Chaudhury, and G. M. Whitesides, "How to Make Water Run Uphill", *Science*, **256** (5063), 1539-41 (1992).
- [23] T. G. Ruardy, J. M. Schakenraad, H. C. van der Mei, and H. J. Busscher, "Preparation and characterization of chemical gradient surfaces and their application for the study of cellular interaction phenomena", *Surface Science Reports*, **29** (1), 3-30 (1997).
- [24] B. E. Collins, K. P. S. Dancil, G. Abbi, and M. J. Sailor, "Determining Protein Size Using an Electrochemically Machined Pore Gradient in Silicon", *Advanced Functional Materials*, **12** (3), 187-91 (2002).
- [25] Y. L. Khung, and N. H. Voelcker, "Multidirectional lateral gradient films with position-dependent photonic signatures made from porous silicon", *Optical Materials*, **32** (1), 234-42 (2009).
- [26] S. B. Carter, "Principles of Cell Motility: The Direction of Cell Movement and Cancer Invasion", *Nature*, **208** (5016), 1183-7 (1965).
- [27] M. L. Usrey, and M. S. Strano, "Adsorption of Single Walled Carbon Nanotubes onto Silicon Oxide Surface Gradients of 3-Aminopropyltri(ethoxysilane) Described by Polymer Adsorption Theory", *Langmuir*, **25** (17), 9922-30 (2009).
- [28] P. Warkentin, B. Wälivaara, I. Lundström, and P. Tengvall, "Differential surface binding of albumin, immunoglobulin G and fibrinogen", *Biomaterials*, **15** (10), 786-95 (1994).
- [29] Y. S. Lin, and V. Hlady, "The desorption of ribonuclease A from charge density gradient surfaces studied by spatially-resolved total internal reflection fluorescence", *Colloids and Surfaces B: Biointerfaces*, **4** (2), 65-75 (1995).
- [30] W. G. Pitt, "Fabrication of a continuous wettability gradient by radio frequency plasma discharge", *Journal of Colloid and Interface Science*, **133** (1), 223-7 (1989).
- [31] C. G. Gölander, and W. G. Pitt, "Characterization of hydrophobicity gradients prepared by means of radio frequency plasma discharge", *Biomaterials*, **11** (1), 32-5 (1990).
- [32] R. M. Pasternack, S. Rivillon Amy, and Y. J. Chabal, "Attachment of 3-(Aminopropyl)triethoxysilane on Silicon Oxide Surfaces: Dependence on Solution Temperature", *Langmuir*, **24** (22), 12963-71 (2008).

- [33] M. Picher, E. Anglaret, R. Arenal, and V. Jourdain, "Self-Deactivation of Single-Walled Carbon Nanotube Growth Studied by in Situ Raman Measurements", *Nano Letters*, **9** (2), 542-7 (2009).

Chapter 5

Mass transport through CNT and pSi membranes

A SWCNT membrane was fabricated by chemically attaching SWCNTs to a pSi membrane support. Since liquid transport through a pSi membrane had not been previously reported, both dye diffusion and pressure driven transport of water through the pSi membranes was studied. It was found that, although brittle, the pSi membranes could facilitate the selective transport of dye molecules depending upon surface functionalisation. In order to fabricate a SWCNT membrane chemical attachment of vertically aligned SWCNTs was achieved upon the pSi membranes followed by polymer deposition via spin coating and water plasma to reveal the SWCNT tips. Pressure driven water transport through the SWCNT membrane was investigated and compared to other experimental and theoretical CNT membranes as well as other commercial membranes.

5.1 Introduction

As described in detail in Section 1.5, due to their inner-wall smoothness and hydrophobicity, CNTs have the potential to act as high flux, high selectivity and low power water filtration membranes.^[1,2] The difficulty lies in the fabrication of a CNT membrane fit for a practical purpose. The most successful membranes thus far have been produced by the groups of Hinds and Holt.^[3, 4] For ease of comparison, schematics of their membrane fabrication methods are shown in Figure 5.1.

The criteria for a CNT membrane include: CNT pores open at both ends, exclusive flow through the CNTs, low diameter CNTs, high CNT density and good membrane strength. While all the listed criteria are important, a few of these are yet to be optimised.

The smallest diameter CNT membrane fabricated at the time of writing is the 2 nm DWCNT membrane reported by Holt *et al.*^[3] Theoretical modelling has suggested that for desalination, the CNT diameter must be less than 0.9 nm to achieve a salt rejection of 95 %.^[5] Such small diameters require the use of SWCNTs. Achieving such low diameters in VA-SWCNT's grown via CVD is rarely reported, and an alternative CNT fabrication method is therefore required.

The percentage CNT pore area density reported by both Holt *et al.*^[3] for their CVD grown DWCNT membrane and Hinds *et al.*^[4] for their CVD grown MWCNT membrane were 2 and 0.15 %, respectively. The low density is a result of the CVD process producing surfaces of various heights and orientations as well as CNTs with catalyst and bamboo like structures that block flow.^[6] The low value will lower the permeability of the produced membranes. The 'microtome cut' method described more recently by Hinds produces membranes with even lower pore area density due to the randomness involved in the membrane fabrication (see Section 1.5.3).

The support for the membranes fabricated by Hinds and Holt differ greatly (Figure 5.1). The Hinds membrane is free standing with no support while the Holt membrane is built across lithographically defined pits (89 ~ 2 mm² pits on a 15 x 15 mm wafer) leading to areas of flat silicon which are not permeable while the permeable areas are suspended between the silicon support. The design of Holt

produces a more stable membrane but the total permeability of the membrane is reduced due to the areas of flat silicon which stop flow.

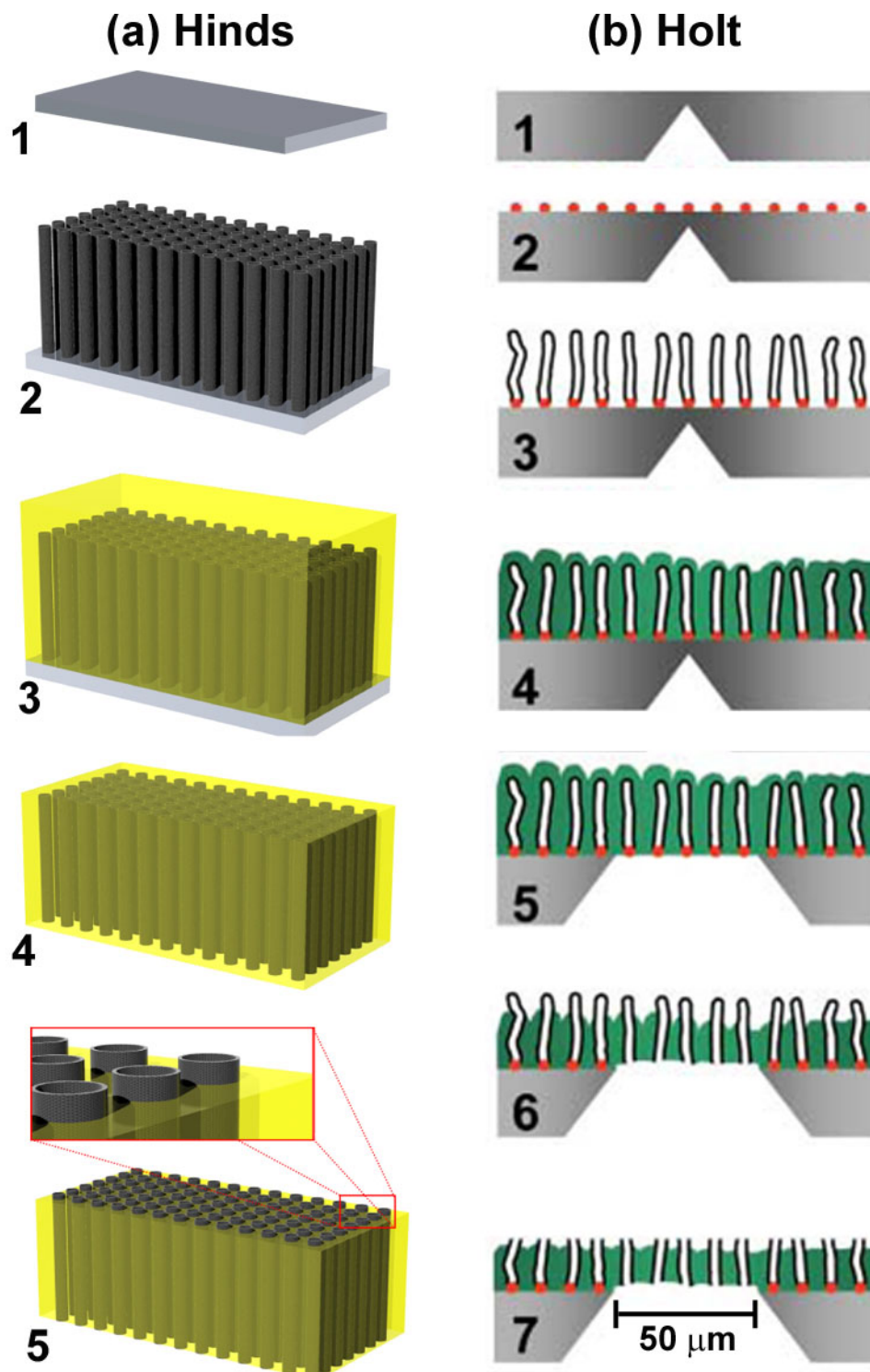


Figure 5.1: Comparison of CNT membrane fabrication procedures followed by (a) Hinds *et al.*^[7] and (b) Holt *et al.*^[3] Detail of fabrication given in Section 1.5.3.

The chemical attachment method to produce VA-SWCNTs offers a potential route to improve upon previously reported CNT membranes. Purchased SWCNTs produced by various techniques have the potential to be of lower diameter with diameter restricted by the supplier. The use of chemically treated CNTs reduces the likelihood of catalyst nanoparticles restricting flow as these are removed during the CNT cutting/functionalisation process.^[8] In order to improve the support without affecting permeability, a pSi membrane will be used as the support.

Despite its apparent advantages, the chemical attachment method of CNTs to substrates does also introduce some difficulties. The smaller length (~360 nm) of acid treated CNTs compared to CVD grown CNT membranes (2 – 10 μm) will make the polymer deposition step much more difficult and the membrane strength will also be reduced. The variation in SWCNT length/height is perhaps greater in chemically attached CNT compared to CVD grown CNTs, further increasing the difficulty.

Porous silicon membranes are thin layers of pSi with pores open at either end (Figure 5.2). Fabrication of pSi membranes has been achieved by etching through an entire Si wafer,^[9] by etching a thin layer of pSi followed by macroscopically etching from the back side^[10] (similar to that describe by Holt in Figure 5.1 (b)) and by the ‘lift-off’ of a pSi layer.^[11, 12] The ‘lift-off’ procedure involves the etching of a pSi film to a desired depth followed by the electropolishing of the bottom of the film to liberate it from the bulk Si. Electropolishing is achieved by increasing the current density and/or decreasing the HF concentration.

To compound the difficulties of the fabrication a CNT membrane on a pSi support the transport of liquids through pSi membranes has not been described previously. Several reports have been made on the fabrication of pSi membranes and their gas transport.^[10, 11] The lack of data is most likely due to the fragility of the brittle pSi membrane.

The proposed membrane fabrication scheme is shown schematically in Figure 5.2. In this Chapter, the fabrication of a pSi membrane suitable for liquid transport will be investigated. The transport and separation of two dyes using changing surface functionality will be studied as well as the pressure driven transport of water. The fabrication of a SWCNT membrane will be achieved by chemically attaching SWCNTs to a pSi membrane, filling the gaps between the SWCNTs with a polymer

and exposing the SWCNT tips through the polymer by etching the surface with a water plasma.

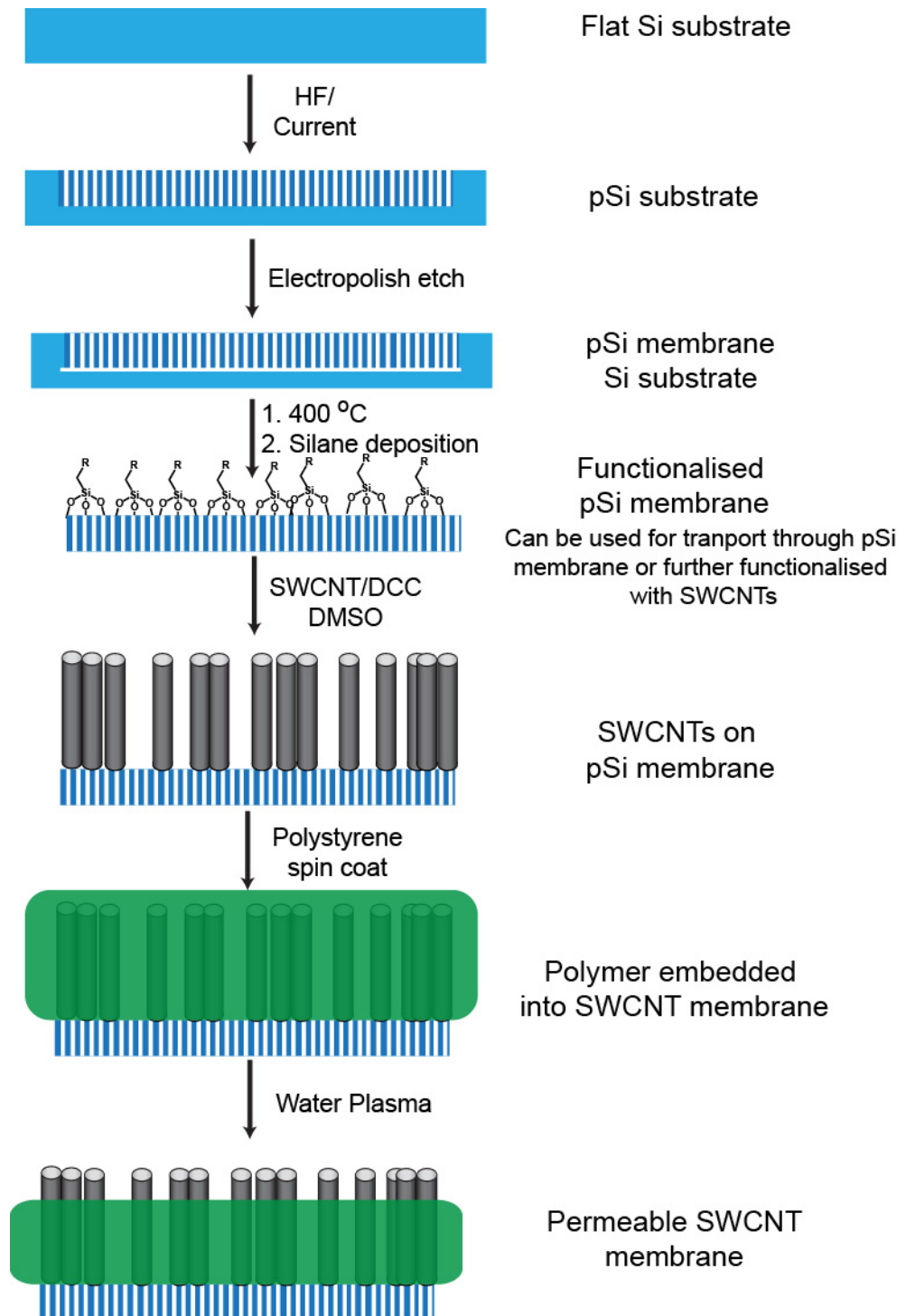


Figure 5.2: Schematic of the assembly of a SWCNT membrane supported on a pSi substrate.

5.2 Experimental details

5.2.1 Fabrication and functionalisation of pSi membranes

Porous silicon was fabricated following the general outline as described in Section 2.2.3 using highly boron doped Si (100, orientation, 0.00055 - 0.001 Ω cm resistivity, Virginia Semiconductor, USA). The formation of pSi membranes was achieved using the 'lift-off' technique which involves etching in two steps. The first etching step creates the pores for the pSi membrane and was carried out at a constant current of 100 mA for 30 min in a solution of 3:1 (v/v) 48 % aqueous HF/ethanol. The HF solution was removed and replaced with a solution of 1:1 (v/v) HF:ethanol for the second etching step which acts to electropolish the bottom of the pSi film, liberating it from the bulk silicon base. A current of 450 mA was applied for 60 sec. The HF solution was then removed and the pSi substrate was washed repeatedly with ethanol, removed from the etching cell and allowed to dry.

After etching, the free-standing pSi membranes were carefully placed in a tube furnace (Labec, Australia) and thermally annealed for 1 hr at 400 °C. The membranes were removed from the furnace and allowed to cool and then either investigated for molecule transport properties or further functionalised with a silane to produce a hydrophobic or hydrophilic membrane (Figure 5.3). For the hydrophobic membrane, the pSi membranes were treated with the hydrophobic silane heptadecafluoro - 1, 1, 2, 2 - tetrahydrodecyl) dimethylchlorosilane (PFDS, Gelest, USA) via the neat silanisation method by placing the membrane within a glass Petri dish, depositing 20 μ L of the silane on-top of the membrane, covering the Petri dish and then placing in an oven at 80 °C for 15 min.^[13] The membrane was then washed repeatedly with ethanol and allowed to dry. For the hydrophilic membrane, the pSi membranes were treated with the hydrophilic *N*-(triethoxysilylpropyl)-*o*-polyethylene oxide urethane (PEGS, Flurochem, UK) via a solution phase deposition method by immersing the pSi in a solution of 1 % (v/v) of the PEGS in dry toluene for 10 min. The now hydrophilic membrane was then washed in toluene and then repeatedly washed in ethanol and allowed to dry. APTES was deposited onto the pSi membranes following the method described in Chapter 2 to facilitate subsequent SWCNT attachment.

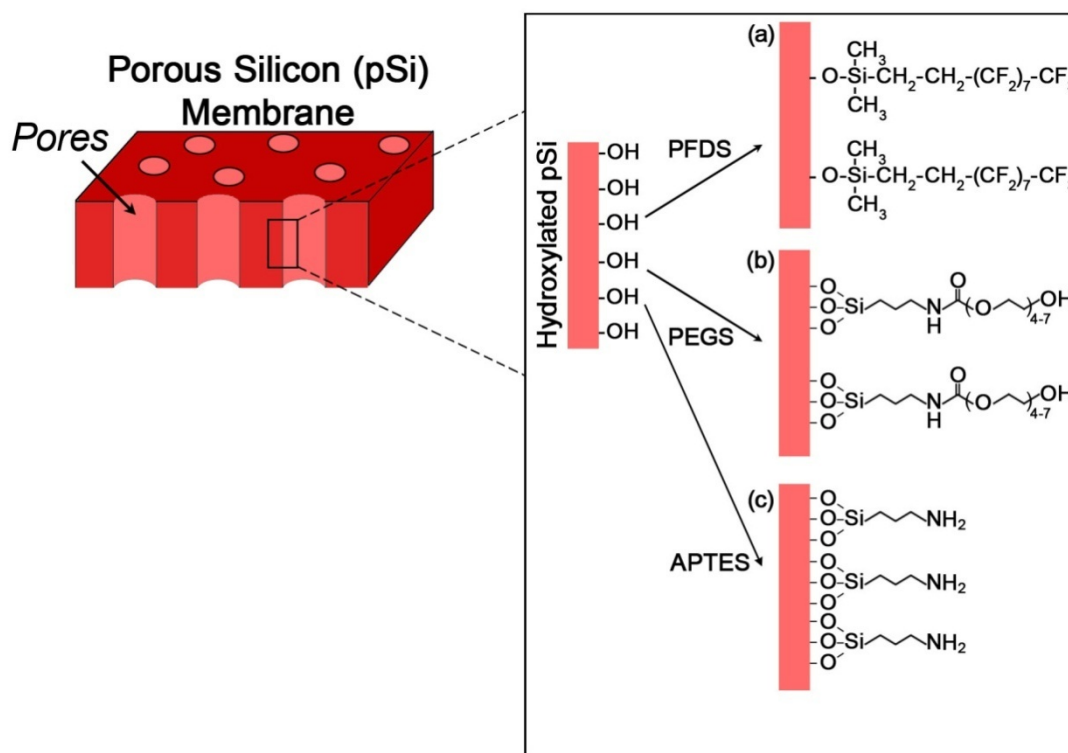


Figure 5.3: Schematic of the chemical modification of pSi membranes with (a) the hydrophobic fluorinated silane (PFDS), (b) the hydrophilic silane (PEGS) and (c) APTES for SWCNT attachment.

5.2.2 Dye transport properties through pSi membranes

The fragile free-standing pSi membranes were supported by sealing the membrane between two pieces of mica with epoxy. Each piece of mica contained a hole with an area of 0.05 cm^2 . The membranes were sandwiched between the pieces of mica and the holes in the mica were aligned thus forming an effective open area of pores of 0.05 cm^2 . The support of the mica provided the ability to clamp the pSi membrane into the transport cell without breaking the membrane. Transport experiments were performed using a U-tube permeation cell in which the membrane separates two half-cells; the feed cell and the permeate cell (Figure 5.4). The transport properties of the pSi membranes were determined with two probe dyes; tris(2,2'-bipyridyl)dichlororuthenium(II) hexahydrate (Rubpy, Aldrich, Australia) with more hydrophobic properties and Rose Bengal (RB, Aldrich, Australia) with more hydrophilic properties (Figure 5.4). Separate permeation experiments were performed with Rubpy and RB in which a 1 mM solution of the dye in ethanol was added to the feed cell and pure solvent was added to the permeate cell. The diffusion

of the dye from the feed cell to the permeate cell was continuously monitored with a UV-Vis fibre optic spectrophotometer (Ocean Optics, USA) at 286 nm and 454 nm for Rubpy or 549 nm for RB. The ratio of the flux for Rubpy to the flux for RB (flux ratio) was determined. Additional transport experiments were performed with feed cell concentrations of 500 μM and 1.5 mM in order to plot the flux of the dye molecule against the concentration difference across the membrane to obtain the permeability.

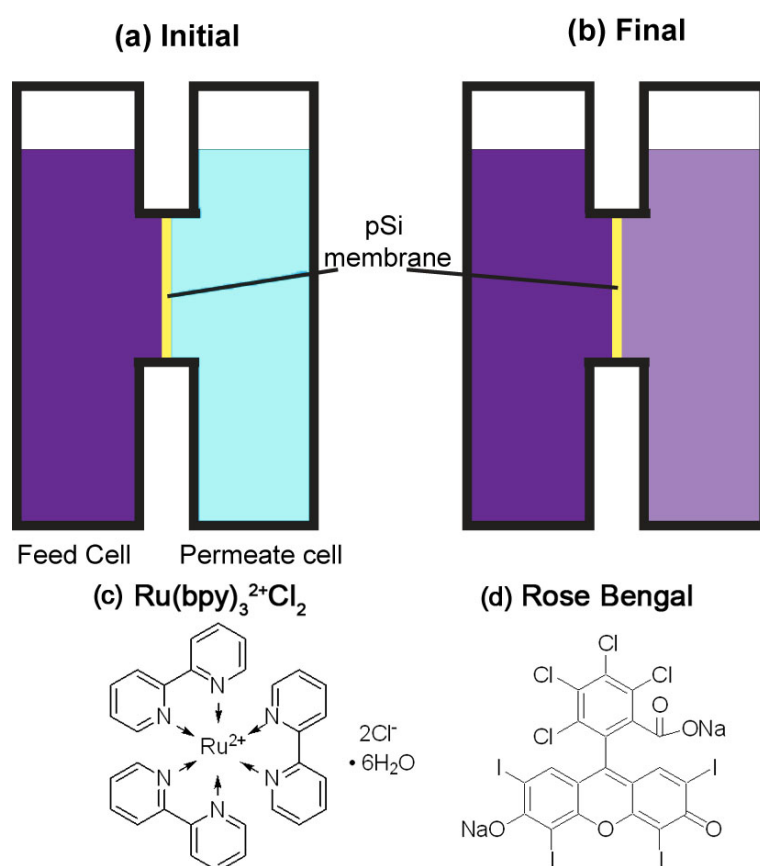


Figure 5.4: (a, b) Schematic of U-tube configuration used for dye diffusion experiments with the pSi membrane separating the feed and permeate cells. (a) initial configuration with solvent only in the permeate cell and (b) after experiment completed with dye in permeate cell. Structure of the two dyes investigated (c) the hydrophobic dye Rubpy and (d) the hydrophilic Rose Bengal (RB).

5.2.3 Water transport

Pressure driven water transport experiments were studied using a custom made computer controlled apparatus in Davide Mattia's laboratory in the School of Chemical Engineering at the University of Bath. The apparatus is shown

schematically in Figure 5.5. A syringe pump (PHD 2000 infusion, Harvard Apparatus) was used to apply pressure to the membrane by adding water at a constant rate. The applied pressure was monitored using a Swagelok pressure transducer (S Model, 0 – 1 MPa). The applied pressure was measured in gauge pressure (barg) which is the pressure reading above ‘normal’ atmospheric pressure. The membrane was placed within a commercial membrane holder (Swinnex non-steriles, Millipore) between two rubber seals. Water passing through the membrane was collected in a beaker on a balance. For a set input flow rate, the mass of water transported and water pressure were recorded simultaneously and visualized on an in-house written LabView program via a USB 2000 link.

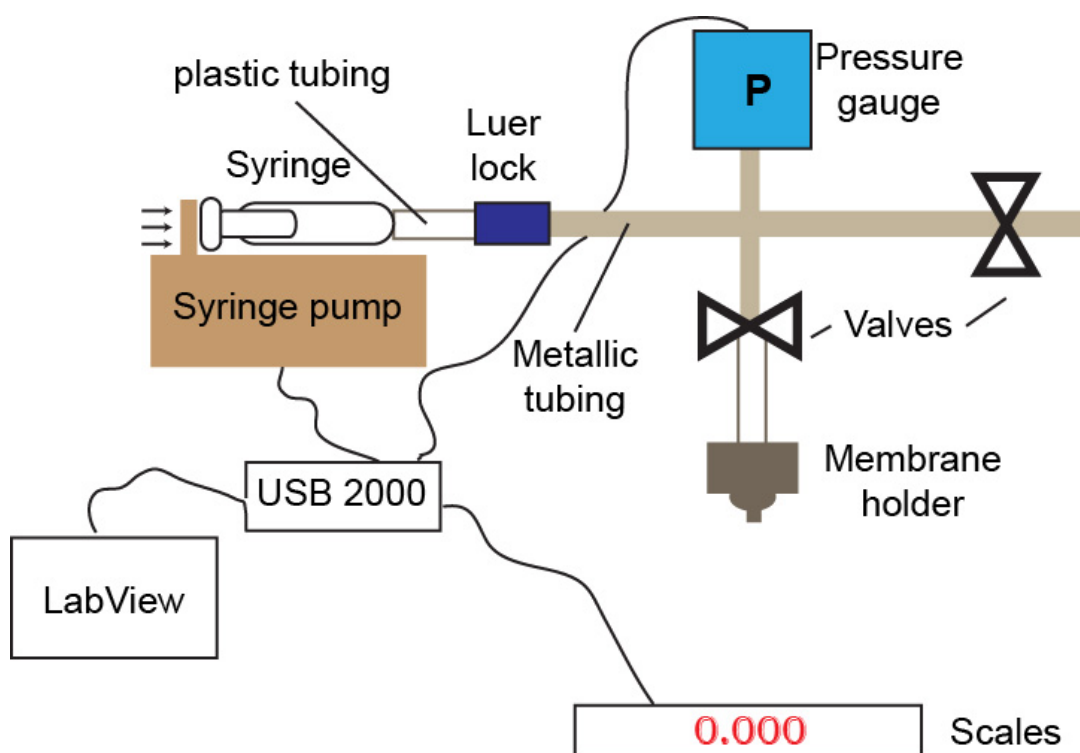


Figure 5.5: Schematic of pressure driven water transport apparatus.

5.2.4 Fabrication of SWCNT membrane

SWCNTs were chemically attached to APTES terminated pSi membranes following the method described in Section 2.3.4.

Thin polymer films were deposited by spin coating 1 % (w/w) polystyrene (MW 100,000, Sigma, Australia) in toluene onto the surface at 6000 rpm for 60 sec on a commercial spin coater (WS-400B-6NPP/LITE 150 mm, Laurell Technologies

Corporation). The polystyrene solution was placed on the surface just prior spinning such that the surface was coated with a thin layer of the solution. The pSi membranes were supported on two pieces of copy paper in order to prevent the vacuum from breaking it.

Surfaces were exposed to a water plasma in a modified Ion Coater (Eiko Engineering Co., Japan). The samples were placed onto a conducting plate and the chamber was evacuated to a vacuum of 0.07 Torr. The chamber was then flushed several times with high purity argon (BOC, Australia) before evacuating to 0.07 Torr. Water vapour was slowly introduced into the chamber through a designed bleed valve to an internal pressure of 0.2 Torr. The stage was then biased with a voltage of ~ 3 kV, igniting a plasma, and a direct current of 5 mA was passed through the stage for a set period of time. The internal pressure and current were maintained manually by adjusting the water vapour inlet and applied voltage.

5.3 Mass transport through pSi

5.3.1 Fabrication and characterisation of pSi membranes

The preparation of a pSi membrane for liquid transport had not previously been reported. As such, experiments were first completed to ensure that mass could be transported through the membranes. The simplest experiment available was the concentration gradient driven transport of dyes through the pSi membrane. These experiments are commonly carried out with multiple dyes with changes to surface chemistry to create change in dye flux. To change the surface chemistry of the pSi membranes, two different silane layers were deposited upon the membrane; a hydrophobic (PFDS) and a hydrophilic (PEGS) were chosen.

Permeable pSi membranes were prepared by a two-step electrochemical etching of silicon in a solution of ethanolic hydrofluoric acid. The two-step process involves an initial etching step to create the pores (Figure 5.6 (a)) and a final electropolishing step to liberate the porous layer from the Si wafer (Figure 5.6 (b)). The long etching time (30 min) was used in order to make a pSi membrane thick enough such that, although it was quite brittle, it was strong enough to be held with tweezers. SEM was used to calculate the pore size and thickness of pSi membranes. Figure 5.7 (a) is an example of a typical image of the top side of the porous layer with the mean pore size calculated to be 12.8 nm with a range of 2 to 30 nm (Figure 5.7 (e)). This pore

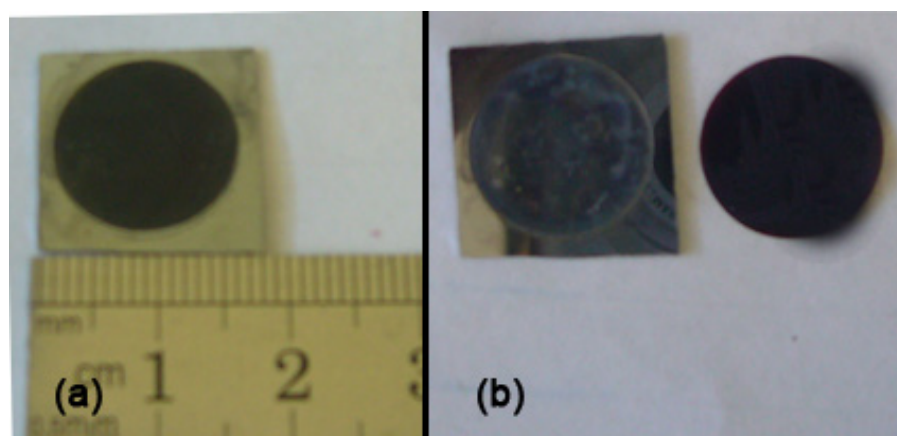


Figure 5.6: Photographs of pSi membranes (a) attached to the silicon wafer and (b) lifted off the silicon wafer.

size region was chosen because it was considered to be large enough for silane penetration into the pore while small enough that the effect of the surface modification with silanes on transport rates will be maximised without blocking transport completely. Additionally, this pore size is well suited for SWCNT attachment. It should be noted that the pores investigated in this study are considerably smaller than those of commonly used materials in similar transport experiments (e.g., Anodisc porous alumina, pore size 20 – 200 nm). The bottom of the porous layer was also imaged with an SEM to ensure the pores were open at both ends to allow for fluid transport. Figure 5.7 (b) shows an SEM image of the bottom of the porous layer. The bottom layer is clearly still open and therefore permeable, and the pore size is approximately 200 % larger on the bottom layer of the pSi. The pores are larger at the bottom because they are etched last and during etching, the concentration of F^- ions decreases which leads to an increased pore size (see Section 1.3.2). The thickness of the pSi membrane was found to be 70 μm (Figure 5.7 (c)). An attempt was made to image along the length of the pores to determine if the pores are truly 1-dimensional and transcend the entire length of the pore. Figure 5.7 (d) is an example of such an image where it is difficult to discern the exact location of pores and as such it is impossible to conclude on the dimensionality of the pores. The difficulty in obtaining such an image for these substrates comes from the small size of the pores and the error involved in breaking the pSi in half.

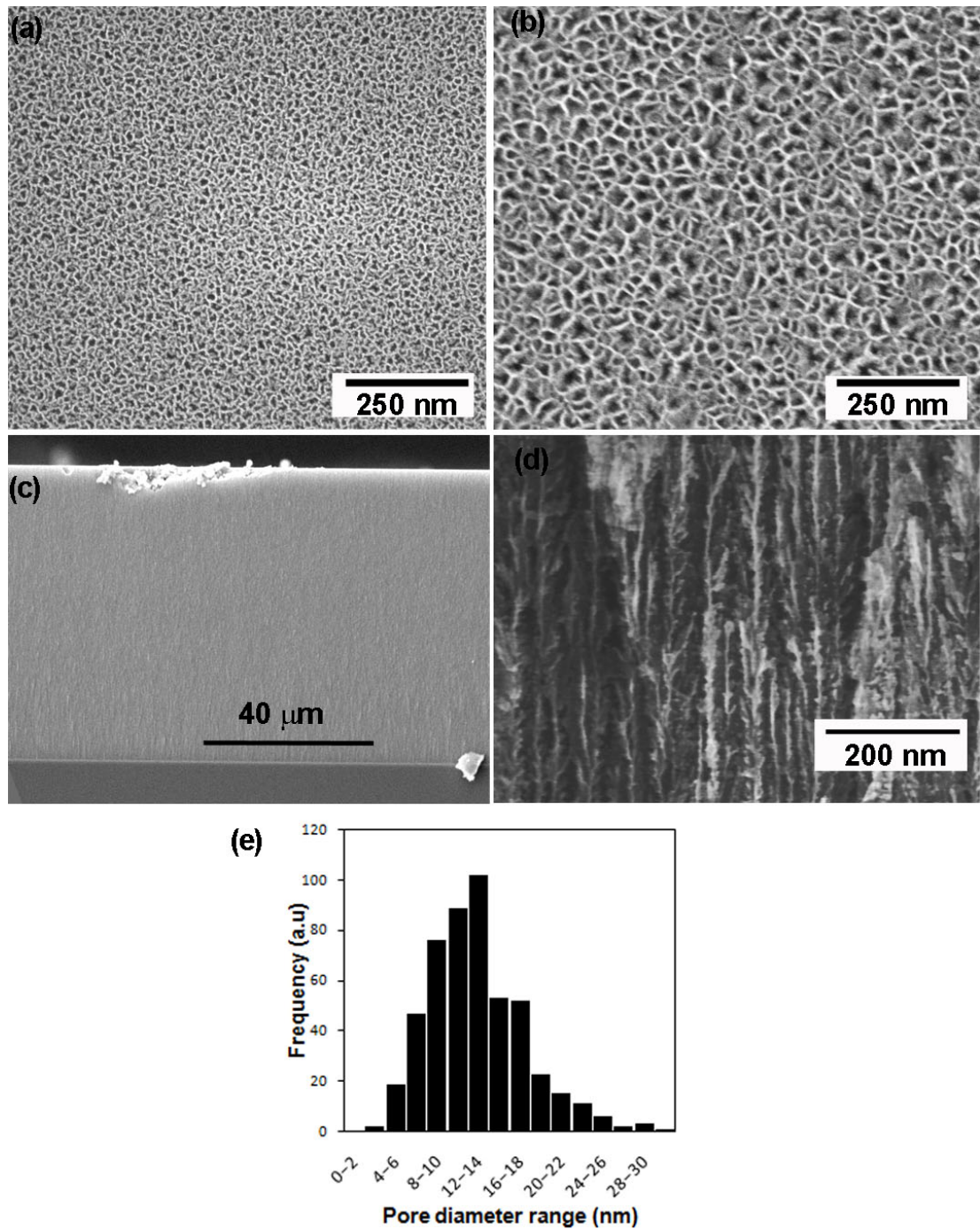


Figure 5.7: SEM images of (a) top and (b) bottom of pSi membrane, (c, d) side views of entire layer (c) and zoom of edge, and (e) pore size distribution graph from the top layer of pSi. Images (a, b, d) from the NanoLab SEM while (c) was from the CamScan.

To improve the level of molecular separation of the pSi membranes, surface functionalisation was carried out to make the surface either hydrophobic or hydrophilic. This was achieved by first oxidising the surface thermally and then depositing silane layers utilising simple silane surface chemistry (Figure 5.3). Surface functionalisation of the pSi membranes was initially confirmed by contact angle measurements. The thermally oxidized pSi membrane showed a hydrophilic WCA of approximately 20° (Table 5.1). This WCA is due to the surface chemistry consisting of silicon to oxygen bonds (e.g. $-\text{Si}=\text{O}$, $\text{Si}-\text{OH}$, $-\text{Si}-\text{O}-\text{Si}-$). When functionalised with the hydrophobic PFDS, silane the contact angle was found to be 135°. The high value is attributed to two factors, the highly hydrophobic nature of the PFDS surface coating and the roughness of the porous structure which has been shown to increase the WCA values.^[14, 15] Table 5.1 also shows a WCA of approximately 13° for the hydrophilic PEGS modified pSi surface. WCA values of between 10-15° have previously been reported for a similar PEGylated silane on a PDMS surface.^[16] The WCA values reported here indicate that the surface functionalisation was successful and that both hydrophobic and hydrophilic pSi surfaces have been created.

Table 5.1: Advancing contact angle measurements for the unfunctionalised, PFDS functionalised and PEGS functionalised pSi membranes.

Surface modification	Contact Angle (°)
Unfunctionalised	19.5 ± 4.5
PFDS	135 ± 13
PEGS	12.9 ± 1.8

To further confirm silane attachment, X-ray photoelectron spectroscopy (XPS) was used. Figure 5.8 shows the survey scans obtained for each surface. The presence of the silane PFDS is obvious from the F 1s peak (Figure 5.8), clearly observable at 685 eV, along with the splitting of the C 1s peak to include both aliphatic carbon (285 eV) and C-F₂ and C-F₃ (293, 294 eV, Figure 5.9).^[17] The confirmation of the presence of the PEGS is more difficult. The presence of carbon in the XPS spectrum is not indicative of the presence of the silane because carbonaceous residue is often accumulated on the sample during storage and transportation between fabrication and analysis. The small N 1s peak (400 eV) in the pSi-PEGS spectrum may be due to the

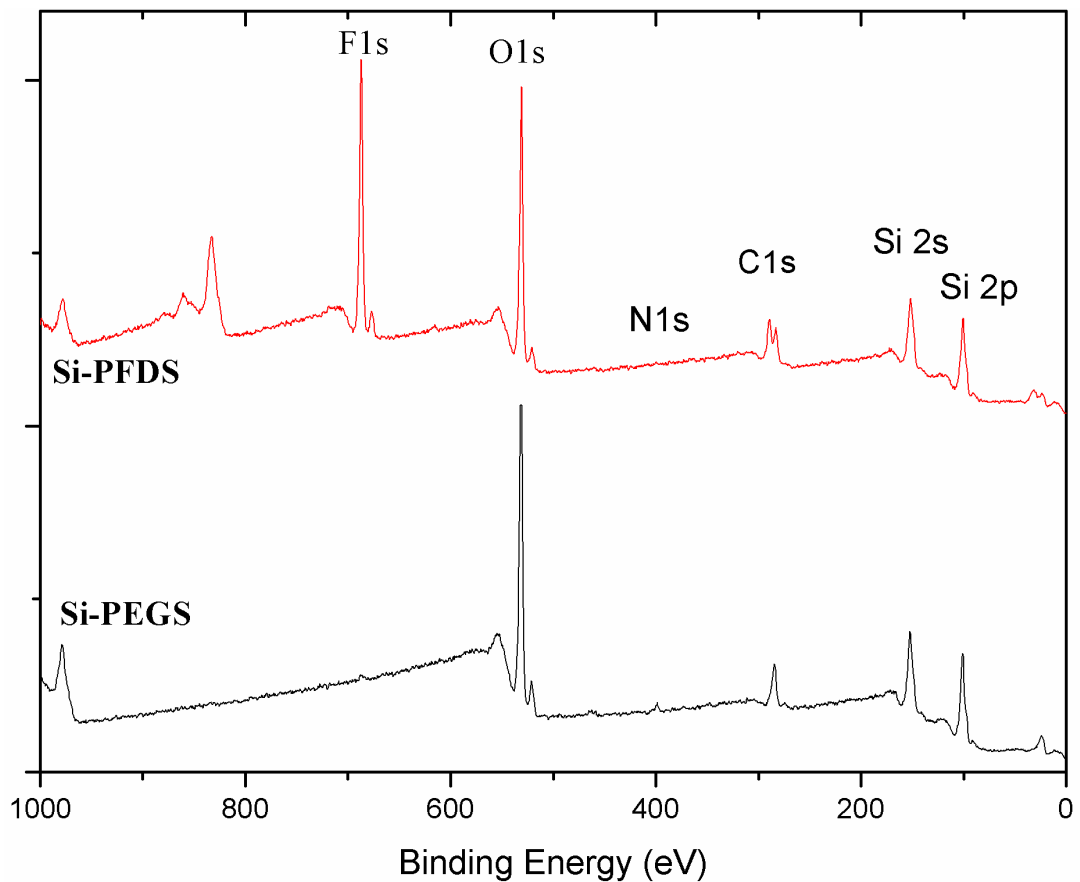


Figure 5.8: XPS analysis of silanes on pSi membranes (red series) pSi-PFDS and (black series) pSi-PEGS.

single nitrogen atom present in the silane but it is not undisputable proof of silane formation. Evidence of the presence of the PEGS comes from the high resolution spectrum of the C 1s peak, observed in Figure 5.9. The C 1s peak of the pSi-PEGS surface shows a broad peak with an undulating shoulder on the higher binding energy side. The shoulders are assigned to carbides, carboxylates, ethers and ketones/esters respectively^[17] all of which are present in the structure of the PEG silane (Figure 5.3).

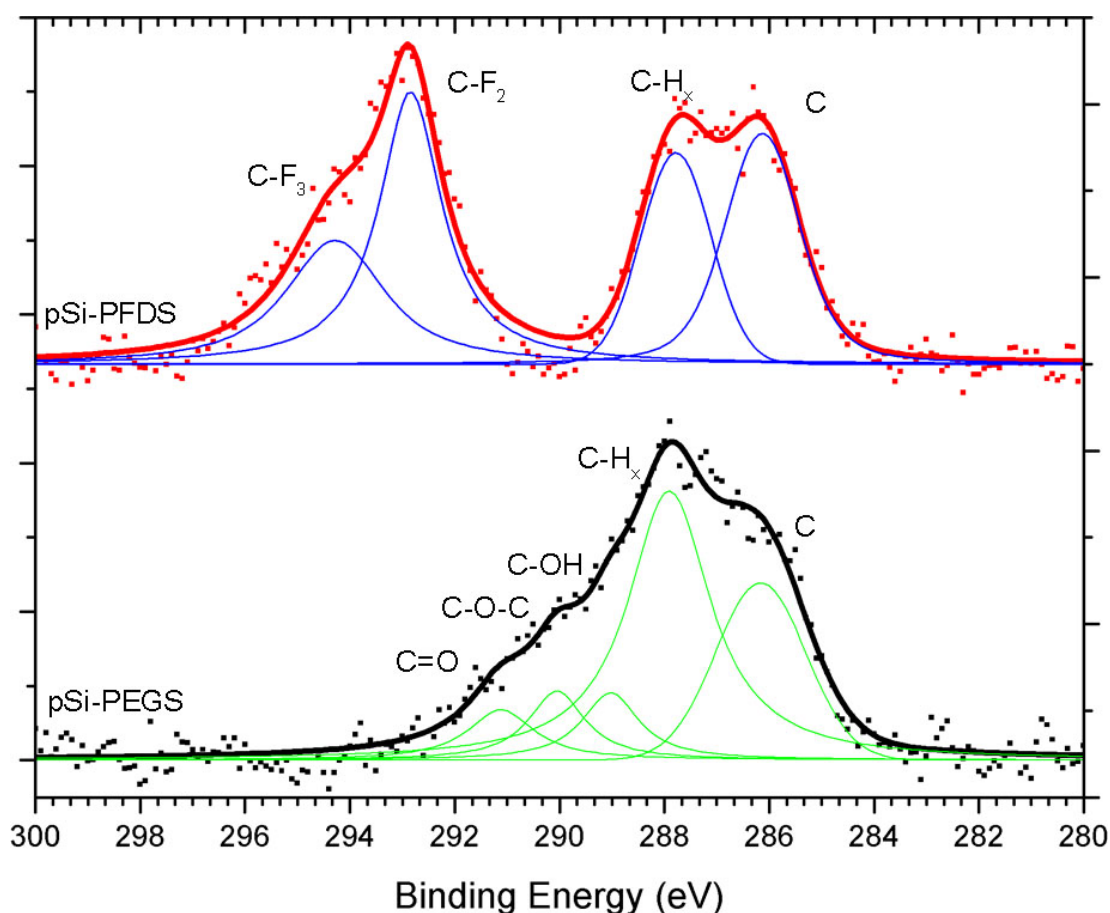


Figure 5.9: High resolution XPS spectra of the C 1s peak from (red series) pSi-PFDS and (black series) pSi-PEGS.

The final proof of the modification of the pSi substrates with the two silanes comes from FTIR spectroscopy. Oxidised pSi shows a broad peak at $\sim 3500\text{ cm}^{-1}$ which is attributed to hydroxyl terminated silicon, the other peak observed is the prominent broad peak at 1100 cm^{-1} which is from Si-O. The pSi-PFDS surface has small peaks at $\sim 2850\text{ cm}^{-1}$ which are attributed to the $-\text{CH}_3$ and $-\text{CH}_2$ stretching bands from the silane. More unique to the PFDS are the $-\text{CF}_2$ stretching ($1225, 114\text{ cm}^{-1}$) and bending (900 cm^{-1}) bands observed.^[18] Once the oxidised pSi surface has been reacted with the PEG-silane, CH_2 methylene vibrational peaks appear at 2900 cm^{-1} , as well as a carbonyl stretching vibrational peak at 1700 cm^{-1} and amide II vibrational peak at 1550 cm^{-1} , both associated with the urethane bond within the silane.^[19]

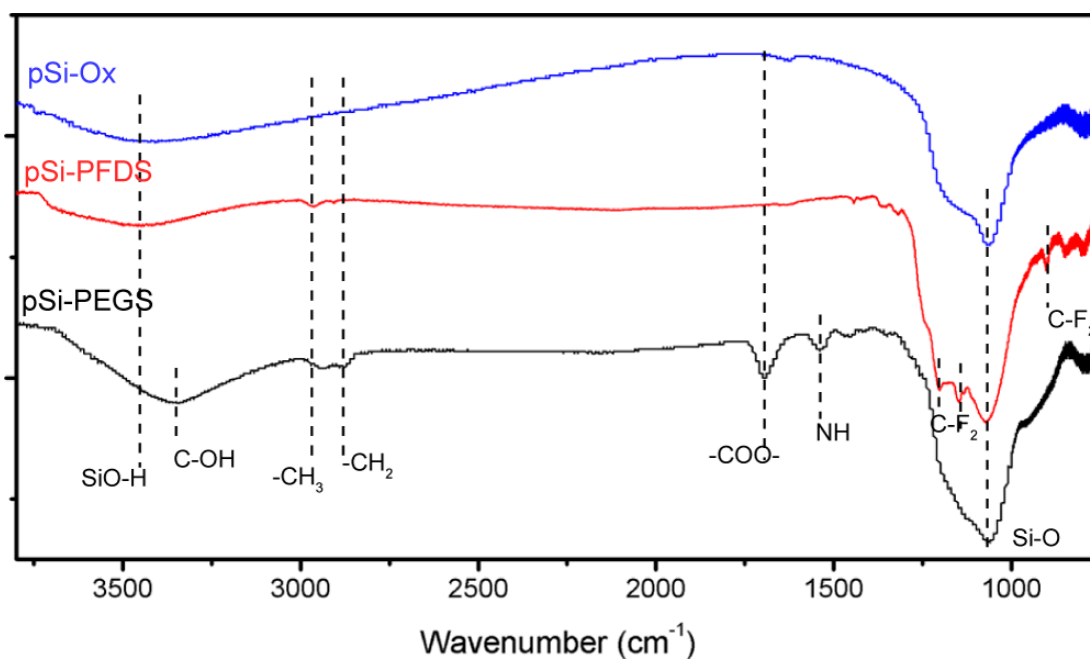


Figure 5.10: FTIR spectra of pSi (blue series) ozone oxidised, (red series) pSi-PFDS and (black series) pSi-PEGS.

5.3.2 Dye transport and selectivity properties of functionalised pSi membranes

To explore the transport and selectivity properties of hydrophobic (PFDS) and hydrophilic (PEGS) modified pSi membranes, the flux of the dyes: Rubpy (hydrophobic) and RB (hydrophilic) was investigated. Figure 5.11 presents the transport of both probe dyes through unfunctionalised pSi membranes and pSi membranes functionalised with PFDS and PEGS, respectively. Straight-line plots are obtained indicating steady state (Fick's first law^[20]) diffusion across the membrane. In order to calculate permeability, multiple initial dye concentrations in the feed cell were investigated (Figure 5.12). The feed cell concentrations varied due to the rate of transport with initial feed concentrations chosen such that 1 – 7 nmoles of dye were transported within 30 min.

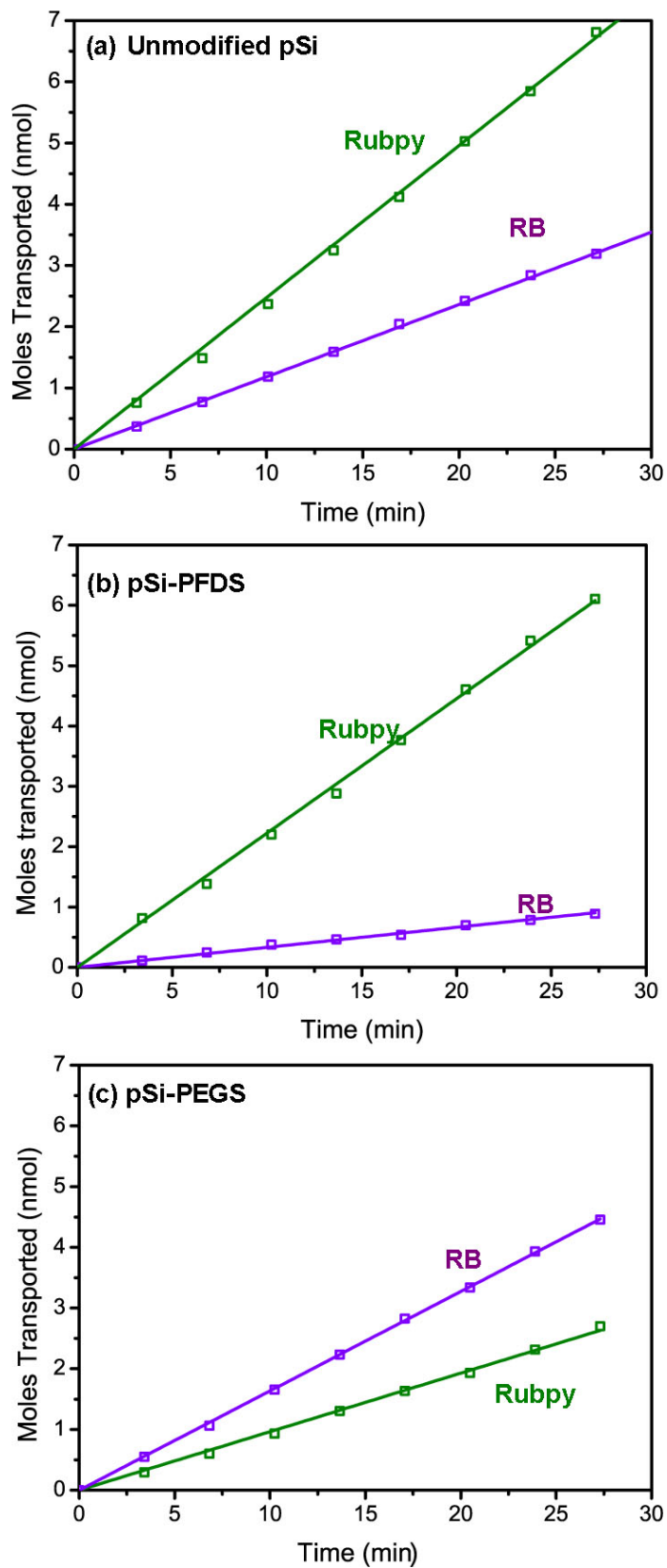


Figure 5.11: Transport of a hydrophobic (Rubpy, green series) and hydrophilic (RB, purple series) dye through pSi membranes. Where (a) is an unfunctionalised membrane, (b) is a hydrophobic (PFDS) functionalised membrane and (c) is a hydrophilic (PEGS) functionalised membrane.

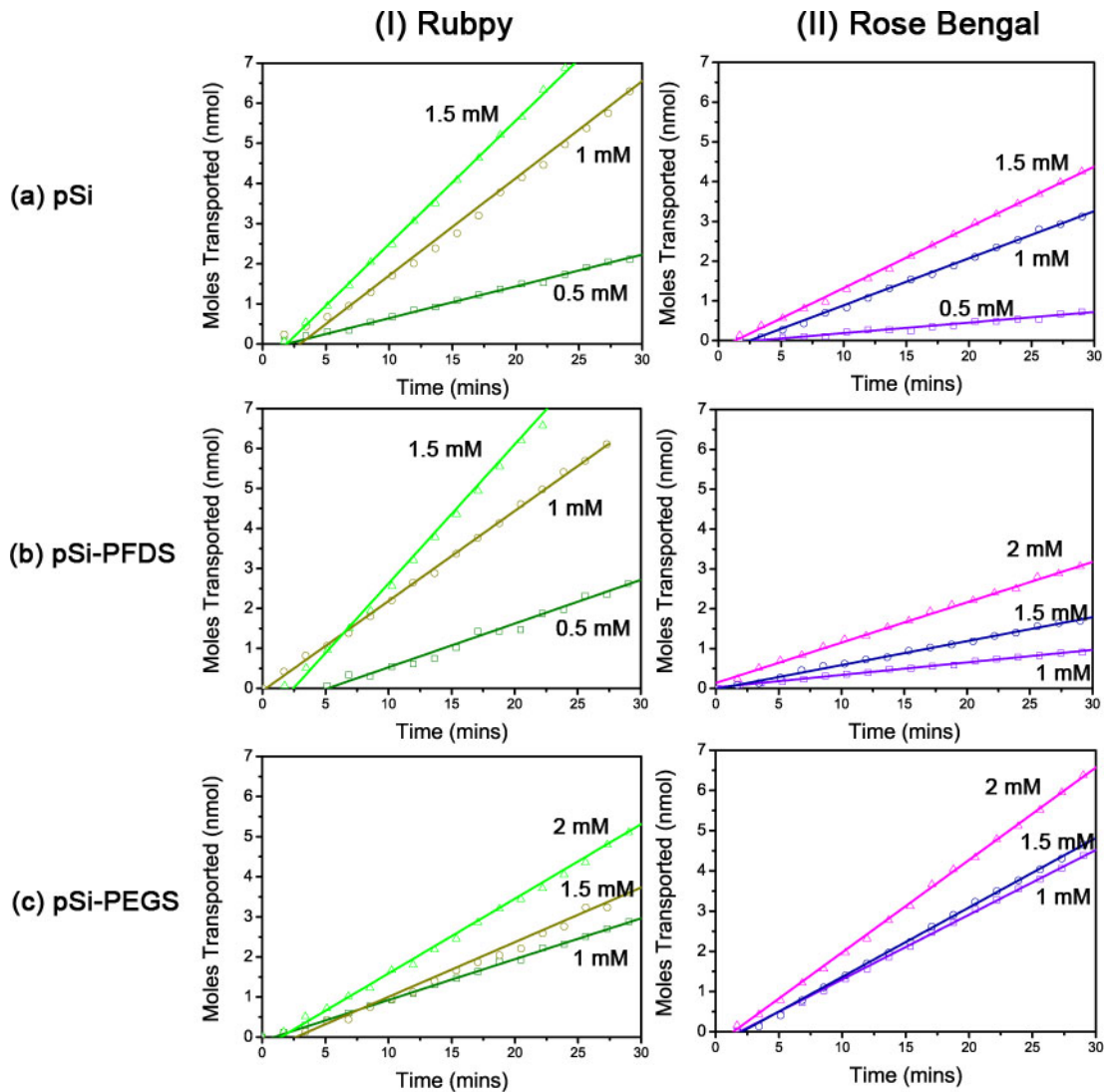


Figure 5.12: Dye transport experiments of (I) Rubpy and (II) RB through (a) unfunctionalised pSi, (b) hydrophobic pSi-PFDS and (c) hydrophilic pSi-PEGS at three different initial dye concentrations.

A summary of the permeation data of these dyes through functionalised and unfunctionalised pSi membranes is presented in Table 5.2. The pSi membrane permeability coefficients were determined from Fick's first law of diffusion (Equation 5.1) for each of the dyes by documenting the flux of the dyes through the various surface functionalised pSi membranes at a minimum of three different feed concentrations; from 0.5 to 2 mM (data for 1 mM shown in Figure 5.11 while data for multiple dye concentrations shown in Figure 5.12).

$$J = \frac{P_c(C_1 - C_2)}{L} \quad \text{Equation 5.1}$$

where J is the flux across the membrane, P_c is the permeability coefficient which describes the molecules ability to permeate into the membrane, L is the thickness of the membrane, C_1 is the concentration in the feed cell and C_2 is the concentration in the permeate cell.^[21]

The permeability coefficient can be expressed as:

$$P_c = DK \quad \text{Equation 5.2}$$

where D is the diffusion coefficient and K is the partition coefficient or “solubility” of the molecules between the membrane and the adjacent solution defined by

$$c_1 = KC_1 \quad \text{Equation 5.3}$$

which describes the partition coefficient as the concentration in the membrane (c_1) divided by the concentration in the solution adjacent to the membrane (C_1). The partition coefficient K is often found to have a more pronounced influence on the permeability or flux than the diffusion coefficient.^[21] From Stokes-Einstein law, the diffusion coefficient D of a molecule is inversely proportional to the radius of the molecule and the viscosity of the surrounding fluid.^[21] Therefore in our case the diffusion coefficient should remain relatively unchanged for each transport experiment. Hence, the major influence on the permeability and flux of a particular dye through the membrane will be due to the ability of the dye to partition into the membrane. The partition coefficient is expected to differ for the different chemical environments introduced into the membranes by means of surface functionalisation.

For an unfunctionalised pSi membrane we find that the flux of RB is 2.11 times smaller than Rubpy (Table 5.2, Figure 5.11 (a)). The observed difference in transport

Table 5.2: Flux and permeability data for Rubpy and RB transport through unfunctionalised, PFDS-functionalised and PEGS-functionalised pSi membranes.

Surface modification	Flux of permeate molecule (mol cm ⁻² h ⁻¹)		Flux ratio Rubpy: RB	Permeability coefficient (cm ² h ⁻¹)	
	Rubpy	RB		Rubpy	RB
Unfunctionalised	3.1 ± 0.17 × 10 ⁻⁷	1.5 ± 0.10 × 10 ⁻⁷	2.11	2.7 ± 0.32 × 10 ⁻⁹	1.4 ± 0.22 × 10 ⁻⁹
PFDS	2.8 ± 0.12 × 10 ⁻⁷	3.9 ± 0.16 × 10 ⁻⁸	7.13	2.9 ± 0.07 × 10 ⁻⁹	4.7 ± 0.74 × 10 ⁻¹⁰
PEGS	1.2 ± 0.01 × 10 ⁻⁷	1.9 ± 0.03 × 10 ⁻⁷	0.65	1.1 ± 0.06 × 10 ⁻⁹	1.4 ± 0.21 × 10 ⁻⁹

is due to the variation in the diffusion coefficients of the dyes which are attributed to factors such as the size, charge, shape and solubilities of the molecules in the solvent. The transport data obtained from the functionalised membranes are compared to the unfunctionalised membrane transport data in order to determine the impact of functionalisation on the transport properties of the membrane.

Figure 5.11 (b) displays the transport of Rubpy and RB through the hydrophobic PFDS modified membrane in which the transport of Rubpy through the PFDS modified membrane remains relatively unchanged in comparison to the transport through the unfunctionalised membrane (Figure 5.11 (a)) resulting in similar permeability coefficients (Table 5.2). Therefore the diffusion of the hydrophobic dye through the hydrophobic functionalised membrane is not hindered with the addition of the adsorbed monolayer and is allowed to pass freely through the membrane. Modification with silanes would be expected to slightly decrease the membrane pore size and consequently decrease the transport. However, it is also important to consider the partitioning of organic solutes into the organic SAM formed within the pores. The ability for molecules to partition into molecular layers such as SAMs and lipid bilayers and the impact this has on transport properties have been explored and reported in the recent literature.^[22-26] In our case, it is likely that the hydrophobic dye can partition into the hydrophobic silane layer and thus diffusion across the membrane can occur through both the silane layer and the solvent in the centre of the pore resulting in similar Rubpy transport rates through PFDS-modified and unfunctionalised membranes. From Figure 5.11 (b) it can be seen that the transport of RB through the PFDS modified membrane is significantly reduced in comparison to the transport through the unfunctionalised membrane (Figure 5.11 (a)). Table 5.2 shows that the permeability coefficient of RB into the PFDS-pSi membrane is approximately 2.8 times smaller than the permeability of the dye into the unfunctionalised membrane. Therefore the partition coefficient for RB transport in the PFDS-pSi membrane has decreased (Equation 5.2). The PFDS-pSi membrane exhibits a hydrophobic environment in which the hydrophilic dye would not enter into easily. Furthermore, it is unlikely that the RB will partition into the hydrophobic organic monolayer and hence the reduction of the transport rate can also be attributed to a reduction in the pore diameter from the adsorbed monolayer. These contributing factors lead to an overall decrease in the transport of RB through the PFDS-pSi

membrane. Thus the PFDS-pSi membrane facilitates the transport of hydrophobic species through the membrane while hindering the transport of hydrophilic species.

The transport rates of Rubpy and RB through the hydrophilic PEGS modified membrane is presented in Figure 5.11 (c). In this case the transport of RB through the membrane is faster than Rubpy resulting in a flux ratio of 0.65 (Table 5.2). The permeability coefficients (Table 5.2) of RB through the PEG-pSi membrane and the unfunctionalised membrane are similar therefore the ability for RB to partition into the PEG-functionalised membrane is unaffected. Furthermore, the permeability of Rubpy through the membrane has decreased considerably which is due to a reduction in the partition coefficient explained by the poor solubility of Rubpy into the hydrophilic environment formed within the pores of the membrane due to adsorption of the hydrophilic PEGS. Therefore, complementary to the transport results obtained from the PFDS-pSi membranes, the transport of hydrophilic species through the PEGS modified membrane is facilitated while the transport of the hydrophobic species is hindered due to the hydrophilic environment exhibited by the PEGS modified membrane.

From Figure 5.11 it is apparent that the PFDS-functionalised membrane favours the transport of the hydrophobic dye over the hydrophilic dye (Figure 5.11 (b)) and the PEGS-functionalised membrane favours the transport of the hydrophilic dye over the hydrophobic dye (Figure 5.11 (c)). After PFDS modification, it is seen that the flux ratio of Rubpy:RB has increased by a factor of 3.38 (from 2.11 to 7.13) while after PEGS modification the flux ratio of Rubpy:RB has decreased by a factor of 3.25 (from 2.11 to 0.65) (Table 5.2). Silane modification has therefore improved the selectivity properties of pSi membranes considerably. Thus chemical sensitivity has been imparted to the membrane through the adsorption of silanes onto the inner and outer surfaces of the membrane resulting in an enhancement in the degree of separation between hydrophilic and hydrophobic molecules. These results confirm that surface modifications can be tailored to favour the transport of molecules with a specific chemical nature.

The controlled release of materials is of interest to the field of drug delivery. Due to its intrinsic biocompatibility pSi has been investigated as a platform for *in situ* drug delivery. This can be achieved by loading drug into the porous silicon structure, thermally oxidising the pSi to entrap the therapeutic material followed by

the slow release of the drug as the pSi degrades in an aqueous environment.^[27] The pSi membranes described here could be used for the controlled release of multiple drugs within the same membrane. This could be achieved by changing the surface chemistry to control the drug release rate such that a particular drug is released quickly while another is released at a slower rate.

5.3.3 *Pressure driven water transport through pSi membranes*

In order to use pSi membranes as a scaffold water transport through CNTs, it was first necessary to ensure the pSi membranes could handle the pressure required for water transport experiments by completing pressure driven water transport through the pSi membranes. Figure 5.13 reveals the results obtained for the pressure driven transport of water through both an unfunctionalised and PFDS functionalised pSi membrane at a constant applied pressure of 0.1 barg. The rate of transport through the unfunctionalised pSi membrane was 4.97 mL min^{-1} while the pSi-PFDS membrane recorded a rate of 0.12 mL min^{-1} which corresponds to a 42 fold decrease. The surprisingly large decrease is likely to be due to the low surface energy of the hydrophobic PFDS restricting the flow of water along the walls of the membrane. The flow rate variation of the two membranes is not the important result in this experiment. The important result is that pressure driven water transport experiments can be completed on pSi and therefore pSi has the capability of being a support for a CNT membrane.

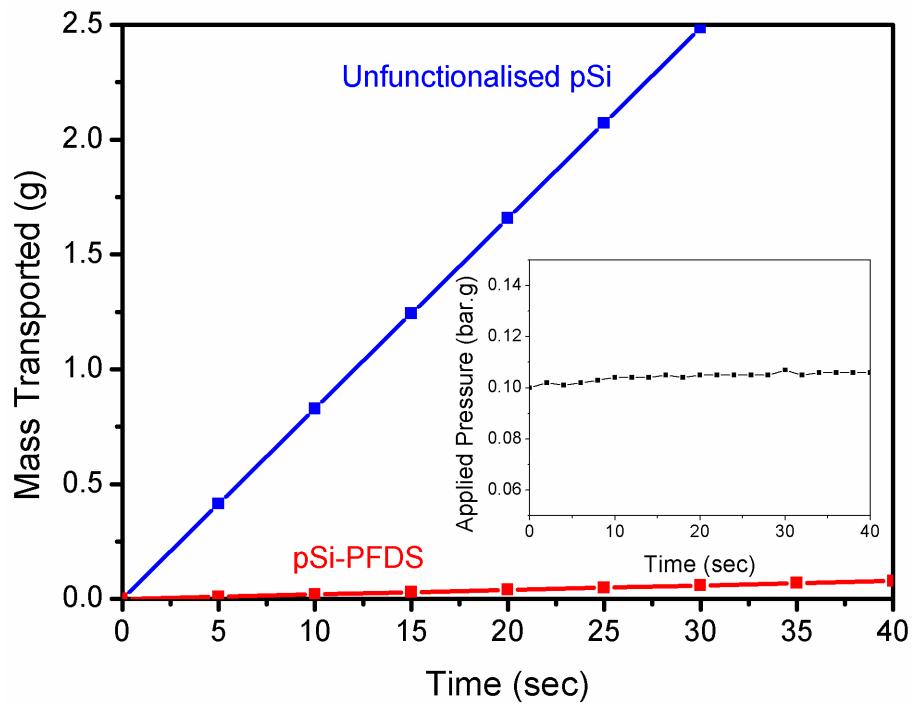


Figure 5.13: Pressure driven water transport through (blue series) unfunctionalised and (red series) PFDS (hydrophobic) functionalised pSi at a constant applied pressure (inset).

5.4 Mass transport through SWCNT membrane

5.4.1 Fabrication of SWCNT membrane

There are two major hurdles to assembling a SWCNT membrane on a pSi base. The first is chemically attaching VA-SWCNT to a pSi membrane and the second is creating a thin polymer film to fill in the gaps between the SWCNTs. Both steps are difficult and were achieved separately before combining them in the final membrane.

SWCNT attachment to a free-standing pSi membrane was completed following a slightly different method to that of the SWCNT attachment to pSi substrate. Ozone oxidation of a pSi membrane resulted in the sudden flash combustion of the membrane within a few seconds of incubation. The high surface area of the silicon hydride terminated surface makes pSi membranes particularly reactive, and is known to facilitate combustion under certain oxidising conditions.^[28] To prevent combustion, a more subtle oxidation technique was required. Thermal oxidation at 400 °C for 1 hr is a common oxidation technique for pSi and a common step prior to silane immobilisation for pSi. Incubation at over 500 °C was found to cause the combustion of the pSi membranes. APTES and SWCNT immobilisation was completed following the same conditions for flat Si and normal pSi described in Chapter 2. Figure 5.14 (a, b) shows an AFM image after 1 hr of incubation of a APTES modified pSi membrane in a SWCNT solution. The surface is completely covered with SWCNTs, more so than for comparable attachments on flat Si or pSi films (e.g., Figure 3.6 and Figure 3.13). The coverage is so high that it was foreseeable that polymer spinning between the SWCNTs will be difficult because there is no space between adjacent SWCNTs for the polymer. The high coverage of SWCNTs was found to be due to incomplete removal of physisorbed SWCNTs on the surface. Normally, adsorbed SWCNTs are removed by vigorous washing with acetone from a squirt bottle. The fragile pSi membrane could not handle such extensive cleaning in that method, leaving a great deal of non-chemically attached SWCNTs on the surface. To remove the un-bound SWCNTs sonication in acetone was attempted. After 1 min slight fraying on the edges of the pSi was observed and the sonication was stopped. AFM imaging after sonication in acetone (the same sample used in Figure 5.14 (a, b)) is shown in Figure 5.14 (c, d) where it is apparent

that a large number of SWCNTs have been removed. The surface appears similar to that observed previously (e.g., Figure 3.13) with a number of both vertically and horizontally aligned SWCNTs. Further sonication did not result in an observable difference in coverage but the membrane did begin to break apart; therefore 1 min of sonication in acetone was used after SWCNT deposition for the remainder of pSi-membrane-SWCNT surfaces. To further increase coverage of covalently attached SWCNTs, a longer deposition time was investigated. Figure 5.14 (e, f) shows a pSi membrane after 2 hr SWCNT incubation and 1 min of sonication in acetone. This surface has a much higher coverage while not being overcrowded with adsorbed SWCNTs. The gaps between the SWCNTs are clearly observable, it is anticipated that a SWCNT membrane made from surfaces such as this should have high flow rate while having gaps large enough that will allow for a polymer back-fill with good integrity. 2 hr SWCNT incubation times were therefore used for fabrication of pSi-SWCNT membranes.

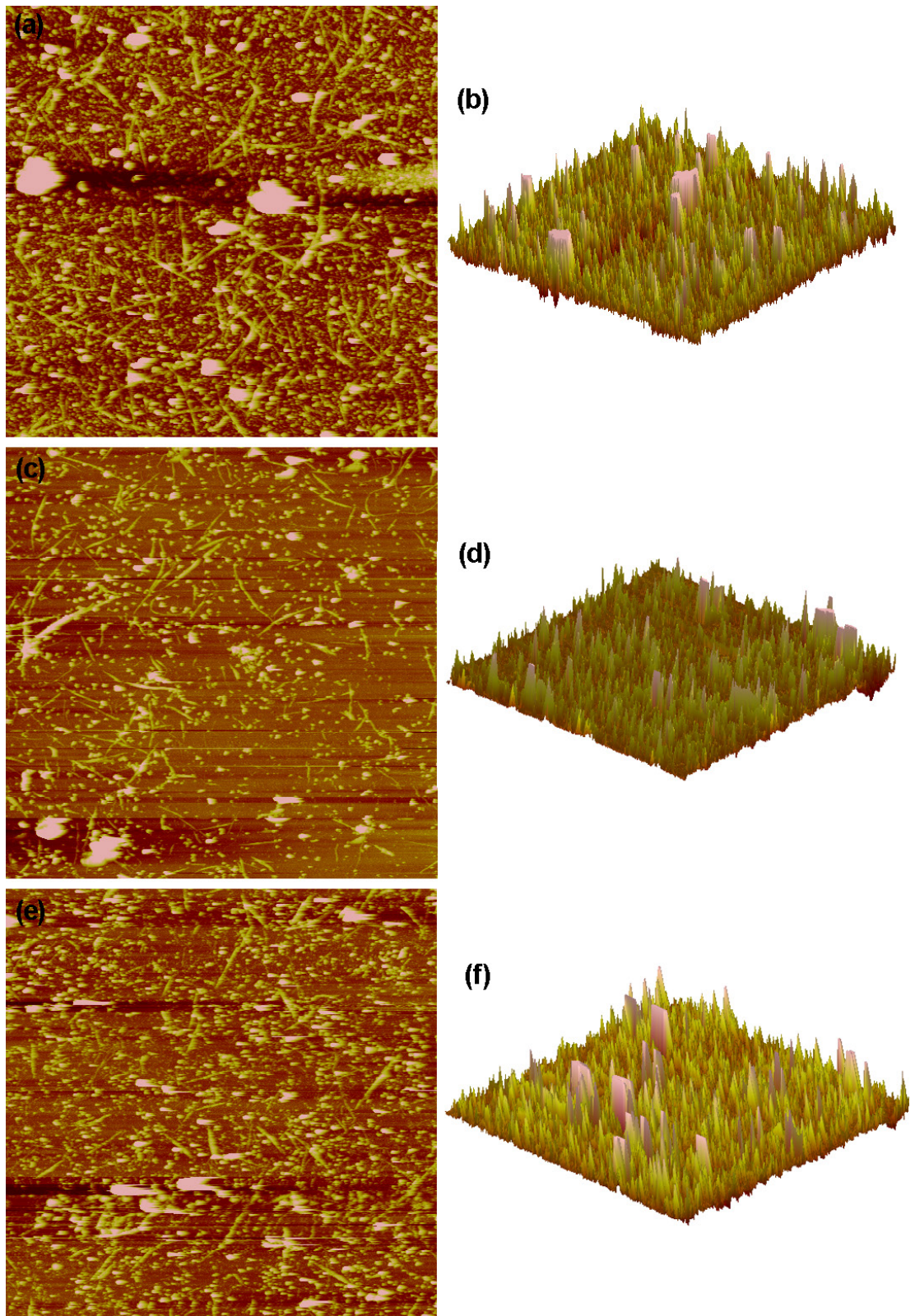


Figure 5.14: Top down (a, c, e) and 3-D (b, d, f) AFM images of SWCNTs on pSi membrane surfaces. Figures (a, b) depict a pSi membrane surface after 1 hr of SWCNT attachment, (c, d) is the same surface after sonication in acetone to remove physisorbed SWCNTs, and (e, f) is a different pSi membrane after 2 hr of SWCNT attachment and sonication in acetone.

Spin coating was chosen as the polymer deposition method as it has been used previously for the fabrication of a CNT membrane.^[4] To ensure that all gaps between the SWCNTs were filled with polymer, it was decided to spin a polymer layer of slightly greater thickness to the height of the SWCNTs and then reduce the polymer thickness by plasma oxidation to reveal the tips of the SWCNTs.

Polymer thickness and the effect of plasma oxidation was first investigated on bare flat Si. Polystyrene (PS) was mixed with toluene (1 % w/w) and dropped onto a Piranha cleaned Si wafer to cover the surface. The surface was then spun at 6000 rpm for 60 sec to produce an evenly coloured light brown film (Figure 5.15). The even colour is an early indicator that the film is of an even thickness across the entire surface. AFM analysis of the polymer films was investigated by gently scratching a cross shape on the surface using a scalpel. A control experiment was completed to ensure that the scalpel did not produce a large indent into the Si by gently scratching a cross onto a cleaned Si wafer. AFM analysis showed that the scalpel produced an indent of 1 - 2 nm in the Si, which is far less than the 20 – 50 nm of polymer that is expected to be deposited onto the Si. Figure 5.15 (a) shows AFM analysis and a microscope image of the pristine PS spun onto the Si wafer. The thickness of the film was found to be ~ 50 nm which is the approximate measured height of the SWCNTs on the surfaces and should be ample to fill the gaps between the SWCNTs. The PS was then etched by a 1 min water plasma treatment. After 1 min of water plasma the same area on the same sample was imaged again (Figure 5.15 (b)) where it was observed that the film became a slightly lighter colour and the film thickness was calculated to be ~28 nm. The same sample was then exposed to a further 1 min of water plasma. After a total of 2 min of water plasma treatment (Figure 5.15 (c)) the film became lighter again and the thickness reduced to ~ 20 nm. After 3 min of water plasma treatment (Figure 5.15) the film became almost too light to be observed and its thickness was found to be ~ 9 nm. The effect of plasma time on the PS film thickness is summarised in Table 5.3. The film reduction for the first 1 min is 22 nm which is then reduced to 8 and 11 nm for the following 1 min exposures. The large initial decrease is attributed to the removal of the more reactive polymer chains within the film.

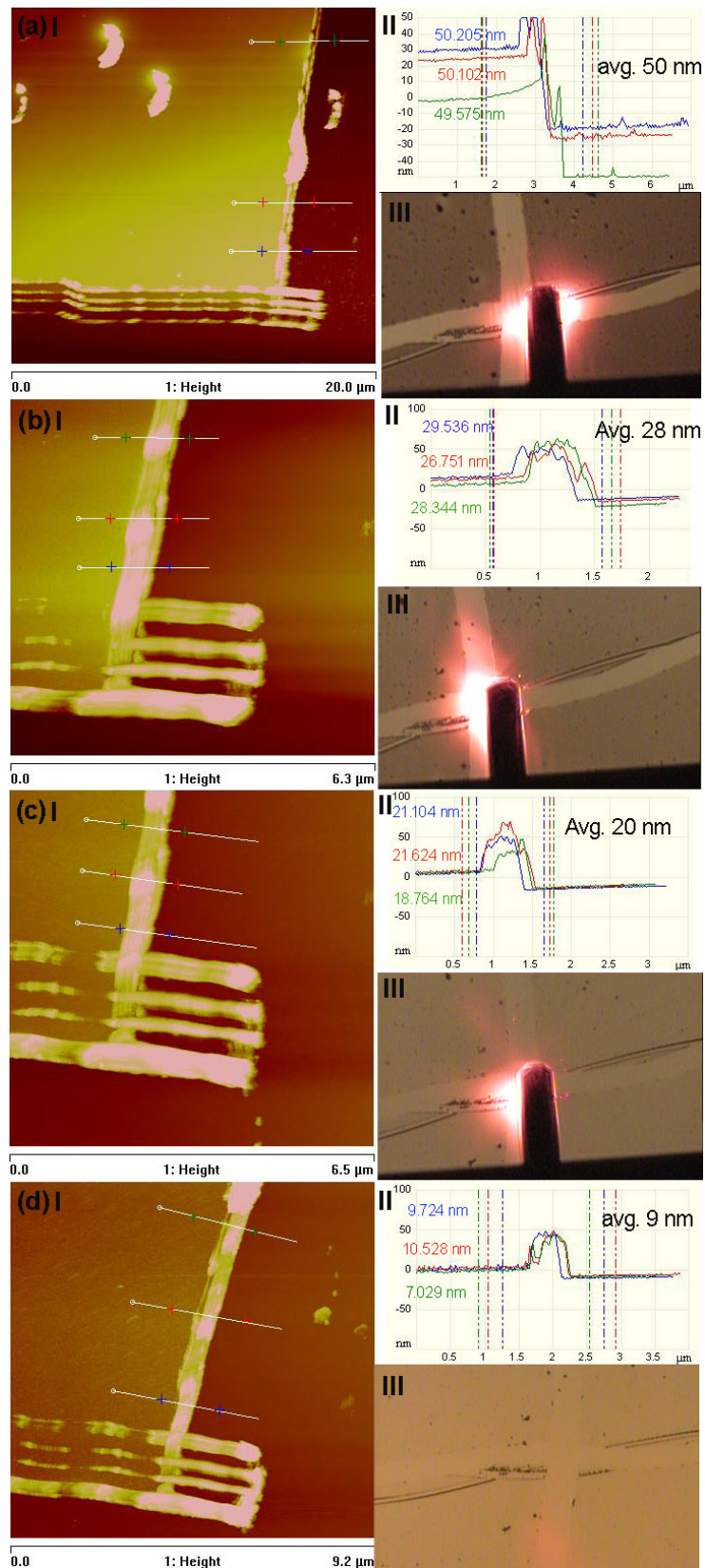


Figure 5.15: (I) AFM (II) AFM cross sectional analysis and (III) 10 x optical microscope images of polystyrene films spun onto silicon with increasing water plasma etching time: (a) 0 min, (b) 1 min, (c) 2 min, and (d) 3 min.

Table 5.3: Effect of water plasma exposure time on polystyrene thin film thickness.

Plasma exposure time (min)	PS film thickness (nm)	Total PS film reduction (nm)	PS film reduction for individual treatment (nm)
0	50	-	-
1	28	22	22
2	22	30	8
3	9	41	11

The next step was to ensure that the PS could be spun into the gaps between SWCNTs on a pSi film, prior to attempting the task on a pSi membrane. A pSi-APTES-SWCNT surface was prepared and PS was spun onto the surface following the same procedure as used for bare flat silicon. Figure 5.16 (a) shows AFM images and analysis of the surface after PS thin film deposition. Some SWCNT features can be discerned but the surface is much flatter and the features are much shorter than those observed for the pSi-APTES-SWCNT (Figure 5.14). This is because the surface has a ~50 nm layer of PS which is covering all but the tallest surface features. To reveal the tips of more SWCNTs the surface was exposed to water plasma for 1 min. After 1 min of treatment more SWCNT tips are exposed to the surface and the 3-D image shows that the features are taller. This is not because the features are physically taller but because the PS film has decreased to a thickness of ~ 35 nm which reveals more of the SWCNT (Figure 5.16). Some variation between Figure 5.16 (a, I) and Figure 5.16 (b, I) may be due to the fact that they are from a slightly different position on the same sample however the expected variation would not account for the great difference in image obtained. A further 1 min of water plasma treatment was carried out with the thickness of the PS film reduced to ~ 18 nm. A larger number of SWCNT tips are revealed with the surface now appearing very similar to the pSi-APTES-SWCNT surfaces without PS. The thickness measurement for this sample was quite difficult because the roughness of the PS layer caused by the exposed SWCNTs (Figure 5.16 (c, IV)) made the determination of the position of the top of the PS film difficult.

PS has been spun between the gaps of the SWCNTs and the SWCNT tips have been revealed by water plasma. The next step, in order to create a SWCNT membrane, was to reproduce these results on a free-standing pSi membrane with chemically attached VA-SWCNTs.

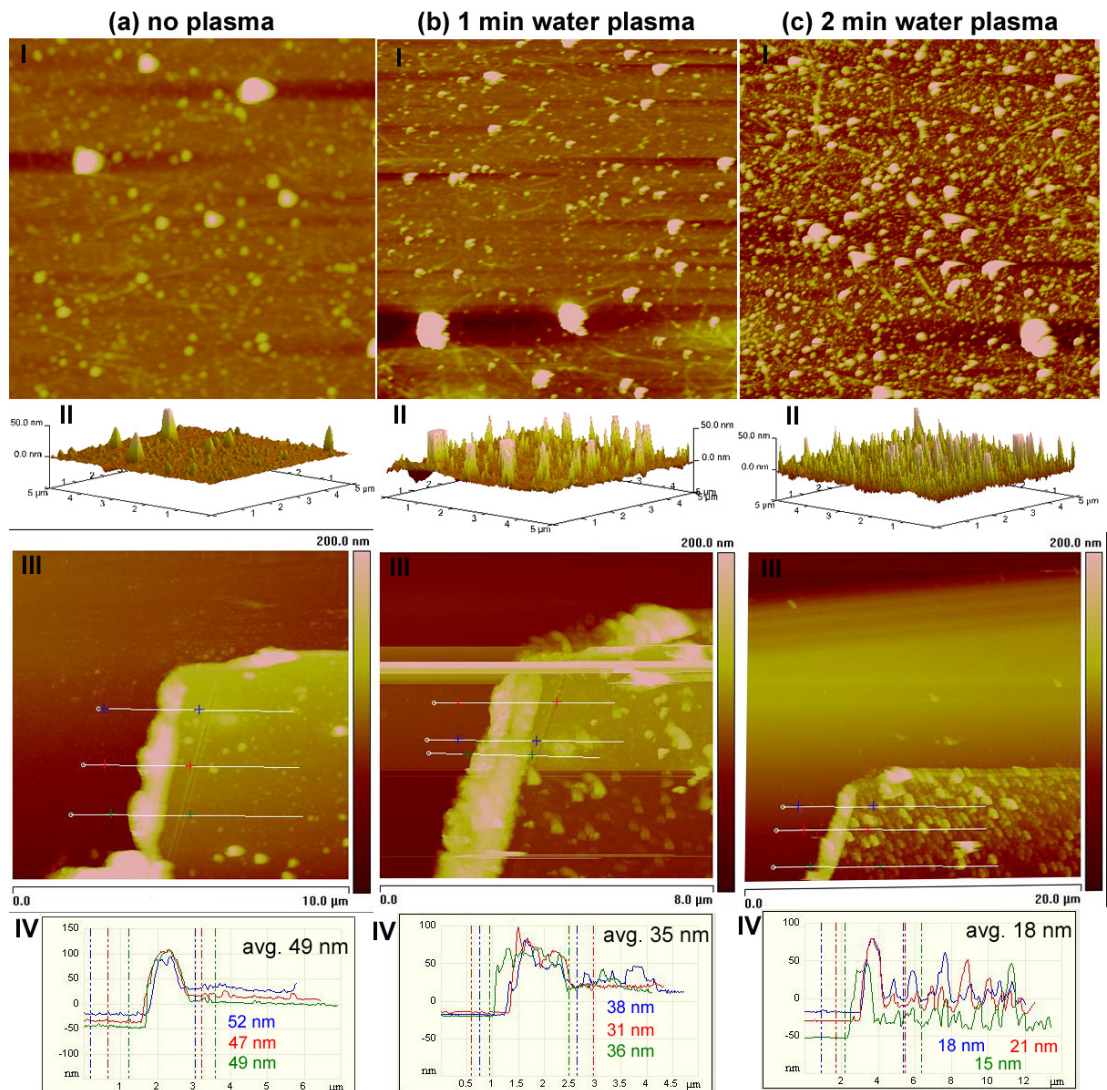


Figure 5.16: (I) Aerial AFM image ($5 \times 5 \mu\text{m}$, z scale 50 nm), (II) 3-D AFM image, (III) AFM image of scratched cross and (IV) cross section analysis of polystyrene spun onto VA-SWCNTs on pSi surfaces including (a) before water plasma exposure, (b) after 1 min of water plasma exposure and (c) after 2 min of water plasma exposure.

The PS deposition method of spin coating became an issue when it was attempted on the permeable pSi membranes. Fail safe mechanisms within the commercial spin coater operations require a vacuum to be maintained between the sample and the sample holder to hold the sample in place before it will spin. Creating a vacuum with a $\sim 70 \mu\text{m}$ thick brittle pSi membrane was difficult to achieve without cracking the membrane in the process. A system was devised where three small pieces of plain copy paper were placed between the spin coater sample holder and the pSi membrane. The slightly permeable paper served to support the pSi membrane while

creating a strong enough vacuum seal to meet the required minimum value before the fail safe mechanism would allow the spin coater to spin. Care was taken to ensure the pSi membrane was placed in the centre of the sample stage and under these conditions the sample could be spun at 6000 rpm for 1 min without damage to the sample.

SWCNTs were attached to pSi membranes and a thin film of PS was deposited via spin coating, the results obtained are summarised in Figure 5.17. It was immediately obvious under the optical microscope that the PS film was not even because of the kaleidoscope of colours observed. Each individual coloured area was imaged with the AFM to see what approximate PS thickness each colour represented. In Figure 5.17 the optical microscope image shows the exact position of the AFM cantilever prior to imaging, the area imaged is therefore the area directly under the tip of the AFM cantilever. An AFM of the purple region is shown in Figure 5.17 (a) where it is apparent that the PS film is thicker than the height of the SWCNTs. The bright light grey areas (Figure 5.17 (b)) show SWCNTs just breaking the surface of the PS layer, similar to that observed in Figure 5.16 (a) on the supported pSi substrate. A few SWCNT features can be discerned in Figure 5.17 (c) but there are very much covered in PS indicating that this area is thicker than that of Figure 5.17 (b). Figure 5.17 (d) is from an area near the edge of the sample which was a dark grey in colour, AFM imaging revealed prominent SWCNT features which would indicate that either the PS film was quite thin or perhaps there was no PS film in this area.

Within the single sample, PS film thicknesses from 0 – 100 nm were observed. This leads to variation in the number of SWCNTs revealed on the surface. Perhaps of more concern was the fact that there were potentially areas that did not have any PS coverage. The cause of the film variation is attributed to the effect of the vacuum on the PS solution. The difference between the pSi membrane and the ‘supported’ pSi films prior to pSi ‘lift-off’ is that the membrane is permeable which means that anything on top of the pSi membrane will be affected by the vacuum which is holding the pSi membrane in place on the spin coater (Figure 5.18). As the PS solution is dropped onto the pSi membrane it is being sucked into the membrane. Once the pSi membrane starts spinning the effect of the vacuum is decreased overall but it is not homogenous across the surface. The PS solution closest to the spinning axis will be spinning at a slower outward velocity and therefore the net effect of the

vacuum on the slower PS solution will be greater. The net effect of the vacuum on the polymer solution is an inhomogeneous polymer layer.

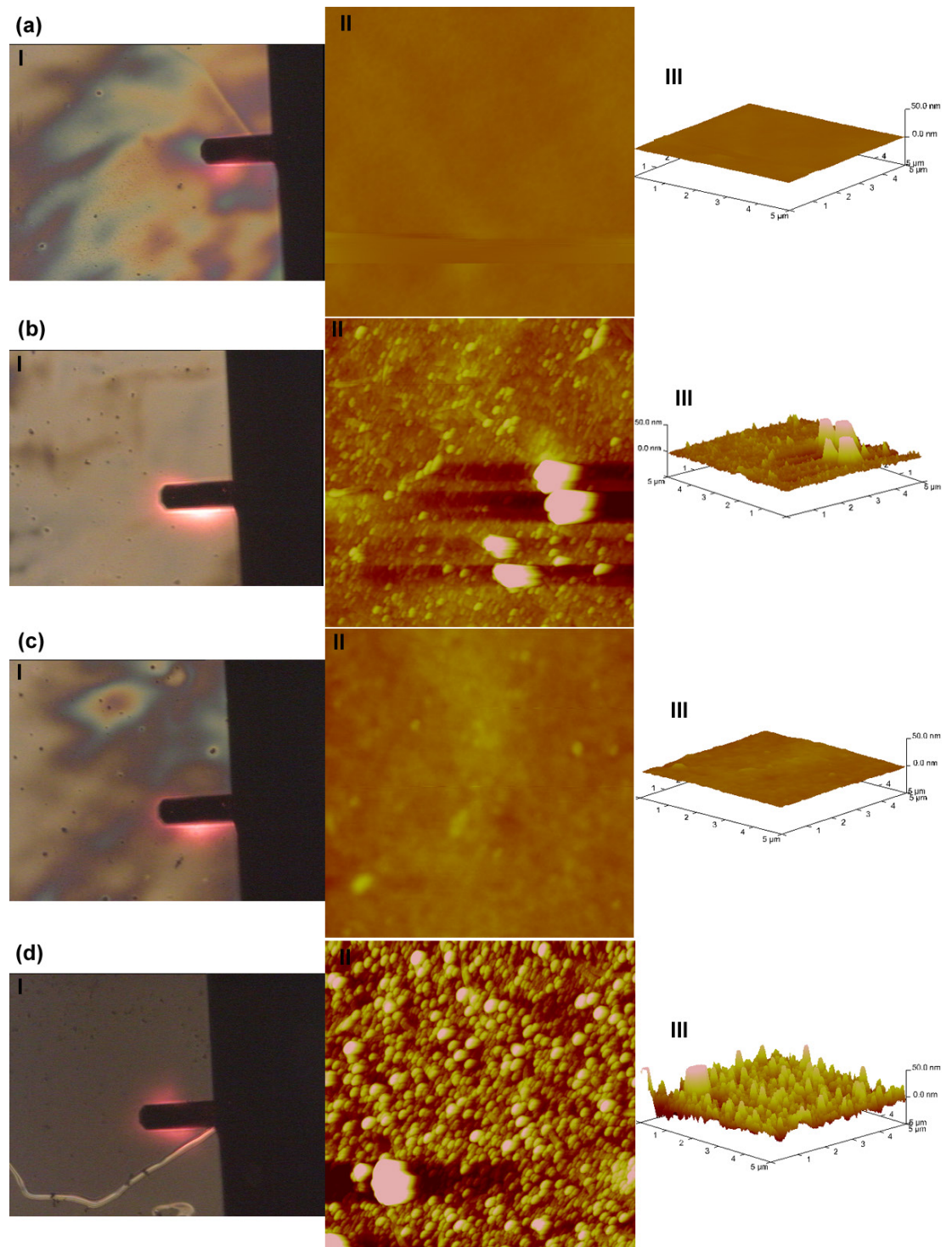


Figure 5.17: (I) Optical microscope, (II) aerial (5 x 5 μm, z scale 50 nm) and (III) 3-D AFM images of different areas (a, b, c, and d) of the same sample prepared by chemically attaching SWCNTs to a permeable pSi membrane and depositing a thin film of polystyrene.

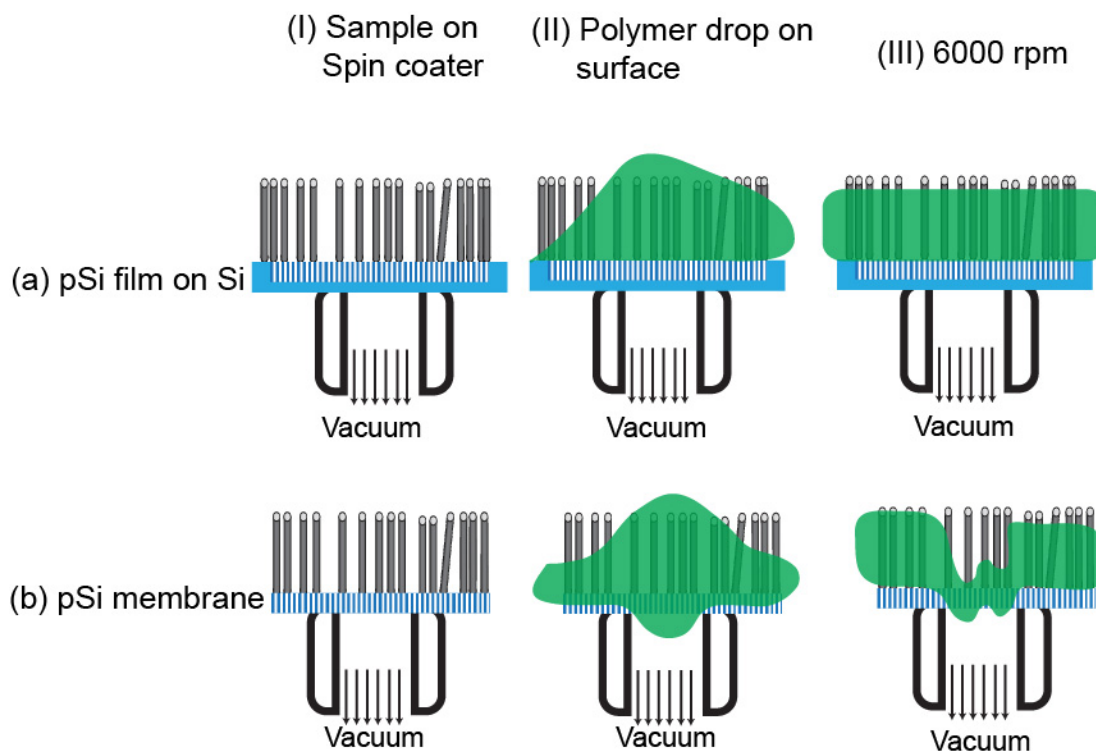


Figure 5.18: Schematic of effect of substrate on polymer deposition. (a) pSi film supported on Si substrate leads to even thin polymer film while for (b) the pSi membrane the vacuum can affect the polymer resulting in a inhomogeneous polymer film.

Changes to spinning time, spinning velocity, PS concentration, PS amount, and differing pSi membrane supports were attempted to make the PS film on the pSi membrane even. The most successful was to spin the pSi membrane and drop the PS solution onto the already spinning sample, the so called 'spin-drop' method. This had success in that a more even film was obtained, however close inspection revealed that there were pinholes in the PS film (Figure 5.19). The presence of pinholes is clearly detrimental toward creating an impermeable PS film so this method was discarded.

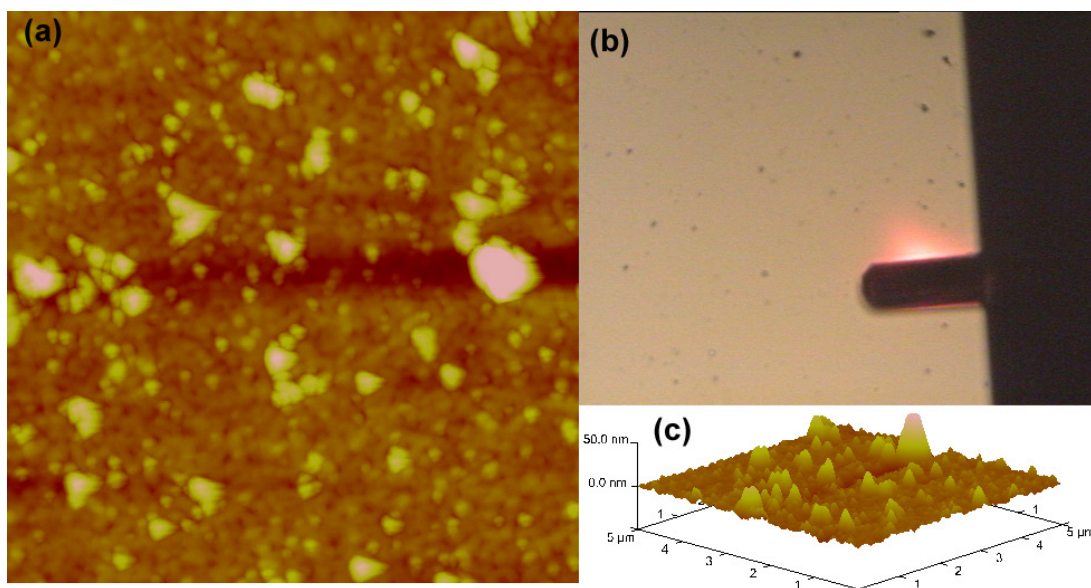


Figure 5.19: (a) Aerial AFM ($5 \times 5 \mu\text{m}$, z scale 50 nm), (b) optical microscope image, and (c) 3-D AFM image of PS thin film deposited by the ‘spin-drop’ method onto a pSi membrane-SWCNT substrate.

In order to create a membrane using the PS deposited via spin coating it was decided to spin PS in the original fashion, view the surface under the optical microscope to ensure that there were no areas without PS (these were assigned to any dark grey areas such as Figure 5.17 (d)). If bare regions were found PS was deposited onto the surface again via spin coating. After ensuring no areas bare of PS remained, it was then confirmed that regions of bright light grey colour were present (same as Figure 5.17 (b)), which were considered to be the best PS coverage for SWCNT membrane preparation. Once completed, the samples were treated with water plasma for 1 min and then sealed into mica supports prior to water transport experiments as was carried out for the pSi membranes in the dye transport experiments from Section 5.3.

5.4.2 Water transport through SWCNT membrane

The fabricated samples for water transport are summarised in Figure 5.20 with the PS covered pSi membrane control, the SWCNT membrane with areas both completely and partially covered with PS and the SWCNT membrane after water plasma where more SWCNT tips are exposed. It was deemed necessary to water plasma treat the pSi-SWCNT-PS samples prior to water transport because even though the SWCNTs appeared to be revealed and clear of polymer in some areas, it

was still a possibility that a thin blocking layer of PS was present on the SWCNT pores.

The first test completed was an attempt at pressure driven water transport through a pSi-PS surface (as represented by Figure 5.20 (a)) to ensure that the PS was capable of blocking water flow. Figure 5.21 shows (a) the mass transported at a given (b) applied pressure for a pSi-PS membrane. For this particular sample, there was no water transport for the first ~ 17.5 min of investigation as the applied pressure was slowly increased, after 17.5 min the pressure suddenly decreased and droplets of water were observed to come through the membrane. Three samples of the same type were investigated, all of which stopped flow for a short amount of time (2 - 15 min) and then a flow rate dependent upon applied pressure was observed. After removing and observing the sample it became apparent that a crack had formed in the membrane allowing water to flow through the crack. The pressure at which the three membranes broke varied from ~ 0.1 to ~ 0.8 barg. Clearly, membranes breaking at such low pressures is a limitation of these membranes. All possible methods to

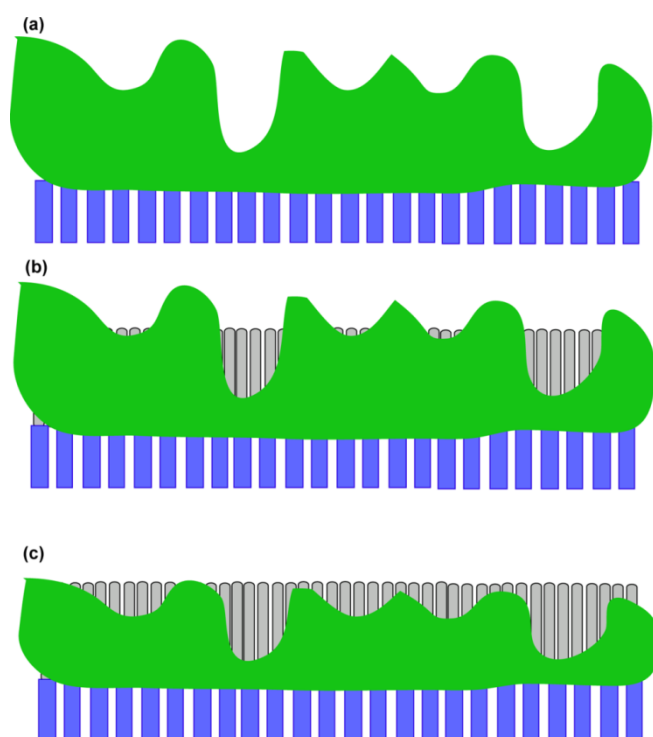


Figure 5.20: Schematic of SWCNT membranes prepared. (a) bare pSi membrane with PS thin film deposited and pSi membrane with attached VA-SWCNTs with PS deposited before (b) and after (c) water plasma exposure.

improve the strength of the membrane (thermal oxidation, increased thickness, encapsulation within mica holder) were completed prior to water transport studies. The strength of the pSi membranes could therefore not be improved further.

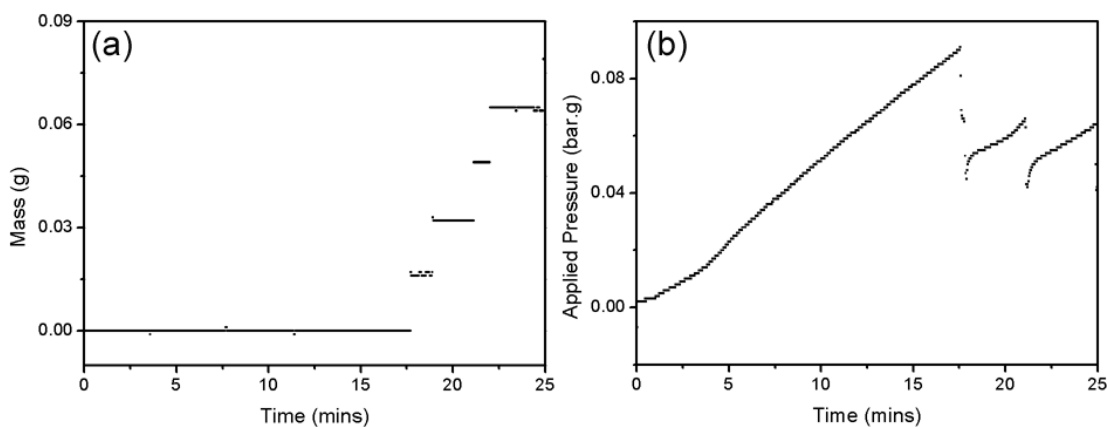


Figure 5.21: Summary of pressure driven water flow through pSi-PS sample showing (a) mass of water transported and (b) applied pressure vs. time.

After ensuring that a PS layer could block water flow, a pSi-SWCNT-PS membrane treated with 1 min of water plasma membrane was investigated. Three samples were investigated, two of which broke early at low pressures before any water transport was recorded or observed (~ 0.1 barg). The results obtained for the third membrane are shown in Figure 5.22. The sample was remarkably resilient and it could withstand a pressure of up to 1.4 barg before breaking after over 3 hr. During the 3 hr of the experiment the membrane holder nipple was constantly observed to determine if a water droplet was forming. At an applied pressure of 0.23 barg it was observed that a water droplet was beginning to form. The motor-controlled syringe needle that was applying the pressure had to continually move as an operation condition of the apparatus. This meant that the pressure would continually rise until the flow rate coming out of the membrane equalled the minimum syringe application rate (0.01 mL min^{-1}). Eventually, the single drop became large enough to drop onto the scales to be recorded (at just over 3 hr). Another drop was forming and was almost at its maximum size and about to drop when the membrane broke (at 3.4 hr) and no further investigation could be completed. Figure 5.22 (c) shows the raw data from the weighing balance prior to and just after the recorded drop of water. It is clear that during the long time scale of the experiment, some drift and perhaps some evaporation in the recorded weight has occurred. To remove the drift, the net

increase in mass is recorded in Figure 5.22 (d) where any negative values from drift or evaporation are cancelled out. The data obtained in Figure 5.22 (d) will be used for further calculations where 12 mg of water was transported through the 0.049 cm^2 membrane over 3 hr.

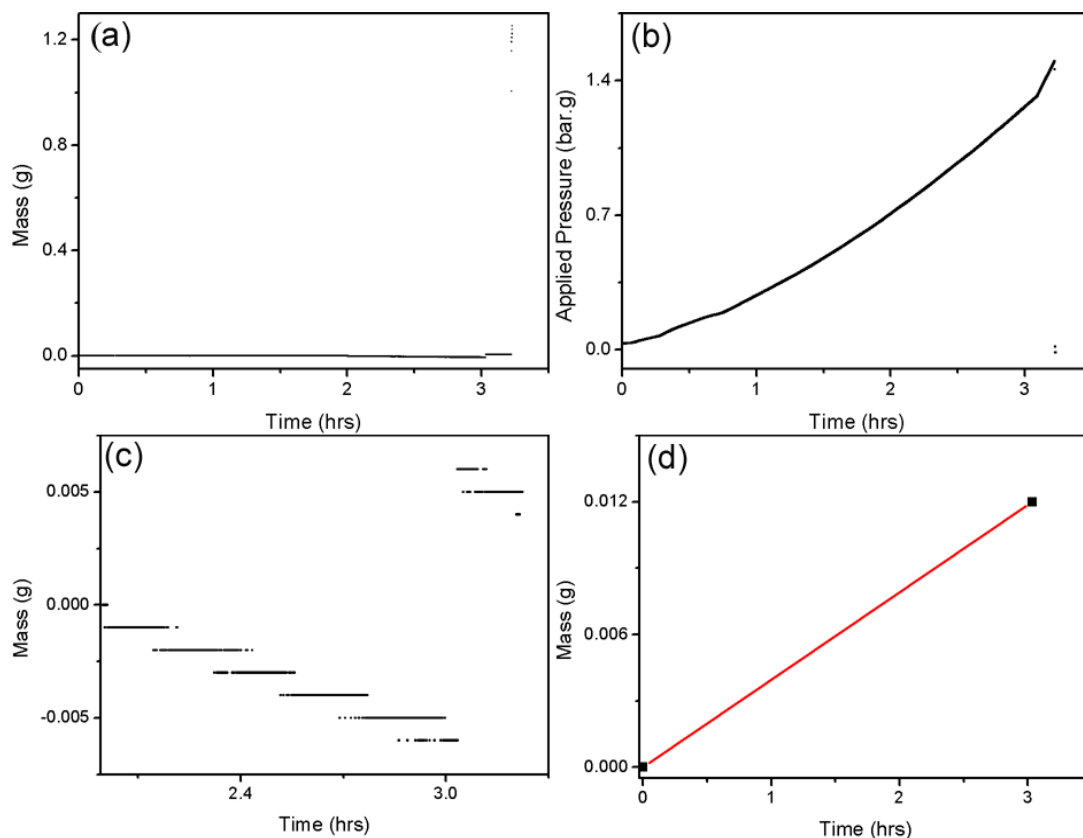


Figure 5.22: Summary of water flow through pSi-SWCNT-PS (1 min water plasma) showing (a) raw data of mass of water collected (b) applied pressure (c) zoom of area from 2.1 to 3.4 hr, and (d) scale drift removed data vs. time.

The water flow rate could be improved if the applied pressure were increased. Due to the fragility of the pSi membranes this was not an option. Chemical attachment of SWCNT to polycarbonate and porous alumina membranes was attempted. It was found that the pore size (100 nm for polycarbonate, ~ 50 nm for porous alumina) was too high for the SWCNT bundles to attach over the pores.

The total volume of water transported was quite low, but the active surface area (0.049 cm^2) and applied pressure (averaged to 1 barg) was also quite low when compared to commercial nanofiltration membranes where upwards of 5 bar of pressure is applied to a membrane of 5 m^2 or greater. The permeability of the pSi-

SWCNT-PS 1 min plasma membrane was calculated to be $0.022 \text{ mm}^3 \text{ cm}^{-2} \text{ s}^{-1} \text{ atm}^{-1}$. To put the obtained permeability into perspective, Table 5.4 compares the permeability values of experimental and theoretical CNT membranes. The MWCNT membrane fabricated by the group of Hinds produced a membrane with a permeability of 450 to 800 times higher while the group of Holt produced a DWCNT membrane with a permeability of 90 to 360 times greater.^[3,4] The comparatively low permeability of our pSi-SWCNT membranes is attributed to two factors. The first is that the individual SWCNTs have a smaller pore area which will reduce the effective porosity of the surface. The second is that in order to produce a membrane that had no gaps between the SWCNTs it was ensured that the polymer layer was at least as thick as the VA-SWCNTs prior to water plasma. Coupled with the unevenness of the polymer film when spun onto the pSi membrane it produced surfaces such as that shown in Figure 5.20 (b) where only a small percentage of the VA-SWCNT are protruding from the polymer matrix. This will lead to a very low number of available SWCNT pores per unit area and subsequently a low permeability.

Table 5.4: Comparison of membrane permeability between experimental and theoretical carbon nanotube membranes

Experimental CNT Membranes	CNT type	Pore Diameter (nm)	Pores per cm^2	Permeability ($\text{mm}^3 \text{ cm}^{-2} \text{ s}^{-1} \text{ atm}^{-1}$)
pSi-SWCNT-PS 1 min plasma membrane	SWCNT	1.4	?	0.022
Hinds <i>et al.</i> ^[4]	MWCNT	7	1×10^9	10 to 17
Holt <i>et al.</i> ^[3]	DWCNT	1.6	2.5×10^{11}	2 to 8
Theoretical CNT Membranes				
Corry <i>et al.</i> ^[5]	(5, 5) SWCNT	0.66	2.5×10^{11}	0.034
	(6, 6) SWCNT	0.81	2.5×10^{11}	0.058
	(7, 7) SWCNT	0.93	2.5×10^{11}	0.090
	(8, 8) SWCNT	1.09	2.5×10^{11}	0.14

Corry et al.^[5] carried out a theoretical study on the applicability of SWCNT membranes for reverse osmosis. In order to simulate a CNT membrane, he set up simulations of SWCNTs of varying diameter embedded within an otherwise impermeable matrix. The CNT density (pores cm^{-2}) he used was the same as the DWCNT membrane fabricated by Holt. Corry's calculations found that the permeability of the various SWCNT membranes varied from 0.034 to 0.14 $\text{mm}^3 \text{cm}^{-2} \text{s}^{-1} \text{atm}^{-1}$ depending upon the SWCNT diameter. The membranes of Corry's calculations vary from 1.5 to 6.4 times greater than the permeability calculated for our membrane.

In order for a CNT membrane to become commercially viable, it must improve upon current technologies. Specifically it must improve upon one or more performance factors including permeability, salt rejection, and cost. Table 5.5 details the membrane type, salt rejection and permeability of various polyamide membranes distributed by DOW Water & Process Solutions. There is a clear inverse correlation between salt rejection and permeability. The membranes designed for nanofiltration and brackish water desalination show permeability values of 9 and 4 times greater than our pSi-SWCNT membrane. The salt water RO membrane has a permeability of approximately 64 % that of our membrane but it does reject 99.7 % of salts. The pSi-SWCNT-PS membrane, although it shows a low permeability when compared to other CNT membranes, has permeability comparable to commercial RO membranes. Although salt rejection tests were not investigated on our membrane, Corry predicted that a 1.09 nm diameter SWCNT would reject 58 % of salt ions. A rough extrapolation to the 1.4 nm diameter SWCNTs used in our membranes indicates that the salt rejection would be much lower (<30 %) than any commercial nanofiltration/RO membrane. However, our membranes currently have a comparable flow to such RO membranes but it is envisaged that the permeability will be greatly increased if the SWCNT porosity is increased. The low rejection of 1.4 nm SWCNT could be improved by utilising the carboxylic acid functional groups that decorate the functionalised SWCNT pore. Specific molecules can be attached to the pore to act as gate-keeper's to increase the salt rejection.

Table 5.5: Permeability values for commercial^a polyamide thin film composite nanofiltration and reverse osmosis membranes

DOW Product Number	Membrane type	Salt Rejection (%)	Permeability ($\text{mm}^3 \text{cm}^{-2} \text{s}^{-1} \text{atm}^{-1}$)
NF90-4040	nanofiltration brackish water	95.0	0.200
TW30-4040	RO	99.5	0.094
SW30HR-380	Salt water RO	99.7	0.014

^a from “DOW Water & Process Solutions”, <http://www.dowwaterandprocess.com/>

In order to fabricate a commercially viable SWCNT membrane for desalination, SWCNTs of diameter of 0.93 nm or less must be utilised with a pore density of $\sim 1 \times 10^{11}$ pores cm^{-2} in order to achieve both high permeability and salt rejection. Vertically aligned CVD growth of such SWCNTs has not yet been achieved. Therefore, the only possible method to produce a low diameter SWCNT membrane is to purchase randomly aligned SWCNTs and then fabricate a membrane following a method such as that attempted here or possibly following the microtome method.^[29, 30] Currently to purchase SWCNT of 0.8 nm to 1.3 nm diameter is US\$ 2000 per gram (<http://www.nanointegris.com/en/hipco>, 13/4/11), which makes such a membrane commercially unviable.

Due to the fragility of the pSi membrane, it will have to be replaced, perhaps by a porous membrane that consists of a network of pores (not single 1-D pores that span the entire membrane) such as a commercial ultrafiltration membrane however chemical attachment and vertical alignment of SWCNTs to such membranes may not be possible. The pSi base could be removed completely if the SWCNTs and polymer matrix are strong enough to be self-supporting. Completing the polymer deposition on flat Si will allow for the spinning of an even polymer film, removing the SWCNT-polymer composite will then yield a highly porous SWCNT membrane. This will require longer ($>1 \mu\text{m}$) VA-SWCNTs which have not yet been achieved following the chemical attachment method.

5.5 Conclusions

A SWCNT membrane supported upon a pSi membrane has been fabricated. The pSi membrane was found to be strong enough for both the diffusion of dyes and pressure driven water transport. The diffusion of dyes is an example of a system where the pSi membranes could be used to release multiple species at different rates. This concept could find applications in drug delivery.

The SWCNT membrane fabrication was monitored at each step by AFM. Each specific step could be achieved on supported pSi, but the spin coating of polystyrene on the pSi membrane led to an uneven film which drastically affected all subsequent results. Pressure driven water transport was achieved with a membrane permeability of $0.022 \text{ mm}^3 \text{ cm}^{-2} \text{ s}^{-1} \text{ atm}^{-1}$ was recorded. The permeability value was 90 – 800 times slower than previously reported CNT membranes.

A low diameter SWCNT membrane could potentially be fabricated using the chemical attachment method to produce a high selectivity, high permeability desalination/nanofiltration membrane. To accomplish this goal more work needs to be carried out on improving both the SWCNT support structure and the polymer matrix.

5.6 References

- [1] J. K. Holt, "Carbon Nanotubes and Nanofluidic Transport", *Advanced Materials*, **21** (35), 3542-50 (2009).
- [2] J. C. Rasaiah, S. Garde, and G. Hummer, "Water in Nonpolar Confinement: From Nanotubes to Proteins and Beyond *", *Annual Review of Physical Chemistry*, **59** (1), 713-40 (2008).
- [3] J. Holt, H. Park, Y. Wang, M. Stadermann, *et al.*, "Fast Mass Transport Through Sub-2-Nanometer Carbon Nanotubes", *Science*, **312**, 1034 (2006).
- [4] M. Majumder, N. Chopra, R. Andrews, and B. J. Hinds, "Enhanced flow in carbon nanotubes", *Nature*, **438**, 44 (2005).
- [5] B. Corry, "Designing Carbon Nanotube Membranes for Efficient Water Desalination", *The Journal of Physical Chemistry B*, **112** (5), 1427-34 (2008).
- [6] J. K. Holt, A. Noy, T. Huser, D. Eaglesham, *et al.*, "Fabrication of a Carbon Nanotube-Embedded Silicon Nitride Membrane for Studies of Nanometer-Scale Mass Transport", *Nano Letters*, **4** (11), 2245-50 (2004).
- [7] B. J. Hinds, N. Chopra, T. Rantell, R. Andrews, *et al.*, "Aligned Multiwalled Carbon Nanotube Membranes", *Science*, **303**, 62 (2004).
- [8] J. Liu, A. G. Rinzler, H. Dai, J. H. Hafner, *et al.*, "Fullerene Pipes", *Science*, **280** (5367), 1253-6 (1998).
- [9] P. C. Searson, "Porous silicon membranes", *Applied Physics Letters*, **59** (7), 832-3 (1991).
- [10] S. Cruz, A. Honig-dOrville, and J. Muller, "Fabrication and optimization of porous silicon substrates for diffusion membrane applications", *Journal of The Electrochemical Society*, **152** (6), C418-C24 (2005).
- [11] C. S. Solanki, R. R. Bilyalov, J. Poortmans, J.-P. Celis, *et al.*, "Self-Standing Porous Silicon Films by One-Step Anodizing", *Journal of The Electrochemical Society*, **151** (5), C307 (2004).
- [12] D. R. Turner, "Electropolishing Silicon in Hydrofluoric Acid Solutions", *Journal of The Electrochemical Society*, **105** (7), 402-8 (1958).
- [13] S. Fiorilli, P. Rivolo, E. Descrovi, C. Ricciardi, *et al.*, "Vapor-phase self-assembled monolayers of aminosilane on plasma-activated silicon substrates", *Journal of Colloid and Interface Science*, **321** (1), 235-41 (2008).
- [14] Y. H. Liu, X. K. Wang, J. B. Luo, and X. C. Lu, "Fabrication and tribological properties of super-hydrophobic surfaces based on porous silicon", *Applied Surface Science*, **255** (23), 9430-8 (2009).
- [15] A. Ressine, D. Finnskog, G. Marko-Varga, and T. Laurell, "Superhydrophobic Properties of Nanostructured–Microstructured Porous Silicon for Improved Surface-Based Bioanalysis", *NanoBioTechnology*, **4** (1), 18-27 (2008).
- [16] V. Sharma, M. Dhayal, Govind, S. M. Shivaprasad, *et al.*, "Surface characterization of plasma-treated and PEG-grafted PDMS for micro fluidic applications", *Vacuum*, **81** (9), 1094-100 (2007).
- [17] J. F. Moulder, W. F. Stickle, P. E. Sobol, and K. D. Bomben, "Handbook of X-ray Photoelectron Spectroscopy", *Perkin-Elmer Corporation*, Eden Prairie, (1992).
- [18] B. H. Stuart, "Infrared Spectroscopy: Fundamentals and Applications", *Wiley-VCH*, Chichester, England, (2004).

- [19] D. Rosu, L. Rosu, and C. N. Cascaval, "IR-change and yellowing of polyurethane as a result of UV irradiation", *Polymer Degradation and Stability*, **94** (4), 591-6 (2009).
- [20] A. Fick, "Poggendorff's Annel", *Physik*, **94**, 59-86 (1855).
- [21] E. L. Cussler, "Diffusion: Mass transfer in fluid systems", *Cambridge University Press*, (2009).
- [22] D. Bemporad, J. W. Essex, and C. Luttmann, "Permeation of small molecules through a lipid bilayer: A computer simulation study", *Journal of Physical Chemistry B*, **108** (15), 4875-84 (2004).
- [23] S. Paula, A. G. Volkov, A. N. VanHoek, T. H. Haines, *et al.*, "Permeation of protons, potassium ions, and small polar molecules through phospholipid bilayers as a function of membrane thickness", *Biophysical Journal*, **70** (1), 339-48 (1996).
- [24] A. Janshoff, and C. Steinem, "Transport across artificial membranes - an analytical perspective", *Analytical and Bioanalytical Chemistry*, **385** (3), 433-51 (2006).
- [25] M. Ulbricht, "Advanced functional polymer membranes", *Polymer*, **47**, 2217-62 (2006).
- [26] D. J. Odom, L. A. Baker, and C. R. Martin, "Solvent-extraction and Langmuir-adsorption-based transport in chemically functionalized nanopore membranes", *Journal of Physical Chemistry B*, **109** (44), 20887-94 (2005).
- [27] E. J. Anglin, L. Cheng, W. R. Freeman, and M. J. Sailor, "Porous silicon in drug delivery devices and materials", *Advanced Drug Delivery Reviews*, **60** (11), 1266-77 (2008).
- [28] J. M. Schmeltzer, and J. M. Buriak, Recent Developments in the Chemistry and Chemical Applications of Porous Silicon in *The Chemistry of Nanomaterials: Synthesis, Properties and Applications* (Eds.: C. N. Rao, A. Müller, A. K. Cheetham), Wiley, Weinheim, 2005, pp. 518-50.
- [29] L. Sun, and R. M. Crooks, "Single Carbon Nanotube Membranes: A Well-Defined Model for Studying Mass Transport through Nanoporous Materials", *Journal of the American Chemical Society*, **122** (49), 12340-5 (2000).
- [30] X. Sun, X. Su, J. Wu, and B. J. Hinds, "Electrophoretic Transport of Biomolecules through Carbon Nanotube Membranes", *Langmuir*, **7** (6), 3150-6 (2011).

Chapter 6

Field emission from CNT electrodes

CNT field emission electrodes were fabricated using the chemical attachment method. SWCNT, DWCNT and MWCNTs were found to field emit with low turn-on voltages and high electric field enhancement factors. The emission stability from each CNT type was found to vary significantly. The emission from the SWCNTs was found to be most stable, which is contradictory to other reported results.

6.1 Introduction

Electron field emission (FE) from CNTs has been an intensely researched topic since the initial reports of the phenomenon in 1995.^[1] This high level of interest is predominantly due to the inherent properties of CNTs, such as the high conductivity and large aspect ratio, which lead to a high maximum current output and low turn-on voltage (E_{to}).^[2, 3] In order to utilise the full effects of the large aspect ratio of the CNTs, it is advantageous to have the CNTs vertically aligned on a substrate. Vertical alignment increases the electric field enhancement, β , around the CNT which reduces the macroscopic applied field required for field emission.^[4]

Much of the previous work has focused upon either directly growing the CNTs from the surface using CVD^[5, 6] or by incorporating the CNTs into a paste and printing them onto a surface.^[7, 8] CVD growth of CNTs leads to a greater control of alignment with the ability to produce an array of vertically-aligned CNTs. However, it is difficult to grow the different CNT types without vastly changing the experimental procedure.^[9] The screen printing method is easily interchangeable between the CNT types, but there is little control over the alignment of the CNTs. Both of these techniques have the drawback of very weak adhesion between the CNTs and the surface which reduces emission stability.^[10, 11]

Field emission from the different CNT types is thought to vary significantly as a result of the difference in diameter and hence aspect ratio. However, very few direct comparisons exist between the field emission from the various CNT types. The accepted theory is that SWCNTs exhibit the best FE characteristics while MWCNTs produce the most stable emission.^[3] This hypothesis is a result of the single shelled SWCNT having the highest aspect ratio whereas the multiple shelled MWCNTs are more robust and are less affected by common FE degradation mechanisms such as ion bombardment.^[8, 11] Recent reports show that DWCNTs have the potential to have even greater FE characteristics than SWCNTs while their extra wall should also improve their stability.^[12] Indeed, the high emission stability of MWCNTs, along with their low cost and ease of manufacture, has resulted in many studies based upon improving of the FE characteristics of MWCNT FE devices.^[13]

In this Chapter, the field emission characteristics and stability from SW-, DW- and MWCNTs chemically attached to Si will be investigated (Figure 6.1). The Si-DWCNT surfaces have the potential to improve upon the field emission properties obtained for the Si-SWCNT surface by maintaining good FE characteristics and improving emission stability. The chemical attachment of the cheaper MWCNTs (when compared to DWCNTs and SWCNTs) could potentially produce a more cost effective FE substrate without significantly decreasing the FE properties.

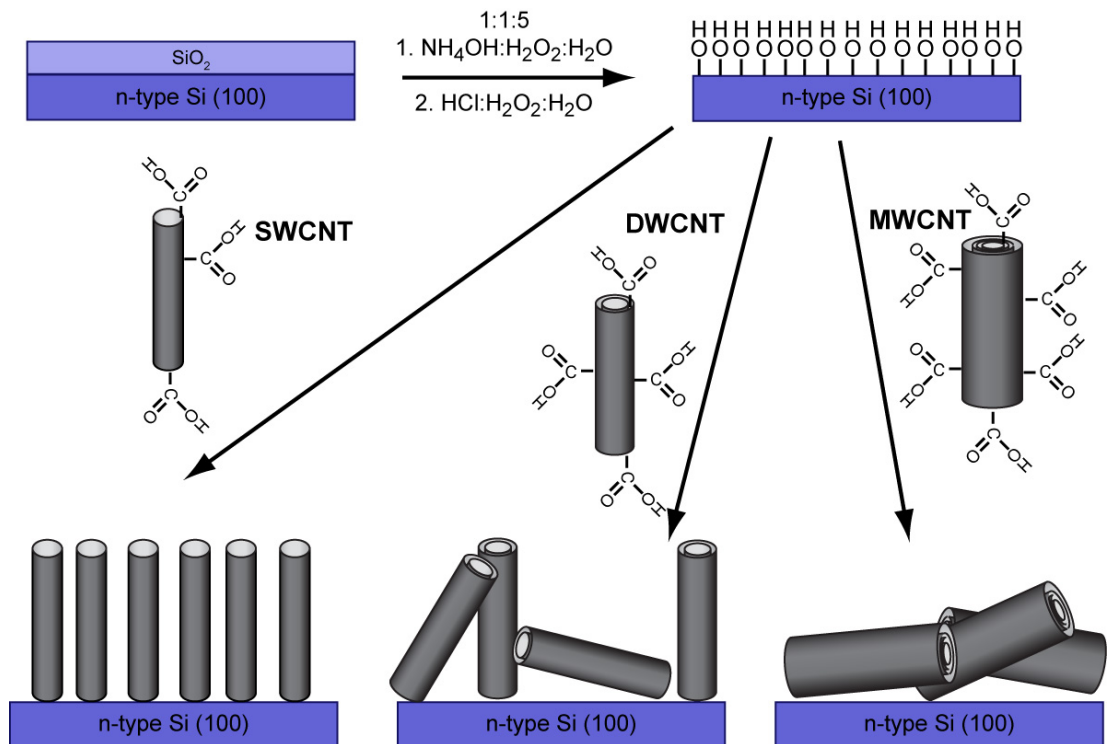


Figure 6.1: Schematic of prepared samples for field emission studies.

6.2 Experimental details

Direct ester attached CNTs were fabricated on antimony doped silicon (n-type, 100 orientation, 0.5 mm thickness, 0.008 – 0.02 Ω cm, Silicon Quest International, USA) following the methods described in Chapter 2. n-type silicon was used as the excess of electrons within the silicon lattice is preferential for field emission studies. The direct ester attachment was used as it involves no linker molecule which could potentially reduce electron transport between the substrate and the CNT.

Field emission experiments were carried out at the Centre for Organic Electronics in the School of Physics at the University of Newcastle in New South Wales in 2008 and 2011. The FE chamber was specifically built to investigate the field ionisation of helium but FE experiments could be carried out with little change in configuration.

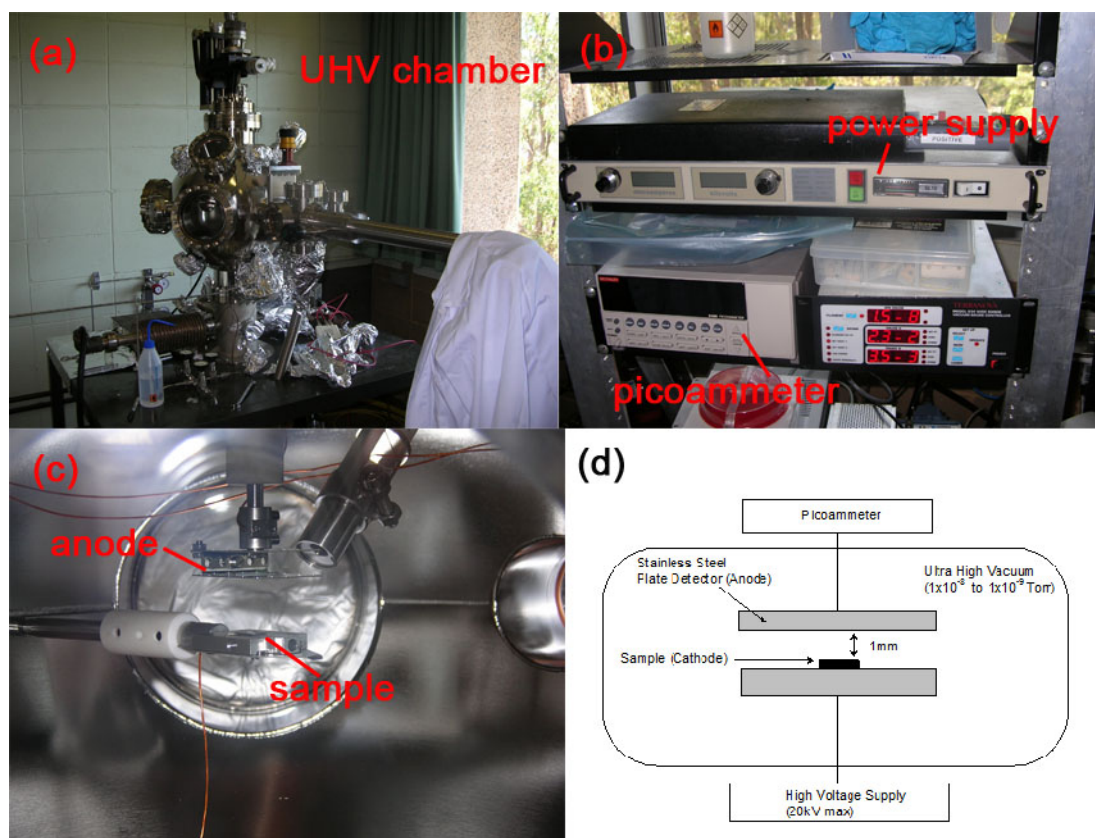


Figure 6.2: Field emission system at the University of Newcastle showing (a) ultra-high vacuum chamber, (b) power supply and picoammeter, (c) sample stage configuration and (d) schematic of field emission experimental apparatus.

FE measurements were performed using both 1 cm² and the 0.25 cm² Si-CNT samples as cathodes separated by a known distance from a metallic anode within an ultrahigh vacuum (Figure 6.2). A large potential difference is applied between the electrodes and the output current is measured. The emitted electrons were collected on a highly-polished stainless steel counter electrode under an average ultrahigh vacuum of $\sim 6 \times 10^{-9}$ Torr (range from 1×10^{-9} - 1×10^{-8} Torr). The distance between the electrodes was measured using a micrometer screw and found to be 2.17 mm for the 2008 experiments and 1.82 mm in 2011. A Spellman SL10 high voltage source unit was used to supply the voltage (up to 8000 V). The FE current produced at the anode was measured using a Keithley 6485 picoammeter. An in-house program written in LabView 8.2 was used to control the voltage and current as well as record the data. Conditioning of the samples was undertaken prior to FE sweeps. The conditioning of the samples involved manually raising the voltage such that the output current was $\sim 10\%$ greater than required for the planned experiments and left for 2 - 5 min until the emission was constant. This procedure stresses the sample and removes adsorbed molecules, making the emission more stable. Current-voltage (I-V) sweeps were obtained by sweeping the voltage from 0 V to maximum of 8 kV in steps of 50 V with each voltage held for 1 sec. Once the current output reached the limiting current (set manually) the voltage was returned to zero. These I-V sweeps were converted to current density-electric field (J-F) sweeps for presentation.

Emission stability tests were completed by manually setting the input current on the power supply such that a desired field emission current was achieved. The LabView program was then used to vary the applied voltage to maintain the input current. The voltage and field emission current were measured every 1 sec for the duration of the stability test.

6.3 Field emission from SWCNTs

6.3.1 Effect of SWCNT attachment time

Initial experiments were carried out to determine the optimum SWCNT coverage for field emission by investigating the FE properties of Si-SWCNT electrodes produced using various SWCNT attachment times.

Field emission sweeps for attachment times of 2 - 72 hr are shown in Figure 6.3 along with an inset displaying their respective Fowler-Nordheim (F-N) plots. The measured current is a result of field emission, as indicated by the linear Fowler-Nordheim plots,^[14] with different attachment times leading to different emission characteristics. The non-linearities in the Fowler-Nordheim plots shown in the inset to Figure 6.3 are commonly observed and are a consequence of the inhomogeneous nature of the field emitting surface. These non-linearities most likely arise from variations in the height and/or tip radius of curvature of the field emitting carbon nanotubes resulting in variations in their enhancement factor (β), although other factors such as adsorbate contamination or space charge effects may also be involved.^[15]

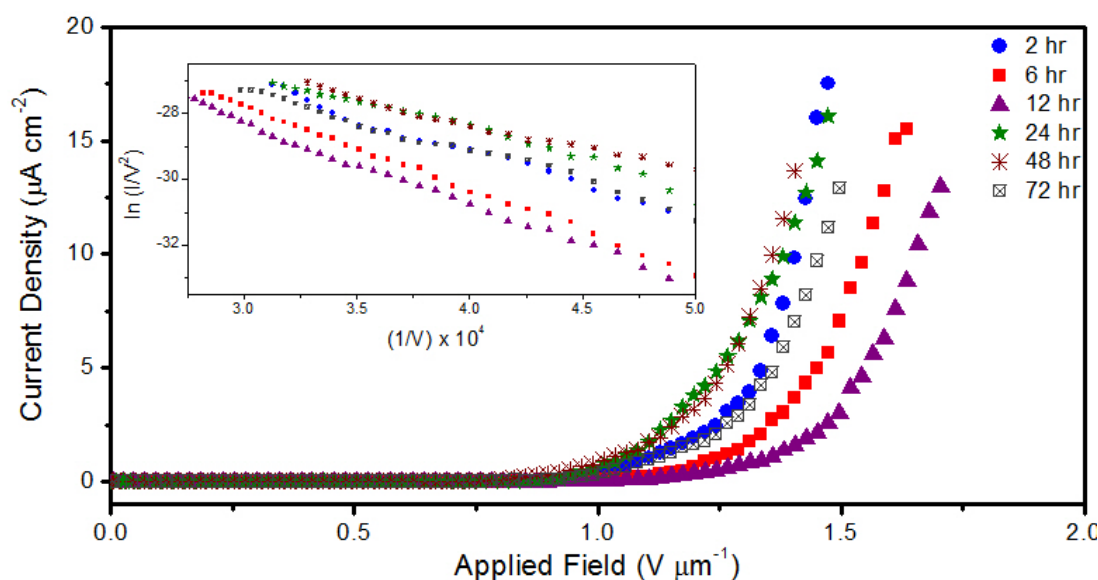


Figure 6.3: Field emission sweeps for SWCNT chemically anchored to n-type silicon for varying SWCNT attachment times with (inset) Fowler-Nordheim plots.

A detailed review of the emission characteristics is shown in Figure 6.4 where the change in average E_{to} and electric field enhancement factor are mapped against SWCNT attachment time. Here we define the E_{to} as the macroscopic electric field required to produce a current density of $10 \mu\text{A cm}^{-2}$. The electric field enhancement in CNT emitters comes from the sharpness of the 1-D nanotubes. This β has often been simplified to be approximately equal to the aspect ratio (height:radius) of the nanotube.^[16] Values of β were calculated from the slope of the F-N plots using the method described in Section 1.6.1. (Fermi Energy (μ) = 1.9 e V as calculated from the Fermi velocity,^[17] work function (Φ) = 4.8 eV^[18]). Since an array of tips is under investigation, the values of β calculated from the F-N plots are weighted toward the emitters that produce the most current. The general variation in both E_{to} and β as a function of attachment time (Figure 6.4) qualitatively match the variation of both the SWCNT content and diameter curves (see Figure 3.3). The variation of E_{to} is consistent with the known dependency of the field emission upon the size, orientation and surroundings of the emitters.^[3] As discussed previously, the AFM analysis shows that as the attachment time increases from 2 to 12 hr the average diameter increases (with a maximum between 10 and 12 hr) and hence the sharpness of the SWCNT bundles decreases resulting in a corresponding decrease in β and increase in E_{to} . For attachment times above 12 hr, the SWCNT content and diameter decrease slightly resulting in a consequent increase in the sharpness of the bundles and, as such, an increase in β and a lower E_{to} value. Further reasoning for the increase in β from 24 – 72 hr is that during this time any SWCNTs that are desorbing are most likely to be the shorter nanotubes due to their weaker van der Waals attraction. After the desorption of the smaller SWCNTs the bundles contain a higher concentration of high aspect ratio SWCNTs and hence a higher β is observed. In addition to the similar trend, the standard deviation of values also increases with attachment time. This is most likely a result of the larger variation of SWCNT coverage between samples for higher attachment times as discussed in Section 3.2 subsequently leading to a larger variation in FE characteristics. Due to the low E_{to} , high β and lowest deviation between samples the 2 hr attachment time surfaces were used for further investigation of FE from Si-SWCNT surfaces.

The values of E_{to} of between $1.37 - 1.64 \text{ V } \mu\text{m}^{-1}$ observed in this work compare quite favourably to the experimental values of other CNT field emission devices

where it has been reported that the value of E_{to} can vary from $\sim 1.1 - 9.8 \text{ V } \mu\text{m}^{-1}$ depending upon the type, orientation, coverage and geometry of the carbon nanotubes.^[3, 6]

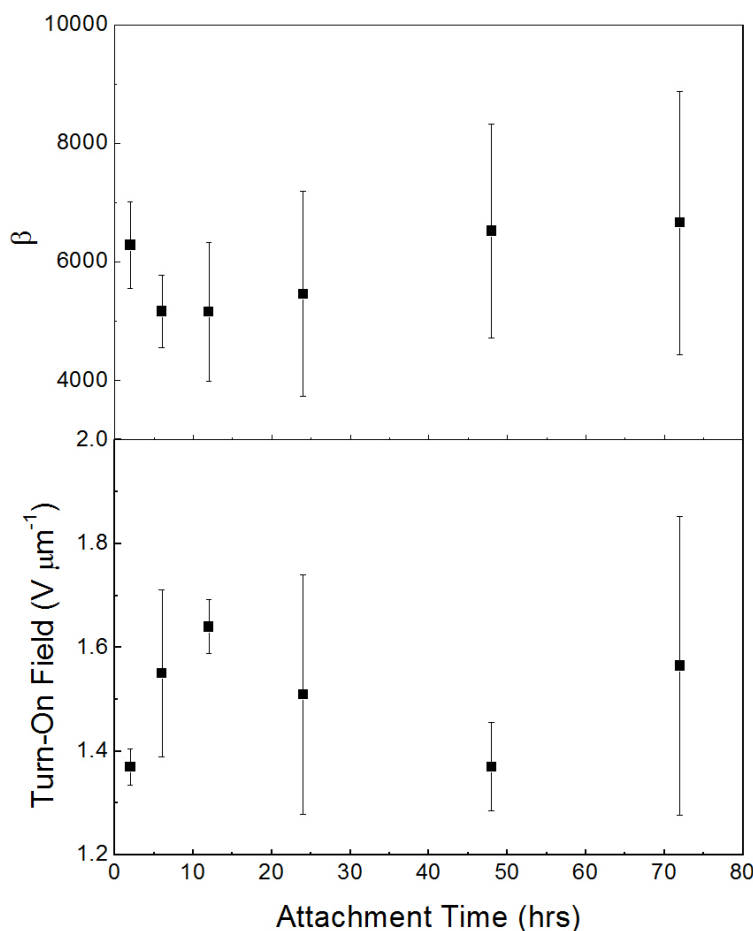


Figure 6.4: Graphs of effect of SWCNT attachment time on (a) electric field enhancement factor (β) and (b) the turn-on voltage (E_{to}).

To our knowledge the only other work involving the field emission of SWCNTs chemically attached to a substrate was by Jung *et al.*^[19] The major difference between the work of Jung *et al.* and the work reported herein is that Jung *et al.* created an array of randomly orientated SWCNTs attached via a silane linker onto a glass plate. The emission characteristic for our devices are superior with a lower E_{to} ($\sim 1.5 \text{ V } \mu\text{m}^{-1}$ vs. $\sim 3 \text{ V } \mu\text{m}^{-1}$) and the reported value of β of Jung *et al.* was 1400 compared to ~ 5800 for this work. We speculate that the significant improvement of the emission performance in this work is due to two main factors: the vertical alignment and the direct attachment of the SWCNTs to the substrate. The vertical alignment allows the maximum field amplification to take place, obviously leading

to a higher β and a lower E_{to} . In addition, the direct attachment allows for the highest efficiency of electron transduction.

The data represented in Figure 6.4 indicate that the chemically attached SWCNTs form very effective field emission structures with values of $\beta \geq 5000$. Interestingly, these high β values are far in excess of the enhancement factors that might be expected from a consideration of just the geometrical aspect ratio for the imaged SWCNT bundles. Indeed, the AFM data yields values of aspect ratio between 0.6 and 0.9 for average nanotube bundles and even assuming that the majority of the field emission comes from SWCNT bundles that are much taller and thinner than the average (eg., height size of ~ 100 nm, diameter of ~ 30 nm) the aspect ratio calculated is only ~ 6.5 . However, for chemically attached SWCNTs, the measured β is far in excess of that expected from a simple consideration of aspect ratio which is similar that which has been observed previously for CVD deposited CNT arrays. Indeed, a great variety of enhancement factors have been observed for various field emitting samples and materials. Earlier work by Chhowalla *et al.*^[20] showed that the field emission properties of CNT forests showed the best values for E_{to} and β when a medium density of ‘short and stubby’ (500 nm height, 400 nm diameter) CNTs were studied. It was found that the β was ~ 100 -1000 times greater than the aspect ratio of the CNTs. Their reasoning for this was the lower electric field screening which occurred between shorter CNTs that were spaced apart by a distance approximately equal to their height. It was found that the inter-nanotube distance was just as important as the aspect ratio in obtaining high values of β .^[20] The surprising field emission properties of the chemically attached Si-SWCNT electrodes presented here are comparable with those of the CVD deposited structures studied by Chhowalla *et al.* indicating that chemical attachment is a simple route to highly effective field emission structures.

Experiments were undertaken to determine the maximum current density possible for the Si-SWCNT electrodes. Initial tests on 1 cm^2 samples showed an exponential increase in current up to $500 \mu\text{A cm}^{-2}$ until the maximum wattage of the power supply was reached (10 W) and the experiment was halted. In order to achieve the maximum current density a sample was cut to 0.25 cm^2 such that a high current density could be achieved at a lower output current. Figure 6.5 shows a recorded current density of up to $780 \mu\text{A cm}^{-2}$ which is the maximum value obtainable, limited

by the picoammeter. Given that there is no evidence of any change in the exponential increase of the current in Figure 6.5, it seems reasonable to infer that the current density would continue to increase with increasing applied voltage. In comparison, previous studies of SWCNT field emitters have shown a decrease in the slope of the I-V curve at currents as low as $1 \mu\text{A cm}^{-2}$.^[8] The high maximum current output is an indicator that there is a large population of emitters on the surface. Any practical application of a CNT based field emission device not only requires a low E_{to} and high β to minimise the working voltage but the device must also be able to produce a large enough current density to be useful in applications and be stable at such current densities. For example, field emission displays require current densities of between $1\text{-}10 \text{ mA cm}^{-2}$.^[21, 22] It is speculated that such current densities are obtainable for the chemically attached Si-SWCNT electrodes.

A major advantage of these structures is that the shortness of the SWCNTs allows the cathode-anode distance be very small ($<1 \mu\text{m}$). CVD grown and CNTs deposited from a paste consist of CNTs with varying heights ($>1 \mu\text{m}$) which means that the cathode to anode distance must be comparatively large. A short distance will allow a small applied voltage to create very large electric field. At a distance of $1 \mu\text{m}$, 3 V of applied voltage could potentially generate an emitted current density $>0.5 \text{ mA cm}^{-2}$.

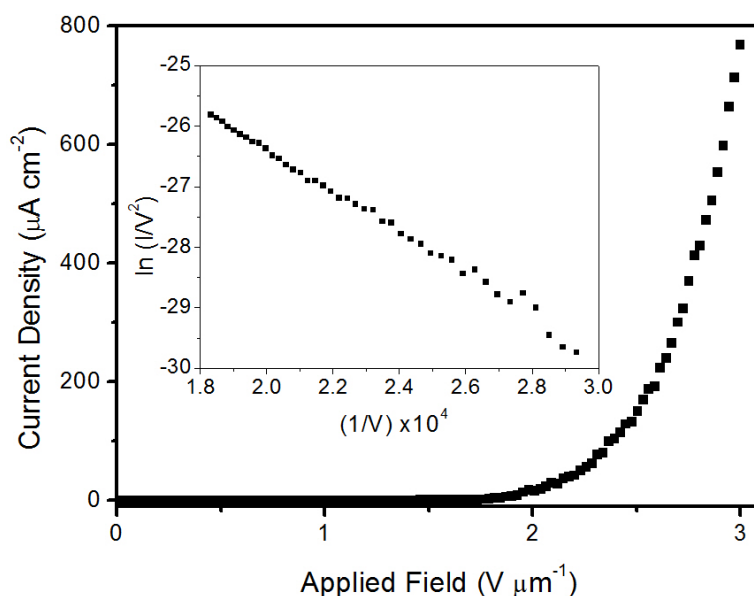


Figure 6.5: J-F curve attempting to achieve maximum current output for Si-SWCNT surface. Maximum wattage output of power supply reached before maximum current from sample.

6.3.2 Field emission from polymer encapsulated SWCNTs

A recent study by Pandey *et al.*^[11] has suggested that encapsulating CNTs within an insulating polymer matrix can improve the field emission properties of the device. This effect was attributed to the dampening of the Coulombic forces between electrons travelling through adjacent CNTs. When no polymer is present, coulombic forces push electrons away from each other, increasing the net distance travelled by the electron through the CNT. Increasing the electron travel distance increases the probability of scattering events, such as Joule heating, which reduce emission performance and stability. When a high dielectric polymer matrix is placed between the nanotubes the coulombic forces are reduced, leading to a shorter travelling distance and subsequently less scattering events and improved emission performance and stability.

Polymer encapsulated samples were made following the method described in Chapter 5. Figure 6.6 shows FE sweeps for SWCNTs with varying thickness of polystyrene. The changing polymer thickness has a clear effect on emission performance as summarised in Table 6.1. After polymer deposition and 1 min of water plasma treatment the surface has a ~30 nm film of polystyrene (PS) (See Figure 5.16). The β increases and E_{t0} decreases indicating an improvement in FE after polymer deposition. The improvement is attributed to two factors: first the reduction of Coulombic forces between electrons in adjacent CNTs, as determined by Pandey *et al.*^[11] and secondly the orientation of the CNTs that are exposed from the surface. With a 30 nm thick PS film, no horizontally aligned CNTs will be exposed while the SWCNTs that are exposed will be the CNTs with the highest aspect ratio. Subsequently, the β value obtained for the surface is much higher than without a PS film. Additionally, a surface with fewer, taller CNTs will experience less electric field screening leading to improved emission performance. When the PS covered surface was treated to 2 min of plasma treatment, both FE properties were improved over the no-polymer surface, while both β and the E_{t0} were lower compared to the 1 min plasma treatment (worse β and improved E_{t0} , Table 6.1). The difference between the two plasma treatments is a result of the increased number of CNTs exposed. The thinner PS film will expose more of the shorter, or less aligned CNTs, resulting in a lowering of the β . Interestingly, the surface exhibits an improved E_{t0} which perhaps is not expected considering the change in β . However,

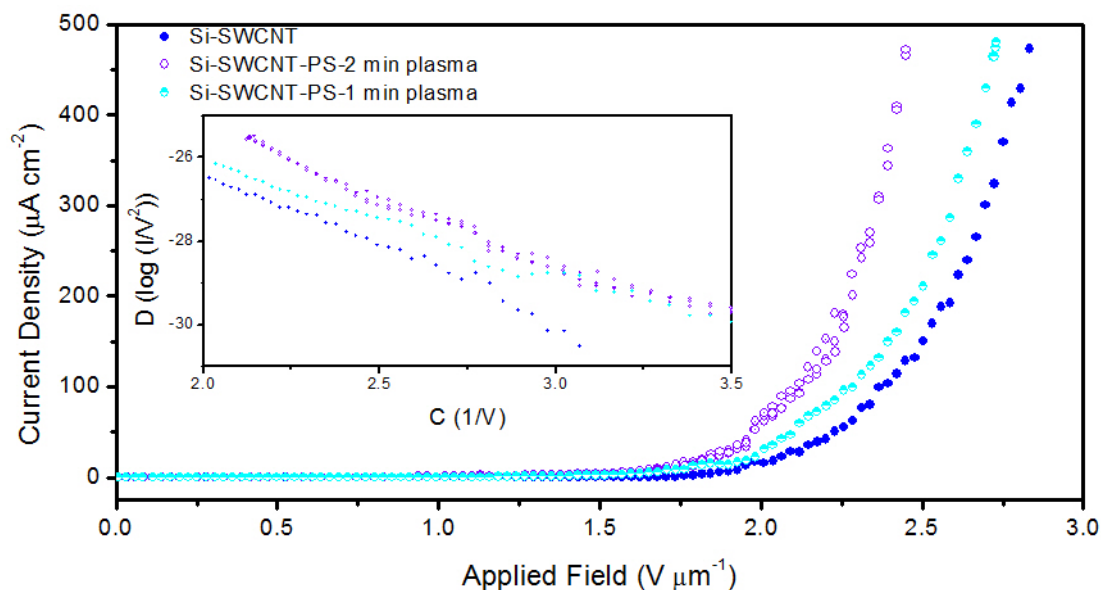


Figure 6.6: FE sweeps for SWCNT surfaces with varying thickness of polystyrene.

Table 6.1: Summary of field emission characteristics of Si-SWCNT surfaces with varying polystyrene film thickness.

Sample	Polystyrene thickness (nm)	β	$E_{to\ 10\ \mu A\ cm^{-2}}$ ($V\ \mu m^{-1}$)	$E_{th\ 100\ \mu A\ cm^{-2}}$ ($V\ \mu m^{-1}$)
Si-SWCNT	0	3929	1.95	2.35
Si-SWCNT-PS-1 min plasma	30	6133	1.76	2.28
Si-SWCNT-PS-2 min plasma	20	4115	1.73	2.12

with more CNTs exposed the total amount of emitting CNTs will increase leading to a higher current density for a given applied field.

The use of thin polymer films offers a simple route to improving the FE performance of CNT arrays. This procedure could find particular use for surfaces that contain both vertically-aligned and horizontally-aligned CNTs where the polymer film acts to cover up the horizontally-aligned CNTs, thus improving FE. The Si-SWCNT-PS sample before plasma treatment was not investigated as it was not known what effect/damage may occur when a potentially insulating sample is exposed to high voltage.

6.4 Field emission from DWCNTs and MWCNTs

To further study the field emission from CNTs chemically attached to Si, the emission from DWCNTs, and MWCNTs were compared to SWCNTs. As determined in Section 6.3 a 2 hr attachment time of SWCNTs lead to a surface with the best, most consistent FE properties. Subsequently, similar CNT coverages were used for the DWCNTs and MWCNTs. A comparison of the AFM images for the different CNT electrodes is shown Figure 6.7. The CNT attachment times were chosen to ensure the CNT coverage was quasi-constant between the samples. Alignment of the CNTs changes with CNT type with the SWCNTs predominantly vertically- aligned while the DWCNTs are a mixture and the MWCNTs appear to be exclusively horizontally-aligned (see Chapter 3 for discussion on CNT alignment). The alignment of each CNT type could not be improved further and the effect of alignment will be taken into account when discussing FE properties from the surfaces.

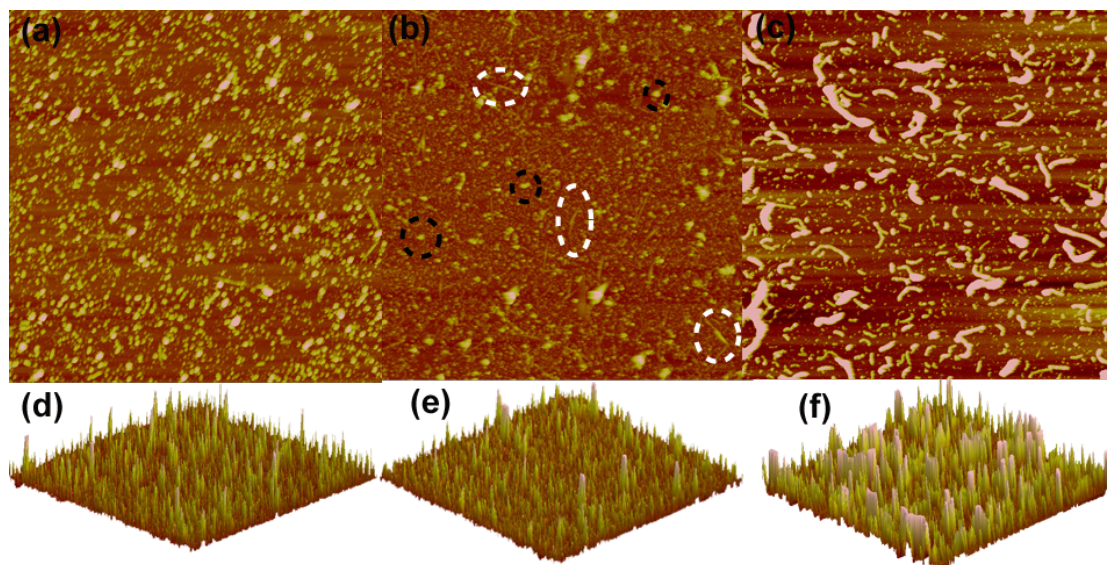


Figure 6.7: (a, b, c) Aerial and (d, e, f) 3-D AFM images of (a, d) SWCNTs, (b, e) DWCNTs and (c, f) MWCNTs chemically attached to silicon. White circles in (b) indicate laying down DWCNTs while black circles indicated VA-DWCNTs.

Field emission sweeps for SWCNT, DWCNT and MWCNTs along with their F-N plots are shown in Figure 6.8. The CNT type had a noticeable effect on both the electric field enhancement and the E_{to} as summarised in Table 6.2. The SWCNT

surface exhibits the best FE properties of the samples investigated with the lowest values for E_{t0} and the highest value for β . This result is expected as the SWCNTs had the lowest diameter and greatest level of vertical alignment. The DWCNT surface demonstrated a higher E_{t0} and lower β compared to the SWCNTs due to the increased diameter and loss of vertical alignment compared to the SWCNT surface. The MWCNT surface exhibited the worst emission characteristics of the three CNT types investigated. The horizontal alignment and the large diameter of the MWCNTs results in a lower value for β and subsequently a higher value for E_{t0} . E_{t0} and β for DWCNTs are often similar to that of SWCNTs due to the small difference in diameter between the two.

Similar to Figure 6.5 attempts were made to measure the maximum current density from the DWCNT and MWCNT electrodes. Figure 6.8 (b) shows the J-F sweeps up to the maximum of the picoammeter where neither sample seems to be nearing its maximum. As discussed earlier this indicates that the chemically attached CNT surfaces could potentially be used in device application. The current density of the DWCNT is less than the other two samples due to the larger size of the DWCNT substrate.

Interestingly, the FE characteristics were much more different in the lower current sweeps (Figure 6.8 (a)) compared to the higher current sweeps (Figure 6.8 (b)). This could indicate that during the high stress, high current tests some extra conditioning occurs on the DWCNT and MWCNT samples which improve FE. The high D/G peak intensity ratio from the Raman spectra of the DWCNT and MWCNT samples (Chapter 3) indicate that there could be a great deal of amorphous carbon present within the samples. The higher fields obtained during the high current tests may also induce alignment of the CNTs which would improve emission performance. The ‘training’ or ‘burning’ of the samples was completed by maintaining a current 10 % greater than the planned current sweep value. The results observed in Figure 6.8 indicate that a higher ‘burn’ current should have been used for the DWCNT, and particularly the MWCNT samples.

The FE of the DWCNT surface presented here compares favourably with other work on FE from DWCNTs where values for E_{t0} of $1.5 - 3 \text{ V } \mu\text{m}^{-1}$ and 1000 - 5000 for β are common.^[23, 24] Similar to the SWCNTs, the DWCNTs show surprisingly good FE characteristics. The arguments made for the results for the SWCNT samples

including low electric field screening and strong chemical attachment can be repeated for the DWCNT (and MWCNT) substrates.

MWCNTs are by far the most extensively studied of the CNT types due to their ease of fabrication. However, MWCNT diameters can vary significantly and as a result a very broad range of FE characteristics are present in the literature. The value of E_{to} can vary from $\sim 2 - 10 \text{ V } \mu\text{m}^{-1}$ depending upon the diameter, orientation, coverage and geometry of the carbon nanotubes.^[3, 13, 25]

Although MWCNTs exhibit worse FE characteristics the cost of the raw material is much less than for the SWCNTs and DWCNTs. Depending upon the device, it may be more financially viable to use MWCNTs and a higher applied electric field in commercial applications.

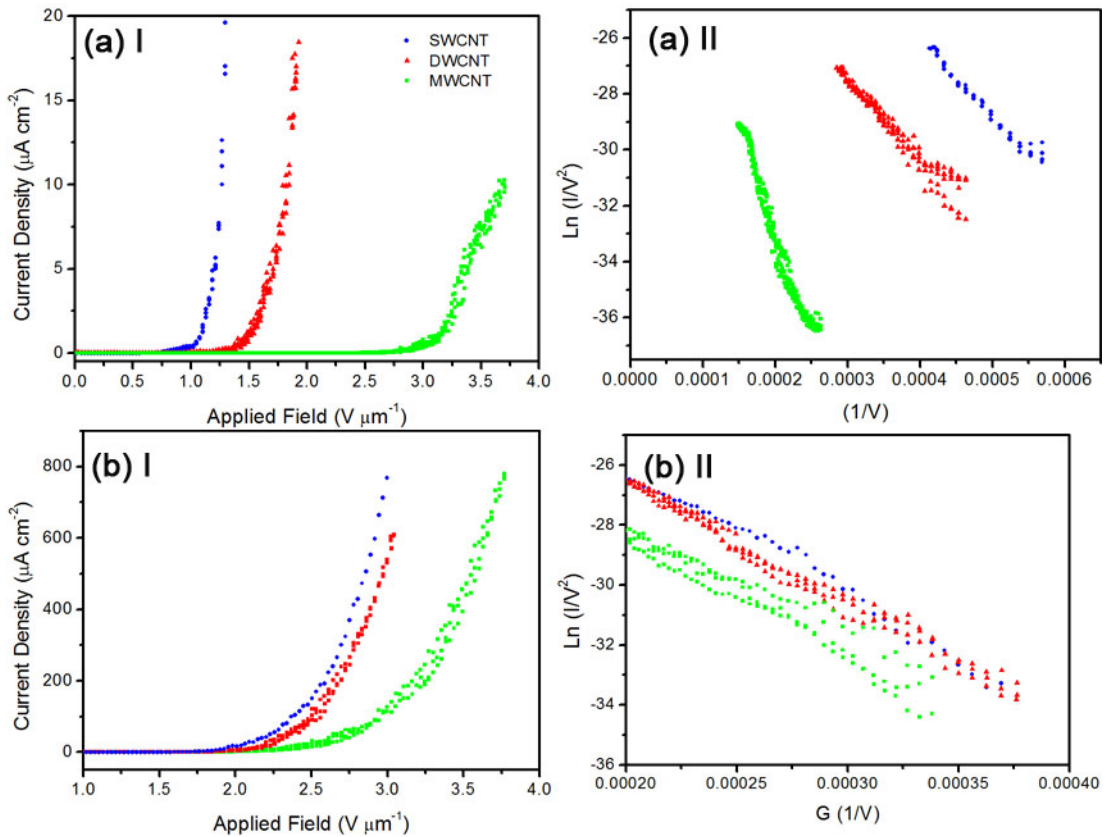


Figure 6.8: Summary of field emission (I) J-F sweeps and (II) F-N plots for different CNT types chemically attached to silicon showing (a) low current and (b) high current sweeps.

Table 6.2: Summary of FE characteristics of SWCNTs, DWCNTs and MWCNTs chemically attached to silicon.

CNT Type	D/G ratio	β	$E_{to\ 10\mu A\ cm^{-2}}$ (V μm^{-1})	$E_{to\ 100\mu A\ cm^{-2}}$ (V μm^{-1})	$E_{to\ 500\mu A\ cm^{-2}}^{\#}$ (V μm^{-1})
SWCNT	0.08	5587 \pm 1571	1.29 \pm 0.042	2.1 \pm 0.357	2.85
DWCNT	0.27	4748 \pm 1133	1.91 \pm 0.165	2.51 \pm 0.265	2.97
MWCNT	1.04	3069 \pm 1150	2.79 \pm 0.62	3.03 \pm 0.147	3.54

[#]no error values shown as only a single sample was tested past 0.5 mA cm⁻².

All CNT types exhibited FE with characteristics in the top 20 % of those reported in the literature. Considering the ease of fabrication and the ability to upscale production, the CNT surfaces produced via chemical attachment have distinct potential toward device fabrication. However, FE devices not only require high current densities at low applied fields but also require stable emission at a set applied field for the lifetime of the device. The next Section examines the FE stability of the CNT substrates.

6.5 Field emission stability from CNTs

Emission stability was investigated by manually setting the value for input current on the power supply such that a desired output current was achieved. The output currents investigated were 10, 100 and $\sim 750 \mu\text{A}$. After manually setting the input current, a program written in LabView was used to adjust the voltage in order to maintain the input current. All CNT types were investigated at the equivalent of a 2 hr attachment time, as described in Section 6.4.

6.5.1 SWCNT field emission stability

Figure 6.9 reveals the FE stability test results obtained by measuring the change in voltage required to keep the current density produced by a Si-SWCNT surface constant at $\sim 10 \mu\text{A cm}^{-2}$ (sample was $\sim 1 \times 1 \text{ cm}^2$). Over the 60 hr of testing, the voltage changed by 14 % but the change was a decrease in applied voltage indicating an improvement of the FE, not the expected degradation. A probable cause for the FE improvement was desorption of SWCNTs that were adsorbed to the bundles but not chemically attached to the Si substrate. When this occurs the bundle diameter will decrease by a small amount and as such slightly increase the β and improve the FE. Additionally, it is likely that this desorption has the effect of making the apex of the bundles more ragged which should create additional sharp points which will be efficient field emitters. The improvement of FE over such a long time is a remarkable result, especially for a SWCNT emitter surface as these have been shown to degrade the fastest of the CNT types.^[26] However, as mentioned earlier the practical application of CNT devices will require currents in the range of 0.5 to 10 mA cm^{-2} . For this reason, subsequent FE stability tests were completed at higher working current densities.

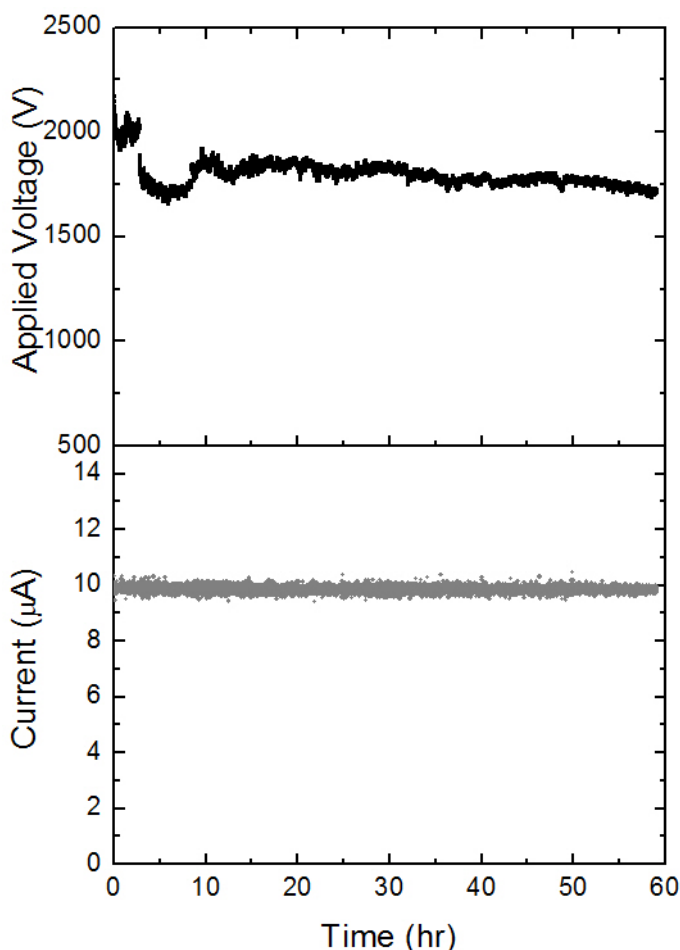


Figure 6.9: A 60 hr FE stability test of a Si-SWCNT surface with a constant current of $10 \mu\text{A}$ ($\sim 10 \mu\text{A cm}^{-2}$).

The FE stability at $\sim 100 \mu\text{A cm}^{-2}$ of the Si-SWCNT surface is shown in Figure 6.10. After some initial instability the input voltage required to maintain $110 \mu\text{A cm}^{-2}$ drops from ~ 3000 to ~ 2720 V after 15 min. The input voltage then becomes more stable with oscillations of ± 40 V (1.5%). The voltage slowly rises for the remainder of the test to 2860 V. The overall change in applied voltage is a decrease of 140 V (4.9%). After initial instability, the voltage increased by 140 V (5.1%) from 15 - 60 min. The SWCNT desorption that was previously improving the emission is most likely still occurring, but common field emission degradation processes such as Joule heating and ion bombardment are now having a greater effect. Once more, over this shorter period but at a higher power output the Si-SWCNT surface produces remarkably stable FE.

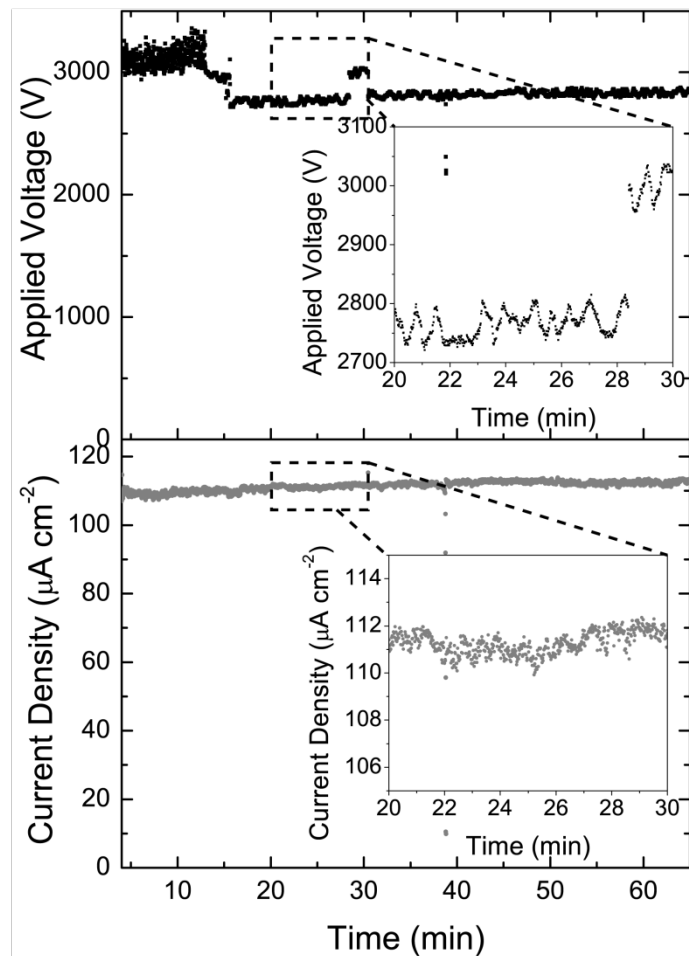


Figure 6.10: A 60 min FE stability test of FE from a Si-SWCNT surface at a current density of $\sim 110 \mu\text{A cm}^{-2}$.

This particular current density ($100 \mu\text{A cm}^{-2}$) was chosen such that direct comparisons could be made to other work on the FE stability of SWCNT electrodes. Resilience tests of SWCNTs are rarely reported however there have been two in depth studies by Kim *et al.*^[27] and Bonard *et al.*^[28] Kim and co-workers printed a SWCNT paste onto an indium tin oxide (ITO) glass plate and measured the change in current at a fixed applied field (with the initial current always $100 \mu\text{A cm}^{-2}$). After 30 hr the FE current had decreased by 50 %. Bonard *et al.* placed filtered arc-discharge SWCNTs onto Teflon covered copper or brass platelets, and then completed the same experiment as that of Kim where it was found that the current density output had decreased by more than 50 % after 10 hr. Comparisons between the results of Bonard and Kim and the result observed in Figure 6.10 are difficult to

draw due to the fact that not only is a % change in current density different to a % change in applied voltage but when the current density (not the applied voltage) is allowed to vary, the stress placed on the system varies with the current density. In the case of Bonard and Kim, the stress on the system would be decreasing as the FE current fell. When the change in voltage is monitored the stress placed on the system is constant for the entire investigation which would lead to a higher rate of degradation. Therefore, although direct comparison of the results is difficult, the fact that the Si-SWCNT electrode was still emitting $100 \mu\text{A cm}^{-2}$ after 1 hr with minimal net change in voltage indicates that the resilience of the emission is superior to that of Bonard and Kim.

Emission degradation was not observed at 10 or $100 \mu\text{A cm}^{-2}$ for the Si-SWCNT surfaces investigated, consequently a higher current density was investigated (the maximum recordable on the FE system used, $\sim 750 \mu\text{A cm}^{-2}$). Figure 6.11 shows how both the applied voltage and the current density changed throughout the experiment. The output current increased to $770 \mu\text{A cm}^{-2}$ within the first 2.5 hr. This was not expected to occur as the current was designed to be constant. However, the resistance of the sample decreased and the output current increased. The increase in current was not a degradation but it was an improvement of the emission as no corresponding change in voltage occurred, such that an applied voltage of 5500 V produced a current of $740 \mu\text{A cm}^{-2}$ at $t = 10 \text{ min}$ and a current of $770 \mu\text{A cm}^{-2}$ at $t = 2.5 \text{ hr}$. After 2.5 hr, the current remained constant as the resistivity of the electrode did not change further. The applied voltage began at 5600 V and dropped 5450 V within the first 1 hr. The drop is an improvement in the emission as it was not coupled with a decrease in output current density. After this time the applied voltage rises slowly to at 5700 V after 15 hr. The total change in applied voltage was 1.8 % for the lifetime of the stability test.

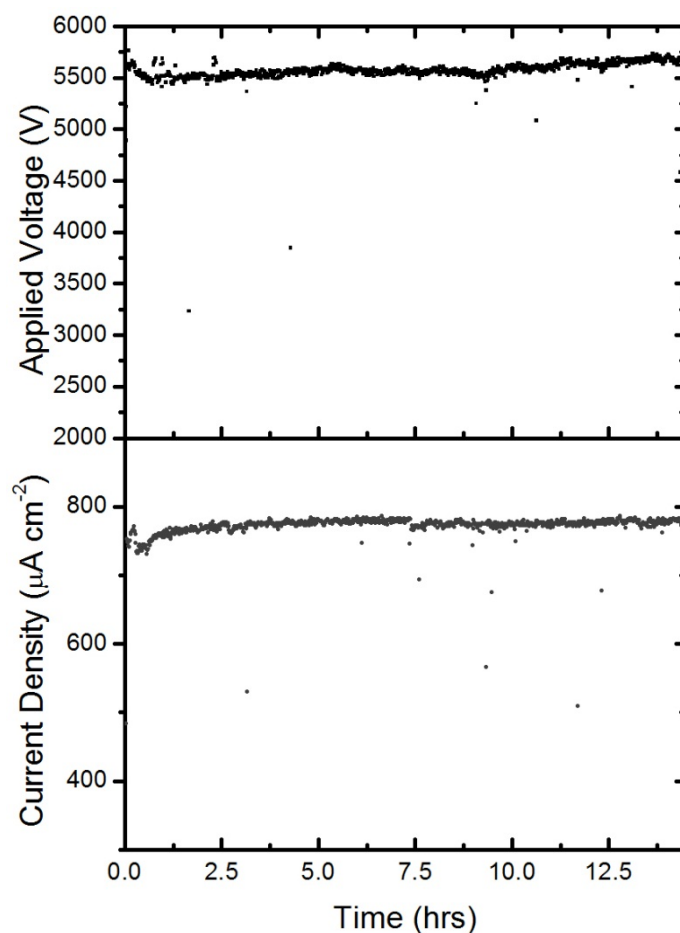


Figure 6.11: A 15 hr FE stability test of a Si-SWCNT surface at a constant current density output of $780 \mu\text{A cm}^{-2}$.

A total voltage change of 1.8 % over 15 hr for an applied current of $\sim 750 \mu\text{A cm}^{-2}$ is very low for a SWCNT field emitting surface compared to the report from Bonard *et al.* who showed a decrease in emitted current of 50 % after 10 hr (initially at $100 \mu\text{A cm}^{-2}$).^[28] The only SWCNT electrode reported in the literature with greater stability was a screen printed SWCNT electrode that was treated with an Xe/Ne plasma to improve stability to the point where a current density of $100 \mu\text{A cm}^{-2}$ was maintained for >50 hr with minimal degradation.^[27] However, the plasma treatment increased the E_{to} of the electrode from 2.9 to $4.3 \text{ V } \mu\text{m}^{-1}$, effectively cancelling out the advantages of using SWCNTs. Additionally, the output current density described here was over 7 times greater, with little emission degradation observed.

Previous experiments have shown that SWCNTs are much less resilient than MWCNTs because of the susceptibility of the single shelled tubes to ionised molecule bombardment and Joule heating.^[28] Improving the resilience of SWCNTs

to ion bombardment and Joule heating is impossible but there is one factor that most researchers do not acknowledge: the vast majority of CNT field emission articles have been based upon CNTs grown onto a surface by CVD^[29-31] or printed using screen printing^[3, 27] where the CNT to substrate adhesion is weak. Bonard *et al.*^[28] observed that after the resilience tests, SEM images of the SWCNT surfaces showed a decrease in density indicating a large amount of CNT desorption. Here, we describe the FE of chemically attached SWCNTs where the SWCNT adhesion to the substrate is strong and thus the degradation due to CNT desorption should be negligible. Additionally, the bundling of the SWCNTs may assist FE stability with the outer most SWCNTs protecting the inner most SWCNTs from ion bombardment. Further, the bundling may assist in heat dissipation by reducing Joule heating. The low electric field screening of the surface may result in a large population of emitting SWCNTs, which will result in a stable FE.

Although a near perfect FE stability was achieved for the Si-SWCNT electrode, a further investigation was carried out on the emission stability from the polymer coated samples from Figure 6.6. Pandey *et al.*^[11] inspired the use of a thin film to improve FE characteristics and also reported the improved FE stability of CVD grown MWCNTs after polymer deposition. Their argument was that the reduced electron travel distance through the CNTs shielded by the dielectric polymer reduced Joule heating, which in turn improved FE stability. The Si-SWCNT-PS-water plasma electrode FE stability was investigated at the maximum current output of the field emission system with a 2 hr test shown in Figure 6.12. After the initial voltage/current ramp a steady emission is achieved at $870 \mu\text{A cm}^{-2}$. The higher current density achieved for this electrode is a result of its smaller size. After a period of time, both the current and voltage concurrently dropped and the FE remained stable for the remainder of the experiment. The voltage/current decrease was not an instantaneous drop but a roll-off occurring over a few seconds. The concurrent roll-off in both voltage and FE current was unusual considering that the input current to the system, as controlled manually by the power supply, was not changed. The drop of both voltage and FE current also indicated that there was no degradation of the surface (see Figure 6.12, the spike at 15 min where both the current and voltage momentarily recover to their previous values). This shows a delayed change in the resistivity of the CNT cathode.

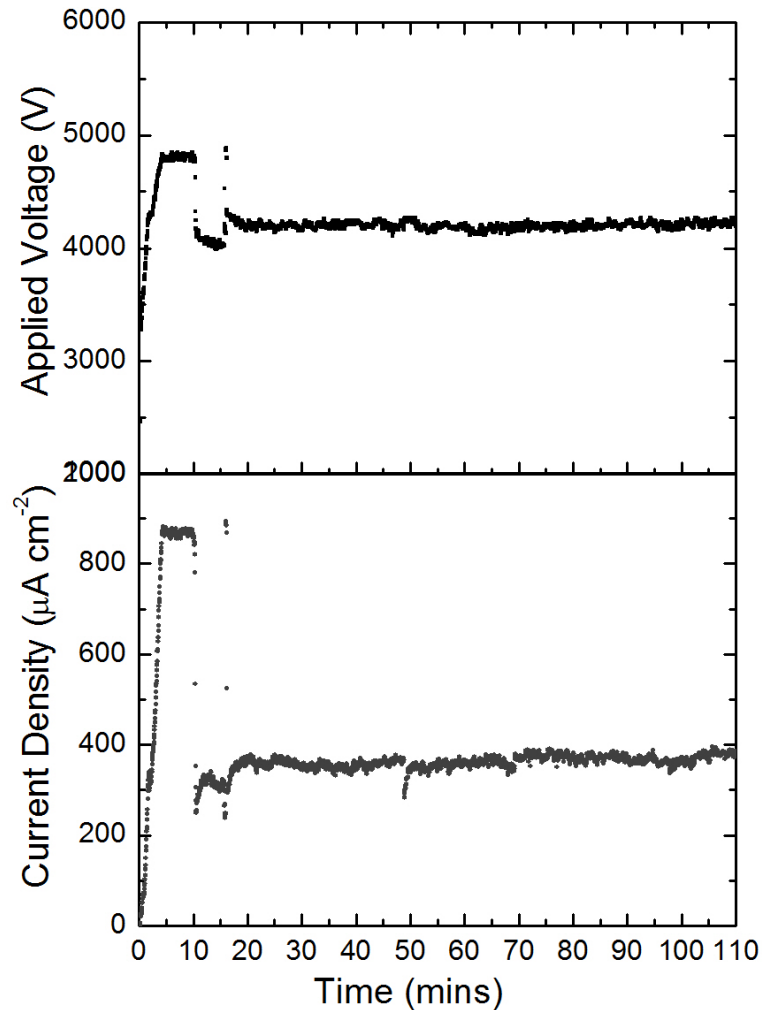


Figure 6.12: FE stability of a Si-SWCNT surface coated with a thin film of PS.

The exact reasoning for the change remains unknown although there are two possible explanations. The first is that the heating of the polymer film that occurs during the FE tests causes the polymer to undergo a phase transition. The hypothesis came about after the observation that the time taken for the current/voltage roll-off was dependent upon the time between subsequent FE experiments. Figure 6.13 illustrates this observation by showing the FE stability results for consecutive tests where the voltage was ramped down and then up as fast as possible after the roll-off pattern occurred. For the first three runs, the roll-off occurred after 20, 10 and then 7 min while the fourth occurred after 20 min. Each of these experiments had similar time gaps between them. Interestingly, after each initial voltage ramp the current and voltage were the same, suggesting that the current roll-off was completely reversible and did not damage the sample. If a polymer phase transition was the cause of the roll-off behaviour, the current/voltage decrease should occur slowly at first and then

faster, as the sample was not allowed to cool between tests. This was observed for the first three tests but not the fourth which takes the same amount of time as the first. This observation suggests that perhaps a more random process is occurring.

A second possible explanation for the roll-off is that over the experimental period, the sample holder had become covered in carbonaceous material, turning the originally white macor into a light brown colour. If the sample holder was covered in material it is possible that the inside of the chamber had also become contaminated. When a strong field was applied within the system, positively charged particles could potentially coat the sample. The carbon film could then potentially act as a resistor within the system if it somehow became connected in series with the CNT cathode.

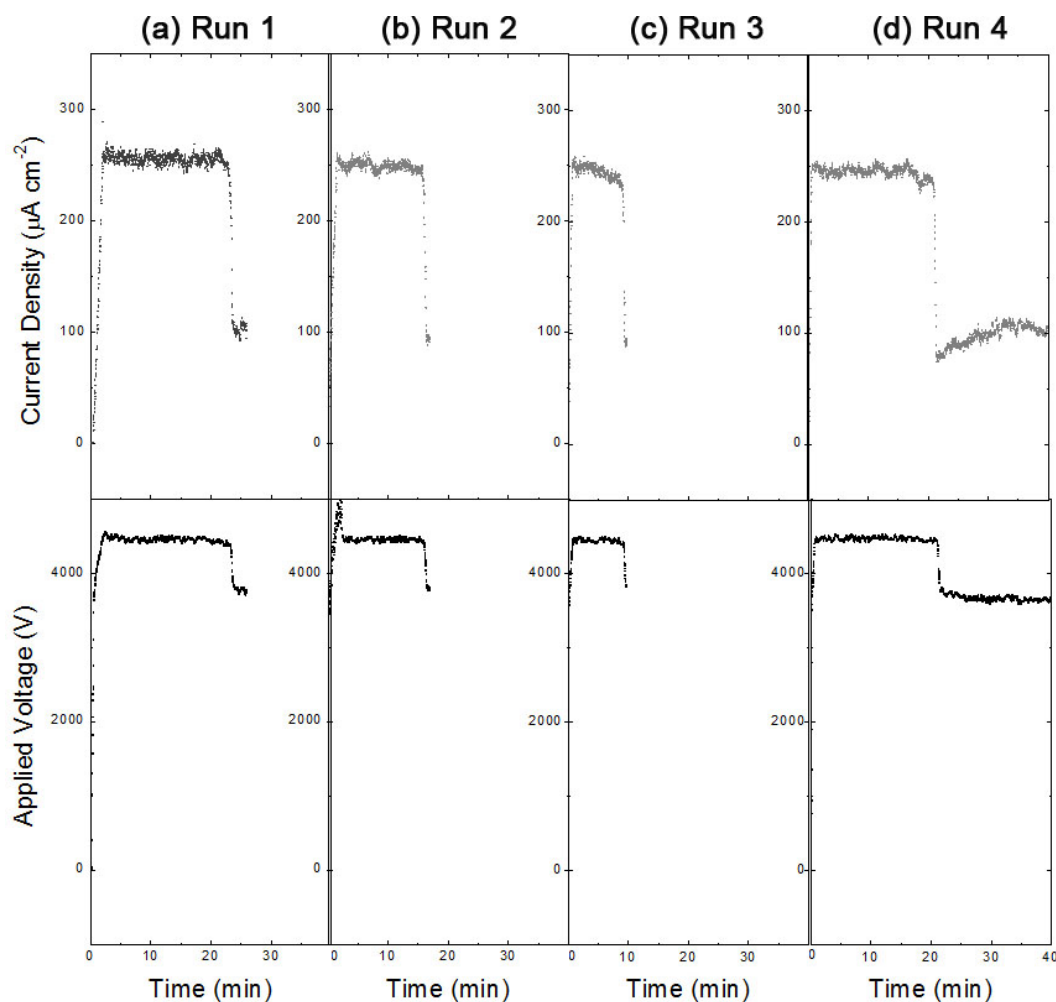


Figure 6.13: Consecutive FE stability experiments from Si-SWCNT-polystyrene electrodes showing the change in time for the roll-off behaviour to occur.

6.5.2 DWCNT field emission stability

The FE stability test of a Si-DWCNT surface is shown in Figure 6.14. During the test the applied voltage rose from 4330 to 4450 V (2.8 % increase) while maintaining a current of $85 \mu\text{A cm}^{-2}$. After an initial voltage drop to 4220 V after 5 min the voltage increased by 5.5 % for the remainder of the test. The difference in output current density between the Si-SWCNT and Si-DWCNT samples investigated comes from the sample size; the output current from both samples was $100 \mu\text{A}$. Throughout the stability test the voltage value oscillated by $\pm 50 \text{ V}$ (1 %).

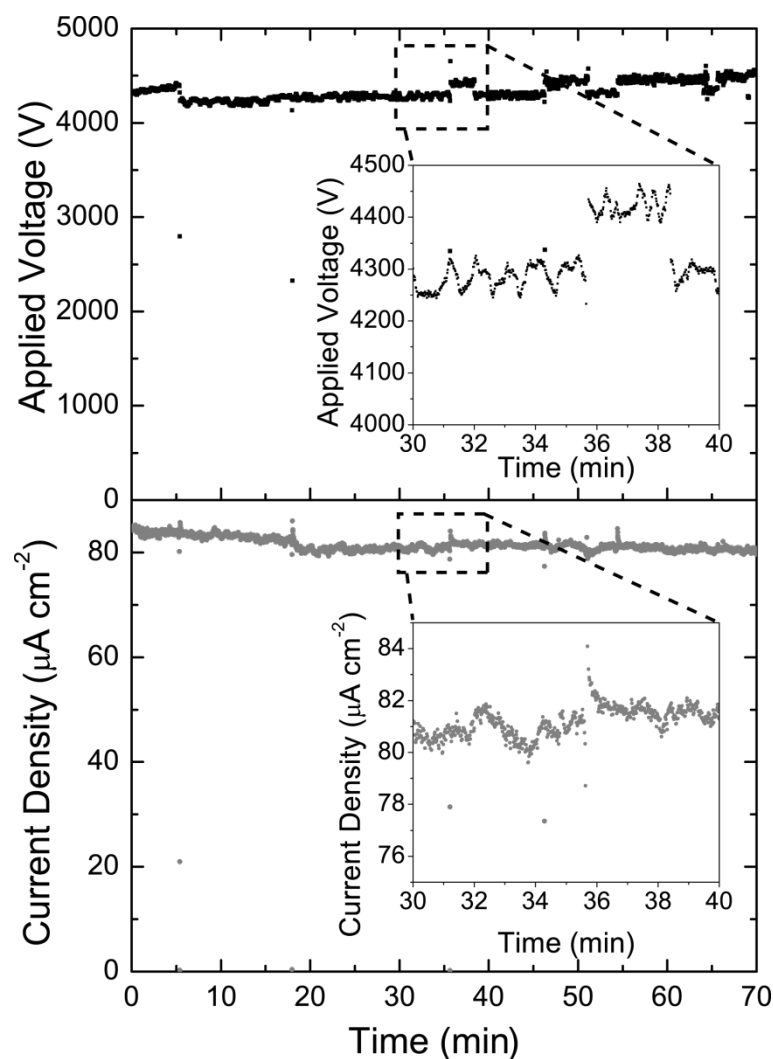


Figure 6.14: FE stability of a DWCNT electrode at $80 \mu\text{A cm}^{-2}$ over 70 min.

It was surprising to observe that the Si-DWCNT surface had a lower FE stability than the Si-SWCNT surface. As the common theory suggests CNT FE stability should increase with number of walls.^[26] In addition, a number of sharp

voltage/current spikes, where both the current and voltage dropped suddenly can be observed in the data (e.g., at 5 and 20 min). Interestingly, only a single such event was observed for the entire duration of the FE stability test conducted on the Si-SWCNT surface.

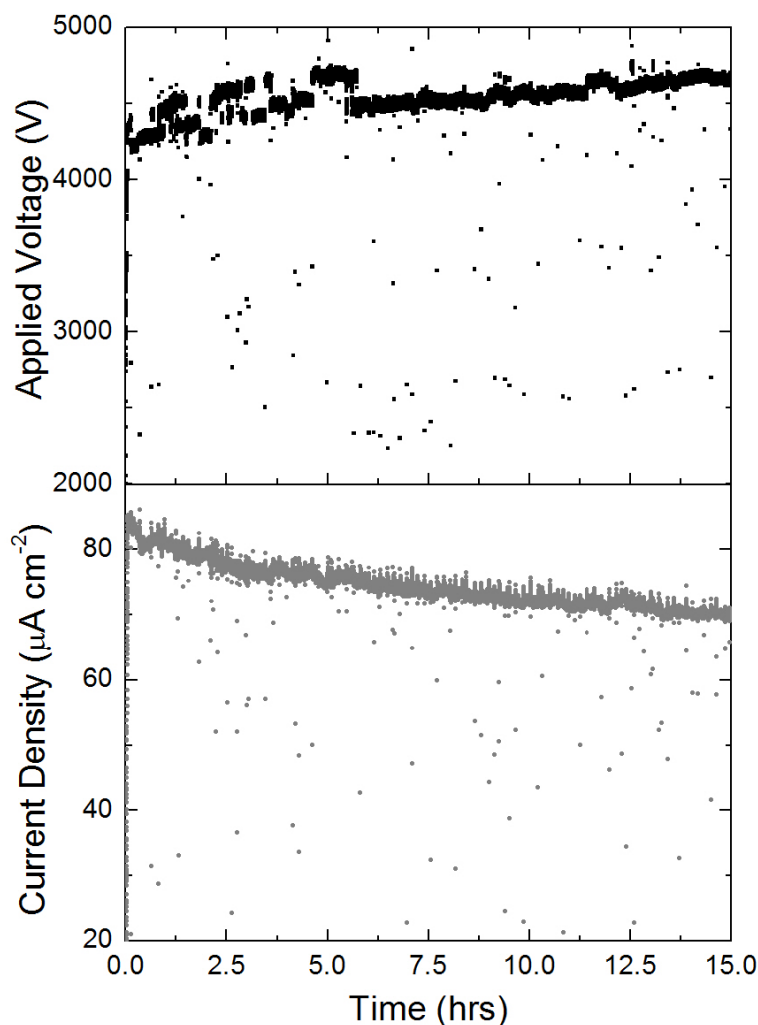


Figure 6.15: FE stability of a Si-DWCNT electrode at $\sim 80 \mu\text{A cm}^{-2}$ over 15 hr.

Previous work on FE from CNT deposited arrays has shown that these spikes are due to CNT fragments that are ejected from the surface.^[32] Given that the chemical attachment should restrict entire CNTs from desorbing, the most likely scenario is that parts of the CNT are being ‘pulled’ from the surface. The DWCNTs have a higher amount of functionalisation than the SWCNTs (as determined by the D/G peak intensity ratio, see Chapter 3) and increased functionalisation has been shown previously to reduce the FE stability of CNT surfaces.^[33,34] It has been reported that these defect sites lead to increased Joule heating which in turn leads to field

evaporation from the CNT which subsequently lowers FE stability.^[26] Although the DWCNTs have an extra shell to reduce the effects of ion bombardment, the increased functionality (which was required to chemically attach them to the surface) leads to the Si-DWCNT surfaces having poorer FE stability than the Si-SWCNT surfaces. The FE stability test of the DWCNT substrate was continued for over 15 hr (Figure 6.15) where the applied voltage rose from 4200 to 4650 V (10 % increase) and the output current density dropped from 85 to 70 $\mu\text{A cm}^{-2}$ (18 % decrease). The supplied current was constant but the output current decreased due to a gradual change in resistance of the sample as the number of emitters decreased. The decrease in current without a subsequent decrease in voltage is a clear indicator of emission degradation.

6.5.3 MWCNT field emission stability

A 100 $\mu\text{A cm}^{-2}$ FE stability test for a Si-MWCNT surface could not be achieved because sharp voltage/current spike events occurred on a regular basis (approx. once every 5 sec) from which the LabView program would take a few sec to return the current to its previous value before another event occurred and eventually the LabView program would fail to restore the current. A 1 hr 10 $\mu\text{A cm}^{-2}$ FE stability test for the Si-MWCNT surface is shown in Figure 6.16. The applied voltage is quasi-constant for the first 45 min of the test with a constant oscillation of ± 175 V (3 %), after which time the emission cycles through four failure and recovery events prior a final failure from which the LabView program could not resurrect emission. Throughout the first 45 min of the FE stability test, 11 sharp current/voltage drop events were observed. These drops are similar to those observed for the Si-DWCNT surface but were more than twice as frequent. Considering the lower applied load to the surface (10 $\mu\text{A cm}^{-2}$ for the MWCNTs compared to 100 $\mu\text{A cm}^{-2}$ for the DWCNTs), the volume of material being ejected from the surface is quite high. This observation is consistent with the mechanism proposed for the DWCNTs since the D/G peak intensity ratio of the MWCNTs is much higher than for the DWCNTs or SWCNTs and as such the defect/functionalisation population on the MWCNTs is much greater. The greater number of defect sites will increase the effect of Joule heating and lead to a higher amount of CNT field evaporation and the lower FE stability of the device. The event at 45 min where the output current dropped to zero

is not a complete catastrophic failure of the system because subsequent I-V sweeps showed FE characteristics similar to before the FE stability test. Repeated experiments observed similar failure events.

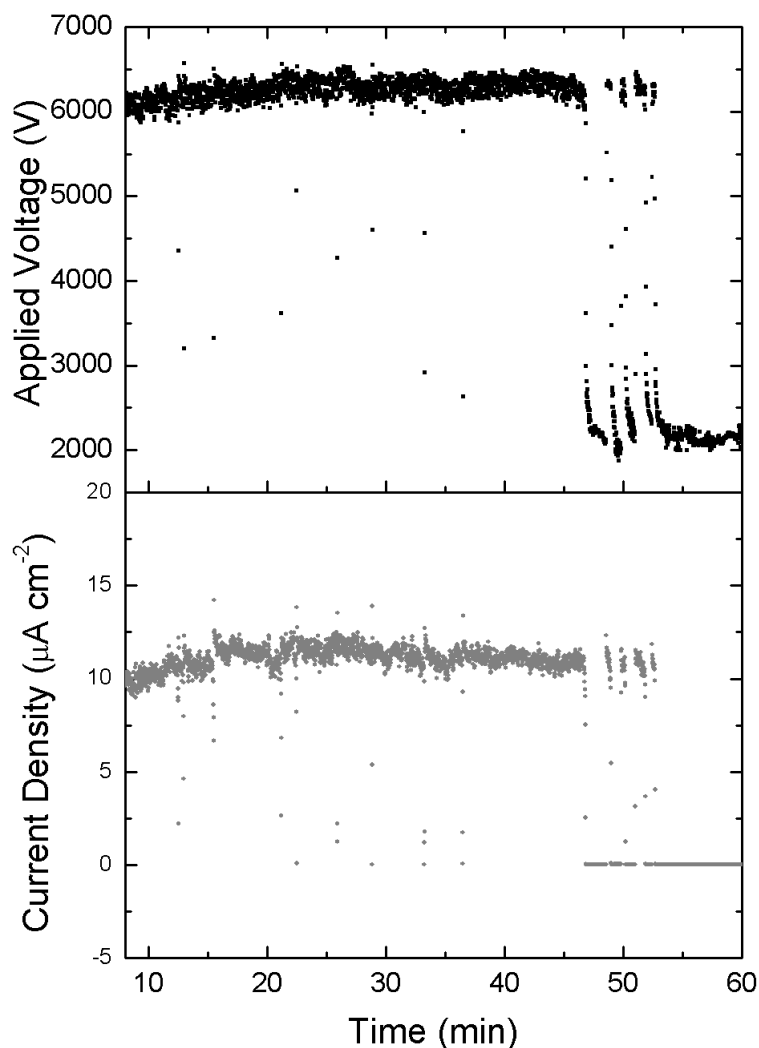


Figure 6.16: FE stability of a Si-MWCNT electrode at $10 \mu\text{A cm}^{-2}$ for 45 min.

The FE emission stability characteristics observed are contradictory to previously reported findings where it is expected that FE from MWCNT emitters is more stable than from SWCNT emitters.^[3] FE stability is affected by a number of variables including CNT adhesion, ohmic contact, ion bombardment and CNT crystallinity. Within this study, CNT adhesion and ohmic contact is constant between CNT types as SWCNT, DWCNT and MWCNT substrates were prepared via identical chemical attachment. The effect of ion bombardment is reported to be reduced by the extra shells of MWCNTs,^[26] thus the lower emission stability observed for the Si-MWCNT substrate cannot result from ion bombardment. The crystallinity of the

CNTs is affected by both their original manufacturing process and functionalization. The DWCNT and MWCNTs were originally produced by CVD which is a process known to produce CNTs with lower crystallinity than arc-discharge, which was used to produce the SWCNTs. The size of the D-band after CNT functionalization in the Raman data further confirms that the crystallinity of the DWCNTs and MWCNTs is lower than for the SWCNT sample (Table 6.2). Therefore the observed trend of emission stability relating to original CNT crystallinity is expected. Future work in this field could involve the chemical attachment and investigation of field emission properties of highly crystalline MWCNTs and DWCNTs produced by arc-discharge.

6.6 Conclusions

CNTs chemically attached to Si produced electrodes suitable for field emission with some unexpected characteristics. The values for turn-on voltage and electric field enhancement factor were within the top 20 % of reported values for each respective CNT type. The FE characteristics were surprisingly good considering the small aspect ratio of the chemically attached CNTs compared to CVD grown CNTs.

The FE from the SWCNT electrodes was remarkably stable by maintaining the maximum current output of the FE system for 15 hr with only a 1.8 % increase in applied voltage required. The FE stability from the DWCNTs and MWCNTs was quite poor in comparison to the Si-SWCNT electrodes. The difference in stability between the CNT types was explained in terms of level of functionalisation, with the more functionalised MWCNT and DWCNT leading to faster FE degradation.

The addition of a thin PS film was found to improve FE characteristics while its effect on FE stability is still under investigation due to the observation of current/voltage roll-off events.

The ease of fabrication, ability to upscale and the small CNT height suggests the chemical attachment of SWCNTs to Si could be a viable process to produce commercial field emission electrodes.

6.7 References

- [1] A. G. Rinzler, J. H. Hafner, P. Nikolaev, P. Nordlander, *et al.*, "Unraveling Nanotubes: Field Emission from an Atomic Wire", *Science*, **269** (5230), 1550-3 (1995).
- [2] B. Q. Wei, R. Vajtai, and P. M. Ajayan, "Reliability and current carrying capacity of carbon nanotubes", *Applied Physics Letters*, **79**, 1172 (2001).
- [3] J. M. Bonard, H. Kind, T. Stokli, and L.-O. Nilsson, "Field emission from carbon nanotubes: the first five years", *Solid-State Electronics*, **45**, 893-914 (2001).
- [4] T. D. Wilkinson, X. Wang, K. B. K. Teo, and W. I. Milne, "Sparse Multiwall Carbon Nanotube Electrode Arrays for Liquid-Crystal Photonic Devices", *Advanced Materials*, **20** (2), 363-6 (2008).
- [5] J.-M. Ting, and W.-C. Lin, "Unprecedented re-growth of carbon nanotubes on in situ re-activated catalyst", *Nanotechnology*, **20** (2), 025608 (2009).
- [6] S. Fan, M. G. Chapline, N. R. Franklin, T. W. Tombler, *et al.*, "Self-Oriented Regular Arrays of Carbon Nanotubes and Their Field Emission Properties", *Science*, **283** (5401), 512-4 (1999).
- [7] C. Xiomara, and *et al.*, "A carbon nanotube field emission cathode with high current density and long-term stability", *Nanotechnology*, **20** (32), 325707 (2009).
- [8] J. M. Bonard, M. Croci, C. Klinke, R. Kurt, *et al.*, "Carbon nanotube films as electron field emitters", *Carbon*, **40** (10), 1715-28 (2002).
- [9] K. T. Constantopoulos, C. J. Shearer, A. V. Ellis, N. H. Voelcker, *et al.*, "Carbon Nanotubes Anchored to Silicon for Device Fabrication", *Advanced Materials*, **22** (5), 557-71 (2010).
- [10] L. B. Zhu, Y. Y. Sun, D. W. Hess, and C. P. Wong, "Well-Aligned Open-Ended Carbon Nanotube Architectures: An Approach for Device Assembly", *Nano Letters*, **6**, 243-7 (2006).
- [11] A. Pandey, A. Prasad, J. P. Moscatello, and Y. K. Yap, "Stable Electron Field Emission from PMMA CNT Matrices", *ACS Nano*, **4** (11), 6760-6 (2010).
- [12] Y.-W. Son, S. Oh, J. Ihm, and S. Han, "Field emission properties of double-wall carbon nanotubes", *Nanotechnology*, **16** (1), 125-8 (2005).
- [13] C. Guohai, and *et al.*, "Improved field emission stability of thin multiwalled carbon nanotube emitters", *Nanotechnology*, **21** (1), 015704 (2010).
- [14] N. Jonge, M. Allieux, M. Doytdcheva, M. Kaiser, *et al.*, "Characterization of the field emission properties of individual thin carbon nanotubes", *Applied Physics Letters*, **85** (9), 1607 (2004).
- [15] X. Lu, Q. Yang, C. Xiao, and A. Hirose, "Nonlinear Fowler-Nordheim plots of the field electron emission from graphitic nanocones: influence of non-uniform field enhancement factors", *Journal of Physics D: Applied Physics*, **39** (15), 3375-9 (2006).
- [16] P. Groning, P. Ruffieux, L. Schlapbach, and O. Groning, "Carbon Nanotubes for Cold Electron Sources", *Advanced Engineering Materials*, **5** (8), 541 (2003).
- [17] W. Liang, M. Bockrath, D. Bozovic, J. H. Hafner, *et al.*, "Fabry - Perot interference in a nanotube electron waveguide", *Nature*, **411** (6838), 665-9 (2001).

- [18] P. Liu, Q. Sun, F. Zhu, K. Liu, *et al.*, "Measuring the Work Function of Carbon Nanotubes with Thermionic Method", *Nano Letters*, **8** (2), 647-51 (2008).
- [19] M.-S. Jung, Y. K. Ko, D.-H. Jung, D. H. Choi, *et al.*, "Electrical and field-emission properties of chemically anchored single-walled carbon nanotube patterns", *Applied Physics Letters*, **87**, 013114 (2005).
- [20] M. Chhowalla, N. Ducati, N. L. Rupesinghe, K. B. K. Teo, *et al.*, "Field emission from short and stubby vertically aligned carbon nanotubes", *Applied Physics Letters*, **79** (13), 2079-81 (2001).
- [21] J. A. Castellano, "Handbook of Display Technology", *Academic Press*, San Diego, (1992).
- [22] Q. H. Wang, A. A. Setlur, J. M. Lauerhaas, J. Y. Dai, *et al.*, "A nanotube-based field-emission flat panel display", *Applied Physics Letters*, **72** (22), 2912 (1998).
- [23] G. Chen, D. H. Shin, T. Iwasaki, H. Kawarada, *et al.*, "Enhanced field emission properties of vertically aligned double-walled carbon nanotube arrays", *Nanotechnology*, **19** (41), 415703 (2008).
- [24] C. Liu, K. S. Kim, J. Baek, Y. Cho, *et al.*, "Improved field emission properties of double-walled carbon nanotubes decorated with Ru nanoparticles", *Carbon*, **47** (4), 1158-64 (2009).
- [25] R. Seelaboyina, S. Boddepalli, K. Noh, M. Jeon, *et al.*, "Enhanced field emission from aligned multistage carbon nanotube emitter arrays", *Nanotechnology*, **19** (6), 065605 (2008).
- [26] J. M. Bonard, C. Klinke, K. A. Dean, and B. F. Coll, "Degradation and failure of carbon nanotube field emitters", *Physical Review B*, **67**, 115406 (2003).
- [27] W. S. Kim, J. Lee, T. W. Jeong, J. N. Heo, *et al.*, "Improved emission stability of single-walled carbon nanotube field emitters by plasma treatment", *Applied Physics Letters*, **87**, 163112 (2005).
- [28] J. M. Bonard, J.-P. Salvetat, T. Stokli, and W. A. De Heer, "Field emission from single-walled carbon nanotube films", *Applied Physics Letters*, **73** (7), 918 (1998).
- [29] C. S. Chang, S. Chattopadhyay, L. C. Chen, K. H. Chen, *et al.*, "band-gap dependence of field emission from one-dimensional nanostructures grown on n-type and p-type silicon substrates", *Physical Review B*, **68** (12), 125322 (2003).
- [30] Y. S. Chen, J. H. Huang, J. L. Hu, C. C. Yang, *et al.*, "Synthesis of single-walled carbon nanotubes produced using a three layer Al/Fe/Mo metal catalyst and their field emission properties", *Carbon*, **45** (15), 3007-14 (2007).
- [31] C. Klinke, R. Kurt, and J. M. Bonard, "Raman Spectroscopy and Field Emission Measurements on Catalytically Grown Carbon Nanotubes", *Journal of Physical Chemistry B*, **106**, 11191-5 (2002).
- [32] K. M. O'Donnell, PhD Thesis thesis, University of Newcastle (2010).
- [33] C. Y. Zhi, X. D. Bai, and E. G. Wang, "Enhanced field emission from carbon nanotubes by hydrogen plasma treatment", *Applied Physics Letters*, **81** (9), 1690-2 (2002).
- [34] B. Ulmen, V. K. Kayastha, A. DeConinck, J. Wang, *et al.*, "Stability of field emission current from various types of carbon nanotube films", *Diamond and Related Materials*, **15** (2-3), 212-6 (2006).

Chapter 7

CNTs as biointerfacial substrates

Interfacing mammalian cells with CNTs has long been considered a potential route for various bioengineering applications. In this Chapter, CNT substrates were fabricated by chemically attaching CNTs to silicon and porous silicon for the purpose of investigating the proliferation, morphology and potential permeabilisation of mammalian neuronal cells.

7.1 Introduction

As discussed in more detail in Chapter 1, the cytoskeleton consists of protein filaments of similar dimensions to CNTs.^[1, 2] For this reason, CNTs offer fertile ground for biointerfacial studies involving mammalian cells. For example CNTs in solution can be used to transport therapeutic materials into the cell membrane^[3] while surface bound CNTs offer a potential substrate for bone engineering or stem cell differentiation.^[4-6]

While the specific cytotoxicity of CNTs bound to surfaces is not an issue, the effect of catalyst particles from CNTs grown by CVD is clearly an issue where transition metal catalysts such as nickel and cobalt are often used and have been found to induce cytotoxicity.^[7] In addition, the fabrication of CNTs by CVD is a process which requires dedicated equipment not readily available within standard biology laboratories. For these reasons and others, biomaterial substrates fabricated by the chemical attachment of catalyst-free CNTs to substrates offers a simple route to study biointerfacial interactions.

Porous silicon is a unique and highly useful biomaterial that has found application in biosensing, cell culture and drug delivery systems.^[8-13] The unique physical and chemical properties of pSi including intrinsic biocompatibility and high internal surface area make this material ideal for a diverse range of biological applications.^[14] pSi can be used for real time monitoring of different cellular functions such as the excretion of enzymes or cell death making it the perfect platform to monitor the effect of CNTs on cellular activity.^[15, 16]

In this Chapter, the chemical attachment and patterning of SWCNTs to pSi for use as a substrate surface for biointerfacial interactions was studied (Figure 7.1). Specifically, the proliferation, attachment and morphology of the human neuronal cell line SK-N-SH on SWCNT substrates was investigated and the potential of the SWCNT substrates to be used as platforms for the electrical stimulation of neuronal cells discussed. Finally, the capability of the SWCNTs to permeabilise the cell membrane and the potential for gene transfection was investigated.

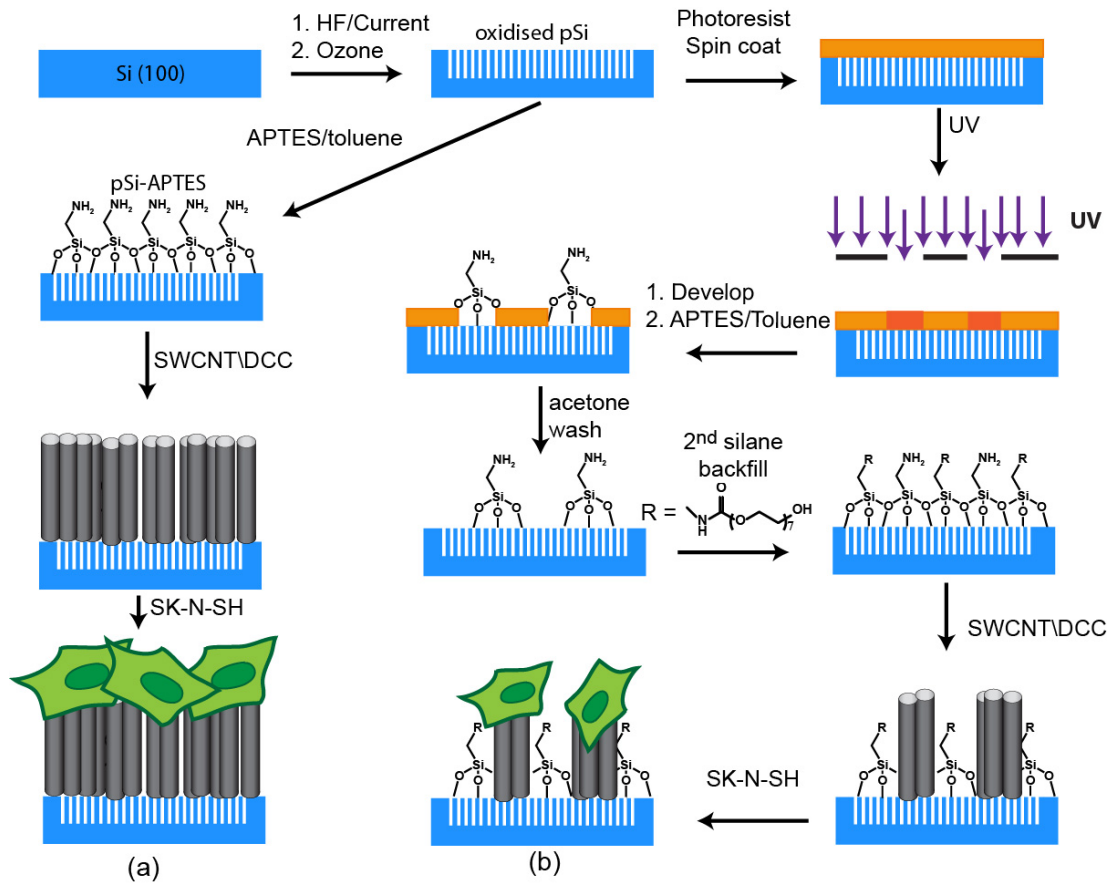


Figure 7.1: Schematic detailing the preparation of (a) a SWCNT-decorated pSi substrate surface and (b) a patterned pSi-SWCNT substrate surface and the resulting attachment of neuroblastoma cells (SK-N-SH). Both preparation schemes involve the chemical attachment of SWCNTs to an amino silane (APTES) on pSi via carbodiimide (DCC) assisted coupling.

7.2 Experimental details

7.2.1 SWCNT biointerface fabrication

The SWCNT substrates for cell immobilisation were fabricated following procedures described in Chapter 2. SWCNT attachment times of 1 min and 2 hr were used throughout the study.

Amine groups were added to the SWCNT substrates by attaching diethylenetriamine (DETA, 99 %, Aldrich) to the carboxyl functional groups on the SWCNTs via carbodiimide coupling. The Si-SWCNT substrate was immersed in a solution containing 10 % (v/v) DETA in DMSO with 0.2 mg mL^{-1} DCC and incubated for 2 hr at $80 \text{ }^\circ\text{C}$. The surfaces were then washed thoroughly with acetone and dried under a stream of nitrogen gas prior to use.

7.2.2 Cell culture and staining

Response of SK-N-SH neuroblastoma cells (a gift from Prof. R. A. Rush, Flinders University) to SWCNT-decorated surfaces was investigated. SWCNT-decorated and control surfaces were placed in 12 well plates (Iwaki) for cell studies. Cells were seeded at a density of $10^5 \text{ cells cm}^{-2}$ in Dulbecco's modified eagle medium (DMEM, Invitrogen, Carlsbad, CA) supplemented with 10 % fetal calf serum (Bovogen), 2 mM L-glutamine, 100 U mL^{-1} penicillin and $100 \text{ } \mu\text{g mL}^{-1}$ streptomycin (Invitrogen). Cell attachment, morphology, viability and permeability were assayed after 4 hr contact with the surfaces, unless otherwise indicated.

Cell morphology was visualised using CellTracker™ Orange CMRA (Invitrogen). Prior to plating on test surfaces, cells were harvested by trypsinisation and stained with the cytoplasmic dye as per manufacturer's instructions. Each surface was then rinsed with Dulbecco's phosphate buffered saline (dPBS) (pH 7.4, 100 mg L^{-1} CaCl_2 and $\text{MgCl}_2 \cdot 6\text{H}_2\text{O}$) to remove any non-specifically or weakly attached cells. Cells were then fixed with 4 % (w/v) paraformaldehyde (Electron Microscopy Sciences, Australia) in PBS (pH 7.4) for 10 min, then washed with PBS prior to mounting in Fluorogel (ProSciTech).

The actin content of the cells was revealed by fluorescently conjugated phalloidin. At the end of the incubation time, weakly adherent cells were removed from the surfaces with PBS and fixed, as detailed above. Alexa Fluor® 594 phalloidin was diluted to 0.165 μM in PBS and the solution was added into each well and incubated in the dark for 30 min. The cells were finally rinsed with PBS and mounted with FluoroGel.

Permeabilisation of cells was detected using propidium iodide (PI) and green fluorescent membrane stain DIOC₁₈ (3) (Invitrogen). Cells were incubated in 12 μM DIOC₁₈ (3) in cell culture media overnight. After overnight incubation DIOC₁₈ (3) stained cells were rinsed once with dPBS before seeding on test and control surfaces. After incubation in contact with surfaces, weakly attached cells were removed by rinsing with PBS, then the surfaces were incubated with PI at a concentration of 7.5 μM in PBS for 5 min in the dark to reveal permeabilised cells. Surfaces were rinsed a final time with PBS and observed immediately.

Cell viability was assayed using fluorescein diacetate (FDA, Sigma). At the end of the incubation time, test surfaces were incubated in a 15 mg mL^{-1} FDA solution in acetone for 10 min at room temperature, and then rinsed with dPBS.

The nucleus stain Hoechst 33342 (Molecular Probes, USA) was added during the final 30 min of the incubation period to the culture solution for each surface to a final concentration of 2 $\mu\text{g mL}^{-1}$.

Prior to AFM and SEM imaging, the cells were dehydrated and fixed on the surface. For cell fixation, the pSi surfaces were carefully removed from the cell culture medium, rinsed once with PBS and fixed in 3.7 % paraformaldehyde in PBS for 10 min at room temperature. Subsequently, the surfaces were washed again twice in PBS and incubated in turn in 50 %, 75 % and 100 % EtOH for 10 min. The surfaces were then washed twice in PBS, incubated in hexane, dried in the laminar airflow, and subsequently coated with platinum (10 nm).

7.2.3 *Fluorescence microscopy*

Fluorescence microscopy was used to visualise the cells after staining. Fluorescence microscopy was performed on an Eclipse 50i microscope equipped with a D-FL universal epi-fluorescence attachment and a 100 W mercury lamp

(Nikon Instruments, Japan). Fluorescence images were captured with a CCD camera (Nikon Instruments, Japan) and images were analysed using NIS-elements v3.07 software (Nikon Instruments, Japan). The following fluorescence filters were used to view fluorescently stained cells. ex. 385-400/em. 450-465 nm, ex. 475-490/em. 505-535 nm, and ex. 545-565/em. 580-620 nm.

7.2.4 Gene transfection by permeabilisation

The transfection of plasmid DNA (pDNA, pEGFP-N1, Clontech) encoding a green fluorescing protein (GFP) was investigated by incubating SK-N-SH cells on the desired surfaces under the incubation conditions described in Section 7.2.2 for 20 hr. The surfaces were then transferred to a solution containing $50 \mu\text{g mL}^{-1}$ pDNA in DNA condensation buffer (EC buffer, Qiagen) with or without the addition of 10 μL Effectene transfection reagent (Qiagen). The samples were incubated in the solution containing pDNA for 10 min at room temperature before being washed with PBS and returned to growth medium under standard incubation conditions for 48 hr before being observed by fluorescence microscopy.

In a variation of this experiment, pDNA was dried on the surface prior to cell culture. In that instance, pDNA was not added to the EC buffer, but otherwise the experiment was identical.

7.2.5 Gene transfection by electroporation

Electroporation experiments were carried out within an in-house built electroporation cell (Figure 7.2). The sample acted as the cathode and was separated by a distance of 1 mm by an o-ring from a gold-coated glass slide counter-electrode. Prior to cell culture, pDNA was dried onto the substrates. Electroporation experiments were carried out in EC buffer by applying a 10 ms pulse (Agilent 33220A 20 MHz waveform generator) of 0 - 48 V. After electroporation, the samples were returned to culture medium and incubated for 48 hr before being observed by fluorescence microscopy.

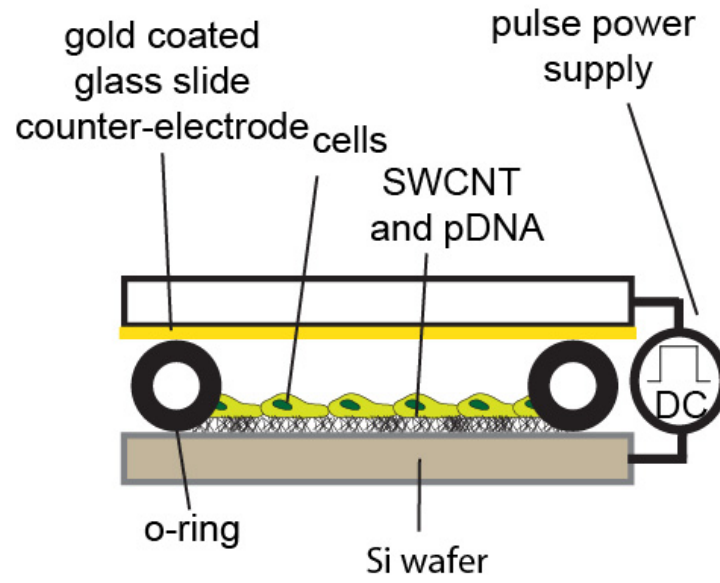


Figure 7.2: Schematic of the electroporation apparatus.

7.3 Cell immobilisation

7.3.1 Cell morphology and proliferation

Initial cell studies used pSi-APTES-SWCNT substrates. The morphology, proliferation and potential permeabilisation of SK-N-SH cells, which are frequently used as a model neuronal cell line, was investigated. Cell staining investigations were conducted on the cells on the SWCNT substrates in conjunction with one or both of oxidised pSi and/or pSi-APTES control surfaces.

Initial cell proliferation and morphology studies used AlexaFluor 594 conjugated phalloidin staining of the cellular actin filaments within the cytoskeleton. Figure 7.3 shows fluorescence microscopy images of the cells after 4 hr of incubation on SWCNT-decorated and control substrates. The cell behaviour on oxidised pSi and APTES-functionalised pSi appeared similar with the cells exhibiting a rounded morphology and frequent cell-cell contacts. The higher magnification images (Figure 7.3 (d, e)) show that lamellipodia are visible and appear to be spreading laterally in all directions on the control substrates. Lamellipodia are particularly pronounced on the APTES-functionalised surface. The presence and radial pattern of lamellipodia is expected on a chemically homogenous surface on the nanoscale. Cells attaching to a SWCNT decorated pSi surface also appeared rounded but had a smaller footprint than cells on the other two surfaces (Figure 7.3). The higher magnification image for the SWCNT substrate shows that cell-cell contacts and lateral lamellipodia are rare (Figure 7.3 (c, f)). The brighter staining suggests that the lamellipodia may be concentrated downward, anchoring toward the SWCNTs. In contrast to the other two substrate surfaces, the SWCNT-decorated pSi is chemically heterogeneous on the scale of tens of nanometres because in between the nanotubes, APTES-functionalised pSi remains.

Cell morphology is known to be dependent upon the wettability of a surface.^[14, 17] To confirm that the surface topography is causing the observed difference in the actin staining and not a change in wettability, the WCA of each surface was measured (Table 7.1). The surfaces exhibit similar WCA values with the SWCNT-decorated pSi showing the lowest WCA of $40 \pm 4^\circ$. The change in WCA between samples is

small and therefore the difference in actin staining observed must be a result of the surface topography induced by the presence of SWCNTs.

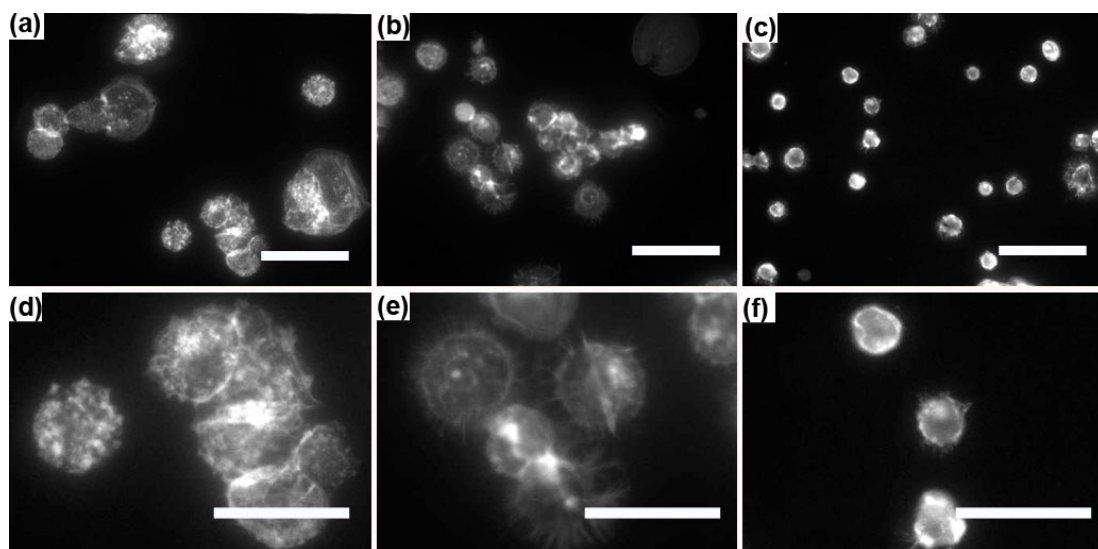


Figure 7.3: Fluorescence microscopy images of phalloidin stained SK-N-SH neuroblastoma cells immobilised on (a, d) oxidised pSi, (b, e) APTES-functionalised pSi and (c, f) SWCNT-decorated pSi. Scale bars (a – c) = 100 μm , (d – f) 50 μm .

Table 7.1: Summary of WCA and cell area measurements of neuronal cells on the three surfaces used as cell culture substrates.

Surface	Contact angle ($^{\circ}$)	Avg. cell area* (μm^2)
pSi	49 ± 8	995 ± 750
pSi-APTES	64 ± 9	589 ± 212
pSi-APTES-SWCNT	40 ± 4	176 ± 41

*calculated from phalloidin staining

In order to investigate the influence of SWCNT coverage, a further cell culture study was carried out where the cells were stained with the cytoplasm stain CellTracker Orange (CMRA). Figure 7.4 shows the results after CMRA staining of cells on an oxidised pSi control, on pSi with a low density of SWCNT and on pSi with a high density of SWCNTs. The SWCNT densities investigated were identical to that shown in Figure 3.13 (b, c) with coverage's of 18 and 40 %, respectively. The cell density is clearly different for the different SWCNT coverages with an average of 154 ± 16 cells per cm^2 obtained for the 18 % SWCNT coverage compared to 266 ± 26 cells per cm^2 for the 40 % SWCNT coverage. This indicates that the

SWCNTs assist cells in attaching to the surface, as already seen for the actin staining (Figure 7.3). An interesting observation is that the stain on the high density SWCNT-decorated surface (Figure 7.4 (c)) is distributed more or less homogeneously within a cell, although the intensity of the staining varies from cell to cell. The outline of the nucleus is not visible in these cells. For the control surface, the nuclei are visible as dark central areas and for the low density SWCNT-decorated pSi surface, nuclei are only visible in some cells. At this point, the meaning of this effect is unclear. It could indicate a different level of anchorage of the cells to the substrate or it simply could reflect the fact that the cells on the SWCNT-decorated surface have a smaller footprint and are more beaded up, whilst the cells on the control surface with a larger footprint are also flatter. All further experiments were completed with the high density SWCNT-decorated substrates.

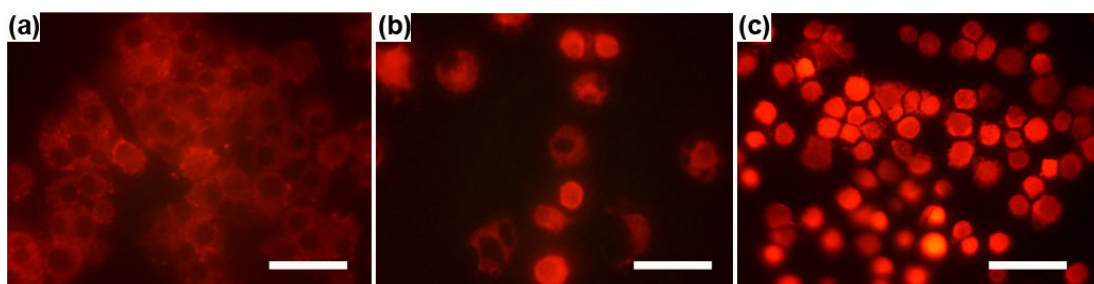


Figure 7.4: Fluorescence microscopy images of cytoplasm stained SK-N-SH neuroblastoma cells using CMRA. (a) pSi control, (b) 1 min of SWCNT attachment (low density) and (c) 2 hr of SWCNT attachment (high density). Scale bar 50 μm .

Figure 7.5 shows the green DIOC₁₈ (3) cell membrane staining of the SK-N-SH cells. This staining procedure was investigated in order to ascertain if the cell membrane was pierced by the vertically-aligned SWCNTs. Indeed, on the SWCNT-decorated surface several cells are visible with dark spots within the cell membrane (see arrows in Figure 7.5 (d)). The membrane staining was rather grainy, which could suggest smaller dark spots in the membrane below the resolution of the optical microscope which may represent areas where the cell membrane is compromised. In contrast, cells on the pSi control did not show dark spots and the membrane staining was more homogenous. Permeabilisation of the cell membrane is a prerequisite for gene transfection into target cells. Previous studies have shown that surface properties such as topography and wettability are critical for surface-induced cell

membrane permeabilisation.^[18, 19] Specifically, vertically-aligned CNTs have been shown to pierce the cell wall to allow small molecules to enter.^[20]

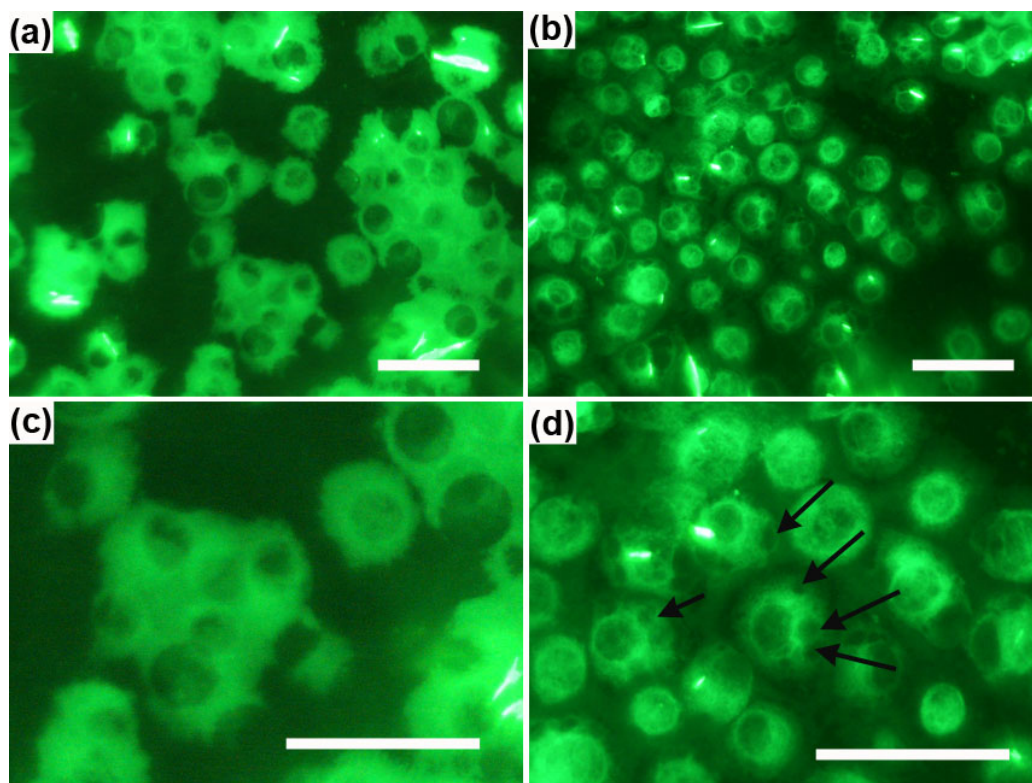


Figure 7.5: Fluorescence microscopy image of membrane stained SK-N-SH neuroblastoma cells using DIOC₁₈ (3) on (a, c) oxidised pSi and (b, d) SWCNT-decorated pSi surfaces at different magnifications. Arrows added in (d) to highlight examples of dark spots observed in membrane. Scale bar 50 μm .

To determine if the dark spots observed in the DIOC₁₈ (3) stained cells in Figure 7.5 were indeed from the SWCNTs permeabilising the cell wall, propidium iodide (PI) staining was performed in conjunction with the DIOC₁₈ (3) membrane stain. PI is a small fluorescent molecule that selectively binds to double-stranded DNA, which is concentrated in the nucleus. In the described experiment, PI will only come into contact with DNA within the cell nucleus if the cell membranes are compromised. Figure 7.6 shows fluorescence microscopy images of the surfaces after PI staining. Cells attached to the SWCNT-decorated surface show a large percentage of fluorescent nuclei while cells on the pSi control surface show no such features.

Comparing the number of green cells from the DIOC₁₈ (3) stain (Figure 7.5) to the number of red cells from the PI stain (Figure 7.6) will give a value of permeabilisation efficiency as these stains were completed concurrently. The

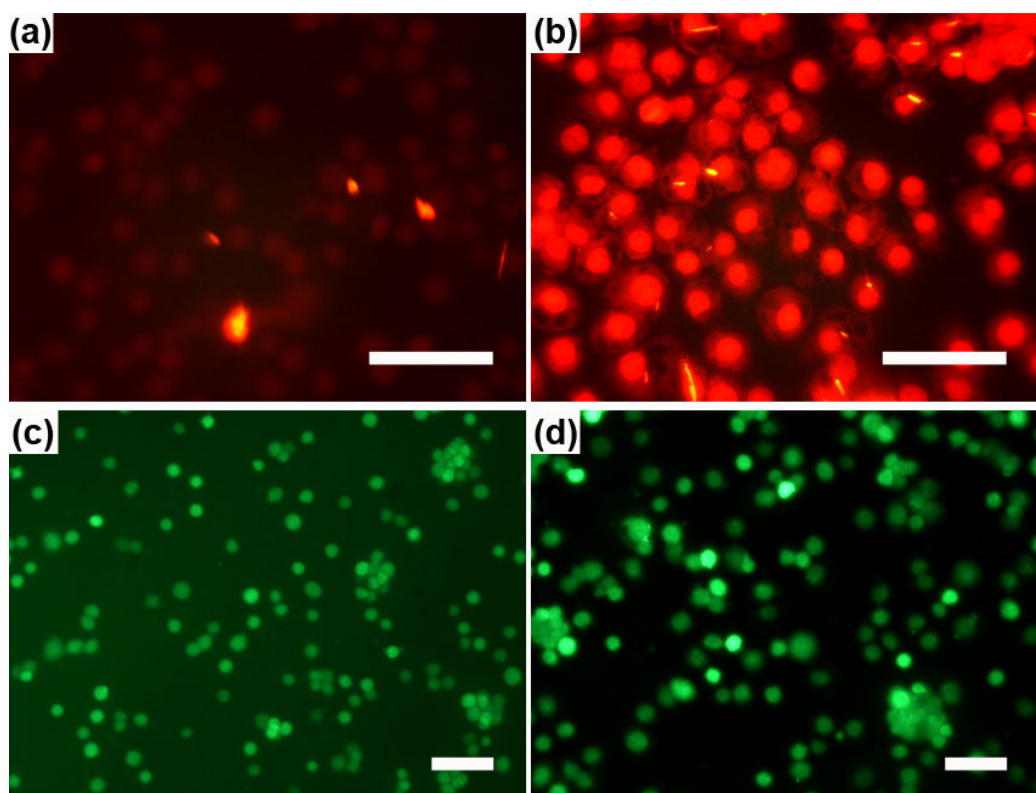


Figure 7.6: Fluorescence microscopy images of SK-N-SH neuroblastoma cells stained with (a, b) propidium iodide (PI) and (c, d) fluorescein diacetate (FDA) on (a, c) oxidised pSi and (b, d) SWCNT-decorated pSi substrates. Scale bar 50 μm .

oxidised pSi leads to less than 5 % permeabilisation by PI while the SWCNT-decorated substrate leads to permeabilisation of over 95 % of cells. This result strongly suggests that the cell membranes are indeed permeabilised by the SWCNTs.

It is well known that PI can also stain non-viable cells where the integrity of the cell membrane is also compromised. Therefore, the PI staining was followed with fluorescein diacetate (FDA) staining of the cells. FDA is a non-fluorescent viability stain, which can enter live cells and is converted into a fluorescent form by enzymes in viable cells. Both the SWCNT-decorated surface and control pSi surface show positive FDA staining, indicating cells on both surfaces are viable. The cells on the pSi-SWCNT surface allow PI to enter the cell membrane to the nucleus while maintaining viability. This indicates that the permeabilisation of the cell wall by the SWCNTs does not adversely affect cell viability. The SWCNTs used in this study protrude <200 nm from this surface (see Chapter 3) which is substantially shorter than the >1 μm CNTs commonly reported. The advantage of shorter SWCNTs is that any permeabilisation will be minor and, most likely, reversible which will not affect

cell viability. In fact, no reduction in viability was observed for up to 48 hr (Figure 7.7).

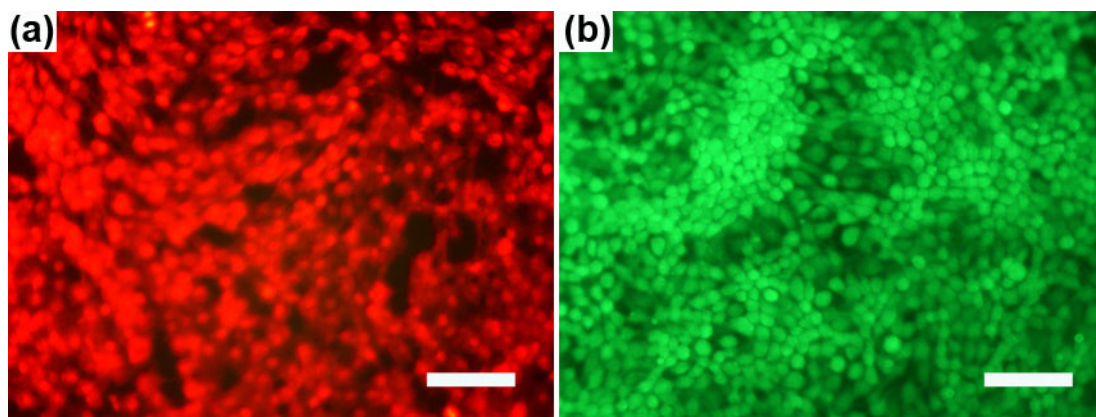


Figure 7.7: Fluorescence microscopy images of SK-N-SH neuroblastoma cells stained with (a) propidium iodide (PI) and (b) fluorescein diacetate (FDA) on a SWCNT-decorated pSi substrates after 48 hr of cell culture. Scale bar 50 μm .

The immobilisation of SK-N-SH cells onto patterned SWCNT substrates was investigated to determine if placement of cells could be controlled. SWCNT patterns were fabricated in a similar fashion to that shown in Chapter 4. Figure 7.8 shows fluorescence microscopy images of CMRA stained neuroblastoma cells on pSi surfaces decorated with SWCNTs confined within a circle and line patterns. In between the features, the surface was functionalised with PEGS. The PEG silane functionalisation was used deliberately to suppress cell attachment as PEG coatings have been shown to prevent the non-specific attachment of extracellular matrix proteins and cells.^[21-23] Indeed, the cells preferentially attached on the SWCNT-decorated regions. The dashed lines were added to guide the eye and represent the boundary of the patterned areas. Control surfaces were prepared without the PEG backfill and in that case the preferential attachment to the SWCNT-decorated regions was not observed. The successful demonstration of patterning of these neuronal model cells is of particular interest as the electrical stimulation of patterned networks of neurons can be used to investigate their function.^[24] The electrical properties of SWCNTs make them ideally suited to interface surfaces with neuronal cells. Here, we present a method where SWCNTs both promote specific attachment while offering the opportunity to directly probe mammalian neuronal cells.

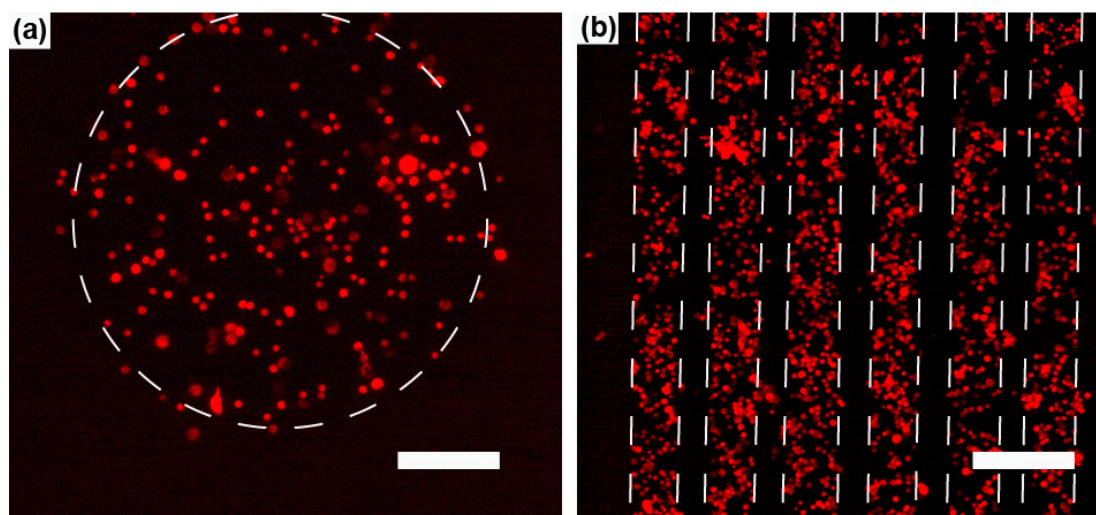


Figure 7.8: Fluorescence microscopy images of SK-N-SH neuroblastoma cells stained with CellTracker Orange showing preferential attachment to SWCNT-decorated patterns on a pSi substrate showing (a) circle and (b) line pattern. The regions in between those decorated with nanotubes were PEG functionalised. Scale bar 100 μm .

The interfacing of mammalian cells with CNTs is in itself not a new concept.^[3] However, methods to immobilise CNTs onto surfaces are still under heavy scrutiny. While other CNT deposition methods require dedicated facilities and machinery, the chemical attachment method described here is straightforward and can be replicated in any standard chemical laboratory. The CNT surfaces produced do not contain toxic materials such as catalyst nanoparticles and can be patterned using simple lithographic techniques.

The chemical attachment of SWCNTs to pSi films rather than flat Si generates surfaces which are suitable for the culture of mammalian cells but have the added advantage of the underlying porous surface which can be loaded with bioactives, functionalised for controlled degradability and the optical properties of which can be used for biosensing of cellular activity without specific cell staining.^[12, 25] The permeabilisation of the cells demonstrated here points to opportunities for gene transfection into the target cells. In addition to gene transfection by permeabilisation, the high aspect ratio and electrical conductivity of the SWCNTs renders them conducive to electroporation-based transfection.^[26, 27]

7.3.2 AFM and SEM imaging

To determine if the SWCNTs were piercing the cell membrane SEM and AFM analysis was completed on the cells immobilised on the SWCNT substrates. Figure 7.9 shows SEM images of SK-N-SH cells immobilised onto pSi-SWCNT substrates. Although the cells appear spread, there is no obvious deformation of their structure caused by the SWCNTs. The higher magnification images, particularly Figure 7.9 (c, d) show cell lamellipodia spreading from the cell. There are a number of published SEM images of long CNTs and nanofibres (see Figure 1.16) clearly skewering cell membranes. This is not observed for the chemically attached pSi-SWCNT substrates. The short height of the SWCNTs (<200 nm) would not allow them to completely skewer through the more than 1 μm thick cells.

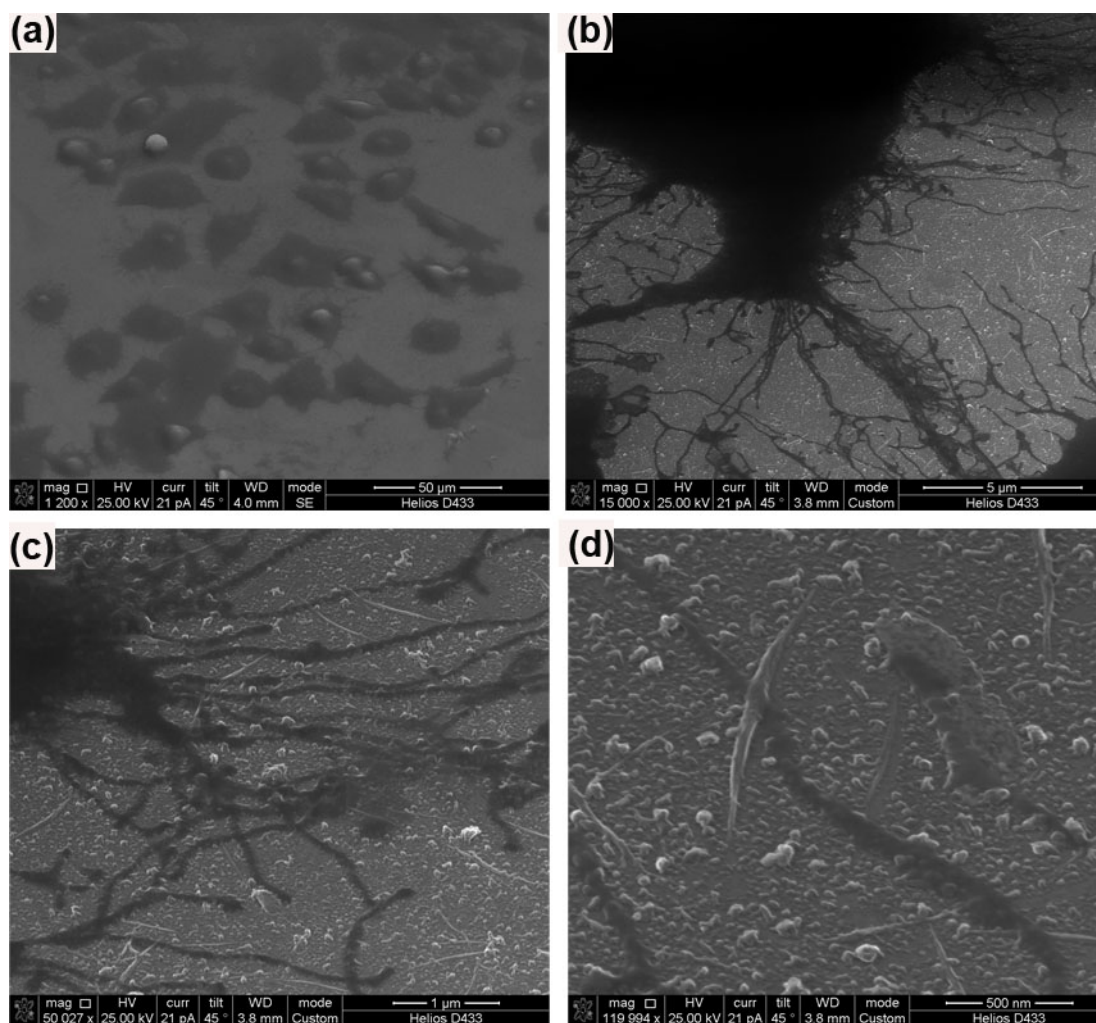


Figure 7.9: Summary of SEM images of SK-N-SH on pSi-SWCNT substrates showing cell culture and spreading of lamellipodia (NanoLab SEM).

In order to determine if the SWCNTs create a subtle change on the cell surface AFM was used to image the cells immobilised onto the pSi-SWCNT substrates (Figure 7.10). The edge of a cell was imaged such that the difference between the pSi-SWCNT substrates and the cell membrane could be ascertained. The thickness at the edge of the cell was approximately equal to the heights of the SWCNTs while the centre of the cell was imaged to be thicker than 2 μm . The cells were dehydrated to be fixed for imaging and as a consequence of the fixing; the cell thicknesses observed may be smaller than the actual value prior to dehydration. The cell topography was imaged to be a mixture of both a gentle and sharp surface undulations. The sharp surface undulations are of similar shape and size to the SWCNTs on the surface (Figure 7.10 (b)). However, it is more likely that such surface roughness is native to the cell structure and not induced by the underlying surface.

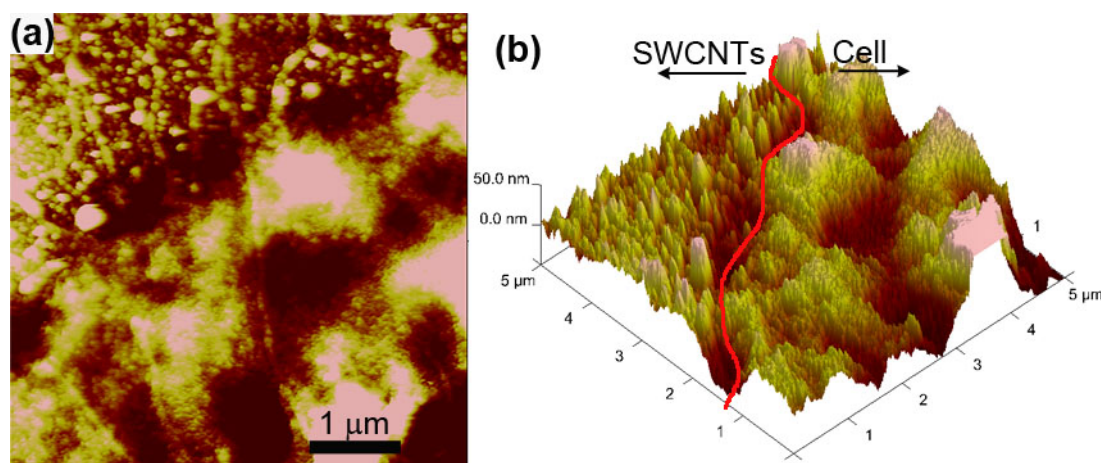


Figure 7.10: AFM image of edge of a SK-N-SH cell on a pSi-SWCNT substrate.

No physical evidence of membrane piercing by the SWCNTs was observed by AFM or SEM. However, this result does not conclude that permeabilisation of the cell wall is not occurring. Small gaps may still be formed on the underside of the cellular structure. Large, obvious holes in the cell wall are often lethal to the cell and as such are not optimal.^[28] Previous studies of gene transfection using larger CNT features indicate that the gene transfection is high but the cell viability is low. Therefore it may be advantageous to use smaller CNT features to produce smaller gaps in the cell membrane for gene transfection studies. Permeabilisation of the cell wall is not only reliant on the SWCNTs piercing the membrane, the integrity of the

cell wall may be compromised by a number of other factors induced by the SWCNT substrates.

7.4 Gene transfection

7.4.1 Gene transfection by permeabilisation

Gene transfection studies were investigated using pEGFP-N1, which is a sequence of plasmid DNA (pDNA) encoded with a green fluorescent protein (GFP). This plasmid was used as an initial test to determine if transfection occurs and could be coupled with a simple nucleus stain to determine the transfection efficiency.

Initial transfection studies used pSi-SWCNT substrates by first immobilising the neuronal cells on the SWCNT substrate (and control surfaces) and then immersing them in a dilute solution containing the pDNA. Fluorescence microscopy was used to determine the number of green cells, indicating transfection of the pDNA, compared to the number of blue cells (from the Hoechst stain), indicating the total number of cells. Testing of transfection following this method resulted in no observable transfection of pDNA into the cells (Figure 7.11).

To improve the transfection efficiency, the transfection agent Effectene was incorporated with the pDNA prior to transfection. Effectene is a cationic lipid which acts to first condense the pDNA into a smaller package and the lipophilic nature of Effectene assists the pDNA to interact and cross the negatively charged cell membrane.^[29] With the inclusion of Effectene, the transfection efficiency increased to 4.4 % for the pSi-APTES-SWCNT substrates compared to 4.2 % for pSi-APTES and 2.5 % for the for bare pSi substrate (Figure 7.12, Table 7.2). The difference in efficiency between the surfaces is statistically negligible. However, the low cell count observed for the pSi and pSi-APTES controls is an interesting observation. A low cell count indicates that the cells did not show a particular affinity to the pSi substrate and are easily removed. This may result in the cells being close to death when the gene transfection studies were completed, which may result in false positive green cells observed. A lower cell count for the control substrates was also observed for the phalloidin and CMRA staining (Figure 7.3 and Figure 7.4) but to a lesser degree. The difference between the cell numbers observed for the previous phalloidin and CMRA staining compared to Hoechst staining in Figure 7.11 and Figure 7.12 is that the gene transfection experiments involved up to 72 hr of cell culture incubation compared to 4 hr for the morphology investigations. The longer

incubation time used for the gene transfection clearly has a greater effect on cell numbers.

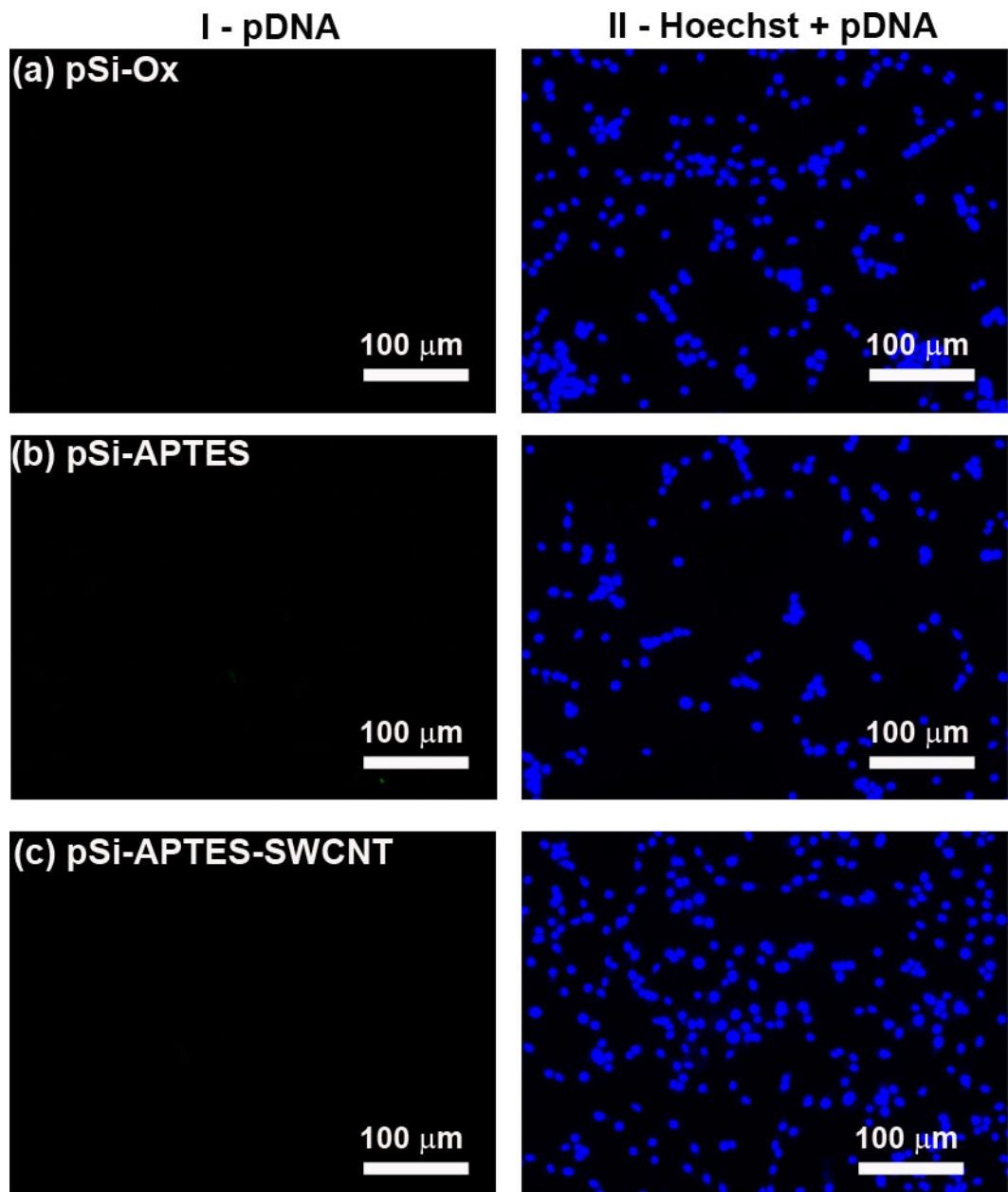


Figure 7.11: I pDNA fluorescence and II Hoechst staining + pDNA of SK-N-SH cells on (a) pSi, (b) pSi-APTES and (c) pSi-APTES-SWCNT substrates after the gene transfection experiment.

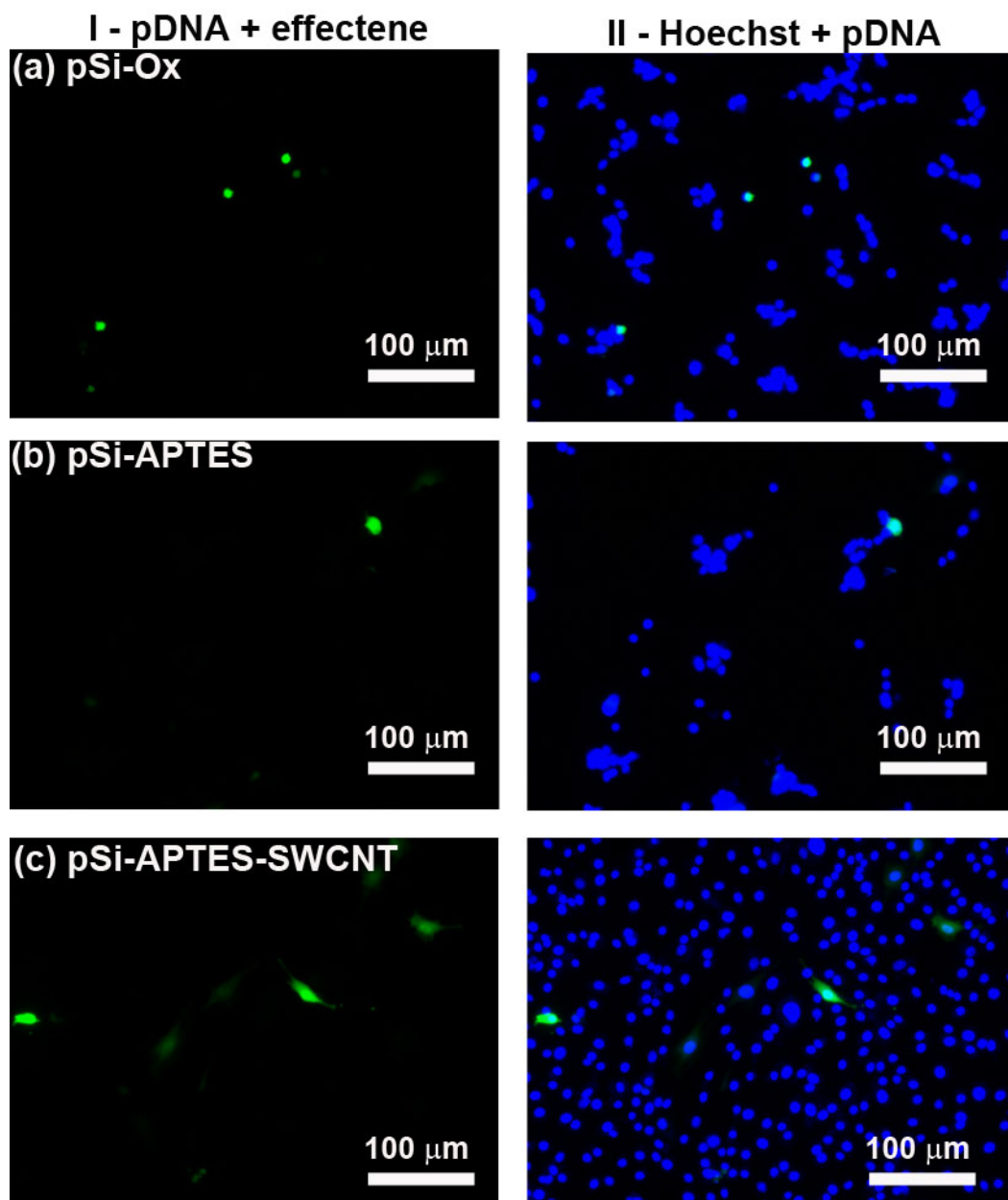


Figure 7.12: I pDNA fluorescence and II Hoechst staining + pDNA of SK-N-SH cells on (a) pSi, (b) pSi-APTES and (c) pSi-APTES-SWCNT substrates after gene transfection experiment with Effectene added.

Table 7.2: Summary of transfection efficiencies for pDNA with Effectene on the pSi based substrates.

Sample	no. green cells	no. blue cells	Transfection efficiency (%)
pSi	4	160	2.5
pSi-APTES	6	96	4.2
pSi-APTES-SWCNT	15	341	4.4

The overall transfection efficiency for the neuronal cells for all surfaces is low; the result is unsurprising considering the SK-N-SH cell line is notoriously difficult to transfect, which was the motivation for the current study. In fact, the biological agent supplier, Qiagen, does not list any transfection agents which have previously been shown to transfect neuroblastoma cell lines (www.qiagen.com). Conversely, the low efficiency is surprising considering the evidence for cell permeabilisation from the PI and DIOC₁₈ (3) staining presented earlier (Figure 7.5 and Figure 7.6). However, the AFM and SEM images suggested that the small height of the SWCNTs resulted in an exclusive interaction with the underside of the cells. Therefore, if the pores induced by the SWCNTs are on the underside of the cells the pDNA (MW = > 600 000 g mol⁻¹) may not physically be able to reach the pores induced by the SWCNTs, while the smaller, more mobile PI (MW = 668 g mol⁻¹) could enter the cell membrane. Additionally, the type of permeabilisation induced by the SWCNTs may enhance the infiltration of PI but fail to show an effect on the infiltration of pDNA.

In order to increase the cell count for the transfection, the same experiment was repeated on a flat Si substrate. The use of flat Si has previously shown to increase the cell number, area and length of SK-N-SH cells when compared to pSi with a pore size range of 5 – 20 nm.^[30] Figure 7.13 displays the transfection results obtained. A lower discrepancy in cell number was obtained, but gene transfection was again shown to be similar between the samples with the Si substrate having an efficiency of 0.3 % compared to 1.7 % and 0.95 % obtained for the Si-APTES and Si-APTES-SWCNT surfaces, respectively. The efficiency values obtained on flat Si were lower than on pSi possibly because the cells are more viable on the flat Si substrate, and therefore the cell membranes are less compromised. Despite the differences in transfection efficiency observed repeatedly, the efficiencies obtained for both substrates were too low to warrant further investigation.

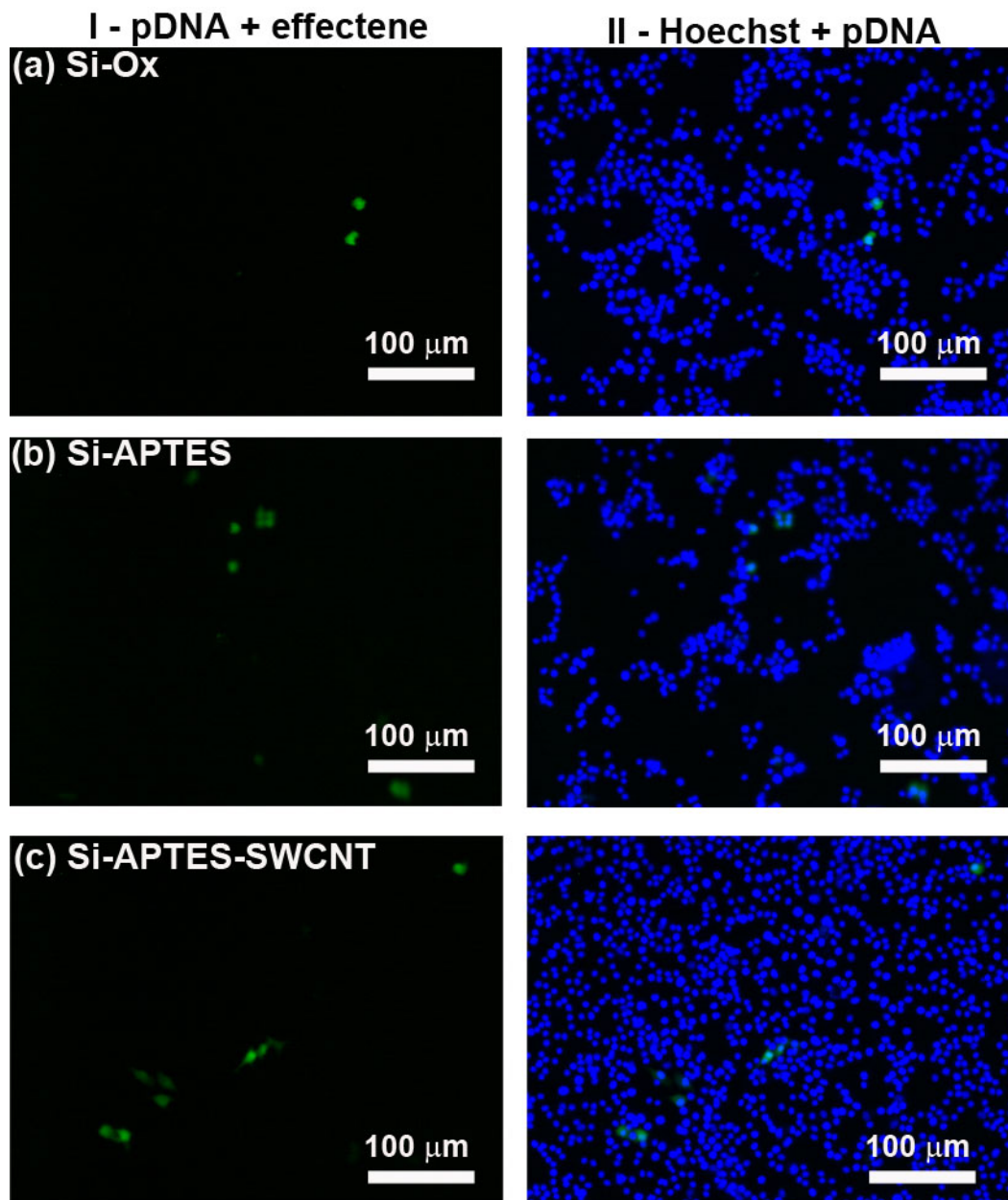


Figure 7.13: I pDNA fluorescence and II Hoechst + pDNA staining of SK-N-SH cells on (a) flat Si, (b) flat Si-APTES and (c) flat Si-APTES-SWCNT substrates after gene transfection experiment with Effectene added.

Table 7.3: Summary of transfection efficiencies for pDNA with Effectene on the flat Si based substrates.

Sample	no. green cells	no. blue cells	transfection efficiency (%)
Flat Si	2	668	0.3
Flat Si-APTES	7	411	1.7
Flat Si-APTES-SWCNT	9	946	0.95

To improve transfection efficiency, attempts were made to place the pDNA onto the SWCNTs prior to cell immobilisation in order to give the pDNA access to the underside of the cells, where the pores are likely to be formed. The difficulty in achieving this is that the pDNA must be bound to the pSi-SWCNT substrate with enough strength to remain on the surface during cell immobilisation while also being able to readily desorb from the surface in order to enter the cells. The simplest method to achieve this is to electrostatically adsorb the negatively charged plasmid to the surface. The Si-SWCNT substrate has a net negative charge from the carboxylic acid groups on the functionalised SWCNTs. Diethylenetriamine (DETA) was attached to the SWCNTs by means of simple amide coupling chemistry in order to introduce amino groups to the ends of the SWCNTs which are known to promote electrostatic binding of DNA (Figure 7.14).^[31]

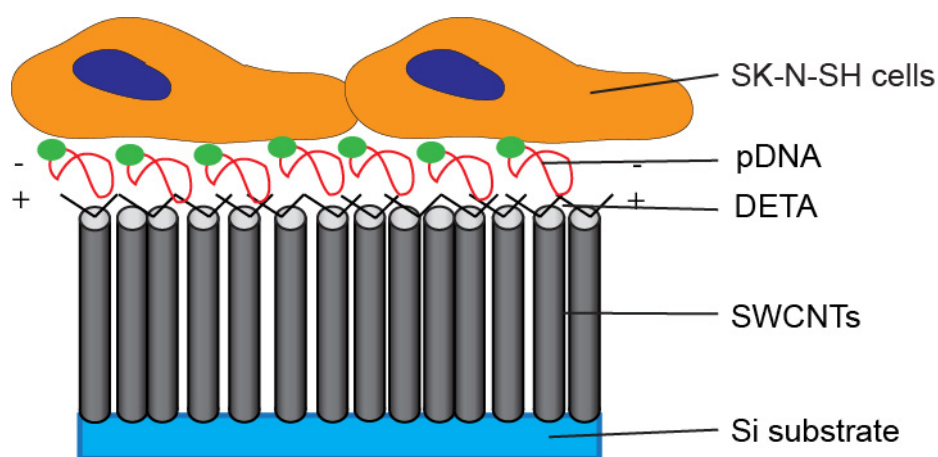


Figure 7.14: Schematic of SWCNTs chemically attached to Si substrates with positively charged diethylenetriamine (DETA) electrostatically binding pDNA to the substrate prior to cell culture.

To confirm that DETA was chemically attached to the SWCNTs, the surface was analysed via XPS. In order to correctly determine the effect of the DETA on pDNA adsorption and subsequent gene transfection, two SWCNT attachment schemes were investigated, direct ester and APTES mediated. This was required because the APTES layer also contains nitrogen atoms which may have influenced the result.

The direct ester SWCNT substrate (Figure 7.15 (a, c)) showed no nitrogen peak at 400 eV until after the DETA attachment. This is clear evidence for DETA immobilisation. Other interesting results from the XPS data of the Si-ester-SWCNT

surfaces include the absence of any N 1s peak prior to DETA attachment which indicates that both DCC and DMSO are completely removed during the washing process. Additionally, the C 1s (≈ 287 eV) peak of the cleaned, oxidised Si (black series in Figure 7.15) is almost of equal height to that after SWCNT deposition. This observation shows that the amount of carbon material collected on a cleaned surface while transporting between laboratories is quite high and that the C 1s spectra in itself is not evidence for the presence of CNTs.

The APTES mediated samples (Figure 7.11 b, d) show small N 1s signals prior to DETA attachment from the terminal amine group from the APTES layer. Similar to the direct ester SWCNT substrates, the APTES mediated substrates show a significant increase in N 1s signal after DETA immobilisation. The N 1s signal after DETA attachment compared to the Si-APTES surface is quite large and may suggest that some unspecific adsorption of DETA has occurred.

After DETA attachment, pDNA was deposited onto the surface and allowed to dry before being rinsed gently with PBS solution. The presence of the pDNA was confirmed by depositing PI onto the surface and observing red fluorescence due to the PI binding to the pDNA. Dropping PI onto a surface without pDNA did not result in any observed fluorescence. Cell culture was carried and the system was visualised with fluorescence microscopy to determine the extent of gene transfection (Figure 7.16). Cell transfection for the SWCNT substrates is summarised in Table 7.4. No significant enhancement had occurred after pDNA adsorption to the surface prior to cell culture. This may be a result from the pDNA being electrostatically bound too tightly to the surface (see the very large N 1s peak in Figure 7.15, indicating a high population of amine groups) or the pDNA may have diffused throughout the culture medium during the 20 hr of the cell culture prior to the addition of Effectene. If the pDNA is spread throughout the solution it will no longer be in close proximity to the SWCNT-cell interface which is where the permeabilisation will occur. The issue with the placement of the pDNA may be overcome by chemically linking the pDNA to the SWCNTs using a cleavable chemical linker.^[32] The chemical attachment of the pDNA to the SWCNTs will not allow the pDNA to diffuse away from the surface during cell culture. Upon exposure to a certain stimulus (e.g., light, pH or enzyme activity) the linker holding the pDNA can be severed, allowing the plasmid to enter the cell. Although promising, this could not be pursued due to time constraints.

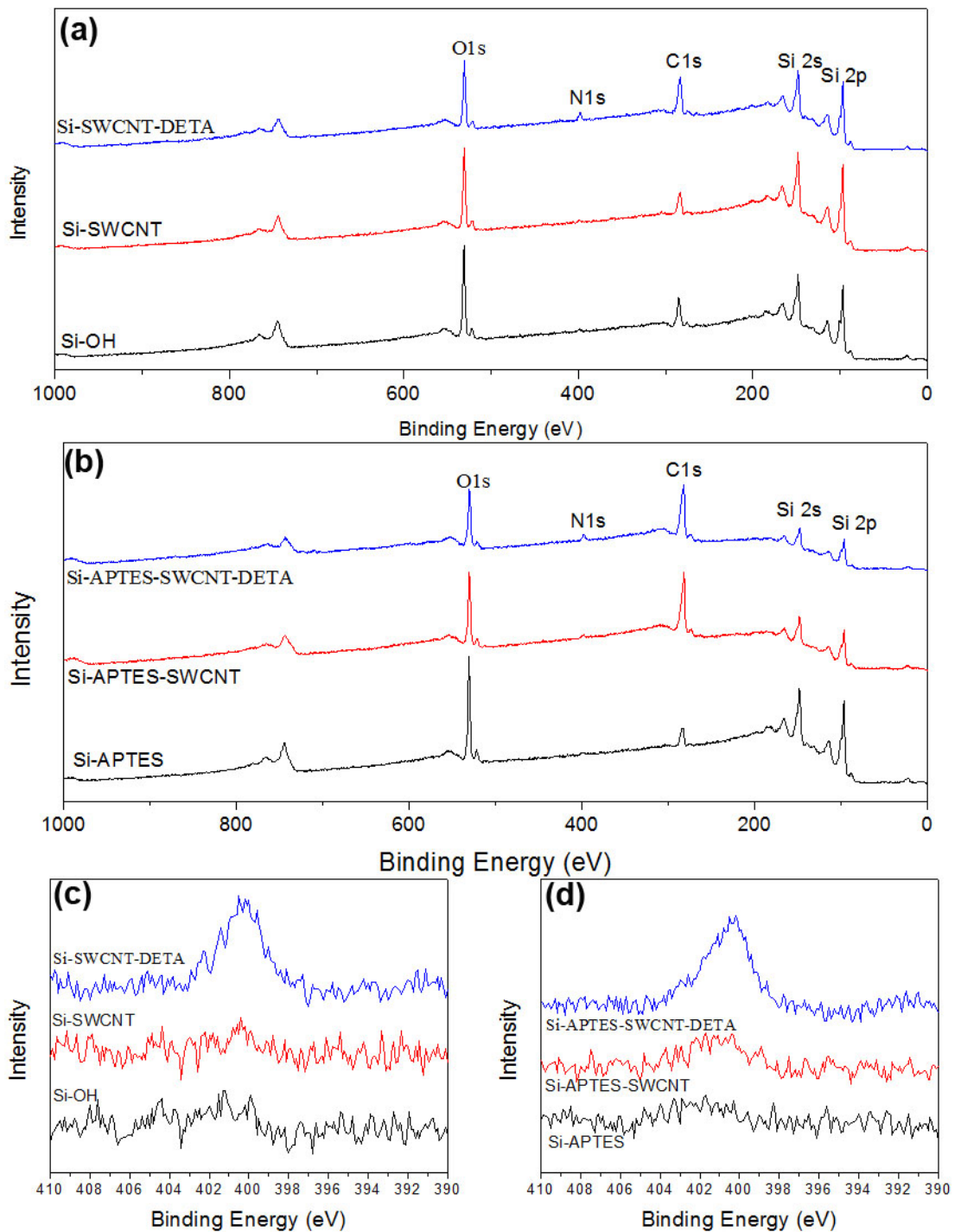


Figure 7.15: XPS analysis to determine if the amine containing diethylenetriamine (DETA) is bound to the surface after SWCNT attachment via (a, c) direct ester attachment and (b, d) APTES mediated attachment showing (a, b) survey scans and (c, d) higher resolution spectra of the N 1s peak.

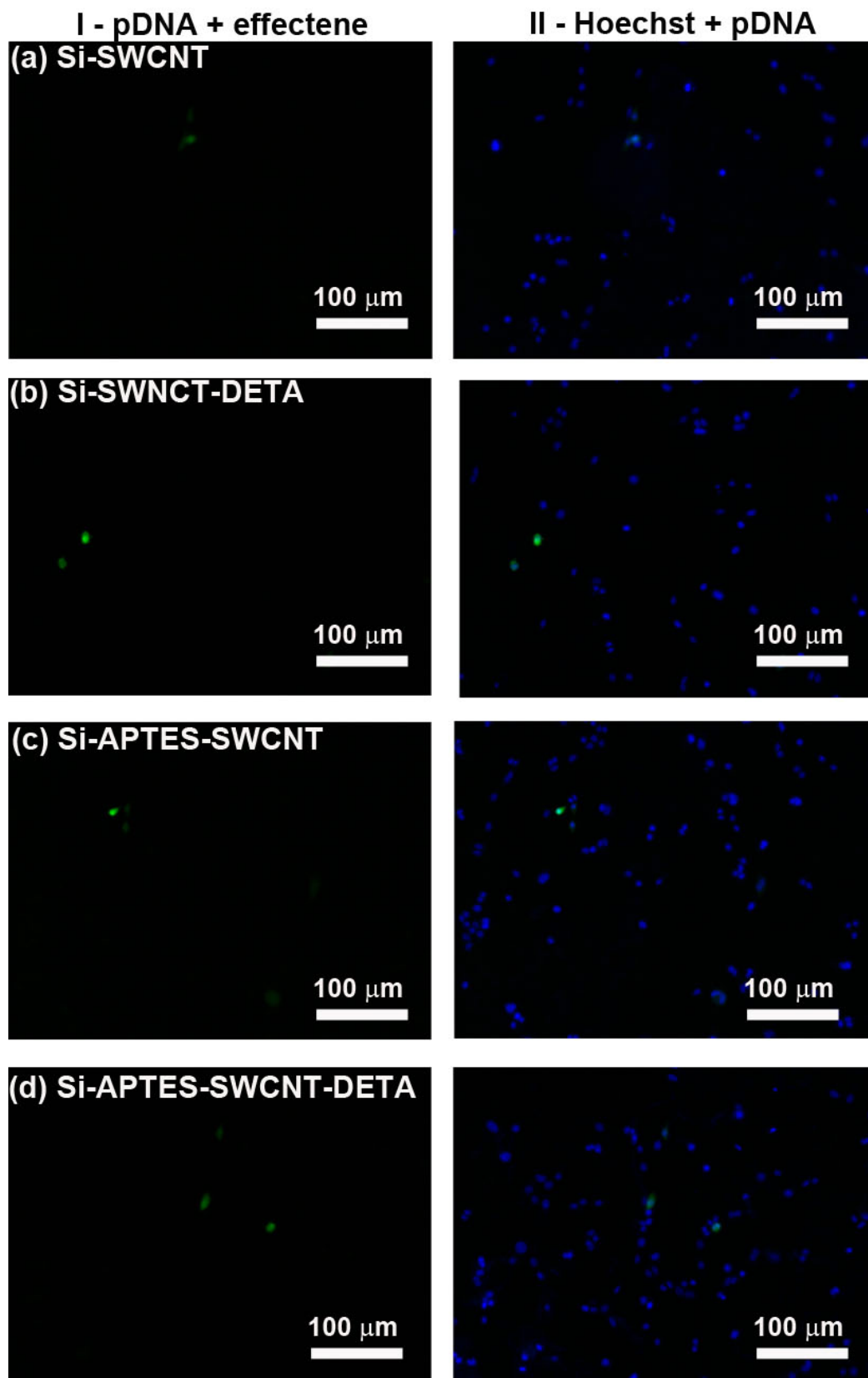


Figure 7.16: I pDNA fluorescence and II Hoechst + pDNA staining of SK-N-SH cells on (a) Si-SWCNT, (b) Si-SWCNT-DETA, (c) Si-APTES-SWCNT and (d) Si-APTES-SWCNT-DETA substrates after gene transfection experiment with Effectene added.

Table 7.4: Summary of transfection efficiencies adsorbed pDNA with Effectene on SWCNT substrates.

Sample	no. green cells	no. blue cells	transfection efficiency (%)
Si-SWCNT	1	80	1.25
Si-SWCNT-DETA	3	83	3.6
Si-APTES-SWCNT	5	105	4.8
Si-APTES-SWCNT-DETA	3	115	2.6

While transfection on the SWCNT substrates was observed, it only occurred in the presence of Effectene. The use of transfection agents is undesirable under some circumstances as they often reduce cell viability.^[33, 34] The low transfection efficiency may not be a result of the mobility of the pDNA but may be in fact caused by the lack of permeabilisation of the cells. Although we have shown some evidence for permeabilisation of the cells, the lack of pDNA transfection indicates that perhaps the induced pores may be too small for the plasmid to enter the cell. To increase the induced pore size, electroporation of neuronal cells was attempted on the Si-SWCNT substrates.

7.4.2 Gene transfection by electroporation

The electric field enhancement factor of the Si-SWCNT substrates demonstrated in Chapter 6 make them prime surfaces for electroporation. Electroporation is the inducement of pores within the cellular structure by the application of an external electric field. The electric field causes the rapid movement of species both within and outside the cell and can create small pores. However, the magnitude of electric field that leads to the highest gene transfection efficiency often also leads to the lowest cell viability. The use of CNTs allows a lower external applied electric field to create a very large local electric field around the apex of the CNTs. Therefore, the pores should be formed on the cells in areas close to the apex of the CNTs while areas away from the CNTs will not be adversely affected by the electric field. This should result in high transfection efficiency while retaining high viability.

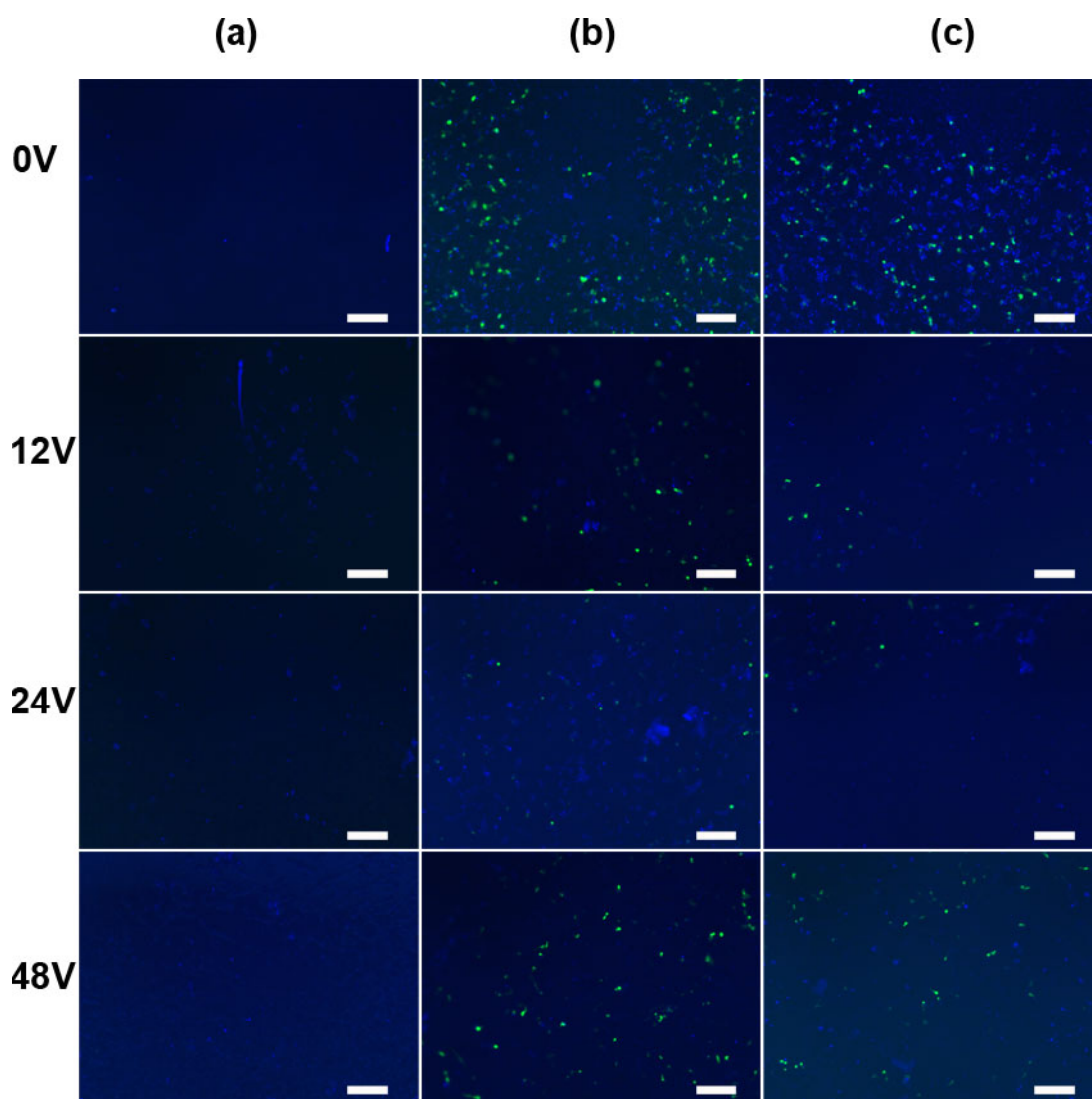


Figure 7.17: Summary of initial electroporation experiments showing fluorescence microscope images of SK-N-SH cells stained with both Hoechst and pDNA on (a) Si-SWCNT, (b) Si-SWCNT + Effectene and (c) Si + Effectene.

Electroporation experiments were completed by using the Si-SWCNT substrate as the negative electrode separated by an o-ring (1 mm thickness) from a gold coated glass slide as the positive electrode. The o-ring was filled with electroporation buffer and a short pulse (10 ms) of voltage was applied to the surface. After the pulse was applied the surface was incubated in standard cell culture conditions for 48 hr. The cells were imaged by fluorescence microscopy where green cells indicate transfection of the pDNA expressing GFP. The electroporation results are summarised in Figure 7.17. No transfection was observed without the presence of the transfection agent Effectene (Figure 7.17 (a)). Gene transfection was obtained when Effectene was added (Figure 7.17 (b, c)) with no particular trend of no. of green cells

vs. applied voltage observed (which is expected if the applied voltage is controlling the gene transfection). A concerning result was that the 0 V and the bare flat Si controls (Figure 7.17 (c)) seemed to produce efficiencies of equal or higher to the Si-SWCNT substrates. Equally concerning was the lower number of blue Hoechst stained cells observed, which may indicate that the electroporation, or the manual handling of the samples may reduce cell viability. Dying cells were more likely to be transfected, giving a false positive result.

To determine the cause of the strange Hoechst stain observed in Figure 7.17 tests were carried out to determine the maximum applied voltage that would not affect viability of the cells. Applied voltages of 0, 12, 24 and 48 V were investigated by with both Hoechst and FDA staining. It was found that the cells remained viable up to an applied voltage of 24 V. All further experiments were completed at applied voltages ranging from 0 – 24 V. FDA and transfection of the pDNA expressing GFP cannot be investigated concurrently as both show green fluorescence.

The electroporation experiment was completed on the Si-SWCNT-DETA surfaces with extra care taken in the manual handling of the samples in order to not adversely affect cell viability. The pDNA transfection results are shown in Figure 7.18. Most importantly, no Effectene was added in these experiments. Hoechst staining shows a much improved cell density compared to Figure 7.17. This experiment is the first time that GFP expression has occurred without Effectene. However, the efficiency is very low ($< 0.1\%$) and the 0 V experiment shows transfection. This may indicate that the manual handling and removal from cell culture conditions of the samples has influenced transfection, not the electroporation itself.

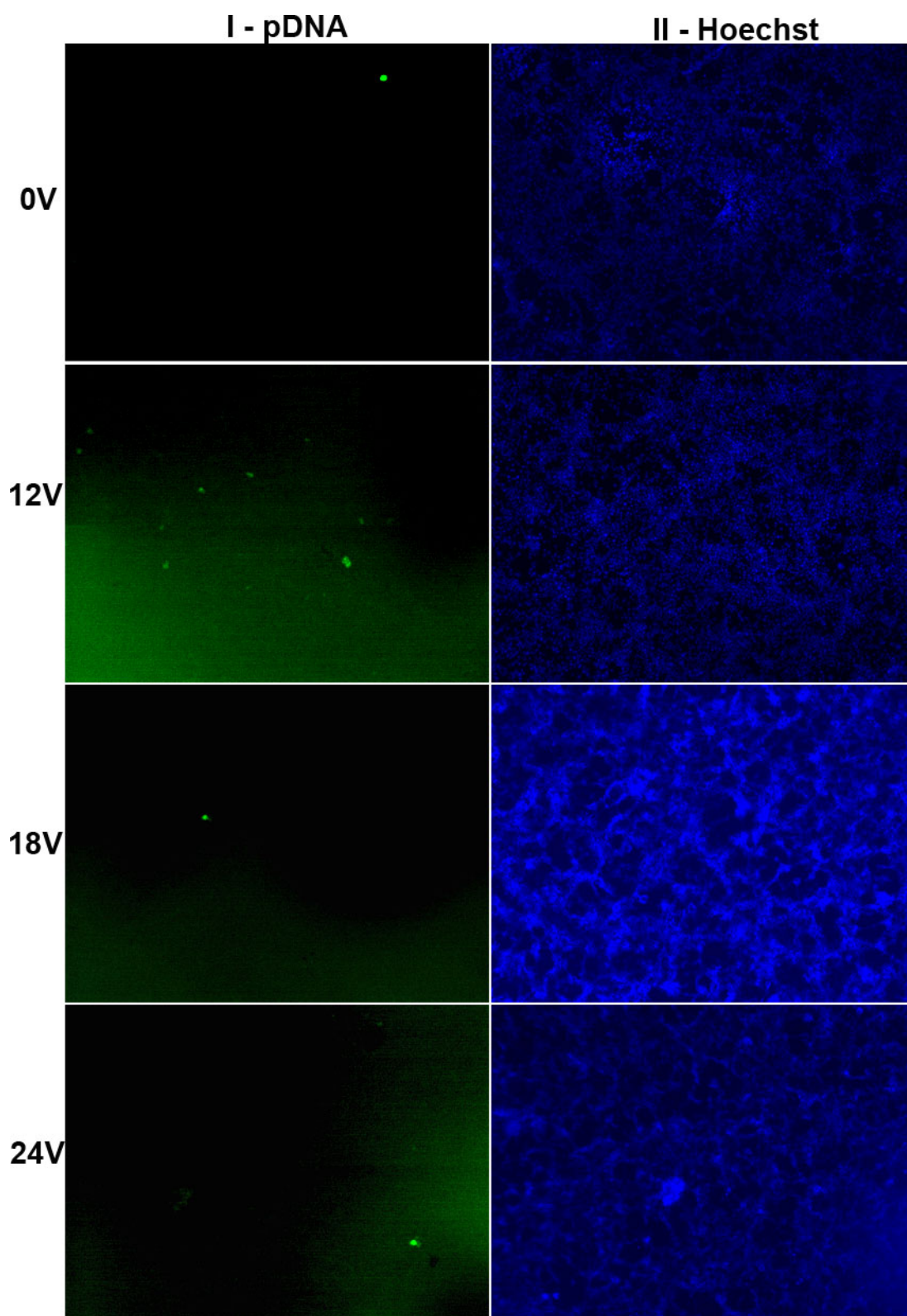


Figure 7.18: Fluorescence microscope images of electroporation of SK-N-SH cells on Si-SWCNT-DETA substrates at varying applied voltages showing (I) pDNA expressing GFP and (II) Hoechst stain.

The electroporation apparatus used was based on the design reported by Iwata *et al.*^[27] However, they did not explicitly mention how the apparatus was put together. A small variation between our methods may in fact make a large difference in the obtained result. The Si-SWCNT substrates prepared clearly exhibit a very large electric field enhancement (as shown by the field emission experiments) and therefore should be perfect substrates for electroporation. Further experiments are required in this promising area. However, a drastic change in the design of the electroporation apparatus might be required. The Si-SWCNT substrate should be kept within the same vessel for both cell culture and electroporation as the manual handling of the sample and subsequent exposure to air and the lack of pH/temperature control was clearly adversely affecting the cells.

7.5 Conclusions

The morphology and permeabilisation of the human neuronal cell line SK-N-SH was investigated on SWCNT-decorated substrates and compared to oxidised and APTES-functionalised pSi. Cytoskeletal and cytoplasmic staining showed that cell density and cell morphology was significantly different on SWCNT-decorated surfaces as compared to pSi without SWCNTs. The SWCNTs gave rise to better cell attachment in terms of cell numbers but at the same time reduced cell spreading. Cell membrane staining suggested that the SWCNTs permeabilise the cell membranes. Incubation with the DNA binding dye PI showed that the small molecule could indeed enter into the cells attached on the SWCNT-decorated substrates but not on pSi alone. FDA staining confirmed the viability of the permeabilised cells. AFM and SEM imaging did not show any major structural deformation of the cellular structure induced by the SWCNTs, indicating that the permeabilisation was restricted to the underside of the cells.

Transfection of pDNA was attempted using two protocols. The first was absorption after permeabilisation, which showed no transfection without the addition of Effectene. Transfection efficiencies, with Effectene, were quite low and showed no statistical increase between the SWCNT and control surfaces. The second transfection mechanism was electroporation, which showed pDNA transfection without the use of Effectene. However, cell viability appeared lower after electroporation suggesting that manual handling and subsequent exposure to air and the lack of pH/ temperature control during the electroporation experiments were responsible for the transfection observed.

The chemical attachment of SWCNTs to pSi is a simple method to produce a platform suitable for studying cellular interactions and may find application in gene transfection and as platforms for the electrical stimulation for neuronal cells. More work is required on gene transfection while investigating other cell lines may provide more advantageous results.

7.6 References

- [1] W. W. Franke, E. Schmid, M. Osborn, and K. Weber, "Different intermediate-sized filaments distinguished by immunofluorescence microscopy", *Proceedings of the National Academy of Sciences*, **75** (10), 5034-8 (1978).
- [2] A. Bretscher, "Fimbrin is a cytoskeletal protein that crosslinks F-actin in vitro", *Proceedings of the National Academy of Sciences*, **78** (11), 6849-53 (1981).
- [3] L. Lacerda, S. Raffa, M. Prato, A. Bianco, *et al.*, "Cell-penetrating CNTs for delivery of therapeutics", *Nano Today*, **2** (6), 38-43 (2007).
- [4] K. Tuzlakoglu, N. Bolgen, A. Salgado, M. Gomes, *et al.*, "Nano- and micro-fiber combined scaffolds: A new architecture for bone tissue engineering", *Journal of Materials Science: Materials in Medicine*, **16** (12), 1099-104 (2005).
- [5] L. P. Zanello, B. Zhao, H. Hu, and R. C. Haddon, "Bone Cell Proliferation on Carbon Nanotubes", *Nano Letters*, **6** (3), 562-7 (2006).
- [6] B. S. Harrison, and A. Atala, "Carbon nanotube applications for tissue engineering", *Biomaterials*, **28** (2), 344-53 (2007).
- [7] A. O. Lobo, E. F. Antunes, M. B. S. Palma, C. Pacheco-Soares, *et al.*, "Biocompatibility of multi-walled carbon nanotubes grown on titanium and silicon surfaces", *Materials Science & Engineering C-Biomimetic and Supramolecular Systems*, **28** (4), 532-8 (2008).
- [8] K. S. Dancil, D. P. Greiner, and M. J. Sailor, "A Porous Silicon Optical Biosensor: Detection of Reversible Binding of IgG to a Protein A-Modified Surface", *J. Am. Chem. Soc.*, **121**, 7925-30 (1999).
- [9] S. D. Alvarez, A. M. Derfus, M. P. Schwartz, S. N. Bhatia, *et al.*, "The compatibility of hepatocytes with chemically modified porous silicon with reference to in vitro biosensors", *Biomaterials*, **30**, 26-34 (2009).
- [10] S. C. Bayliss, R. Heald, D. I. Fletcher, and L. D. Buckberry, "The Culture of Mammalian Cells on Nanostructured Silicon", *Adv. Mater.*, **11** (4), 318-21 (1999).
- [11] E. J. Anglin, M. P. Schwartz, V. P. Ng, L. A. Perelman, *et al.*, "Engineering the Chemistry and Nanostructure of Porous Silicon Fabry-Perot Films for Loading and Release of a Steroid", *Langmuir*, **20** (25), 11264-9 (2004).
- [12] A. Jane, R. Dronov, A. Hodges, and N. H. Voelcker, "Porous silicon biosensors on the advance", *Trends in Biotechnology*, **27** (4), 230-9 (2009).
- [13] B. S. Flavel, M. J. Sweetman, C. J. Shearer, J. G. Shapter, *et al.*, "Micropatterned Arrays of Porous Silicon: Toward Sensory Biointerfaces", *ACS Applied Materials & Interfaces*, **3** (7), 2463-71 (2011).
- [14] S. P. Low, K. A. Williams, L. T. Canham, and N. H. Voelcker, "Evaluation of mammalian cell adhesion on surface-modified porous silicon", *Biomaterials*, **27** (26), 4538-46 (2006).
- [15] K. A. Kilian, L. M. H. Lai, A. Magenau, S. Cartland, *et al.*, "Smart Tissue Culture: in Situ Monitoring of the Activity of Protease Enzymes Secreted from Live Cells Using Nanostructured Photonic Crystals", *Nano Letters*, **9** (5), 2021-5 (2009).

- [16] M. P. Schwartz, A. M. Derfus, S. D. Alvarez, S. N. Bhatia, *et al.*, "The Smart Petri Dish: A Nanostructured Photonic Crystal for Real-Time Monitoring of Living Cells", *Langmuir*, **22** (16), 7084-90 (2006).
- [17] J. Watanabe, T. Eriguchi, and K. Ishihara, "Cell Adhesion and Morphology in Porous Scaffold Based on Enantiomeric Poly(lactic acid) Graft-type Phospholipid Polymers", *Biomacromolecules*, **3** (6), 1375-83 (2002).
- [18] J.-Y. Shiu, C.-W. Kuo, W.-T. Whang, and P. Chen, "Observation of enhanced cell adhesion and transfection efficiency on superhydrophobic surfaces", *Lab on a Chip*, **10** (5), 556-8 (2010).
- [19] S.-R. Ryoo, Y.-K. Kim, M.-H. Kim, and D.-H. Min, "Behaviors of NIH-3T3 Fibroblasts on Graphene/Carbon Nanotubes: Proliferation, Focal Adhesion, and Gene Transfection Studies", *ACS Nano*, **4** (11), 6587-98 (2010).
- [20] T. E. McKnight, A. V. Melechko, D. K. Hensley, D. G. J. Mann, *et al.*, "Tracking Gene Expression after DNA Delivery Using Spatially Indexed Nanofiber Arrays", *Nano Letters*, **4** (7), 1213-9 (2004).
- [21] M. J. Sweetman, C. J. Shearer, J. G. Shapter, and N. H. Voelcker, "Dual Silane Surface Functionalization for the Selective Attachment of Human Neuronal Cells to Porous Silicon", *Langmuir*, **27** (15), 9497-503 (2011).
- [22] K. L. Prime, and G. M. Whitesides, "Adsorption of proteins onto surfaces containing end-attached oligo(ethylene oxide): a model system using self-assembled monolayers", *Journal of the American Chemical Society*, **115** (23), 10714-21 (1993).
- [23] Z. Chen, W. Chen, B. Yuan, L. Xiao, *et al.*, "In Vitro Model on Glass Surfaces for Complex Interactions between Different Types of Cells", *Langmuir*, **26** (23), 17790-4 (2010).
- [24] E. Ben-Jacob, and Y. Hanein, "Carbon nanotube micro-electrodes for neuronal interfacing", *Journal of Materials Chemistry*, **18** (43), 5181-6 (2008).
- [25] M. P. Schwartz, A. M. Derfus, S. D. Alvarez, S. N. Bhatia, *et al.*, "The Smart Petri Dish: A Nanostructured Photonic Crystal for Real-Time Monitoring of Living Cells", *Langmuir*, **22** (16), 7084-90 (2006).
- [26] G. L. Prasanna, and T. Panda, "Electroporation: basic principles, practical considerations and applications in molecular biology", *Bioprocess and Biosystems Engineering*, **16** (5), 261-4 (1997).
- [27] Y. Inoue, H. Fujimoto, T. Ogino, and H. Iwata, "Site-specific gene transfer with high efficiency onto a carbon nanotube-loaded electrode", *Journal of The Royal Society Interface*, **5** (25), 909-18 (2008).
- [28] T. Tryfona, and M. T. Bustard, "Enhancement of biomolecule transport by electroporation: A review of theory and practical application to transformation of *Corynebacterium glutamicum*", *Biotechnology and Bioengineering*, **93** (3), 413-23 (2006).
- [29] F. M. Ausubel, R. Brent, R. E. Kingston, D. D. Moore, *et al.*, "Current Protocols in Molecular Biology", *John Wiley & Sons*, New York, (2003).
- [30] Y. L. Khung, G. Barritt, and N. H. Voelcker, "Using continuous porous silicon gradients to study the influence of surface topography on the behaviour of neuroblastoma cells", *Experimental Cell Research*, **314** (4), 789-800 (2008).
- [31] Z. Zhang, W. Knoll, and R. Förch, "Amino-functionalized plasma polymer films for DNA immobilization and hybridization", *Surface and Coatings Technology*, **200** (1-4), 993-5 (2005).

- [32] N. W. S. Kam, Z. Liu, and H. Dai, "Functionalization of Carbon Nanotubes via Cleavable Disulfide Bonds for Efficient Intracellular Delivery of siRNA and Potent Gene Silencing", *Journal of the American Chemical Society*, **127** (36), 12492-3 (2005).
- [33] W. T. Godbey, K. K. Wu, and A. G. Mikos, "Poly(ethylenimine)-mediated gene delivery affects endothelial cell function and viability", *Biomaterials*, **22** (5), 471-80 (2001).
- [34] H. Lv, S. Zhang, B. Wang, S. Cui, *et al.*, "Toxicity of cationic lipids and cationic polymers in gene delivery", *Journal of Controlled Release*, **114** (1), 100-9 (2006).

Chapter 8

Conclusions

8.1 Conclusions

The chemical attachment of carbon nanotubes to silicon was investigated for use in water filtration, field emission and as a scaffold for biomaterial immobilisation. Single, double and multi-walled carbon nanotubes were chemically attached to silicon. The alignment of each CNT type varied depending upon their level of functionalisation. SWCNTs were shown to orient vertically from the surface while DWCNTs were shown to attach with both vertical and random alignment and the MWCNTs were shown to attach with an exclusive horizontal alignment.

Control over the placement of SWCNTs was shown by producing both surface coverage gradients and patterns of SWCNTs on Si substrates. Surface coverage gradients were achieved using both a topographical surface gradient and a surface chemical gradient. Both gradient fabrication procedures produced surfaces with a broad range of CNT coverage values which have the potential to efficiently determine the optimal CNT coverage for a particular application. SWCNT patterning was achieved by producing a silane pattern using conventional photolithographic means. Subsequent SWCNT chemical attachment to the silane pattern produced SWCNT patterns with dimensions limited by the original pattern fabricated on the photoresist material.

SWCNT membranes were fabricated by chemically attaching SWCNTs to a pSi membrane support, filling the gaps between the SWCNTs with polymer followed by revealing the SWCNT tips via plasma treatment. Water transport was observed through the membranes at permeability values approximately equal that of a commercial reverse osmosis membrane but 90 – 800 times lower than other CNT membranes reported. The low permeability of the SWCNT membranes was attributed to the inhomogeneity of the polymer layer and the brittle nature of the pSi membrane support. The chemical attachment of SWCNTs to pSi is not an optimal fabrication process for a CNT membrane.

Field emission from the Si-CNT substrates was shown to exhibit FE characteristics (turn-on field and electric field enhancement factor) within the top 20 % of values reported. The field emission stability from the Si-SWCNT electrodes was shown to be superior to that of the DWCNT and MWCNT electrodes, which is

in contrast to other results in the literature. The Si-SWCNT electrode was shown to maintain a current density of $\sim 750 \mu\text{A cm}^{-2}$ for over 14 hr with negligible change in applied voltage. The increase in stability was attributed to the chemical attachment reducing CNT desorption.

The pSi-SWCNT substrates proved to be a suitable scaffold for the investigation of the proliferation and morphology of the mammalian neuronal cell line SK-N-SH. Patterning of the surface lead to patterning of the immobilised cells. Evidence from staining specific cellular elements suggested that the SWCNTs permeabilised the cell membrane. However, the efficient transfection of a plasmid DNA was not achieved. Electroporation of the cells immobilised on Si-SWCNT scaffolds was attempted but the effect of the SWCNTs was negligible compared to the control substrates.

8.2 Future directions

It does not seem likely that a commercial water filtration membrane will be prepared using CNTs chemically attached to a supporting substrate. The small height of the chemically attached CNTs make it difficult to produce a membrane strong enough to withstand the applied pressure required. Increasing the height of the chemically attached CNTs is not a trivial exercise. Although it seems simple that cutting the CNTs (ultrasonication in mixed acid) for a shorter time will lead to longer CNTs in solution and hence taller CNTs on the surface, this does not occur in practice. In fact, cutting for a shorter time seems to produce SWCNT solutions that are less soluble, as the number of functional groups on the SWCNTs decrease, and therefore are less likely to chemically attach to the surface. When Si-SWCNT substrates are produced from a solution of 'longer' SWCNTs AFM imaging reveals CNTs of similar height but at a lower surface coverage (compared to the 'standard' CNT length). To increase the strength of the CNT membrane, polymers with higher strength could be used. Such polymers may be difficult to deposit in thin films. The other possibility to increase membrane strength is to use a support other than pSi. Porous alumina (pAl) is a possible candidate. pAl is formed by the electrochemically etching of aluminium disks.^[1] The surface chemistry of pAl is different to that of silicon but the deposition of silane layers onto pAl has been reported.^[2] The major drawback of pAl is that the current minimum pore size reported is 20 nm with pore size ranges of 70 – 150 nm most common. The chemical attachment of SWCNTs to pAl with pore sizes of this range was investigated and it was found that the diameter of the SWCNT bundles was not large enough to transcend the pores, making them ill-suited for membrane applications.

The most promising area of CNT membrane fabrication for water filtration is the CVD growth of vertically aligned CNTs. As the CVD process is further refined, the growth of pristine CNTs of consistent height and diameter will become possible. The next barrier to creating a membrane is the polymer deposition. To ensure that the polymer – CNT adhesion is strong, without gaps there should be a covalent interaction between them. To achieve this, the ideal CNT membrane will consist of DWCNTs with a pristine inner CNT of low diameter (< 1 nm) for enhanced, selective flow of water molecules while the outer CNT wall can be functionalised

(e.g. via plasma treatment) with groups that will promote adhesion with the polymer filler. For example, reverse addition fragmentation chain transfer (RAFT) polymerisation chain transfer agents (CTAs) could be formed on the surface of the outer CNT where a polymer can be then be grafter-from or grafted-to the CNT.^[3, 4] The growth of an entire polymer film may not be plausible but better mixing between the CNTs and a second deposited polymer (e.g., spin coating or CVD) may be possible.

The Si-SWCNT electrodes proved to be a remarkable field emitting substrate, considering their ease of fabrication. While the emission stability seemed promising, a commercial product will require an output current density of 1 – 10 mA cm⁻² to be stable for a greater period of time. For example, as an electron source in a SEM or TEM a SWCNT field emission electrode may be required to last 100's of hours whereas in a television or computer monitor the SWCNT field emission electrode will be required to be stable for 1000's of hours. There is no evidence to suggest that the Si-SWCNT electrodes could not achieve the required current density for application, further investigation into the maximum current density output (and the emission stability at that output) of the Si-SWCNT electrodes is urgently required.

After the initial wave of reports of field emission from CNTs, the number of publications has begun to decrease in recent years (Figure 8.1). This decrease may be caused by a number of reasons but a major factor is that no commercial product that uses a CNT field emission electron source is currently on the market. Improvements to emission stability are required. As the CVD production of CNTs is continually refined, the growth CNTs with high aspect ratio and little defects will become possible. The deposition of a thin polymer layer should increase emission stability by reducing CNT desorption.^[5]

A second factor in the decrease in publications could be the changing market of display technologies. Electron sources were the major component of cathode ray tube televisions and monitors which have recently been replaced by LCD (liquid crystal display) and plasma technologies. Although it may be argued that they are in competition, CNT surfaces have the potential to be used as a component in LCD screens. Pictures are formed on LCD screens by the manipulation and alignment of liquid crystals under the application of an applied field. The electric field enhancement of CNTs can be used to reduce the voltage required to control the

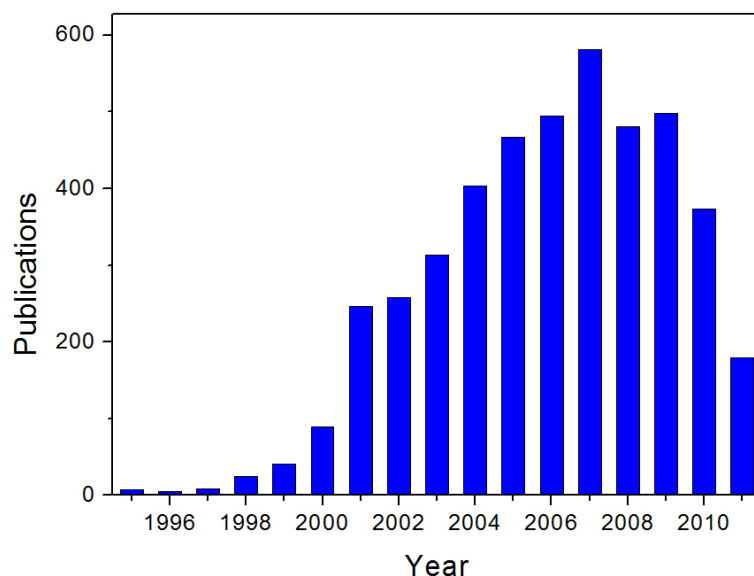


Figure 8.1: Publication number for articles containing both “carbon nanotube” and “field emission” obtained using SciFinder search function 8/8/11.

crystals, reducing power consumption.^[6] The resolution of the display created will be determined by the spacing of patterned CNT features with feature resolution of less than $2\ \mu\text{m}$ desired.^[7] The photolithography patterning of SWCNTs chemically attached to silicon described in Chapter 4 could produce patterns in the region of $10\ \mu\text{m}$. In order to pattern the SWCNTs down to the $1\ \mu\text{m}$ scale e-beam lithography^[8] or AFM nanolithography^[9] could be used.

The investigation of cellular interactions with nanoarchitectures is predominantly studied in biology based research groups. These research groups often do not have access to the sophisticated equipment required for the growth of vertically-aligned CNTs by CVD methods. It is for this reason that the chemical attachment of SWCNTs to surfaces to produce scaffolds for cellular interfacing is an exciting area of research. The interaction of SWCNTs with various cell lines and under various conditions can be investigated by a vast array of research groups which otherwise would not have the opportunity.

The adsorption of the pDNA to the SWCNTs is a vital component of gene transfection by both permeabilisation and electroporation. To further control the adsorption and release of the DNA, the use of a cleavable linker could be investigated. Recent research has shown that a chemical linker with a disulphide

moiety can be used to bind plasmid DNA to CNTs. Enzymatic activity within the cell membrane is then capable of cleaving the linker, leaving the DNA to be freely taken into the cell.^[10] This process can be repeated on the chemically attached SWCNTs using the remaining carboxylic acid functional groups. Figure 8.2 details a possible mechanism where simple coupling chemistry is used to functionalise the SWCNTs with first ethylenediamine (molecule a in Figure 8.2) and then the cleavable linker containing the desired moiety for transfection (molecule b).

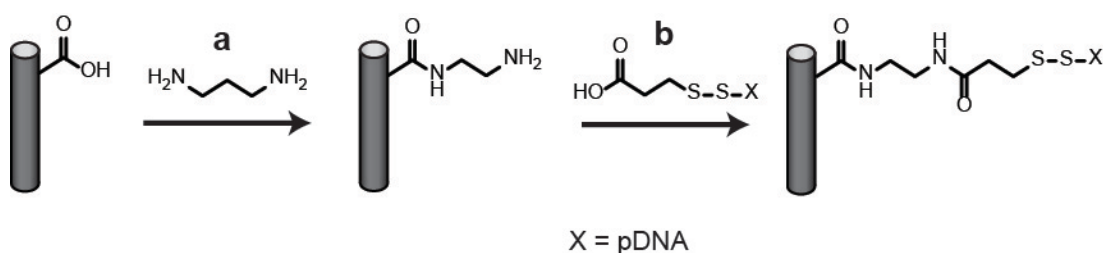


Figure 8.2: Proposed schematic of the chemical attachment of DNA to carboxy-CNTs via a cleavable linker containing a disulphide group.

Although the observed gene transfection was low for the SK-N-SH cell line, there are many other cell lines of interest which may behave differently upon SWCNT scaffolds. Of particular interest will be cells that have a preference for rough substrates such as human umbilical endothelial cells.^[11]

The electroporation experiments were surprisingly unsuccessful considering the large electric field enhancement observed in the field emission experiments. Improvements to the electroporation apparatus may be necessary. The electroporation procedure used required the Si-SWCNT-cell substrate to be removed from the culture plate for electroporation. The manual handling of the substrate and manoeuvring of the o-ring was considered to be a major cause in the lower viability observed for the cells after electroporation. To remove the need to handle the Si-SWCNT substrates after cell culture, an electroporation apparatus that could be used for both cell culture and electroporation should be designed. The ideal apparatus would be similar that shown in Figure 8.3 where a substrate is sealed into place in a custom-built Teflon cell with a fixed height cavity where a platinum electrode can be placed for electroporation experiments.

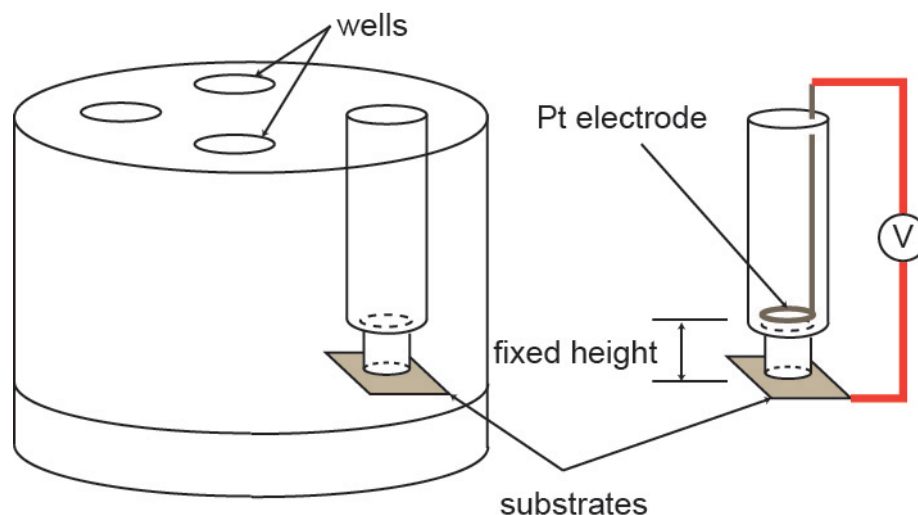


Figure 8.3: Schematic of proposed improved electroporation apparatus where both cell culture and electroporation are completed within the same cell.

This Thesis has shown that the chemical attachment of SWCNTs to silicon can be used to create field emission electrodes and scaffolds for bioengineering but there are further applications that surfaces created in this fashion may find use. Chemical and biological sensors as well as photovoltaic devices have already been reported.^[12-14]

The electrical conductivity of these surfaces makes them suitable scaffolds for storage of molecular hydrogen.^[15] The obstacles for application in hydrogen storage include the relatively low surface area of the thin films created and the inaccuracies in calculating the mass of attached CNTs. A high surface area is desirable as it will increase storage capacity; the chemical attachment of CNTs to 3-dimensional nanostructured surfaces and the use of MWCNTs have the potential to increase the surface area of the Si-CNT substrates. The accurate calculation of CNT mass is required to determine the storage efficiency and applied charge required during experimentation. The value of CNT mass could potentially be calculated by attaching CNTs to a gold surface within a quartz crystal microbalance. However, whether the value obtained on a gold surface will be the same as for Si is debateable.

Despite the promise of device application, a major problem must be addressed before the commercialisation of devices based on chemically attached CNTs can become a reality. The variability, regarding CNT density and alignment, in surfaces produced can be quite vast (see error bars in Figure 3.4). The variability is attributed to the use of the coupling agent DCC which is well known to produce various side

products.^[16] To improve the surface chemistry, additives such as 1-hydroxy-1*H*-benzotriazole (HOBt) or 1-hydroxy-7-azabenzotriazole (HOAt) can be used in conjunction with DCC and have been shown to reduce the number of side reactions in DCC assisted coupling.^[17] In addition, coupling agents other than DCC can be used, DIC (diisopropylcarbodiimide) is a different form of carbodiimide coupling agent which has been shown to produce less side products while HATU (O-(7-azabenzotriazol-1-yl)-1,1,3,3-tetra-methyluronium hexafluorophosphate) is a uronium/aminium salt which is considered an elite coupling agent.^[18, 19]

It is clear that the properties of CNTs make them attractive for a large number of applications, many of which require surface-bound CNTs. The chemical attachment of CNTs to Si is a promising route toward device application.

8.3 References

- [1] M. Whitby, L. Cagnon, M. Thanou, and N. Quirke, "Enhanced Fluid Flow through Nanoscale Carbon Pipes", *Nano Letters*, **8** (9), 2632-7 (2008).
- [2] V. Szczepanski, I. Vlassioux, and S. Smirnov, "Stability of silane modifiers on alumina nanoporous membranes", *Journal of Membrane Science*, **281** (1-2), 587-91 (2006).
- [3] G. Moad, E. Rizzardo, and S. H. Thang, "Living Radical Polymerisation by the RAFT Process", *Australian Journal of Chemistry*, **58** (6), 379-410 (2005).
- [4] G. Viswanathan, N. Chakrapani, H. Yang, B. Wei, *et al.*, "Single-Step in Situ Synthesis of Polymer-Grafted Single-Wall Nanotube Composites", *Journal of the American Chemical Society*, **125** (31), 9258-9 (2003).
- [5] A. Pandey, A. Prasad, J. P. Moscatello, and Y. K. Yap, "Stable Electron Field Emission from PMMA CNT Matrices", *ACS Nano*, **4** (11), 6760-6 (2010).
- [6] T. D. Wilkinson, X. Wang, K. B. K. Teo, and W. I. Milne, "Sparse Multiwall Carbon Nanotube Electrode Arrays for Liquid-Crystal Photonic Devices", *Advanced Materials*, **20** (2), 363-6 (2008).
- [7] D. Qing, and *et al.*, "Transparent liquid-crystal-based microlens array using vertically aligned carbon nanofiber electrodes on quartz substrates", *Nanotechnology*, **22** (11), 115201 (2011).
- [8] W. Chen, and H. Ahmed, "Fabrication of 5-7 nm wide etched lines in silicon using 100 keV electron-beam lithography and polymethylmethacrylate resist", *Applied Physics Letters*, **62** (13), 1499-501 (1993).
- [9] B. S. Flavel, J. Yu, J. G. Shapter, and J. S. Quinton, "Patterned attachment of carbon nanotubes to silane modified silicon", *Carbon*, **45**, 2551-8 (2007).
- [10] N. W. S. Kam, Z. Liu, and H. Dai, "Functionalization of Carbon Nanotubes via Cleavable Disulfide Bonds for Efficient Intracellular Delivery of siRNA and Potent Gene Silencing", *Journal of the American Chemical Society*, **127** (36), 12492-3 (2005).
- [11] F. Gentile, L. Tirinato, E. Battista, F. Causa, *et al.*, "Cells preferentially grow on rough substrates", *Biomaterials*, **31** (28), 7205-12 (2010).
- [12] M. A. Bissett, and J. G. Shapter, "Photocurrent Response from Vertically Aligned Single-Walled Carbon Nanotube Arrays", *The Journal of Physical Chemistry C*, **114** (14), 6778-83 (2010).
- [13] J. J. Gooding, R. Wibowo, J. Liu, W. Yang, *et al.*, "Protein Electrochemistry Using Aligned Carbon Nanotube Arrays", *Journal of the American Chemical Society*, **125**, 9006-7 (2003).
- [14] J. Yu, J. G. Shapter, J. S. Quinton, M. R. Johnston, *et al.*, "Direct attachment of well-aligned single-walled carbon nanotube architectures to silicon (100) surfaces: a simple approach for device assembly", *Physical Chemistry Chemical Physics*, **9**, 510-20 (2007).
- [15] A. Züttel, P. Sudan, P. Mauron, T. Kiyobayashi, *et al.*, "Hydrogen storage in carbon nanostructures", *International Journal of Hydrogen Energy*, **27** (2), 203-12 (2002).
- [16] E. Valeur, and M. Bradley, "Amide bond formation: beyond the myth of coupling reagents", *Chemical Society Reviews*, **38** (2), 606-31 (2009).
- [17] L. A. Carpino, "1-Hydroxy-7-azabenzotriazole. An efficient peptide coupling additive", *Journal of the American Chemical Society*, **115** (10), 4397-8 (1993).

- [18] L. A. Carpino, and A. El-Faham, "The diisopropylcarbodiimide/ 1-hydroxy-7-azabenzotriazole system: Segment coupling and stepwise peptide assembly", *Tetrahedron*, **55** (22), 6813-30 (**1999**).
- [19] A. El-Faham, and F. Albericio, "Morpholine-Based Immonium and Halogenoamidinium Salts as Coupling Reagents in Peptide Synthesis", *The Journal of Organic Chemistry*, **73** (7), 2731-7 (**2008**).